LASER DOPPLER VELOCITY INSTRUMENT

by E. Rolfe, J. K. Silk, S. Booth, K. Meister,
and R. M. Young

NASA CR-1199

LASER DOPPLER VELOCITY INSTRUMENT

By E. Rolfe, J. K. Silk, S. Booth,
K. Meister, and R. M. Young

Distribution of this report is provided in the interest of
information exchange. Responsibility for the contents
resides in the author or organization that prepared it.

Issued by Originator as Report No. R67-4450

NATIONAL AERONAUTICS AND SPACE ADMINISTRATION

ABSTRACT

This document is the final report on an analytical and experimental program directed to the development of a Laser Doppler Velocity instrument for the measurement of gas velocity. The instrument measures the doppler shift of light scattered from particles moving with the gas, using Mie (Rayleigh-Gans) scattering. The velocity thus measured is independent of particle temperature.

The basic design parameters were clearly determined, and forms of the important analytical relationships verified experimentally. An experimental comparison of the hot wire anemometer with the Laser Doppler Velocity instrument demonstrated excellent correspondence between the two.

Measurements of velocity up to approximately Mach 2 were made in the Seven Inch Wind Tunnel at the NASA George C. Marshall Space Flight Center, which compared well with simultaneous velocity measurements using the existing conventional tunnel instrumentation.

Measurements were made with a one watt argon laser, and with a 50 milliwatt helium-neon laser.

Several methods of signal processing were investigated and an optimum design concept established. This consisted of a wide range narrow band frequency tracker, whose output can be directly recorded on tape to give all necessary information on turbulence and velocity.

A three dimensional form of the instrument was designed, built, and is now being lined up and calibrated ready for use at NASA facilities.

ACKNOWLEDGEMENTS

CONTENTS

CONTENTS (Continued)

CONTENTS (Continued)

CONTENTS (Continued)

CONTENTS (Continued)

ILLUSTRATIONS

ILLUSTRATIONS (Continued)

ILLUSTRATIONS (Continued)

ILLUSTRATIONS (Continued)

ILLUSTRATIONS (Continued)

Section I

INTRODUCTION

During the past year, intensive work by the Raytheon Company
in partnership with the Aero-Thermal-Physics section of George C.
Marshall NASA Space Flight Center was directed to the development
of a Laser Doppler Velocity Instrument. The results of this work
have been the development and demonstration of a device capable
of measuring both turbulence and mean velocity in subsonic and
supersonic gas flows. The work followed naturally from explora-
tory investigations of optical doppler frequency shifts as a
means of measuring velocity, started independently by the Raytheon
Company and by the NASA team some three years ago.

Using an experimental laboratory system, gas velocities up
to Mach 2 were measured in the NASA Seven Inch Wind Tunnel
facilities. The turbulence power spectrum of flow from a nozzle
was obtained by computer processing the output signal from the
instrument. The resulting power spectral density curve matched
very closely that obtained with the use of a hot wire anemometer.

With smoke injected into gas flow to provide scattering
particles, signal to noise ratios of 20 to 30 db were obtained
using a one watt Argon laser. An optimization study of the most
important instrument parameters produced a clear understanding of
basic principles with good agreement between analysis and experi-
ment, and permitted the definition of explicit operating modes
for optimum signal to noise ratio. Design principles thus
established were applied to the development of an instrument for
measurement of the three components of the instantaneous fluid
velocity vector. This instrument is now being aligned and checked
before being used for wind tunnel flow and turbulence measurement

at MSFC and AEDC.

Further work remains to be done on several problems: 1) The construction of a special signal frequency tracker, which should result in an improved signal to noise ratio and wider operating range, 2) the establishment of a more acceptable injectant material for the light scattering process, 3) the acquisition of turbulence data in a number of different systems, using the 3-D vector velocity instrument, 4) the investigation of methods of reducing or eliminating instrumental frequency broadening, 5) the further development of the device for cross correlation measurements.

With these improvements, the instrument range of application will be even further extended. Experiments have shown that with an increased instrument sensitivity, scattering from natural air contaminants, such as dust and water drops may prove feasible, eliminating the use of artificial injectants.

2. TECHNICAL DISCUSSION

In the following material the important basic characteristics and parameters of the Laser Doppler Velocity Instrument are analyzed in detail, with supporting experimental data.

2.1 Scattering of Electromagnetic Waves by Particles

This section presents the technical background, analytical treatment and important fundamental features of the scattering of electromagnetic waves by particles, used in a system for Mie scattering measurements of moving gas stream velocity and turbulence.

2.1.1 Mie and Rayleigh Scattering

A review of the fundamental aspects of Mie and Rayleigh scattering, and recent laboratory studies in the visible spectrum is presented below. The discussion of the conventional theory of light scattering is based on the comprehensive treatment of van de Hulst (1).

2.1.2 Fundamental Aspects

The rigorous theory of light scattering from arbitrary spheres was derived from Maxwell's equations by Mie (2). In limiting cases simpler treatments can be used. For example, if the wavelength of the radiation is large compared with the size of the scatterer, the electric field at the scattering center can be taken to be constant and the Rayleigh scattering formula is obtained. Another case of interest occurs when the index of refraction (n) is nearly equal to unity and the size of the scatterer is arbitrary. For these conditions, the Rayleigh scattering by each element of volume of the target can be summed (with the appropriate phase), and the Rayleigh-Gans scattering formula is obtained. This latter situation is sometimes called Mie Scattering, although the term Rayleigh-Gans scattering, used

by van de Hulst, is probably less likely to lead to confusion. The terminology and limiting cases can be conveniently displayed in a map of the n-x plane shown in Figure 2.1-1, where n is the index of refraction relative to the surrounding medium, x is $\frac{2\pi a}{\lambda}$ where a is the size of the scatterer and λ is the wavelength of the radiation.

2.1.3 Rayleigh Scattering

The conventional theory of Rayleigh scattering assumes that the size of the scatterer is much less than $\lambda/2\pi$, i.e., that the scatterer is small compared with a wavelength of the radia- tion. It is further assumed that the applied field penetrates the scatterer so fast that the static polarization is establish- ed in a time small compared with the wave period, i.e., that $|n|$ x size $<< \lambda/2\pi$. The second assumption is equivalent to saying that the particle must be small compared with the wave- length inside the scatterer.

The cross-section for Rayleigh scattering is given by

$$\sigma_{sca} = \frac{8\pi}{3} k^4 |\alpha|^2 , \tag{1}$$

where α is the polarizability tensor and

$$|\alpha|^2 = \ell^2 |\alpha_1|^2 + m^2 |\alpha_2|^2 + n^2 |\alpha_3|^2 \text{ where } \ell, m, n, \text{ are the}$$

direction cosines of the incident radiation $\vec{E}$ vector with res- pect to the principal axes of the polarizability tensor. The quantity k is as usual, $2\pi/\lambda$. For isotropic scatters,

$\alpha_1 = \alpha_2 = \alpha_3 = \alpha$ and $|\alpha|^2$ is a scalar. When α is scalar, if the

incident $\vec{E}$ vector is in the plane of scattering, the angular dependence is $\cos^2\theta$ where θ is the scattering angle, and the differential scattering cross-section, do, for power scattered
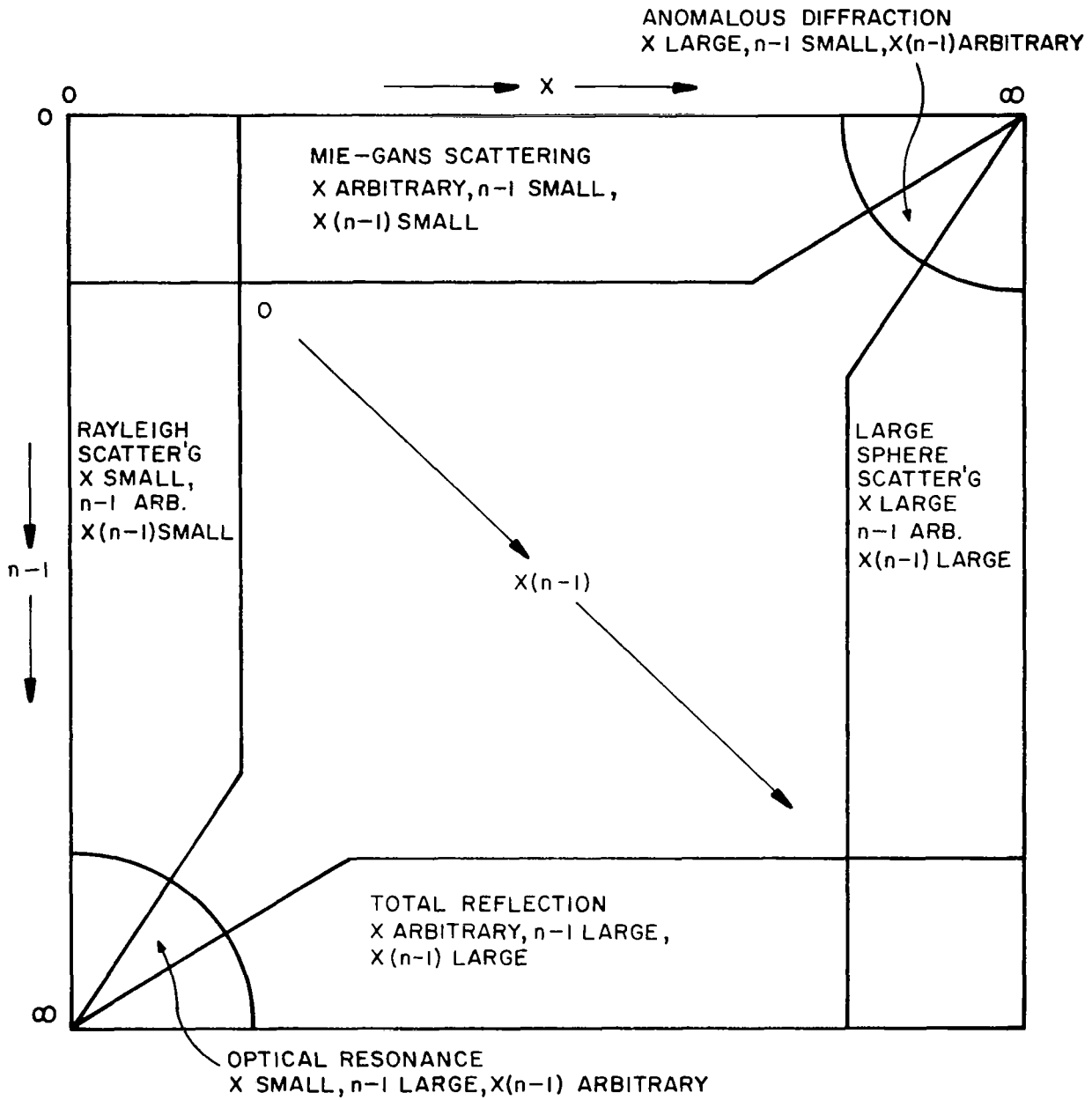
Figure 2.1-1.   Map of n - x Plane

into the solid angle $d\Omega$ is

$$\frac{d\sigma}{d\Omega} = k^4 \alpha^2 \cos^2\theta \tag{2}$$

When the $\vec{E}$ vector is perpendicular to the plane of scattering, the angular distribution is isotropic. For spheres radius of a, α is given by the Lorentz-Lorentz equation (1)

$$\alpha = \frac{n^2 - 1}{n^2 + 2} a^3 \tag{3}$$

2.1.4 Rayleigh-Gans (Mie) Scattering

Rayleigh-Gans, commonly called Mie, scattering is derived under two assumptions:

a). The refractive index of the scatterer is on the order of unity: $|n - 1| \ll 1$

b). The difference in phase between a light beam passing through the same distance in the surrounding medium is small, so that $2 k a |n - 1| \ll 1$, where a is the radius of the spherical scatterer.

The scattered amplitude is the Rayleigh-scattered amplitude multiplied by a factor $R(\theta, \phi)$. For $\theta = 0$, $R(\theta, \phi) = 1$ so that forward scattering is given by the Rayleigh formula. For particles with simple geometrical form, $R(0, \phi)$ can be found by simple integration.

The scattering cross-section is given by

$$\sigma_{sca} = \pi a^2 |n - 1|^2 \phi(x) \tag{4}$$

2.1-4

where $x = \frac{2\pi a}{\lambda}$ and $\phi(x)$ is a function tabulated on page 90 of Reference (1). For small spheres, $\phi(x)$ is such that σ_{sca} is the Rayleigh cross-section; while for large spheres $\sigma_{sca} = 2(n-1)^2 x^2$.

2.1.5 Mie Scattering in a Weakly Ionized Gas Containing Carbon Particles

This section briefly illustrates the relative magnitudes of the various scattering processes which will occur in a gas which is weakly ionized (i.e., say 1% or less) and which contains, for example, carbon particles or macromolecules. Such conditions will be found in a high velocity wind tunnel, in a shock tube, or in the exhaust plume of a rocket engine.

Then the total light power, (watts/sec), scattered from any scatterer illuminated by monochromatic light is

$$P(\omega) \propto N \, \sigma_{tot} \tag{5}$$

where N = concentration of scatterers
σ_{tot} = total scattering cross-section.

Directionality of scattering is neglected here for simplification. The following table (2.1-1) gives relative scattered powers calculated for typical scatterers in a representative gas with entrained carbon particles.

TABLE 2.1-1

TYPICAL RELATIVE POWERS OF RAYLEIGH, MIE AND
THOMSON SCATTERING*

Particle	Concentration (number/cm^3) N	Total Scattering Cross-Section σ_{tot} (cm^2)	Relative Scattered Power ($\propto N\sigma_{tot}$)
Gas Molecule (Rayleigh)	10^{19} (Approx. 1 atmos.)	~6 x 10^{-27}	1.7 x 10^{-10}
Carbon Particle Dia. 500 Å (Mie)	10^{16}	3.5 x 10^{-14}	1
Electron (Thomson)	10^{14}	6.7 x 10^{-25}	1.9 x 10^{-13}

*at Wavelength 6493Å

These numbers illustrate that the scattered light from dust particles is relatively intense. This is partly because the effective cross-section is proportional to the square of the volume of the particle. Below is presented a brief discussion of the amplitude of scattering from carbon particles, selected as a probable constituent of rocket exhaust gases.

2.1.5.1 Cross-Sections

Carbon absorbs light and hence has a complex index of refraction. In the vicinity of visible laser wavelengths, the complex refractive index has been measured (3). It is n = 1.59 - 0.66 i. Hence for 500Å diameter carbon particles, n - 1 = .83, x - .227, x (n - 1) = .188. This set of values of the scattering parameters does not provide a clear indication if any of the limiting cases is an adequate description. However the use of Mie's general result in the form of a series expansion shows that a single term, corresponding to the Rayleigh Scattering Limit, is sufficient.

Reference (1) gives a scattering efficiency (defined as the ratio of the scattering cross-section to the geometric cross-section) as

$$Q_{sca} = \frac{8}{3} x^4 \left| \frac{n^2 - 1}{n^2 + 2} \right|^2 \left[1 + \frac{6}{5} \left| \frac{n^2 - 1}{n^2 + 2} \right| x^2 + - - - - \right] \qquad (6)$$

For 500Å diameter carbon particles and 6943Å wavelength, the second term in the series is about 0.02 and can be neglected. Numerical evaluation yields

$$Q_{sca} = 1.8 \times 10^{-3} \qquad (7)$$

and hence $\sigma_{sca} = Q_{sca} A = 3.5 \times 10^{-14}$ cm^2 for 500 Å diameter carbon macromolecules. The cross-section is a quite sensitive function of the particle diameter as is shown in Figure 2.1-2. The angular distribution is $\cos^2 \theta$ for incident light polarized in the plane of scattering, and is uniform for light polarized perpendicular to the scattering plane. Thus the differential scattering cross-sections are:

Unpolarized Light:

$$\frac{d\sigma}{d\Omega} = 9.25 \times 10^{-15} (1 + \cos^2 \theta) \frac{cm^2}{ster} \qquad (8)$$

Polarized parallel to scattering plane:

$$\frac{d\sigma}{d\Omega} = 9.25 \times 10^{-15} \cos^2 \theta \frac{cm^2}{ster} \qquad (9)$$

Polarized perpendicular to scattering plane:

$$\frac{d\sigma}{d\Omega} = 9.25 \times 10^{-15} \frac{cm^2}{ster} \qquad (10)$$
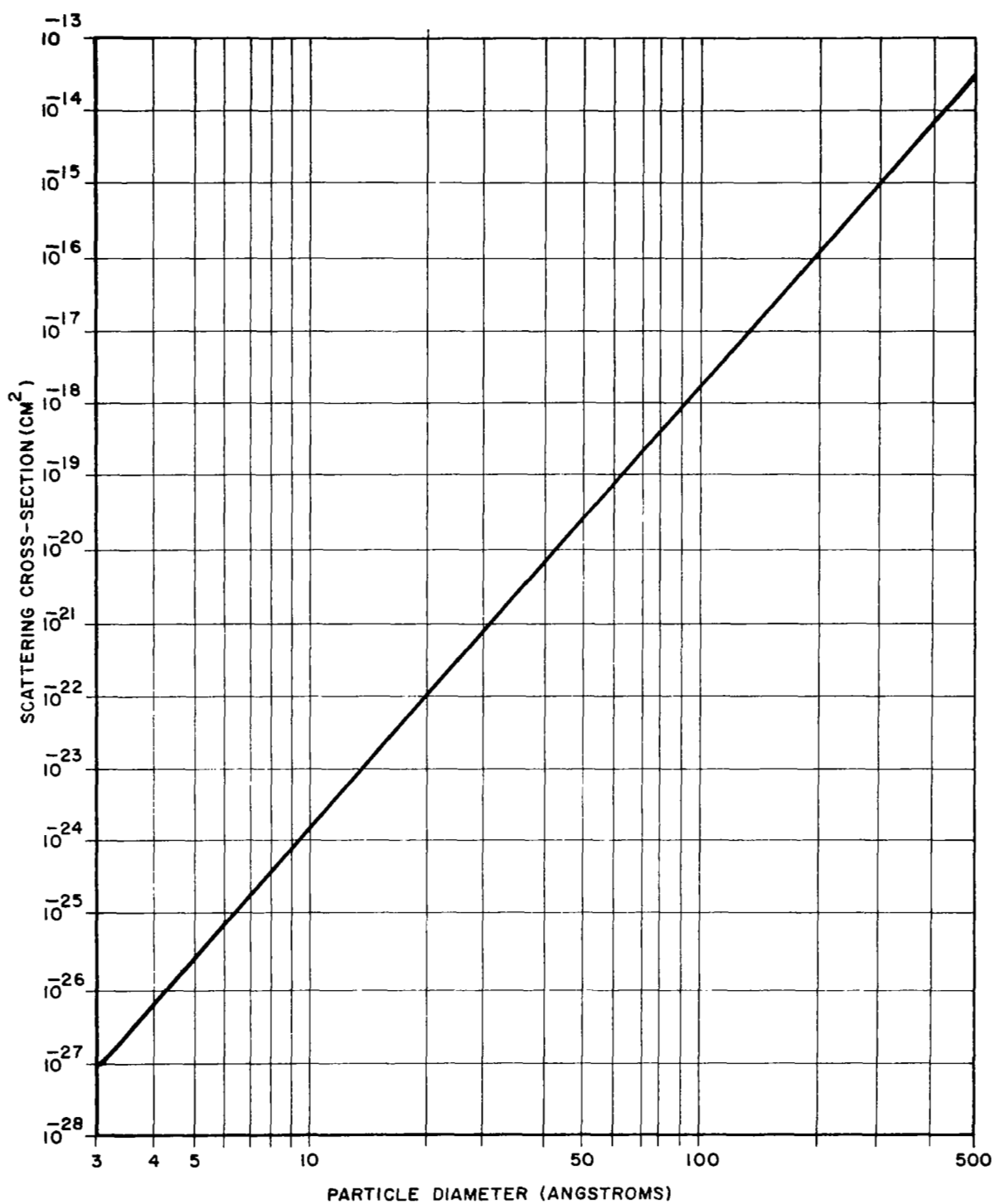
Fig. 2.1-2. Scattering Cross-Section of Carbon Macromolecules.
(Wavelength 6943Å)

2.1-8

These cross-sections are very much larger than the Rayleigh cross-section for scattering from gas molecules (on the order of 6×10^{-27} cm^2) or the Thomson cross-section for scattering from free electrons (6.65×10^{-25} cm^2). Clearly even a very small concentration of macromolecules will dominate the scattering in total intensity. Certainly, in a rocket exhaust we would expect this situation to hold. Our experiments with smoke-injected wind tunnels have shown scattering of laser light to continue even when the smoke injectant is no longer visible to the eye!

REFERENCES FOR SECTION 2.1

1. van de Hulst, H. C., _Light Scattering by Small Particles_, John Wiley & Sons, Inc., New York (1957)

2. Mie, G., Ann Physick, _25_, 377 (1908)

3. George, T. V., Goldstein, L., Slama, L., and Yokoyama, M., Phys. Rev., _137_, A369 (1965).

2.2 Doppler Frequency Shift of Waves Scattered by Moving Particles

This section discusses the Doppler shift of the frequency of light scattered from moving particles. The basic equation relating the Doppler shift to the flow velocity and scattering angles is derived.

Consider a laser beam incident upon a flowing stream of gas, velocity $\vec{v}_s$, at angle α and scattering through an angle θ as shown in Figure 2.2-1. The incident frequency seen by an observer moving with the stream is (1)

$$f' = f_o \left(1 - \frac{v_s \cos \alpha}{c}\right) ; \quad \begin{array}{l} f_o = \text{laser light frequency, sec}^{-1} \\ c = \text{velocity of light, cm- sec}^{-1} \end{array}$$

In the reference frame moving with the stream, the scattered photons have this frequency. The photons scattered by a particle in the gas and received by a stationary detector are further Doppler shifted to frequency f_s given by (1)

$$f_s = f' \left(1 + \frac{v_s \cos (\theta + \alpha)}{c}\right)$$

Thus the scattered frequency is given in terms of the incident frequency by

$$f_s = f_o \left(1 - \frac{v_s \cos \alpha}{c}\right) \left(1 + \frac{v_s \cos(\theta + \alpha)}{c}\right) \tag{1}$$

The frequency shift Δf_s is given by

$$\Delta f_s = (f_s - f_o),$$

which, to order $\frac{v_s}{c}$, is
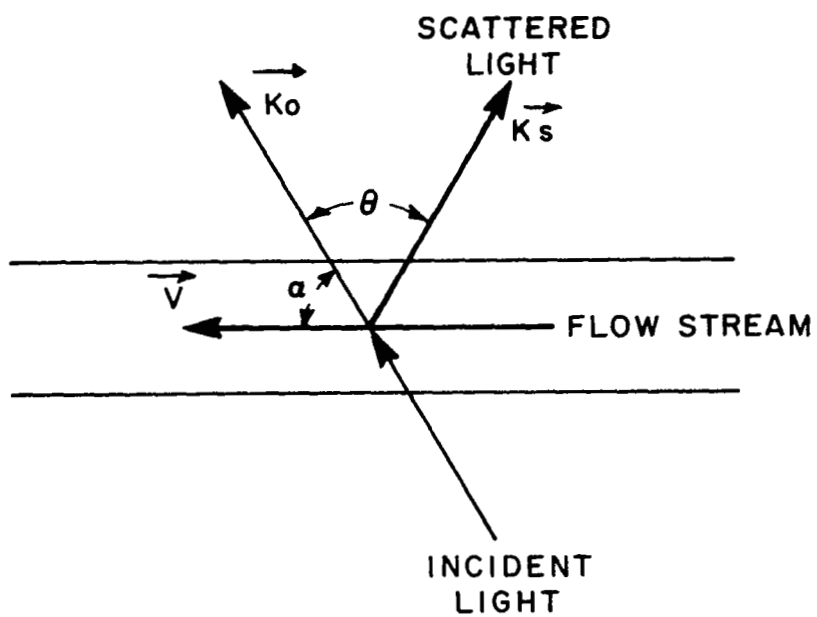
Figure 2.2-1 – Scattering of Light from a Stream of Moving
            Particles

$$\approx f_o \frac{v_s}{c} \left[\cos(\theta + \alpha) - \cos \alpha \right]$$

$$\Delta f_s = f_o \frac{v_s}{c} \left[(\cos \theta - 1) \cos \alpha - \sin \theta \sin \alpha \right] \tag{2}$$

Hence the stream velocity can be determined from the relation

$$v_s = \frac{\Delta f_s}{f_o} c \left[(\cos \theta - 1) \cos \alpha - \sin \theta \sin \alpha \right]^{-1}$$

$$= \frac{\lambda}{\left[(\cos \theta - 1) \cos \alpha - \sin \theta \sin \alpha \right]} \Delta f_s \tag{3}$$

The Doppler shift has been calculated for a laser of wavelength 6328 Å (He-Ne), and is plotted as a function of scattering angle for various angles of incidence in Figure 2.2-2, assuming a gas particle velocity of 3.48×10^4 cm/sec. (i.e., Mach 1).

To obtain the Doppler frequency shift at another wavelength, λ', multiply equation (2), and the ordinate of Figure 2.2-2 by $\frac{\lambda}{\lambda'}$.

It should be noted that equation (3) gives only the magnitude of $|v_s|$, so that measurement of only Δf_s leaves an ambiguity of direction of $\underset{\sim}{v_s}$.

DOPPLER SHIFT vs SCATTERING ANGLE
FOR VARIOUS ANGLES OF INCIDENCE
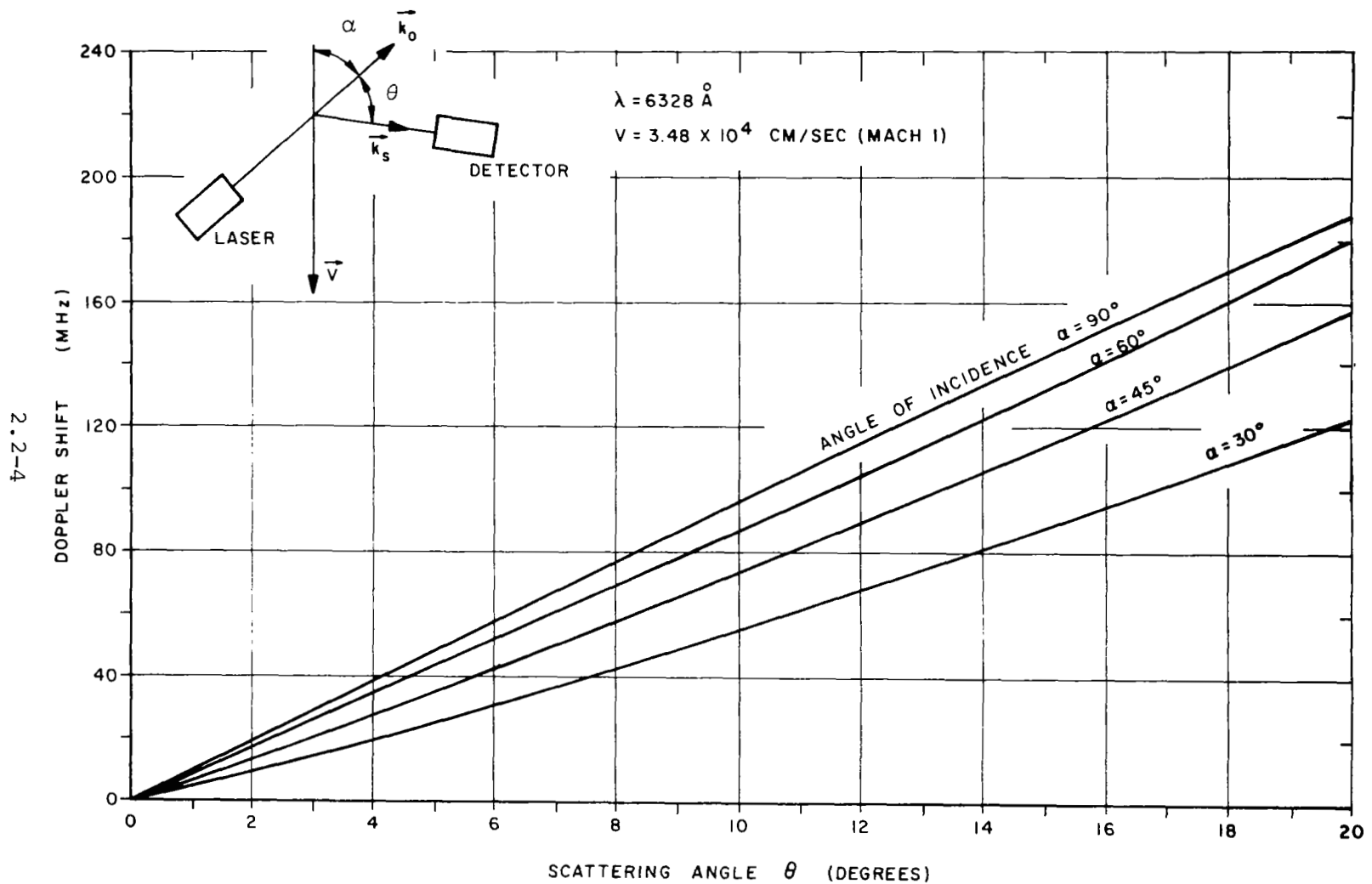
Figure 2.2-2 - Doppler Shift versus Scattering Angle for Various Angles of Incidence

REFERENCES FOR SECTION 2.2

1. Landau and Lifshitz, The Classical Theory of Fields, 11, Addison-Wesley Publishing Company (1959).

2.3 Coherence of Electromagnetic Waves

If two electromagnetic waves of the same amplitude E, frequency, and phase, impinge together on an absorbing surface, the time average power absorbed is proportional to the average of the (total field)^2. In this instance the two field amplitudes would be directly additive, so that the average power absorbed would be proportional to $(2E)^2$, i.e., $4E^2$. These two waves are then said to be coherent.

If, on the other hand, we have two electromagnetic waves of the same amplitude, but having phases which vary randomly with respect to one another, the powers, but not the amplitudes, add; so that the total power absorbed by the surface is now $2E^2$, i.e., one half the power absorbed in the first example. In the second case, the waves are said to be incoherent. It is shown (in Equation (5), Section 2.5.3.1) that this power difference is just the heterodyne signal power which we wish to analyze in the laser doppler velocity meter.

In the case of real light sources, it is impossible to obtain light of a single frequency, since even the sharpest spectral line has a finite width, and a finite physical size. If we consider two different points in the wave field produced by a quasi-monochromatic* extended light source, the two points being close together, the fluctuations of the wave amplitudes at these points, and also the fluctuations of the phases, will not be independent. "Close together" in this case means that $\Delta s \ll \bar{\lambda}$, where Δs is the difference in path length between the source and the two points and $\bar{\lambda}$ is the mean wavelength. In this case, fluctuations at the

---

*defined as a source in which $\frac{\Delta\lambda}{\bar{\lambda}} \ll 1$, where $\bar{\lambda}$ is the mean wavelength of the source, and $\Delta\lambda$ the range of wavelengths of its components around $\bar{\lambda}$.

two points will be effectively the same. If Δs is increased, some correlation between the fluctuations will still be found, provided that, for all points on the source, Δs does not exceed the <u>coherence length</u> cΔt. Here $\Delta t = \frac{1}{\Delta \nu}$ where Δν is the effective spectral width of the light source, and is called the <u>coherence time</u>. Thus $c\Delta t = \frac{c}{\Delta \nu} = \frac{\overline{\lambda}^2}{\Delta \lambda}$. The region over which Δs is less than the conerence length is called the <u>region of coherence</u> around any point in a wave field.

It is clear that in a real wave field, vibrations can be found between which there is nether complete coherence nor complete incoherence. This condition is called <u>Partial Coherence</u>. An excellent and detailed discussion of partially coherent .light appears in Reference (1), and a very readable and practical description in a paper by Zernike (2) who first defined the concept of "degree of coherence" in a way particularly well suited to experiment.

At this time, a detailed discussion on Partial Coherence is unnecessary, and will be developed in later reports as needed. We will close by presenting (but not deriving – see 1, 2) the definition of Complex Degree of Coherence, γ_{12} (τ), of light vibrations of amplitude V_1 and V_2 at two points P_1 and P_2:

$$\gamma_{12}\ (\tau) = \frac{\Gamma_{12}(\tau)}{\sqrt{\Gamma_{11}(o)\ \Gamma_{20}(o)}} = \frac{\Gamma_{12}(\tau)}{\sqrt{I_1}\ \sqrt{I_2}}$$

where $\Gamma_{12}(\tau)$ = $<V_1\ (t + \tau)V_2^{*}(t)>$

= the Mutual Coherence Function of the wave field.

τ = the time difference between measurements of the light amplitudes at P_1 and P_2.

t = time

$$\left\{\begin{matrix} \Gamma_{11} & = & <V_1\ (t + \tau)V_1^{*}(t)> \\ \Gamma_{22} & = & <V_2\ (t + \tau)V_2^{*}(t)> \end{matrix}\right\}$$

= Self Coherence of the light vibrations at P_1 and P_2 respectively.

and $\Gamma_{11}(o) = I_1$
$\left.\right\}$ = ordinary light intensity when $\tau = o$
$\Gamma_{22}(o) = I_2$

While this presentation is somewhat elaborate for such a brief summary, nevertheless we wish to introduce it to show the strong mathematical resemblance between the nature of partially coherent light and of turbulent fluctuations in a fluid flow field.

This becomes evident when we note that, in the general theory of stationary random processes, $\Gamma_{12}(\tau)$ is called the Cross-correlation function of $V_1(t)$ and $V_2(t)$, and $\Gamma_{11}(\tau)$ the Auto-correlation function of $V_1(t)$. This suggests that the degree of fluid turbulence, which is measured by just such functions, is intimately connected with the change in the Degree of Coherence which occurs when quasi-coherent light is scattered from particles in the turbulent flow. The connection is left for later study, but begins to emerge in the results of the analysis presented in Section 2.2.8 where we consider scattering from random scatterers.

REFERENCES FOR SECTION 2.3

1. Born, M., and Wolf, E., _Principles of Optics_, 2nd Ed., Ch. X, The Macmillan Company, N.Y. (1964).

2. Zernike, F., Physica, $\underline{5}$, 785 (1938).

2.4 The Laser Doppler Velocity Instrument

Figure 2.4-1(a) shows a simple form of Laser Doppler Velocity Instrument. The beam from a CW laser is focused by lens L1 on to a small volume in the moving gas stream. Part of the light is scattered, collected by lens L2 and focused on to the cathode of a photomultiplier. The unscattered light is collected by a third lens L3, suitably attenuated by a neutral density filter, brought back by a mirror and beam splitter on to the same axis as the scattered beam, and also focused on to the photomultiplier cathode. The two beams beat together (heterodyne), with the photomultiplier acting as a mixer and intermediate frequency amplifier. Subsequent electronic apparatus extracts and processes the required turbulence and velocity information from the heterodyne signal in terms of conventional fluid flow parameters.

The system is straightforward in concept. However, a number of physical mechanisms are involved, each of which must be correctly set up, which implies that it be understood and analyzed. To achieve an understanding of these mechanisms in the considerable detail needed for system design and optimization, was clearly one of the prime tasks in the investigation. The important mechanisms are listed below, with details in later sections of the report:

1. Source power requirements
2. Source wavelength
3. Source coherence length
4. Scattering volume and instrument resolution
5. Reference beam intensity for maximum signal to noise ratio
6. Atmospheric coherence losses
7. Target coherence losses
8. Geometry of beam alignment and spot size for acceptable mechanical tolerances
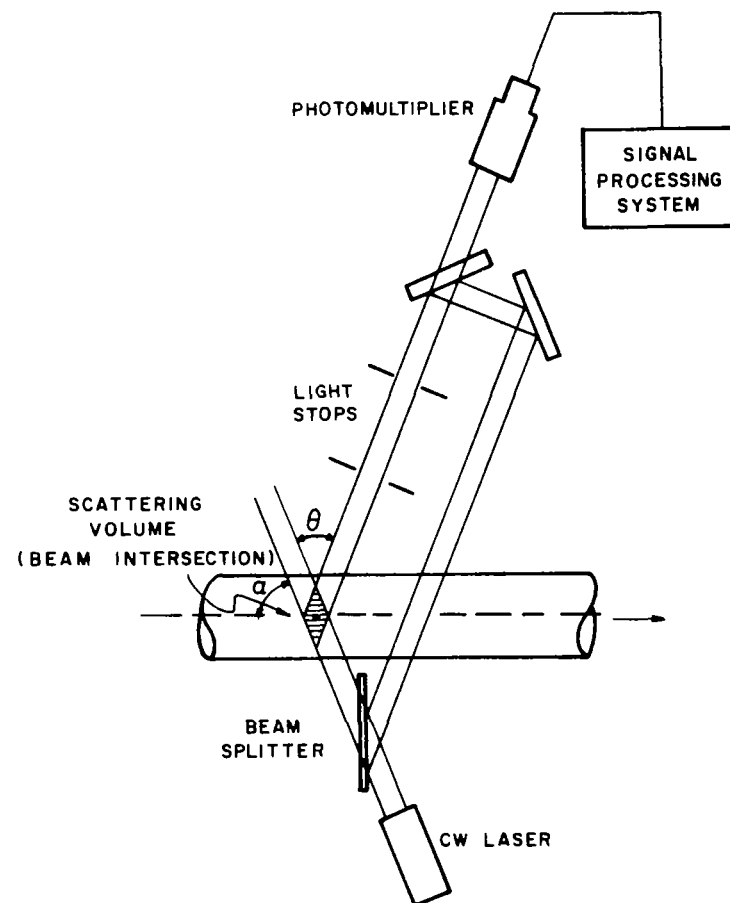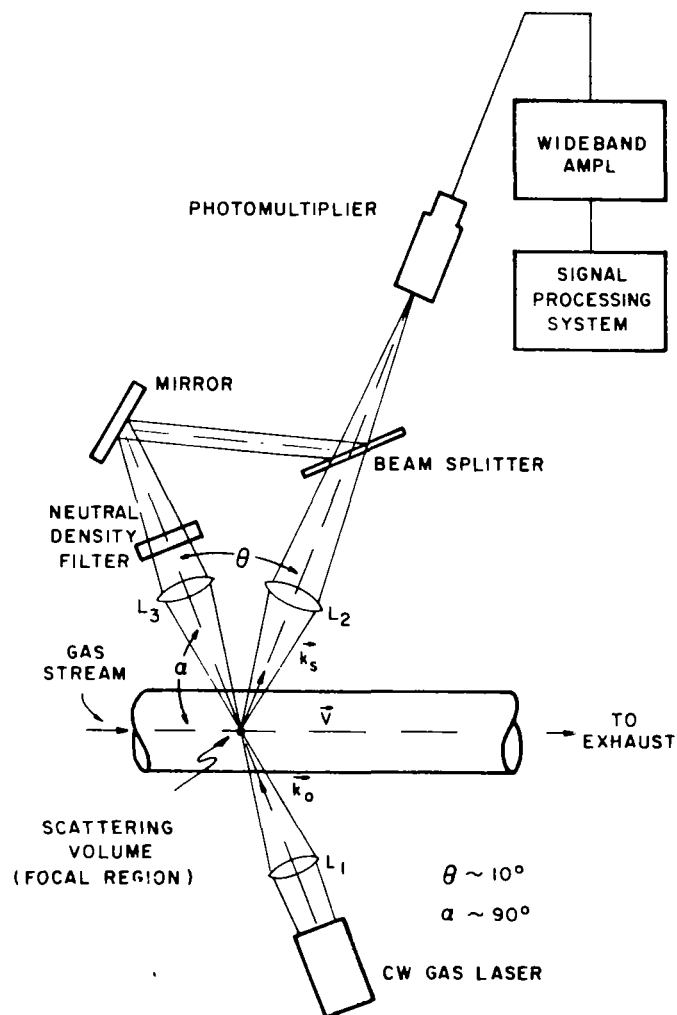
(a) Simple Focussed-beam System, Reference Beam Passing through Flow Stream

(b) Simple Parallel Beam System, Reference Beam Bypassing Flow Stream

Figure 2.4-1 Typical Laser Doppler Velocity Instrument Schematic Diagrams

9. Geometry of beam alignment and spot size for maximum signal to noise ratio

10. System bandwidth in relation to velocity range

11. System bandwidth in relation to system signal to noise ratio

12. Electronic system needed to process in real time, and to record on tape, the time varying Doppler shift, so as to produce velocity and turbulence parameters as outputs

13. Spectral and instrumental broadening of the Doppler signal

A good instrument design must take into account all of these numerous factors. They are incorporated in the 3-D instrument design described later.

A wide variety of different arrangements can be used in the Laser Doppler Velocity Instrument, depending somewhat on the geometry of the system in which measurements are to be made.

Figures 2.4-1(a), 2.4-1(b), 2.4-2(a) and 2.4-2(b) show several possible arrangements, each with its own particular advantages, such as:

Fig. 2.4-1(a): Scattering volume set by lens apertures can be extremely small.

Fig. 2.4-1(b): Allows selection of larger scattering volume.

Fig. 2.4-2(a): Eliminates instrumental broadening - output is twice Doppler frequency shift.

Fig. 2.4-2(b): Eliminates loss of scattered light at the beam splitter necessary in the other three arrangements - output is true Doppler frequency shift.

Numerous other possible arrangements come to mind. Arrangements suitable for remote wind sensing are described in a separate report.
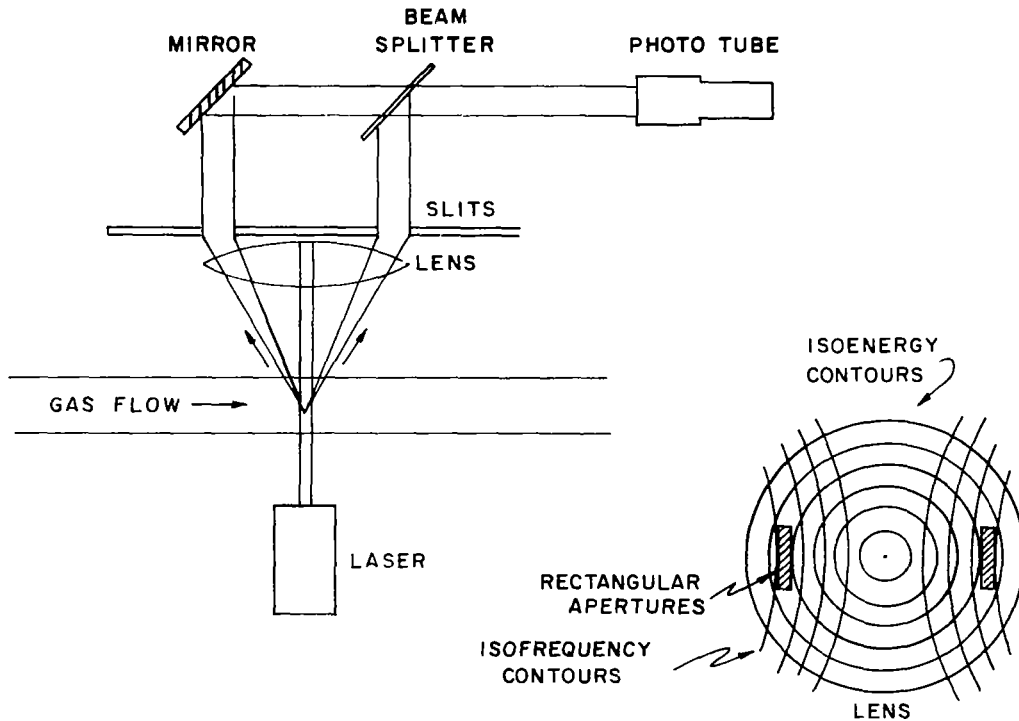
(a) System for Elimination of Instrumental Broadening   (Reference
    R.L. Bond, J.P. Storey, University of Arkansas Graduate
    Institute of Technology)
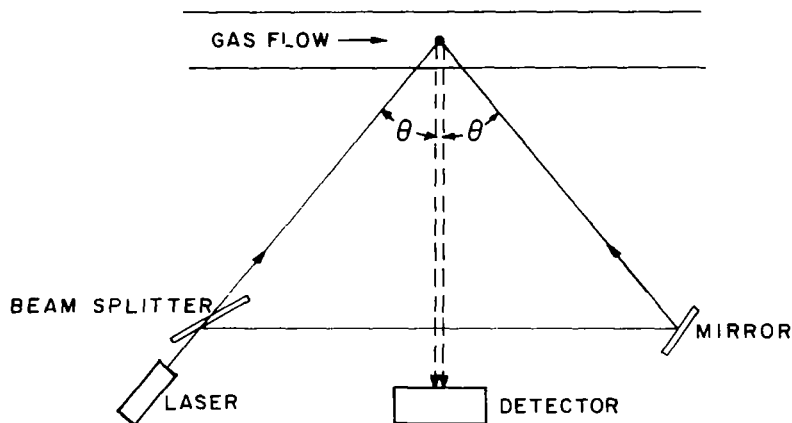
(b) System Eliminating Loss of Scattered Light at Beam Splitter
    (Reference F. Shigemoto, NASA-Ames Research Center)

Figure 2.4-2   Further Laser Doppler Velocity Instrument Systems

To make use of readily available photomultiplier tubes and circuits, it is necessary to hold the Doppler shift frequency (assuming a separate reference source or optical single sideband modulator is not used) down to about 250 MH$_z$ or less. For supersonic stream measurements this means that relatively small scattering angles, $\theta < 10°$, must be used. As discussed in later sections, one pays a price for small scattering angles in terms of greater instrumental broadening. However, with care in design and signal processing, velocities up to, say, Mach 3.5 can be measured satisfactorily without major changes in components.

At higher Mach numbers, a relatively straightforward change to a different type of light mixer, such as a travelling wave phototube, or solid state detector has to be made. At much higher velocities, one may consider the use of a different kind of optical interferometric technique, such as a Fabry-Perot configuration, for the optical signal mixing stage. The lower limit on such a technique is determined by the narrowest line width which is attainable with practicable optical flatness requirements. In other words, extending the instrument range upward requires no modification in principles, but merely further straightforward work on specific components. For this reason no work on these problems of extended range design has been considered justifiable at the present stage of instrument development. In view of the excellent results of the present work, however, the study of a high Mach number system should be started at an early date.

2.5 Heterodyne Signal to Noise Ratio:
The Photomultiplier as a Mixer

The photomultiplier may be used in two different ways: it
may be used as a <u>detector</u> of (usually low-level) electromagnetic
waves, as in astronomical or spectographic applications; it may
also be used as a <u>mixer</u> of electromagnetic waves, as in the
present application. It is important to note that, while the
physics of light interaction, electron multiplication, and so
forth for the two cases are the same, nevertheless the operating
principles from the most important aspects of signal reception,
detection and processing, are quite different.

In any electronic system, the two most significant parameters
which determine limitations in the performance of its designated
functions are frequency bandwidth and signal-to-noise ratio.
These two are generally intimately related as we shall see in
this section. The discussion will be generally based on the
examination of signal and of signal-to-noise ratio. The absolute
level (i.e., of either power, voltage or current) of the signal
per se is of minor importance. By the addition of amplifiers at
later, high signal level stages of the electronic system one can
always achieve any desired signal level needed to perform a
specific function.

In comparing the two applications of the photomultiplier on
the basis of signal-to-noise ratio and bandwidth, the strong
differences become rapidly apparent. The important noise contri-
butions are different, the bandwidth requirements are different,
and the relationships expressing signal-to-noise ratio are
different. This is firstly because as a low-level detector, the
photomultiplier is operated as near as possible to its lower
limit of detection capability, whereas when used as a mixer, it
should be operated at the highest possible level, as we shall
see; and secondly because the calculation of signal-to-noise
ratio follows along quite different lines in the two applications.

In basic signal concept and function, the photomultiplier mixer is the close counterpart of the microwave mixer. Functional elements are the same, although of course the physical principles of operation are different. The similarity is so close that a microwave element of the same parametric relationship can be found for each functional stage of the photomultiplier. For reasons connected with their physical differences, however, the elements are combined in a somewhat different way in the two cases.

In studying the use of photomultipliers for any application, one is struck by the relative lack of recent literature on this device. Further, most material has been published specifically bearing on applications to low-level detection (1, 2, 3, 4, 12). To date, our findings of published literature relating to the use of photomultipliers as mixers has been very meager. Much of the useful material is available in manufacturers' literature. Since this portion of the Laser Doppler Velocity Instrumentation has, perhaps, the strongest effect on overall performance of the whole system, the important features have been studied and presented here in some detail. We are somewhat encouraged to find that the experimental results of Section 2.18 substantiate the analytical findings.

Literature on microwave mixers is in a much more satisfactory state. One of the better and more clearly written accounts appears in Reference (5), of which the relevant portions of Chapters 1 and 2 provide an excellent introduction in a very readable form. Considerable material has since been published on the subject, but will not be reviewed here. The results of our study of the mixing properties, signal-to-noise ratio, and bandwidth limitations of the photomultiplier operated as a mixer are now presented.

2.5.1 The Photomultiplier as a Mixer

The Laser Doppler Velocity Instrument receives its
information on gas velocity in the form of a light signal gener-
ated by the scattering of laser light from particles in the gas
stream. As has been shown, all the velocity information is
contained in the <u>frequency</u> spectrum of this light signal beam.
Since we have no simple means of measuring these frequencies
directly, we must use a form of Signal Receiver known in radio
frequency circles as the Superheterodyne Receiver (5). This
makes use of a frequency converter, which changes the signal into
one centered at a different frequency, generally (and certainly
in our case) much lower. The signal is then amplified at this
new frequency before further processing to extract the information
desired, in our case velocity parameters, as discussed in Section
2.12. This lower frequency is generally termed the Intermediate
Frequency and the amplifier the i.f. amplifier. The latter is
followed by some form of signal amplitude detector, frequency
discriminator or phase discriminator, depending on the form
(amplitude modulation, frequency modulation or phase modulation)
in which the needed information is being transmitted. The signal
detector or discriminator is generally operated at a relatively
high signal level. Subsequent amplifiers raise the final signal
to that needed to drive the reproducing device. A general block
diagram is shown in Figure 2.5-1(a).

A key element in the receiver, the Frequency Converter,
consists of the combination of a Local Oscillator and a Mixer.
In RF systems, the local oscillator is just a continuous wave
(CW) oscillator operating at a frequency somewhat different from
that of the received RF signal. In the Laser Doppler Velocity
Instrument, the local oscillator can simply be a portion of the
light split off from the laser output. In the mixer, a super-
position of the local oscillator wave and the output signal
takes place. A beat, or heterodyne, frequency equal to the

BASIC BLOCK DIAGRAMS OF SUPERHETERODYNE RECEIVERS AND ELEMENTS

A. SUPERHETERODYNE RECEIVER
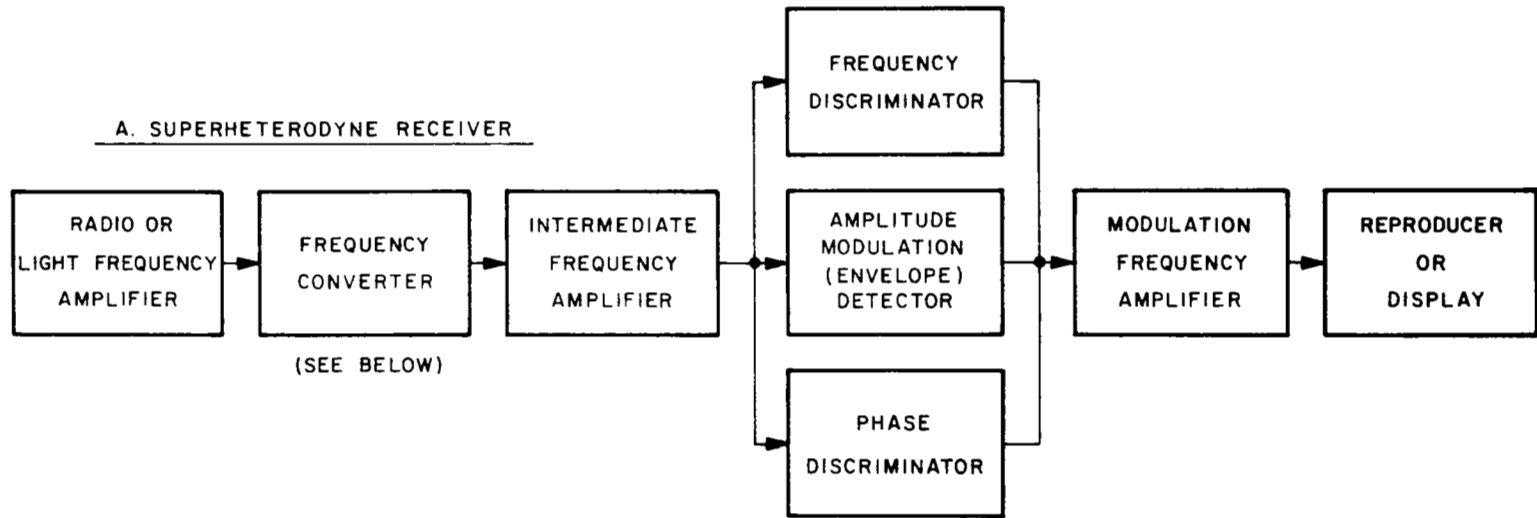
B. BLOCK DIAGRAM OF A FREQUENCY CONVERTER
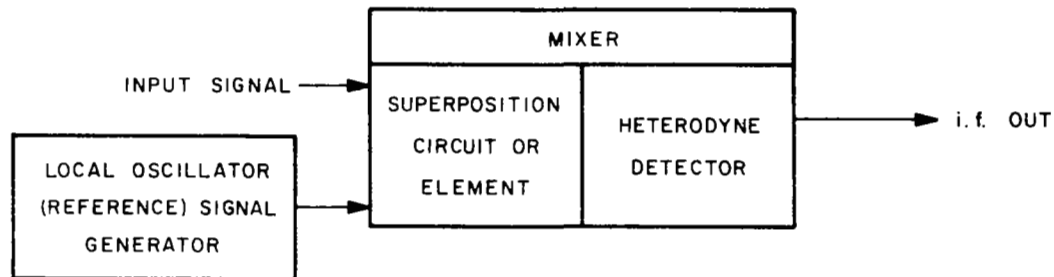
Figure 2.5-1   Basic Block Diagrams of Superheterodyne Receivers and Elements

difference frequency between the two waves exists as an amplitude modulation component on the superposition of waves in the mixer. This heterodyne frequency is detected in the mixer by a suitable detector, which consists of a non-linear circuit element sensitive either to signal power or to signal amplitude. At the terminals of the mixer is thus produced a voltage or current corresponding to this heterodyne frequency.

If the input signal is modulated in some way, either in frequency or amplitude, it may be analyzed as a combination of Fourier components, each of which produces its own heterodyne frequency. The output signal from the mixer contains a component for each component in the incoming signal, the amplitude, frequency and phase relations between these components being preserved as the signal passes through the mixer. Hence the signal passing into the IF amplifier contains the same modulation as the RF signal, but is centered at the intermediate frequency. Only those frequency components falling within the passband of the IF amplifier will continue through the receiver, so that the bandwidth of the whole receiver system is just the bandwidth of the IF amplifier.

With a local oscillator frequency f_{LO}, and signal frequency f, both sum and difference frequencies (f_{LO} + f) and (f_{LO} - f) in principle appear at the output of the mixer. In the photomultiplier, the photocathode plays the part of the superposition circuit and detector, and the electron multiplier chain (and subsequent external amplifiers) function as the IF amplifier. Since both f_{LO} and f are of the order of 10^{14} Hz, and the IF amplifier bandwidth is of the order of 10^5 to 10^6 Hz, clearly only (f_{LO} - f) passes through the system. This difference frequency is just the Doppler shift f_D caused by the laser light being scattered from moving particles. A difference between this system and more commonly encountered superheterodyne receivers lies in the fact that f_D is fluctuating with time, in

response to the turbulent motion of the gas, so that the IF frequency is actually variable, and the IF amplifier and output signal detection system bandwidth must either be large enough to cover the whole range of f_D, or the center frequency of the system bandwidth must in some way be continuously moved up and down to follow f_D. This is quite different from the more usual IF system which operates at a fixed frequency, and has a rather narrow bandwidth. This difference poses a major problem in the design of the Laser Doppler Velocity Instrument "receiver" system, so that we have analyzed it in detail. The results of our studies of this problem appear in Section 2.12.

An understanding of the Heterodyne Detector operation is important. Two types of detector are commonly encountered in microwave mixers. One functions as a rectifier, that is, current flows in one direction only through it. Typical of this type are the vacuum tube diode and triode, and the crystal. In each of these a relatively large local oscillator voltage is applied. Current flows only during the positive half-cycles of the input voltage, which consists of the superposition of the small signal on a relatively large local-oscillator voltage. The average current depends on the magnitude of the input voltage, i.e., the IF frequency in the superheterodyne receiver. As long as the signal voltage is small compared with the local-oscillator voltage, the heterodyne-frequency current flowing must be directly proportional to the signal amplitude. A mixer using this type of detector is therefore a linear device. It will be noted that the output current contains a relatively large DC component. This is blocked out of the signal channel by capacitor coupling. It is, however, also used to monitor the magnitude of the local-oscillator voltage applied to the mixer.

The linear detector contrasts with the second type of detector, used generally for the simple detection of low level signals; that is, not as part of a mixer. Here, the circuit is

entirely passive, in that there is no source of energy other than the input signal. Both crystals and diodes can also be used in this mode, and function as detectors because of the non-linear relationship between the current induced in them and the magnitude of the impressed voltage. This non-linearity occurs at low currents, hence the application as a low-level detector. In the non-linear region, less current flows during negative half-cycles of the signal voltage than during the positive ones, so that there is a net positive current having magnitude related to the magnitude of the impressed voltage. The current may be expressed, analytically, as a function of the voltage in the form of a Taylor series. The non-linearity is expressed by terms in powers of the voltage higher than the first. For very small voltages, the term in the second power of the voltage is large compared with the higher-power terms. Hence the rectified current produced from a very small signal must be proportional to the square of the impressed magnitude of the AC voltage. For this reason, low-level detectors are generally referred to as "square-law" detectors. The square-law detector clearly delivers an output proportional to the input signal <u>power</u> instead of the input signal amplitude as in case of the linear detector. Again, a DC component exists in the output current which is used to monitor the operating point on the detector curve.

In a photomultiplier, because of the nature of the fundamental photoelectric process, not because of any non-linear voltage current relationships, the photocathode delivers a current proportional to the power, not the amplitude of the light waves falling on it. In RF terminology, it combines the function of the superposition circuit with a square-law detector. In addition to the signal output, the photomultiplier also has a DC output. Again, this is used to monitor the photomultiplier operating point.

2.5.2 Noise

In the photomultiplier mixer, the minimum detectable
signal is determined by the masking effect of random noise. In
the photomultiplier-mixer system, noise derives from two kinds of
source. The first is that associated with the generation of
noise in electronic circuits of any kind, and the second stems
from the peculiarities of the photomultiplier tube itself. The
two modes of operation of a PM tube described earlier, i.e. as a
low-level light detector or as a mixer, determine the relative
importance of the two sources of noise.

Noise of the first kind is developed because electric cur-
rents are not steady, but consist of the flow of large numbers
of electrons. Thermally excited fluctuations of the electrons
in resistive circuit elements give rise to small potentials in
the circuit at random frequencies. This thermal agitation noise
is called "Johnson noise" after J. B. Johnson (6, 7, 8, 9). The
mean square of the noise voltages in the frequency band Δf Hz is
given by:

$$\overline{E^2} = (k)\ TR\ \Delta f \tag{1}$$

where: k is Boltzmann's constant = 1.38 x 10^{-23} Joules/deg K

   T is the absolute temperature of the circuit element in
      deg. K,

   R is the resistive component of the circuit element im-
      pedance in ohms.

This type of noise is often called "White noise", since it
is approximately uniform in level over wide frequency ranges (as
compared with black body radiation which follows Planck's Law).
In a chain of circuit elements containing stages of amplification,
it generally turns out that the noise developed in the "front end"
components plays the dominant role in determining output noise,

since this noise is amplified the most. The degradation of signal-to-noise ratio through any circuit network is measured by the "noise figure" F(5), which is unity for a perfect device, meaning that a signal arriving at the output terminals is masked by noise no more nor less than it was at the input terminals. The more the degradation of signal-to-noise ratio, the higher the noise figure. For reasons which have to do with their respective modes of operation, signal-to-noise relationships are different for the various kinds of detectors and mixers (5, 10, 11). They will not be pursued further here, except in the case of the photomultiplier.

In a photomultiplier, as in resistive circuit elements, the noise generated in the device arises because of random electron motions. However, because of the different physical processes involved the generation processes are quite different. Because they are still random in nature, the noise developed is also "white noise". Three basic noise sources are identified in a photomultiplier tube:

(1)   Dark current - when the photomultiplier tube is operated in the absence of incident light, an anode current flows which sets a limit to the lowest intensity of light which can be measured. It is mostly caused by thermionic current emitted from the sensitized coating, with smaller contributions from other sources, such as glass flourescence caused by electrons emitted from the dynode system (eliminated with the cathode operated at ground potential), radioactive contamination of the window, field emission, etc., (2, 12).

(2)   When a light flux input is applied to a multiplier phototube, the observed output

noise also increases, usually quite
markedly, as a result of the sta-
tistical fluctuations of the photo-
emission current modified by the
gain variation of the multiplier.
This added noise is called "shot
noise" or "noise-in-signal", since
it is a function of the "signal"
flux input (3, 4).

(3)   Shot Noise contributed by extraneous
       background light (i.e. light which
       is not part of the light signal to
       be measured).

Of these, because the photomultiplier must be operated near
peak output for best signal-to-noise ratio, as shown by the
analysis below, the dark current and dark current noise may be
neglected. Only the "Noise-in-Signal" shot noise (from all light
flux sources) is of importance in the mixer mode of operation.
Hence cooling of the photomultiplier tube, which is of great
benefit for the reduction of dark current in the detection of
low-level signals, is quite pointless when the device is used as
a mixer as in the laser Doppler flowmeter.

Background noise, noise-in-signal and photocathode thermionic
emission noise, but not other types of dark noise, can be predicted
from the following basic shot noise relationship (derived in (3),
and also discussed in (4):

$$i_n^2 = 2 \ eUkI\Delta f \tag{2}$$

where: i_n = rms noise current component in the anode circuit
                  corresponding to the particular input flux under
                  consideration.

e = electronic charge, 1.6×10^{-19} coulombs.

U = multiplier gain.

k = multiplier noise factor (see Section 2.5.4).

I = DC anode current component corresponding to the same input flux.

Δf = effective noise bandwidth, in this case the bandwidth of the IF amplifier chain (photomultiplier and following external amplifiers).

We now proceed to analyze in detail the explicit form of the photomultiplier output when used as a mixer, and then to derive the equation for signal-to-noise ratio. Calculations based on these analyses give curves from which the best operating modes may be deduced.

2.5.3 Photomultiplier Heterodyne Output Signal

As described in detail in the preceding portions of this section, the photomultiplier operated as a mixer is, in itself, almost a complete superheterodyne receiver (Figure 2.5-1), containing a superposition element, a detector, and an IF amplifier. It lacks only a local oscillator and a modulation detector or discriminator to make it a complete receiver. Continuing the analogy, the output from the photomultiplier anode load resistor is the IF output. Because of the special nature of the laser Doppler flowmeter system, this IF frequency varies over a range of the order of 1 to 200 MHz or more. Its mean value f is proportional to the mean gas velocity, the frequency deviation on either side of the mean, f_D, is proportional to the intensity of turbulence (see References 13 and 14 for definitions of turbulence parameters), and the frequency with which the deviation from the mean occurs is proportional to the scale (L, ℓ, or λ – see (13) and (14)) of turbulence and is called the signal frequency in FM receiver terminology.

The separation of these frequency components is studied in Section 2.12. At this point in the system we are merely concerned with the calculation of the amplitude of this variable intermediate frequency output, on the assumption that the frequency range capability of the photomultiplier is sufficient to handle the whole frequency spectrum, and that we know how to process this variable frequency signal after we have obtained it.

The calculation is performed in the following section, and is valid for any type of mixer (Figure 2.5-1) having a square-law type detector; i.e., a detector which is sensitive to power (see earlier discussion on mixers and detectors), as in the case of a photocathode (experimental observation, original observations referenced in (15)), or a crystal as a square-law detector (because of its non-linear voltage-current characteristic). This calculation has a more general application, therefore, than just to photomultipliers, and may be useful in later investigations of higher Mach number systems, whose frequency range exceeds the limitations of photomultiplier tubes. Numerical calculations have been performed, and curves drawn for a number of operating conditions appropriate to the RCA 8645 tube to be used in the 3-D system (Section 2.20).

For reasons which became apparent in the discussion of mixers, however, it turns out that the key parameter which determines the performance of the electronic data processing system following the photomultiplier system is actually signal-to-noise ratio, rather than signal alone. The calculation of signal-to-noise ratio for photomultiplier tubes is presented following the signal calculation. Again, curves are given for the RCA 8645 tube. The characteristics of these curves are peculiar to photomultiplier tubes used as mixers. It must be emphasized that, because of the special way in which photomultipliers generate noise (Equation (1), the signal-to-noise characteristics are different from those typical of other kinds of mixers, such as microwave mixers.

2.5.3.1 Heterodyning Signal

We now present the derivation of the output signal from a photomultiplier used as an optical signal mixer generating a heterodyne output signal. An expression for the photomultiplier heterodyne frequency output current in the absence of noise is derived. It is shown that under certain conditions this current has a maximum. There are two regimes of heterodyne operation corresponding to high and low scattered light power. Recipes for maximizing the heterodyne signal in each regime are presented.

To make the problem as simple as possible, the two light beams incident upon the photocathode are represented by $E_s \sin \omega_s t$ and $E_{LO} \sin \omega_{LO} t$, where E denotes electric field amplitude; ω the radian frequency of the light; subscripts s and LO denote the scattered light and local oscillator (or reference) beams, respectively. The two beams are superimposed on the cathode to form a total wave whose electric field is

$$E_T = E_s \sin \omega_s t + E_{LO} \sin \omega_{LO} t \qquad (3)$$

under the assumption that the beams have the same linear polarization direction. The output current is proportional to the power (intensity) of the light beam (15), hence assuming that current amplification by the electron multiplier dynodes (i.e., the IF amplifier first stage) is constant, then the photomultiplier anode current (instantaneous) is given by:

$$I_{TA} = S \, E_T^2,$$

$$= S \left[E_s^2 \sin^2 \omega_s t + E_{LO}^2 \sin^2 \omega_{LO} t + 2 E_s E_1 \sin \omega_s t \sin \omega_{LO} t \right]$$

$$I_{TA} = S \left\{ E_s{}^2 \left(\frac{1 - \cos 2\omega_s t}{2} \right) + E_{LO}{}^2 \left(\frac{1 - \cos 2\omega_{LO} t}{2} \right) \right.$$

$$\left. + E_s E_{LO} \left[\cos (\omega_s - \omega_{LO})t - \cos (\omega_s + \omega_{LO})t \right] \right\}$$

<div align="right">(4)</div>

where S = a constant of proportionality.

Because of bandwidth limitations in the photomultiplier mixer (see earlier discussion on system bandwidth), it does not respond to the currents oscillating at frequencies $2\omega_s$, $2\omega_{LO}$ and $(\omega_s + \omega_{LO})$. Hence the observed current output from the photomultiplier anode (i.e., IF output in terminology defined earlier) is given by

$$I_{TA} = S \left(\frac{E_s{}^2 + E_{LO}{}^2}{2} + E_s E_{LO} \cos \Delta\omega t \right)$$

or

$$I_{TA} = S_A \left(P_s + P_{LO} + 2 \sqrt{P_s P_{LO}} \cos \Delta\omega t \right) \tag{5}$$

where: P = light power (watts) falling on the photocathode,

$\Delta\omega = (\omega_s - \omega_{LO})$,

S_A = radiant sensitivity of the photomultiplier (amps/watt)

The current I_{TA} has a DC component I_{DCA}, and an AC component I_{SA} oscillating at the heterodyne difference frequency $\Delta\omega$. Figure 2.5-2 shows the total anode current and its components.

PHOTOMULTIPLIER ANODE CURRENT COMPONENTS

SINE WAVE OF HETERODYNE
FREQUENCY

$I_{ACA} \propto 2\sqrt{P_S P_{LO}}$
= PHOTOMULTIPLIER OUTPUT
SIGNAL CURRENT
AMPLITUDE

AMPLITUDE

$I_{SA} \propto P_S$

$I_{LOA} \propto P_{LO}$

I_{DCA}

$I_{PEAK\ ANODE}$

TIME
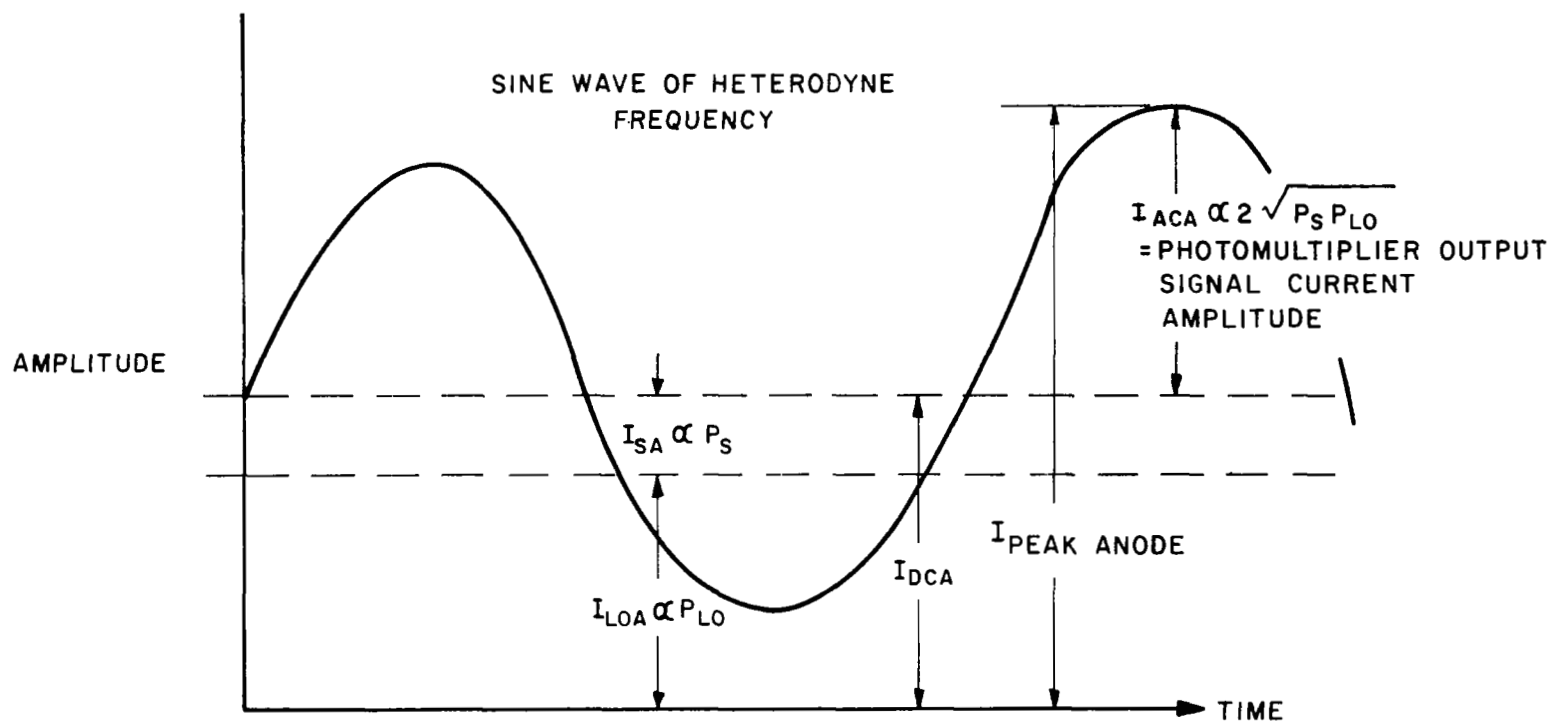
NOTES —

1. ANODE CURRENT $\propto$ LIGHT INTENSITY (POWER)
2. HETERODYNING EFFICIENCY ASSUMED 100 %

Figure 2.5-2   Photomultiplier Anode Current Components

In reality the amplitude of the AC current is $2\mu \sqrt{P_s P_{LO}}$, where μ $(0 \leq \mu \leq 1)$ can be called the heterodyning efficiency. In Equation (5) μ has been set equal to one, which is an idealization. The heterodyning efficiency is less than one due to effects such as imperfect alignment of the wave fronts of the two beams and loss of coherence between the two beams. These limitations are considered in more detail in Section 2.6.

From Equation (5) it can be seen that the heterodyne signal[*] can be increased by increasing either P_s or P_{LO}. However, the input light power cannot be increased without limit. For example, the maximum rated anode current allowed by the manufacturer of the type 8645 photomultiplier used in our 3-D system, denoted by I_{mA}, is 0.5 milliamps (16). Hence the maximum input light power, P_m, is given by

$$P_m = \frac{I_{mA}}{S_A} \tag{6}$$

In practice it may be necessary to impose a lower maximum current limit to avoid fatigue effects and to insure stability (1). An acceptable working level to avoid fatigue effects is about $\frac{1}{2} I_{mA}$. When maximum stability is required, the manufacturer recommends holding the average anode current to 0.5 microamps. Such extreme stability is not considered necessary in the present application, however, since we are not concerned with the continuous measurement of very low-level light signals. The choice of a different I_{mA} and hence P_m would change the numerical results presented below but would not alter the general shape of the computed curves. Determination of the shapes of the curves, which point up the optimum operating procedures, is the important result of this analysis because the assumption of 100% heterodyning efficiency means that the absolute numerical results represent an ideal condition, as noted earlier.

- -

* but not Signal to Noise ratio - see Section 2.5.4.

The maximum power condition is applied by setting the peak power incident on the photocathode equal to the maximum allowable power. The peak power is thus given by Equation (6), with I_{TA} from Equation (5) set equal to the maximum allowable current I_{mA}, and $\cos \Delta\omega t = 1$, so that:

$$P_m = P_s + P_{LO} + 2 \sqrt{P_s P_{LO}} \tag{7}$$

When operating at the limit I_{mA} posed by this condition, P_s and P_{LO} are then interdependent. For any given scattered light power, the local oscillator power is clearly given by the solution of Equation (7) for P_{LO}, i.e.,

$$P_{LO} = P_s + P_m - 2 \sqrt{P_s P_m} \tag{8}$$

We wish to set the operating conditions for the photomultiplier in such a way as to maximize the heterodyne signal current subject to the condition of Equation (7). The maximum is obtained straight-forwardly by substituting (8) into the expression for the hetero-dyne signal amplitude, i.e. $2P_s P_{LO}$ and setting the derivative of the resulting expression equal to zero. After some algebra, we find that the maximum occurs when $P_s = P_{LO} = (1/4)P_m$. At the maximum, the amplitude of the difference frequency anode current (i.e., I peak anode in Figure 2.5-2) is $I_m/2$. This maximum is shown in Figure 2.5-3 where the current at the heterodyne fre-quency is plotted as a function of scattered light power for various photomultiplier applied voltages.

In operation at fixed voltage at low scattered light power, the heterodyne signal increases with increasing scattered light power until a maximum is reached. When the scattered light power increases further with the photomultiplier voltage still
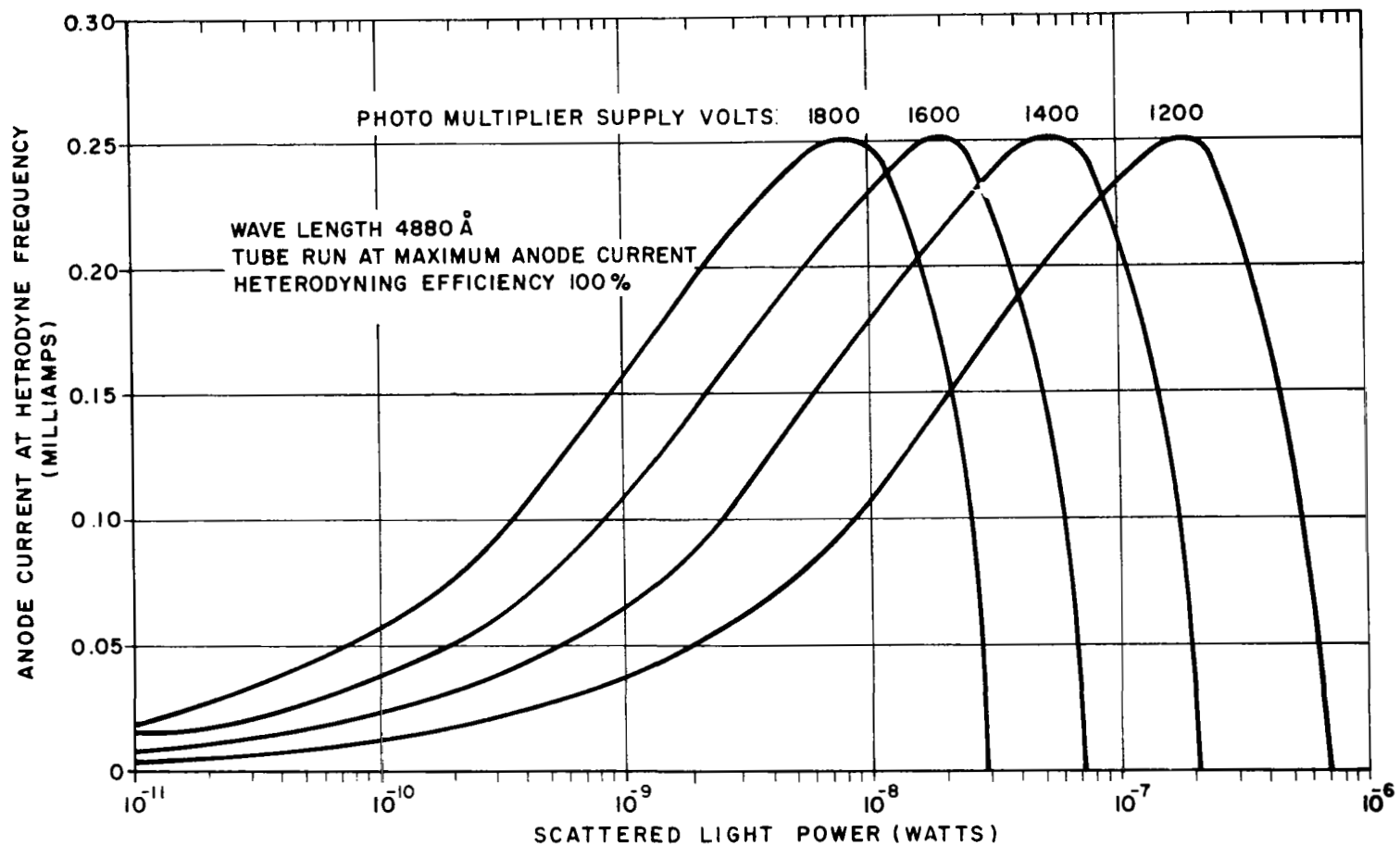
Figure 2.5-3   Anode Current at Heterodyne Frequency for RCA 8645 Photomultiplier
versus Scattered Light Power

fixed, the local oscillator light power must be reduced to avoid
exceeding the maximum current. The result is a decreasing hetero-
dyne signal. As the applied voltage is decreased from the maximum
voltage, the curve shifts toward higher scattered light power.

The scattered light power at which the peak occurs in the
curve for maximum applied voltage divides the graph into two
regimes. For the 8645 tube the maximum applied voltage is 1800
volts and the peak occurs when $P_s = 7.3 \times 10^{-9}$ watts. The tube
may be operated at lower voltages, and therefore on different
curves. For a given scattered light power, the photomultiplier
applied voltage must be adjusted to give maximum heterodyne signal
current. Each regime has its own recipe for maximizing the hetero-
dyne signal current as follows:

High Signal Power Regime $(P_s > P_m/4)$. Adjust the local
oscillator light power so that it is equal to the scattered light
power and turn up the tube voltage until the peak allowable anode
current is reached. From Figure 2.5-2, this is seen to be the
sum of the DC component plus the peak value of the AC heterodyne
current component.

Low Signal Power Regime $(P_s < P_m/4)$. Turn up the tube vol-
tage to the maximum allowable and increase the local oscillator
light power until peak allowable anode current is reached.

In the high scattered light power regime, the local oscilla-
tor light power and the applied voltage can always be adjusted to
give the same peak heterodyne signal current. For example, for
the conditions assumed in this section, a current of 0.25 milli-
amps can always be obtained. In other words there is a maximum
heterodyne signal current which cannot be exceeded no matter how
much scattered light power is available. The heterodyne signal
current cannot always be increased by supplying more scattered
light power, because of power handling limitations of the photo-
multiplier tube.

2.5-19

In practice the peak photomultiplier anode current will be less than 0.25 milliamps*because of imperfect heterodyning and because the tube probably will not be driven at maximum rated anode current to avoid fatigue. It is important to realize, however, that the operating level of the photomultiplier tube is not very critical. This is because the level of the signal output from the tube anode (IF output) is not critical, since we can always add further stages in amplification following the PM tube. In setting the PM tube operating voltage as described above, one should keep in mind that scattered light power and local oscillator (reference) beam power may vary during a measurement. Hence, a check should be made of PM anode current over the extremes of range (so called "dynamic range") of incident light powers, and suitable adjustments made as above to insure satisfactory working over the total dynamic range.

We now come to the calculation of a signal parameter which is far more important than mere heterodyne signal power, namely the ratio of heterodyne signal power to noise power "Signal-to-Noise Ratio". Unlike the signal power alone this ratio cannot be controlled by apparatus we are able to add or adjust in following circuit stages. It is a fundamental property of the system and, in conjunction with system bandwidth, determines the upper limit on system capability and performance.

2.5.4   Heterodyning Signal-to-Noise Ratio

This section presents the derivation of the signal-to-noise ratio for the heterodyne output of a photomixer. It is shown that the maximum signal-to-noise ratio is insensitive to the voltage applied to the tube. At higher scattered light power, the signal-to-noise ratio is maximized by turning up the local oscillator power while turning down the applied voltage to avoid exceeding the anode current rating. So long as $P_{LO} >> P_S$ the signal-to-noise ratio is independent of P_{LO}.

- - - - - -

*for the RCA-8645 photomultiplier tube

2.5-20

As described in Section 2.5.2, there are three contributions to the total noise current emitted by the photocathode:

(a) Dark noise, due to fluctuations in the dark current.

(b) Background noise, due to random fluctuations in the current emitted in response to extraneous light (i.e. light that is unrelated to the signal light).

(c) Noise in signal, due to similar random fluctuations in the signal current.

These fluctuations are a consequence of the statistical nature of the light wave and photo-emission process. In the laser Doppler flowmeter system only the noise in signal need be considered. If the tube is run near maximum anode current as suggested in Section 2.5.3.1, to give the highest signal output level into the electronic system connected to the photomultiplier anode, the dark current is negligible compared with the current emitted in response to the laser light, and hence the dark noise is negligible. The background noise can be reduced to a negligible level by placing apertures and light bandpass optical filters in front of the photocathode as has been done in the present laboratory set up (Section 2.18).

The total current emitted by the cathode in response to the laser light is, following the results of Section 2.5.3.1

$$I_k = S_k \left(P_{LO} + P_s + 2 \sqrt{P_{LO} P_s} \cos \Delta\omega t \right) \tag{1}$$

where S_k is the cathode radiant sensitivity, $\Delta\omega$ is the difference between the local oscillator and signal frequencies and the other symbols have been defined previously. The square of the noise current is given by the shot noise equation (3, 12, 4)

$$i_k^2 = 2e \Delta f I_K$$

$$= 2e \Delta f J_K (P_{LO} + P_s + 2\sqrt{P_{LO}P_s} \; \Delta\omega t) \qquad (2)$$

Now this noise current consists of random voltages at random frequencies spread over the whole spectrum of frequencies covering the bandwidth Δf. This type of noise is generally termed "white noise". The only way we can measure this noise is to measure its total power, or "heating effect" over the bandwidth Δf. This total power, in turn, is measured by $<i^2>R$, where $<i^2>$ is the mean square current, and R is the resistive component of the circuit impedance. Averaging i_k^2 to get the mean square noise current yields, simply,

$$<i_k^2> = 2e \Delta f S_k (P_{LO} + P_s), \qquad (3)$$

since the average value of cos $\Delta\omega E$ is zero.

The heterodyne a.c. signal component of the cathode current at the difference frequency is, from equation (5) of Section 2.5.3.1, with the cathode radiant sensitivity S_k substituted for S_A,

$$I_{sk} = 2S_k \sqrt{P_{LO}P_s} \; \cos \; \Delta\omega t \qquad (4)$$

so the mean square signal current is, since $<\cos^2 \Delta\omega t> = 1/2$,

$$\langle I_{sk}^2 \rangle = 2S_k^2 \, P_{LO} P_s \qquad\qquad (5)$$

Since the circuit resistive component R is the same for both currents, the cathode signal to noise power ratio is given by

$$\left(\frac{S}{N} \right)_k = \frac{\langle I_{sk}^2 \rangle}{\langle i_k^2 \rangle} = \frac{S_k P_{LO} P_s}{e \, \Delta f (P_{LO} + P_s)} \qquad\qquad (6)$$

In the multiplier chain the signal to noise ratio is degraded by fluctuations in the secondary emission process, a process which is analyzed in clear detail in Reference (12). From the results of this analysis, we find that the signal to noise power ratio at the anode is given by:

$$\left(\frac{S}{N} \right)_A = \frac{1}{k} \left(\frac{S}{N} \right)_k = \frac{S_k P_{LO} P_s}{ek \, \Delta f (P_{LO} + P_s)} \qquad\qquad (7)$$

where $k = \sigma/\sigma - 1$ and σ is the average gain per state of the multiplier chain (12). This is not the same result that would be obtained by taking the signal to noise ratio to be

$$\langle I_{sA} \rangle / \langle i_A^2 \rangle$$

where I_{sA} is the anode current at the difference frequency and i is the noise current computed by the shot noise equation using

2.5-23

the total anode current. The two ratios are related by

$$\frac{<I^2_{sA}>}{<i^2_A>} = kU \frac{S}{N}_A$$

where U is the multiplication factor for the dynode chain. Thus
taking $<I^2_{sA}>/<i^2_A>$ as the signal to noise ratio over-estimates the
signal to noise ratio by a large factor.

The reason for this difference is that the photomulti-
plier is actually not just a simple mixer, but a mixer plus an
i.f. amplifier, the dynode multiplier chain. The cathode noise
current is amplified by the multiplier chain. As pointed out in
Section 2.5.2, for any amplifying chain, the noise input from the
"front end" components is amplified the most, and therefore makes
the greatest contribution to the total noise at the output end.
Thus, in the photomultiplier, while some shot noise is added in
the multiplication process itself, the biggest overall contri-
bution is that from the cathode and first dynode. In fact, it is
clear from equation (7) that the total reduction in S/N intro-
duced by the multiplier is independent of the number of dynodes,
since k is independent of the number of dynodes. To quote from
Reference (12), "Herein lies the virtue of photomultiplier tubes."
It is well to note that, while this statement is correct, the
same independence of S/N from the addition of further stages of
gain would be found in any chain of amplifiers (5), as already
pointed out. The important feature is that the significant noise
coming from the "front-end" (cathode and first dynode) of the
photomultiplier is orders of magnitude lower than the Johnson
noise from the front end of a chain of ordinary amplifiers. The
effect of the multiplier chain is to bring the signal, at the
cathode and signal to noise ratio, to a level where the Johnson
noise from subsequent r.f. amplifiers is negligible (Section 2.12).

References (12) and (3) bring out some of these points, but not quite in the way presented here, since they are concerned with low level detection rather than signal mixing.

The next question to consider is maximizing $(S/N)_A$. For a given detector this ratio is maximized by maximizing the quantity

$$\kappa = P_{LO}P_s/(P_{LO} + P_s),$$

from equation (7). For fixed P_s, κ approaches P_s as P_{LO} is made large compared with P_s. This is readily seen if we rewrite κ in the form:

$$\kappa = P_s \frac{1}{1 + \dfrac{P_s}{P_{LO}}}, \tag{8}$$

When P_{LO} is not large compared with P_s, κ is equal to P_s multiplied by $P_{LO}/(P_{LO} + P_s)$ a factor which is less than 1 but which comes closer and closer to 1 as P_{LO} is increased. This means that to maximize the signal to noise ratio, P_{LO} should be as large as possible. However, for a given P_s, P_{LO} cannot be made so large that the maximum anode current is exceeded. The maximum local oscillator power is given by equation (7) or (8) of Section 2.5.3.1. Substituting P_s from either of these into (7) above yields another expression for the signal to noise power ratio:

$$\left(\frac{S}{N}\right)_A = S_k \frac{P_{LO}(P_m + P_{LO} - 2\sqrt{P_m P_{LO}})}{ek\Delta f(P_m + 2P_{LO} - 2\sqrt{P_m P_{LO}})} \tag{9}$$

For fixed voltage (i.e., fixed P_m and k) this function of P_{LO} is maximized when $P_{LO} = 1/4\ P_m$. The maximum value is

$$[(S/N)_A]\ max = (S_k P_m)\ /\ (8\ ek\Delta f)$$

At this maximum $P_{LO} = P_s$.

2.5.4.1 Results and Conclusions from Anode Signal to Noise Calculation

Figure 2.5-4 shows the signal to noise ratio as a function of signal power, under the condition expressed by equations (7) or (8) of Section 2.5.3.1. As before, 100% heterodyning efficiency is assumed. The bandwidth is taken to be 1 MHz for convenience. Figure 2.5-5 shows the signal to noise ratio as a function of local oscillator power for four fixed values of signal power and of applied voltage.

Figure 2.5.4 shows that for small P_s ($P_s < 2 \times 10^{-9}$ watts), the signal to noise ratio is proportional to P_s. This is because in this regime maximum anode current is achieved with $P_{LO} \gg P_s$ so that the ratio κ, defined earlier, is nearly equal to 1. Actually, it is an approximation to draw a single line showing that $(S/N)_A$ is independent of the applied photomultiplier voltage in this region. However, the variation of $(S/N)_A$ with voltage is too small to be shown clearly on the graph. The variation can be seen in Figure 2.5-5 by comparing the curves for 1200 and 1800 volts.

For higher scattered light power, each fixed voltage curve in Figure 2.5-4 goes through a maximum just as the curves of Figure 2.5-3 did. The maxima occur at the same point, namely $P_s = P_{LO} = P_m/4$, at which the heterodyne anode current maxima occur. Again as in the Heterodyne Anode Current curves, the maxima occur at higher scattered light power for lower applied photomultiplier voltage.
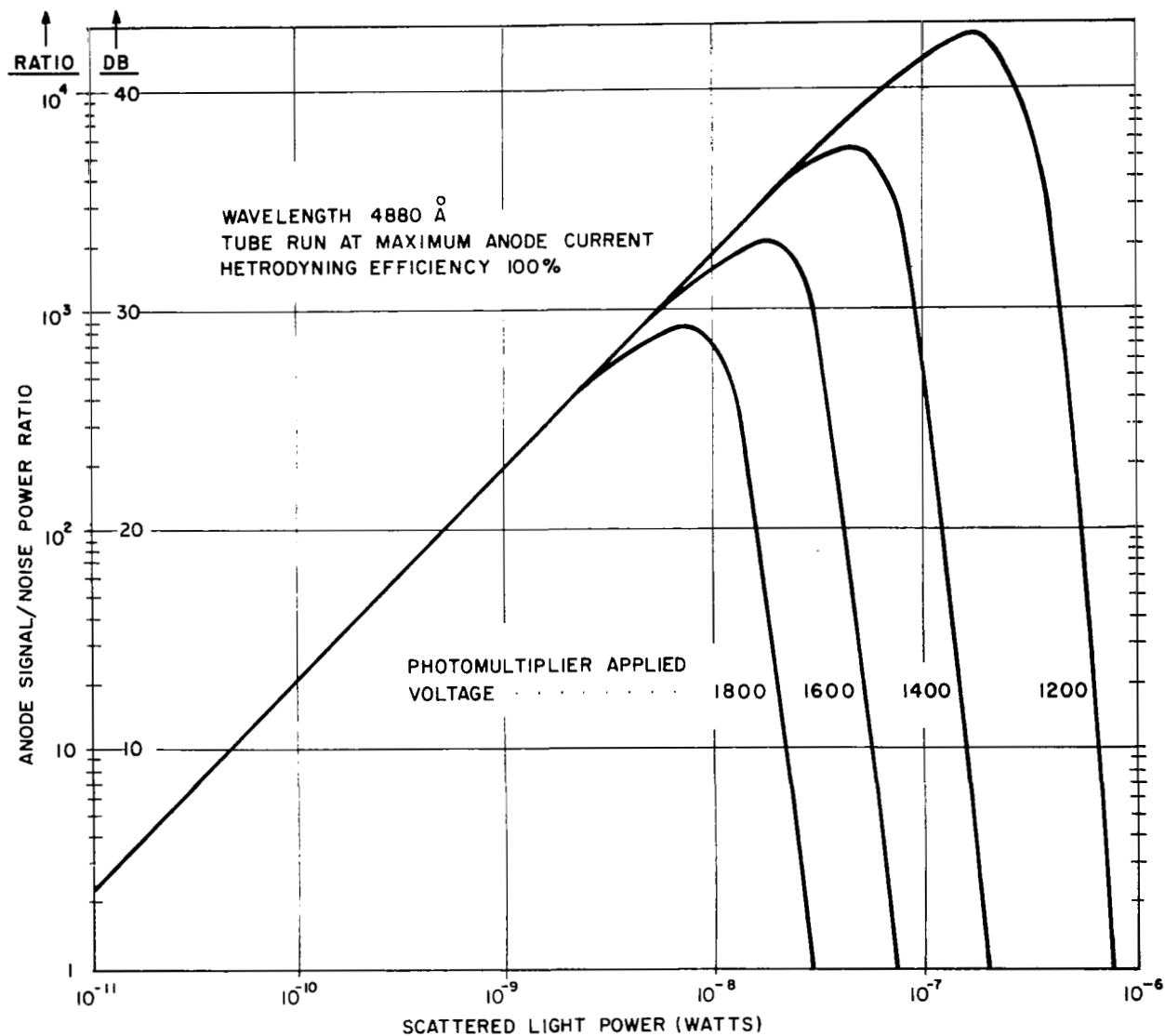
Figure 2.5-4   Anode Signal to Noise Ratio for RCA 8645 Photo-
multiplier versus Signal Power (Calculated)

However, an important point shown by the curves of Figure 2.5-4 is that at high scattered light power, a higher signal to noise ratio can be obtained by running the tube at less than the maximum applied photomultiplier voltage. This is because at lower voltage more local oscillator power can be applied to the tube, and the signal to noise ratio increases with local oscillator power, as shown in Figure 2.5-5. The signal to noise ratio increases until P_{LO} becomes large compared with P_s, when the ratio becomes essentially independent of P_{LO}. Thus the recipe for making the signal to noise ratio as large as possible is the same for all values of scattered light power: always make $P_{LO} >> P_s$. When P_s is low ($P_s < 2 \times 10^{-9}$ watts for 8645), this can be done no matter what voltage is applied to the tube. When P_s is high ($P_s > 2 \times 10^{-9}$ watts for the RCA photo tube type 8645), the tube must be operated at less than maximum voltage to avoid exceeding the maximum anode current rating.

These are most significant conclusions and provide the guidelines for design for an optimum laser doppler velocity instrumentation system. They were experimentally confirmed (Section 2.18) and used in the design of the 3-D instrument (2.20). It is fair to say, however, that their implications were not fully understood until much experimental work had been conducted.
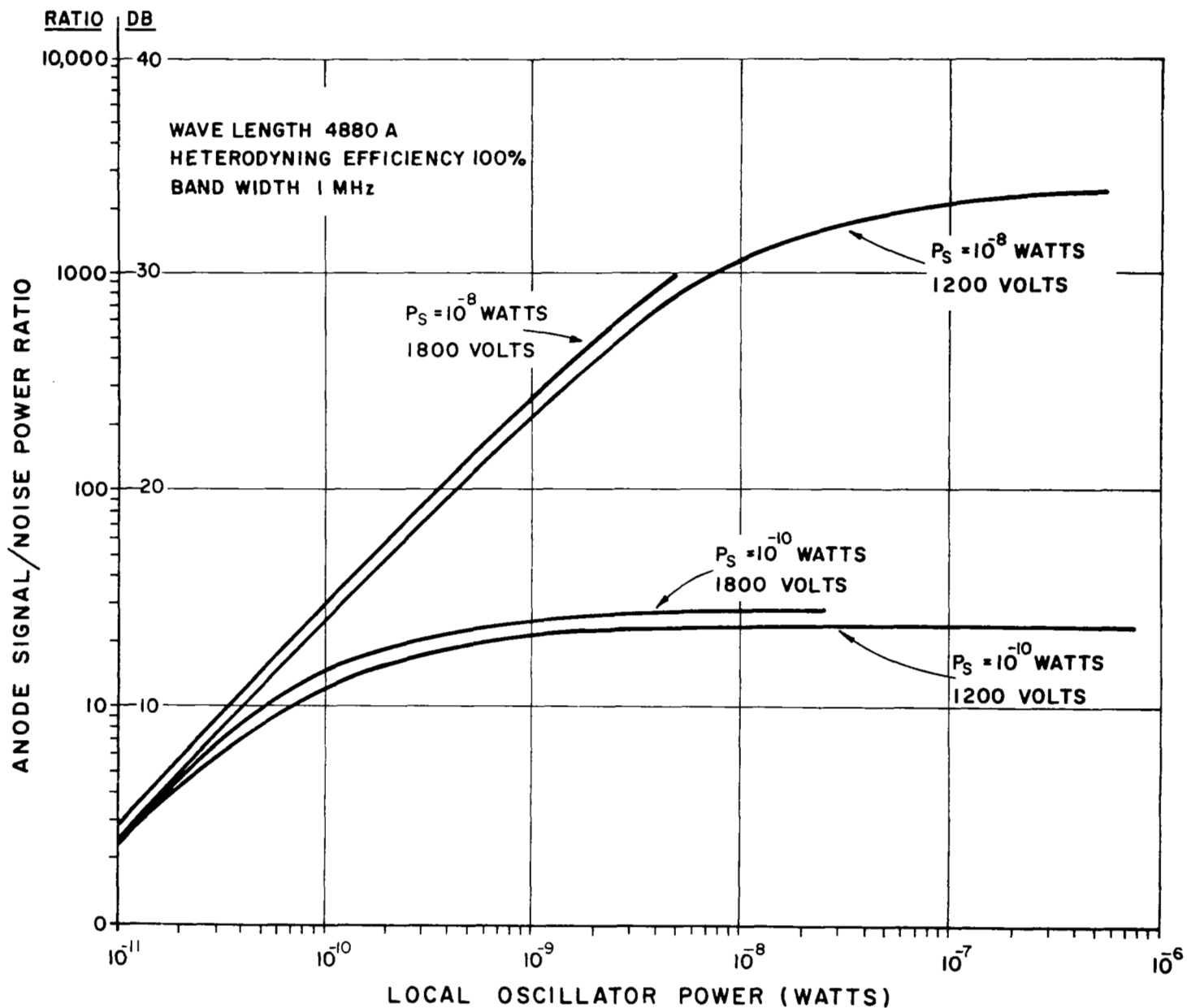
Figure 2.5-5   Anode Signal to Noise Ratio for RCA 8645 Photo Multiplier versus Local Oscillator Power (Calculated)

REFERENCES FOR SECTION 2.5

1. Engstrom, R. W., "Multiplier Photo-tube Characteristics: Application to Low Light Levels," J. Optical Soc. Am., 37, 420 (June, 1947) – and references listed on the first page of this paper.

2. Sharpe, J., "Dark Current in Photomultiplier Tubes," Document Ref. No. CP-5475, EMI Electronics, Ltd., Hayes, Middlesex, England (Oct. 1964).

3. Sharpe, J., "Photoelectric Cells and Photomultipliers," EMI Electronics, Ltd., Hayes, England (1961).

4. Application Note E2, "Threshold Sensitivity and Noise Ratings of Multiplier Phototubes," ITT Industrial Laboratories, Fort Wayne, Indiana (May 1964).

5. Pound, R. V., Microwave Mixers, p. 24, and early chapters, M.I.T. Radiation Lab. Series #16, (1948).

6. Johnson, J. B., Phys. Rev. 32, 97 (1928).

7. Nyquist, M., Phys. Rev. 32, 110 (1928).

8. Johnson, J. B., and Llewellyn, F. B., Elec. Engrg., N. Y., 53, 1449 (1934).

9. Williams, F. C., Wireless Section, IEE, 13, 53 (March 1938).

10. Torey and Whitmer, Crystal Rectifiers, M.I.T. Radiation Lab. Series #15.

11. Van Voorhis, Microwave Receivers, M.I.T. Radiation Lab. Series #23.

12. Eberhardt, E. H., "Noise in Photomultiplier Tubes," Research Memo #309, ITT Industrial Laboratories, Fort Wayne, Indiana (Oct. 1959, Rev. Nov. 1960).

13. A Turbulence Primer, University of Illinois.

14. Landau and Lipshitz, Fluid Mechanics, Pergamon Press and Addison-Wesley Publishing Co., Inc. (1959).

15. Richtmeyer, Kennard and Lauritsen, Introduction to Modern Physics, 91, McGraw-Hill Book Co. (1955).

REFERENCES FOR SECTION 2.5 (Continued)

16. Data Sheet for RCA 8645 and 8646 Photomultiplier Tubes, RCA, Camden, N.J.

2.6 Heterodyning Efficiency (Coherence Loss Factor)

In Section 2.5 it has been shown that the mean Square System Signal-to-Noise Power Ratio, measured at the anode of the photo-multiplier-mixer is given by

$$\left(\frac{S}{N}\right)_{MS} = \frac{S_k \; P_{LO} \; P_s}{e \; k \; \Delta \; f \; (P_{LO} + P_s)} \tag{1}$$

where parameters are defined in 2.5.

It was also shown that there are two modes of operation possible, in terms of the optimum value of P_{LO}, namely a large scattered signal power, P_s, and a small scattered signal power. Since operating problems generally arise only in the case of small P_s, the following discussion will be slanted towards this case. It will also hold in general for the high P_s case, with the exception of any comments made with regard to the proper operating level of P_{LO}.

For low P_s (for high P_s case, see Section 2.5), rewrite (1) as

$$\left(\frac{S}{N}\right)_{MS} = \frac{S_k \; P_s}{e \; k \; \Delta f} \; \frac{1}{\left(1 + \dfrac{P_s}{P_{LO}}\right)}$$

$$\approx \frac{S_k \; P_s}{e \; k \; \Delta f} \; , \qquad P_{LO} \gg P_s \tag{2}$$

In the formulation of this equation, no acccunt was taken of losses and inefficiencies of the scattering and heterodyning process. These act to reduce $\left(\frac{S}{N}\right)$ ratio either by reducing signal power, by increasing noise power, or both. For convenience, and with some physical justification, express this inefficiency by

suitable modification of equation (2) as follows:

$$\left(\frac{S}{N}\right)_{MS} = \mu_T \left(\frac{P_s}{\Delta f}\right) \left(\frac{S_k}{ek}\right) \left(\frac{1}{1 + \dfrac{P_s}{P_{LO}}}\right)$$

$$\approx \mu_T \left(\frac{P_s}{\Delta f}\right) \left(\frac{S_k}{ek}\right), \qquad P_{LO} >> P_S \qquad (3)$$

where $\mu_T \equiv$ a constant called Coherence Loss Factor, a number less than unity.

$\equiv \mu_D \ \mu_S \ \mu_{Tr} \ \mu_C$,

$\mu_D =$ detector alignment factor

$\mu_S =$ scattering target coherence loss factor

$\mu_{Tr} =$ transmission path coherence loss factor

$\mu_C =$ source coherence length factor.

An important experimental objective, which determines the limitations, design parameters and even the feasibility of a practical Laser Doppler Velocity Instrument, is the measurement of these constants which together make up μ_T. A value of μ_T has been obtained experimentally for the case of a rotating plastic disc, and for a nozzle flow measurement (Sections 2.18 and 2.19). The determination of proper laser power level, of scattering injectant type and concentration all depend on measurements of these constants.

The constants are analyzed in relation to the physical parameters of the instrument system in Sections 2.7 through 2.10. In brief, their effect in reduction of $\left(\frac{S}{N}\right)$ stems from three

basic causes:

1) Attenuation of loss in signal power P_s, i.e. reduction below ideal of the numerator in equation (1);

2) Increase in noise over the minimum theoretically possible, i.e. an increase in the denominator of equation (1);

3) Loss of coherence, caused by "scrambling" of light wave phase.

(1) and (2) act on the amplitudes of the mixed light beams, while (3) operates on the phases and frequency spectrum.

2.7   Source Coherence Length

A brief resume is given below of parameters which define the coherence properties of the source. These coherence properties have a vital bearing on the limits of resolution of the inter- ference pattern between two light beams, and, in our case, on the magnitude of the heterodyne signal we will obtain from the Laser Doppler Velocity Instrument by mixing the scattered and reference (or "local oscillator") light beams.

The explicit derivation of these parameters by calculation of the quality of "interference" images or "heterodyne" signals in terms of wave optics of wavetrains of finite lengths is presented fully in References 1, 2, 3. Of these the first gives rigorous treatment which is very clearly written and relatively easy to follow, the second gives a good account with specific emphasis on experimental implications, while the third gives a rigorous treatment, clearly written, but in much more detail than might be needed at first exposure. Reference 4 provides excellent supplementary material on some specific aspects of partial coherence.

Since the details are somewhat lengthy, the rigorous deri- vations are left to the references. The following simplified approach, however, provides a useful physical picture (2):

Consider two waves one at the frequency ν and the other at the frequency $(\nu - \Delta\nu)$*. Let c be the free-space velocity of light and λ the wavelength at the frequency ν. Then

$$c = \nu\lambda, \qquad\qquad\qquad\qquad (1)$$

- -

*   Defining the waves each in terms of a single frequency automatically also defines them as being wavetrains infinite in extent – an impossible assumption in a real case (5).

and the phase ϕ in the wave equation is given by

$$\phi = 2\pi\nu \tag{2}$$

Let the two waves be in phase at some time t_o. After a propagation time $(t - t_o)$, over a distance

$$L = c \ (t - t_o) = c\Delta t, \tag{7}$$

the two waves will be out of phase by an amount

$$\Delta\phi = [2\pi \ \nu\Delta t - (\nu - \Delta\nu) \ \Delta t]$$
$$= 2\pi \ (\Delta\nu)(\Delta t) \tag{3}$$

By differentiating (2),

$$\Delta\phi = 2\pi\Delta\nu, \tag{4}$$

and by differentiating (1),

$$\Delta\nu = -\frac{\nu}{\lambda} \ \Delta\lambda, \tag{5}$$

where $\Delta\lambda$ is the wavelength difference corresponding to the frequency difference $\Delta\nu$.

Substituting (4) and (5) in (3), we obtain

$$\Delta\phi = -2\pi \ c \ \frac{\Delta\lambda}{\lambda^2} \ \Delta t \tag{6}$$

We may now define, arbitrarily, a coherence length L_{ϕ_o},

which is the length L for which the phase difference between the two waves is equal to $\Delta\phi_0$. By combining (6) and (7), we obtain

$$L_{\phi_0} = \frac{\Delta\phi_0}{2\pi} \frac{\Delta\lambda}{\lambda^2} \, , \tag{8}$$

and $\Delta t_{\phi_0} \equiv \tau = \dfrac{L_{\phi_0}}{c}$ from (7). $\tag{11}$

Some differences arise at this point between the choice of $\Delta\phi_0$ by different authors. Stroke (2) chooses $L_{\phi_0} = \frac{\pi}{2}$, so that L_{ϕ_0}, and the corresponding Coherence Time $\Delta t_{\phi_0} \equiv \tau$ are

$$L_{\phi_0} \text{ (Stroke)} = \frac{1}{4} \frac{\lambda^2}{\Delta\lambda} \tag{9}$$

$$\tau \text{ (Stroke)} = \frac{1}{4c} \frac{\lambda^2}{\Delta\lambda} \, ; \tag{9a}$$

whereas Born and Wolf (3) and Francon (1) choose

$$\phi_0 = 2\pi, \text{ so that}$$

$$L_{\phi_0} \text{ (B \& W, F)} = \frac{\lambda^2}{\Delta\lambda} = \frac{c}{\Delta\nu} \tag{10}$$

$$\tau \text{ (B \& W, F)} = \frac{1}{c} \frac{\lambda^2}{\Delta\lambda} = \frac{1}{\Delta\nu} \tag{11}$$

The former is more suited to an experimental discussion, whereas the latter falls more readily out of the analytical expressions when dealing with partially coherent wave trains.

Whatever the choice of ϕ_o , the remaining relationships remain unchanged. We now jump, with no apology, from an idealized picture of two monochromatic (infinite) wave trains to wave packets of finite length, which therefore necessarily must be defined by a frequency spread $\Delta\nu$, and wavelength spread $\Delta\lambda$ (5). The wave packets are assumed to emanate from the same source, but to reach the point of study (the interferometer screen, or the Laser Doppler Velocity Instrument photocathode) by paths of different lengths. The same expressions and definitions hold true, except that now

$\Delta\nu$ = effective frequency range of the Fourier spectrum of the source light

$\Delta\nu$ = effective wavelength range of the Fourier spectrum of the source light,

and we summarize:

COHERENCE LENGTH   L (Born & Wolfe, Francon) $= \dfrac{\lambda^2}{\Delta\lambda} = \dfrac{c}{\Delta\nu}$

                       L (Stroke) $= \dfrac{\lambda^2}{4\pi\Delta\lambda} = \dfrac{1}{4}\dfrac{c}{\Delta\nu}$

COHERENCE TIME τ (Born & Wolf, Francon) $= \dfrac{1\lambda^2}{c\Delta\lambda} = \dfrac{1}{\Delta\nu}$

                       τ (Stroke) $= \dfrac{1}{4c}\dfrac{\lambda^2}{\Delta\lambda} = \dfrac{1}{4\Delta\nu}$

The important practical point is (3) that in the Laser Doppler Velocity instrument, the path length difference between

the source and the photocathode, via the scattering volume and
via the reference beam, must be small compared with the coherence
length of the light. For the best monochromatic thermal sources,
the coherence time is of the order of 10^{-8} sec., whereas for
lasers, it can be of the order of 10^{-2} sec. The corresponding
Coherence Lengths are, respectively, of the order of 300 cms and
3 million metres. Therein lies the desirability of using a laser
light source instead of a thermal source for the Laser Doppler
Velocity instrument.

There is, of course, one more important reason for the choice.
The Coherence Times and Lengths say nothing about the intensities

of the light beams. In a thermal source, the intensity of light
contained within $\triangle v$ is orders of magnitude below that for a laser.
The Signal-to-Noise Ratio of the Laser Doppler Velocity instrument
is directly proportional to intensity of scattered light (see
sections 2.5 and 2.18). It is unlikely that any realizable
thermal source would be capable of giving the required output in
the necessary narrow $\triangle v$. Even if such a source were available,
the amount of light energy used by the instrument system would
be infinitesimal compared with the energy outside the frequency
range $\triangle v$, which would be thrown away.

REFERENCES FOR SECTION 2.7

1. Francon, M., _Optical Interferometry_, Academic Press (1966).

2. Stroke, G. W., _An Introduction to Coherent Optics and Holography_, Academic Press (1966).

3. Born, M., and Wolf, E., _Principles of Optics_, (2nd Ed.), Macmillan Company, Pergamon Press (1964).

4. Beran and Parrent, _Theory of Partial Coherence_, Prentice-Hall, Inc., (1964).

5. Stratton, J., _Electromagnetic Theory_.

2.8 Scattering from Random Scatterers

This section presents a discussion of the analytical work
performed on the problem of scattering from a random collection
of particles.

The physics of this process is one of the key elements which
determine the heterodyne signal amplitude of the laser doppler
flowmeter system. It encompasses the fundamental optical scat-
tering parameters of velocity distribution inside the scattering
volume (and therefore size of the scattering volume, since velocity
distribution depends on how much of the flow field we probe at any
instant), the scattering angle, the amplitudes of the reference
and scattered beams, and the source linewidth or coherence length
(Section 2.7). This last parameter has not yet been incorporated
into the analysis, but work on this additional feature is in pro-
gress.

A general expression for the heterodyne current for a cylin-
drical distribution of particles with random velocities and loca-
tions is obtained. The expression involves an integral that has
not yet been evaluated except for some simplified cases. To
obtain insight into the physical behavior of the problem the
simplified case of nearly forward scattering from a line distribu-
tion of scatter is considered. The result shows that the heterodyne
signal decreases with increasing scattering angle and increasing
breadth of the spectrum of scattered light. The situation to be
considered is shown in Figure 2.8-1. A region of space contains
a collection of N particles with random velocities and positions.
A plane wave is incident on the scatterers and spherical waves
emanate from each scatterer. A detector receives the scattered
waves and a portion of the incident wave that serves as a local
oscillator input (see Section 2.5 for detailed discussion of the
local oscillator and signal mixing process). A phase reference
plane is chosen with its surface parallel to the incident wave

2.8-1

SCATTERED WAVE

PHASE
REFERENCE
PLANE

$\odot (\rho_D, 0, z_D)$

θ

Z

PLANE WAVE
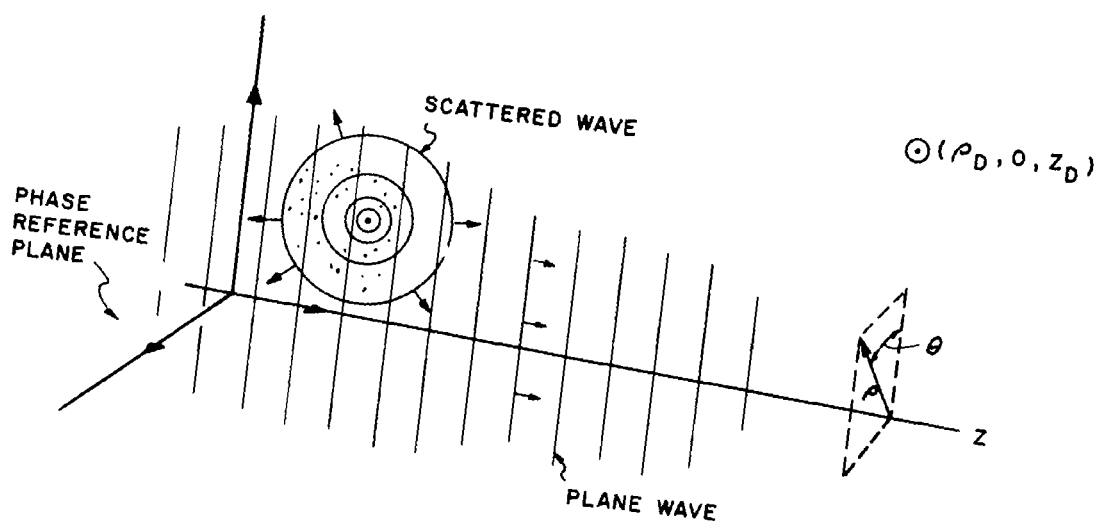
Fig. 2.8-1. Geometry of Scattering from Random Scatterers.

2.8-2

front and located at the left-hand boundary of the region containing the scattering particles. The phase of the incident wave at the phase reference plane at instant t is $w_o t + \varphi_o$, where w_o is the frequency of the incident wave and φ_o is arbitrary. At the same instant, the phase of the incident wave at the location of the ith scatterer is $w_o t + \varphi_o - l_i k_o$, where l_i is the distance from the phase reference plane to the ith scatterer and k_o is the magnitude of the incident wave vector*. Under the assumption that there is no phase change introduced by the scattering process, the phase of the spherical wave emanating from the ith scatterer at instant t at the location of the scatterer is equal to the phase of the incident wave. The phase of the spherical wave at a distance measured radially out from the scatterer is $w_s t - k_s r + \varphi_s$, where w_s and k_s are the scattered wave frequency and the wave number, and φ_s is fixed by the requirement that the phase of the scattered and incident waves match at the location of the scatterer:

$$\varphi_s = w_o t - w_s t + \varphi_o - l_i k_o. \tag{1}$$

Thus, at a detector at a distance r_D from the scatterer, the phase is given by

$$\Phi(D) = w_o t - k_s r_D - l_i k_o + \varphi_o. \tag{2}$$

At first glance it appears that the frequency of the scattered wave is the same as the frequency of the incident wave, w_o. However the motion of the particle gives k_s, r_D, and l_i a time dependence. Hence the true frequency, w_i, the time derivative of the phase, is

$$w_i = w_o - k_s \frac{dr_{Di}}{dt} - \frac{dk_s}{dt} r_D - \frac{dl_i}{dt} k_o. \tag{3}$$

* i.e., the wave number.

The terms subtracted from w_o represent the Doppler Shift. The $\frac{dr_D}{dt}$ and $\frac{dl_i}{dt}$ terms are independent of time for uniform particle motion. The $\frac{dk_s}{dt}$ term is independent of time if the dependence of Doppler shift on angle is neglected. When these assumptions are made, the scattered signal has a unique frequency, which is independent of time. Then

$$\Phi_D = \Phi_D(t = o) + t \left[\frac{d\Phi_D}{dt}\right]_{t = o}$$

$$= w_i t - k_i r_{Di} - l_i k_o + \varphi_o. \qquad (4)$$

With this phase, the electric field amplitude of the wave scattered by the ith particle is, at the detector,

$$E_i^s (D) = \frac{E_s}{r_{Di}} \sin \left[w_i \left(t - \frac{r_{Di}}{c}\right) - w_o \frac{l_i}{c} + \varphi_o\right], \qquad (5)$$

where c = velocity of light.

The total electric field at the detector is given by

$$E_{tot} (D) = E_{LO} \sin w_o \left(t - \frac{l_o}{c}\right) + \sum_{i=1}^{n} E_i^s (D), \qquad (6)$$

where l_o is the length of the path travelled by the local oscillator beam from the phase reference plane to the detector, and E_{LO} is the peak amplitude of the local oscillator electric field.

The output of the detector is proportional to $E_{tot}^2 (D)$, which is equal to

$$E_{tot}^2 (D) = E_{LO}^2 \sin^2 \left[w_o \left(t - \frac{l_o}{c} \right) - \varphi_o \right] + \sum_{i=1}^{n} \left[E_i^S (D) \right]^2$$

$$+ 2E_{LO} \sin \left[w_o \left(t + \frac{l_o}{2} \right) + \varphi_o \right] \sum_{i=1}^{n} E_i^S (D)$$

$$+ 2E_i^S (D) \sum_{i=2}^{n} E_i^S (D) + \ldots + 2E_{n-1}^S (D) \ E_n^S (D). \quad (7)$$

When the expression for $E_i^S (D)$ is substituted into this equation, trigonometric identities can be used to rewrite it in terms that are independent of time; terms oscillating at $2w_i$, $i = 0, 1, \ldots n$; terms oscillating at $2w_i$, $i = 0 \ldots n$; and terms oscillating at $w_i \pm w_j$, $i, j = 1, \ldots, n$. The $2w_i$, $w_o + w_i$, and $w_i + w_j$ terms are neglected because the detector cannot respond to such high frequencies. The $w_i - w_j$ terms are neglected because they are at low frequencies compared to the true heterodyne signal, which oscillates at $w_o - w_i$. The heterodyne current out of the detector, I_h, is given by

$$I_h = k \ E_{LO} \ E_s \sum_{i=1}^{n} \frac{1}{r_{Di}} \cos \left[w_o \left(t - \frac{l_o}{c} + \frac{l_i}{c} \right) - w_i \left(t - \frac{r_{Di}}{c} \right) \right]$$

$$= k \ E_{LO} \ E_s \ N \ \langle f \rangle, \quad (8)$$

where k is the sensitivity of the detector, $\langle f \rangle$ denotes an average over the n particles, and f is

$$f = \frac{1}{r_{Di}} \cos \left[w_o \left(t - \frac{l_o}{c} + \frac{l_i}{c} \right) - w_i \left(t - \frac{r_{Di}}{c} \right) \right]. \quad (9)$$

To perform the average over the scattering particles, the function
f is rewritten in terms of the position of the n particles, and
distribution functions for the position and frequency variables
are assumed. A cylindrical coordinate system is chosen with its
origin in the phase reference plane and the z axis orthogonal to
that plane. For convenience, the azimuthal coordinate is measured
from the plane containing the z axis and the detector as shown in
Figure 2.8-1.   Then

$$l_i = z_i$$

$$\text{and } r_{Di} = \sqrt{\rho_D^{\,2} + \rho_i^{\,2} - 2\rho_D\rho_i \cos\theta_i + \left(z_D - z_i\right)^2}, \qquad (10)$$

and

$$f(w_i, \rho_i, \theta_i, z_i) = \frac{\cos\left[w_o\left(t - \dfrac{l_o}{c} + \dfrac{z_i}{c}\right) - w_i t + \dfrac{w_i}{c} r_{Di}\right]}{r_{Di}} \qquad (11)$$

The distribution functions assumed for the random variables w_i,
ρ_i, θ_i, and z_i are as follows:

$$p(w_i) = \frac{1}{\sqrt{2\pi\sigma^2}}\, e^{-\dfrac{(w_i - <w>)^2}{2\sigma^2}} \qquad 0 \le w_i \le \infty, \qquad (12)$$

where $<w>$ is the mean value of the scattered frequency and t is
the standard deviation. This distribution corresponds to the
Gaussian spectrum of a Doppler broadened line:

2.8-6

$$p(\rho_i) = \frac{1}{\rho_M} \qquad 0 \le \rho_i \le \rho_M \qquad p(\rho_i) = 0 \text{ elsewhere}$$

$$p(\theta_i) = \frac{1}{2\pi} \qquad 0 \le \theta \le 2\pi \tag{13}$$

$$p(z_i) = \frac{1}{z_M} \qquad 0 \le z_i \le z_M \qquad p(z_i) = 0 \text{ elsewhere}$$

These distributions correspond to a cylindrical region containing the scatterers with all points equally likely locations for a scatterer.

With these distribution functions, $<f>$ is given by

$$<f> = \frac{1}{2\pi} \frac{1}{\sqrt{2\pi t^2}} \frac{1}{z_M} \frac{1}{\rho_M} \int_0^\infty d\omega_i \int_0^{\rho_M} d\rho_i \int_0^{2\pi} d\theta_i \int_0^{z_M} \frac{dz_i}{r_{Di}} \exp\left[-\frac{(\omega_i - <\omega>)^2}{2\sigma^2}\right] \cos X$$

$$\tag{14}$$

where
$$X \equiv \left[\omega_0 \left(t - \frac{l_0}{t} + \frac{z_i}{c}\right) - \omega_i t + \frac{\omega_i}{c} r_{Di}\right] \tag{14a}$$

and r_{Di} is given by Equation (10). The evaluation of this integral for the cylindrical distribution of scatterers cannot be done exactly in analytical form. Work is underway to obtain approximate analytical evaluation and/or numerical evaluation.

To illustrate the physical behavior of the problem, the limiting case of almost forward scattering from a collection of scatterers distributed randomly along a line is considered. For a line distribution of scatterers, $\rho(\rho_i) = \delta(\rho_i)$, $\rho(\theta_i) = \delta(\theta_i)$,

where δ is the Dirac delta function. The integral for $<f>$ becomes

$$<f> = \frac{1}{z_M} \frac{1}{\sqrt{2\sigma^2}} \int_o^\infty dw_i \int_o^{z_M} dz_i \; \frac{\exp\left[-\frac{(w_i - <w>)^2}{2\sigma^2}\right] \cos X_1}{\sqrt{\rho_D^2 + (z_D - z_i)^2}} \tag{15}$$

where $X_1 \equiv \left[w_o \left(t - \frac{l_o}{c} + \frac{z_i}{c} \right) - w_i t + \frac{w_i}{c} \sqrt{\rho_D^2 + (z_D - z_i)^2} \right]$ (15a)

When the distance from the scattering volume to the detector is large compared with the dimensions of the scattering volume and the scattering is nearly in the forward direction, $z_i \ll z_o$ and $\rho_D \ll z_D$, then the square roots in the integral can be expanded. The resulting integral can be evaluated with the further approximation of extending the lower limit of the θ integration to $-\infty$. This is legitimate because the exponential factor in w_i makes the integral appreciable only in the neighborhood of $w_i \approx <w>$, a large positive number. The result of carrying out the integration is that

$$I_h = \left\{ E_{LO} E_s \right\} \left\{ \cos \psi \right\} \left\{ \cos X_2 \right\} \left\{ \exp\left[-\left(t - \frac{r_D}{c} \right)^2 \frac{\sigma^2}{2} \right] \right\} \tag{16}$$

where $X_2 = \left[(w_o - <w>) \; t - \frac{w_o l_o}{c} + \frac{<w> r_D}{c} \right]$ (16a)

While this expression has been obtained under various approximations, the result shows interesting features of the physical

behavior of the heterodyne signal obtained in scattering from
random particles. The factors contained in the various curly
brackets are now considered one by one. The factor $\left\{E_{LO}\ E_s\right\}$ shows
the dependence of the heterodyne signal as discussed in Sec-
tion 2.5.   The $\left\{\cos\ \psi\right\}$ factor shows that the heterodyne signal
is maximum for forward scattering. Away from the forward direc-
tion, the optical path from source to scatterer to detector is
slightly different for each particle. In the forward direction,
particles farther from the source are closer to the detector, and
the variations in source to particle path length are cancelled
by the corresponding variations in particle to detector path length.

   The time dependent terms in the $\left\{\cos\left[(\omega_o - <\omega>)\ t - \dfrac{\omega_o}{c} + \dfrac{<\omega>\ r_D}{c}\right]\right\}$
factor show oscillation at a frequency that is the difference be-
tween the local oscillator beam and the beam frequency of the
scattered light.

   The other terms in the argument of the cosine show an inter-
ferometer effect. If there were no frequency shift due to the
scatterer motion, there would be a steady light or dark fringe at
the detector. The time independent terms in the argument of the
cosine are approximately the path difference between the local
oscillator and scattered beams, and determine whether the fringe
would be light or dark.

   The exponential term shows that the heterodyne signal is not
a single frequency. If the Fourier transform of the signal were
taken to get the spectrum, the exponential term would give the
frequency spread. The extent of the frequency spread depends on
σ, which is the parameter describing the width of the spectrum of
the scattered light and hence the spread of velocities in the
scattering volume.

   The term $\left(t - \dfrac{r_1}{c}\right)$ in the exponential factor requires some
consideration. It is the difference between some unspecified
time, and the time taken for a scattered wave to travel from the
scattering volume to the detector. The "unspecified time" is

present, because of the unrealistic assumption of monochromatic plane waves (which have travelled for an undetermined time) incident on the scatterers. In fact, the waves are neither monochromatic nor plane. They emanate from a laser source whose light output has a finite bandwidth (or coherence length - see Section 2.7), the light beam also being slightly divergent if shone directly onto the scatterers, or convergent if it is focussed. The analysis of this more complex case is in progress. When completed, physical intuition suggests that the "unspecified time t" will be replaced by a term like $\frac{r_s}{c}$, where r_s is the distance of the source from the detector. Thus the exponential factor will then also be a measure of loss of coherence due to the difference between the scattered and reference beam path lengths. The exact form of the exponential has yet to be determined for the real case.

Thus, it is seen that the simple case of nearly forward scattering from a line distribution of particles gives important information on the physical behavior of the Laser Doppler Flowmeter System. Further work to evaluate the more realistic model of a cylindrical collection of scatterers at all scattering angles will yield more precise quantitative information. This requires the numerical integration of Equation (16), which is to be the next task in our analysis, to be carried out after the source coherence length has been incorporated.

2.9 Transmission Path Coherence

During their passage through the atmosphere, the scattered
and reference laser beams will potentially suffer some degrad-
ation affecting their ability to produce coherent heterodyne
signals at the photomultiplier mixer. For convenience (Section
2.6) we have arbitrarily, but with some physical justification,
treated this effect on the heterodyne signal as a factor (less
than 1) by which the Signal-to-Noise Ratio at the photomixer is
multiplied; and have termed it μ_{Tr} ≡ Transmission Coherence Loss
Factor.

The causes of the loss factor can be understood by consider-
ing the processes by which the laser beam light wave magnitudes
and phases (assuming the light has a finite line-width) can be
changed by passage of the laser beam through the atmospheric
(or wind tunnel) gas path. These are, briefly:

1) Fluctuations in intensity of the light beam caused
by varying extinction -- these will not affect the
Laser Doppler Velocity Instrument, since its signal
processing apparatus is designed to be virtually in-
sensitive to amplitude changes, and only sensitive
to frequency changes in the heterodyne signal.
(Section 2.12) In any case the signal-to-noise
ratio is independent of the reference beam intensity
when operated in the low scattered signal mode
(Section 2.5).

2) Fluctuations in effective transmission path length
caused by fluctuations in path density, and there-
fore, refractive index and wave velocity; and by
fluctuations in geometrical path length with bent
rays. Hence the phase ϕ will change with time, and
therefore, the transmitted frequency ($\equiv \frac{d\phi}{dt}$) will
fluctuate.

3) Scattering from atmospheric (or gas) particles out-
side the instrument scattering volume, which will
contribute their own doppler shift spectrum to the
transmitted light beam.

Sources (2) and (3) are clearly the only effects which have
to be considered since they result in exactly the same kind of
frequency changes in the heterodyne signal as the wanted Doppler
shifts. Under normal circumstances it is to be expected that
they are quite negligible. However, their effects could become
appreciable in extended high temperature regions, say around the
base of a large rocket. While it is expected, even then, that
their signal magnitudes will be low compared with those from the
instrument designed scattering volume, nevertheless further study
should be made of this factor when considering combustion or
high Mach Number flows.

Apart from the latter case, transmission path effects are,
in general, of more importance to the remote sensing of wind
velocity (the other major task in the present contract) because
of the much greater atmospheric transmission path lengths in-
volved. No further study is planned with respect to Wind Tunnel
measurements for the time being.

2.10 Optical Mixer Geometry and Alignment

One of the most significant design considerations to be found in the Laser Doppler Velocity Instrument lies in the geometry of the Scattered and Reference beam superposition process at the Optical Mixer, i.e., at the Photomultiplier Cathode surface. The design of the superposition geometry will directly affect system Signal to Noise Power Ratio, the criticality of alignment procedures, and the susceptibility of the whole instrument to external noise, vibration and temperature changes. The complete problem is relatively complicated, and is to be considered in several alignment elements, each related to different elements of the six degrees of freedom. Alignment in all six degrees of freedom of each of the superposition elements must be considered, i.e., each beam and the PhotomultiplierMixer (PM) cathode. They will be analyzed as shown in Table 2.10-1, each group being related to its freedom in a particular dimension.

Both the Signal Power in the numerator and the Noise Power in the denominator of the Signal to Noise equation (3) of Section 2.6 are modified by alignment geometry, the integrated effect being expressed for convenience as a single loss factor μ_D. In the following discussion, the objective has been to extract the information needed to design for non-criticality of alignment, and minimum loss of S/N when practical limits of precision are considered. From this material, the design bases become quite clear. Curves showing the effects of parametric variations on the loss factor would be invaluable as additional tools to aid design judgment. These have not been produced so far in view of limitations in time.

TABLE 2.10-1

DEGREES OF FREEDOM IN ALIGNMENT GEOMETRY

Degrees of Freedom	Alignment Element	Degree of Freedom Restraints for each alignment element		
		Scattered Beam	Ref. Beam	P. M. Cathode
Two rotational degrees about axes transverse to the optical axis	Each of two beams in angular alignment, each perpendicular to the P. M. cathode	2	2	2
One rotational degree about the optical axis.	Coincident polarization between the two beams	1	1	-
Two translational degrees of freedom, transverse to the optical axis.	Each of two beams in transverse alignment	2	2	* −
One translational degree of freedom parallel to the optical axis	Each of the two beams in focus on the P.M. cathode	1	1	1
	Total	6	6	3

* Assuming PM cathode is appreciably larger in size than the transverse dimensions of the two beams.

2.10.1 Angular Misalignment Between Scattered and Reference Beams

An excellent analysis of the effects of angular beam misalignments has been reported in Reference 1. A note on results of a similar study at the Raytheon Company is given as Appendix A to this report.

In summary, Figure 2.10-1a shows the principle of the signal loss process. Considering, first, misalignment between the beams, the two beams XX, and YY arrive at the photomultiplier cathode AB with an angular misalignment θ radians, assumed small. One beam is assumed perpendicular to AB, and the analysis is presented in one dimension for simplicity. In the figure, the extreme lower boundary of each beam is shown arriving on AB at the same time. It will be seen that the other sides of each of the beams, X' and Y' will arrive at different times. As shown in Appendix A, the time difference of arrival is approximately the small distance $\ell_D\theta$, divided by the velocity of light c , where ℓ_D is the distance across the detector face illuminated by the beams. Hence the heterodyne signal magnitude will be reduced below maximum, because the two electromagnetic field vectors will be out of phase by $\frac{2\pi \ \ell_D\theta}{\lambda}$ radians. Thus the magnitude of the terms in equation (4) of Section 2.5.3.1 will each be multiplied by a factor depending on the phase difference. Appendix A shows that the multiplying factor is zero (i.e., no heterodyne output) when

$$\frac{2\pi \ \ell_D\theta}{\lambda} = \pi, \tag{1}$$

i.e., a phase angle corresponding to half a wavelength difference in path length of the extreme boundaries of the two light beams when spread ℓ_D across the PM cathode AB.
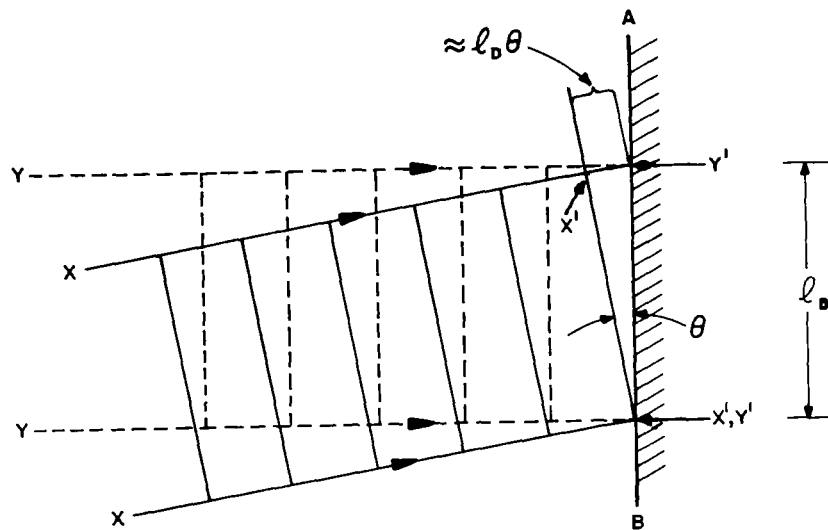
a). <u>Angular Misalignment of Beams and PM Cathode.</u>

BESSEL FUNCTION
EQUAL AREAS

RECTANGULAR EQUAL AREAS
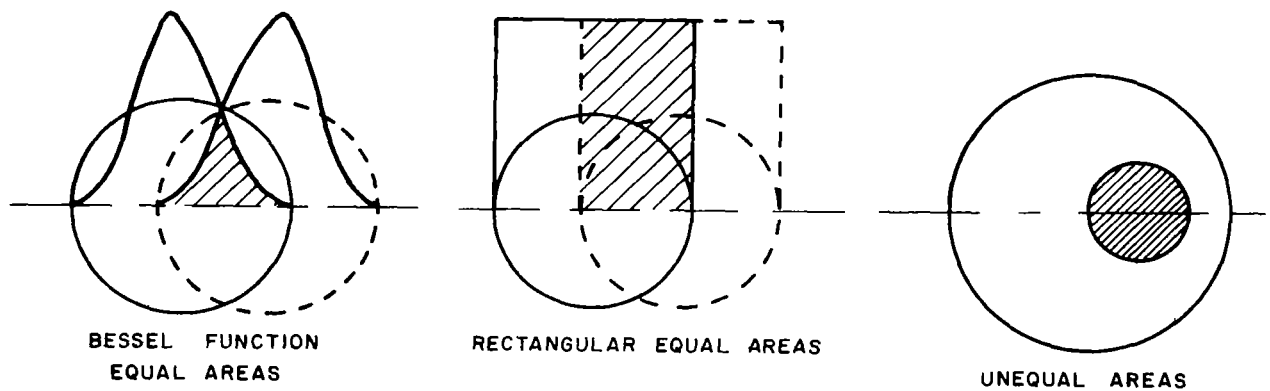
UNEQUAL AREAS

b). <u>Transverse Misalignment of Beams for Bessel Function,
Rectangular Distributions, and Unequal Areas.</u>

Fig. 2.10-1. <u>Angular and Transverse Misalignments of Scattered
and Reference Beams and Photomultiplier Cathode</u>

As a reasonable design goal we will restrict the path difference over ℓ_D to one quarter of a wavelength, i.e., $\frac{\pi}{2}$ radians. Equation (1) then becomes

$$\frac{2\pi \ \ell_D \theta}{\lambda} = \frac{\pi}{2}$$

or

$$\theta_{\frac{\pi}{2}} = \frac{\lambda}{4 \ell_D} \tag{2}$$

If, for example, the beam diameters were .1 cm at 4880 Å wavelength,

$$\theta_{\frac{\pi}{2}} = \frac{4880}{10^8} \ \frac{1}{4} \ \frac{1}{1} = 1.22 \times 10^{-4} \ \text{rad} \approx 26 \ \text{seconds}$$

This value for θ would make design requirements onerous indeed.

An alleviation of this condition is therefore sought. Clearly, since the choice of the laser light wavelength is restricted, the solution is to decrease ℓ_D, so that the allowable misalignment is larger.

This can be done either by focusing each of the two beams on to the PM cathode, or by reducing the diameter of the parallel beams by a convenient arrangement of lenses, or by a combination of the two. In the focused beam case, the analysis for parallel beams still holds, because at the focus of a diffraction limited lens, the wavefronts in the Airy pattern are plane, and perpendicular to the incident light propagation vector.

As an illustration of the advantages of focused superposition, two cases will be calculated:

1. <u>Focus to Airy Disc Diameter</u>

Then Airy disc diameter (3)

$$= \ell_D = 2.44 \ \lambda \ \frac{f}{D} = 2.44 \ \lambda F, \tag{3}$$

where

f = focal length

D = diameter of the lens

F = F Number of lens $\equiv \dfrac{f}{D}$.

Substituting into equation (2),

$$\theta_{\frac{\pi}{2}} = \frac{\lambda}{4 \ (2.44 \ \lambda \ F)} = \frac{1}{9.76F} \tag{4}$$

where $\theta_{\frac{\pi}{2}}$ is the beam angular misalignment at which a difference in path length of one quarter wavelength occurs across the PM photocathode.

For example, for an allowable $\theta_{\frac{\pi}{2}}$ misalignment of $\frac{1}{2}°$, the lens F number must be no greater than

$$\frac{180}{(9.76) \ (0.5) \ (\pi)} = 11.7, \text{ a reasonable parameter for optical}$$

design purposes. If a larger F number is used for the lens, the allowable misalignment between the beams will be reduced in inverse proportion.

In this case, ℓ_D = Airy disc diameter

$$= \frac{(2.44) \ (4880) \ (11.7)}{10^8}$$

$$= .0014 \text{ cms}$$

Evidently the smaller the F number (i.e., the smaller the focal length and larger the lens aperture), the greater the latitude we are allowed in misalignment of the two beams.

2. Reduce to a Small Diameter Parallel Beam

By equation (2),

$$\ell_D = \frac{\lambda}{4 \; \theta_{\frac{\pi}{2}}}$$

For $\frac{1}{10}$ degree allowable misalignment,

$$\ell_D \approx \frac{(4880) \qquad 180}{(4)(10^8)(0.1)(\pi)(2.54)} = .003 \text{ inches.}$$

i.e., something of a problem may arise in producing a parallel beam small enough to allow some practicable tolerance on θ.

Hence it is concluded that a focused beam system has very important advantages over a parallel beam, unless the latter is reduced to a very small diameter.

2.10.2 Angular Misalignment Between the Light Beams and the PM Cathode

The misalignment analysis for this case goes essentially the same as that for the two beam misalignment. Assume the two beams are in perfect angular alignment, one with the other, and that XX in Figure 2.10-1(a) represents the two coincident beams. Path difference $\ell_D\theta$ in this case arises because of misalignment between the PM cathode AB and the incoming superimposed beams XX.

By similar reasoning, we obtain an equation of the form of (2) above. Here, however, the important difference arises that the wavelength we are concerned with corresponds to the heterodyned difference frequency $f_H = (\omega_{Doppler} - \omega_o) \frac{1}{2\pi}$ and

$$\lambda_H = \frac{c}{f_H} \quad .$$

$$(\theta_{\frac{\pi}{2}})_H = \frac{\lambda_H}{4\ell_D} \tag{3}$$

If, say, $f_H = 60 \times 10^6$ Hz, compared with the laser light frequency $f_O \sim 6 \times 10^{14}$ Hz, then

$$\lambda_H = \frac{6 \times 10^{14}}{60 \times 10^6} \frac{(4880)}{(10^8)} \approx 500 \text{ cms}$$

Hence with $\ell_D \sim 1$ cm,

$$(\theta_{\frac{\pi}{2}})_H \approx \frac{500}{4}$$ – an absurdly large number, since our

analysis was only true for small θ. However, this illustrates that, provided the two beams are in accurate mutual alignment, their joint misalignment with the PM cathode is much less critical.

These large differences deduced between sensitivities to the two different parts of the alignment problem appear to be supported by our experiences in aligning optical heterodyning systems.

2.10.3 Transverse Alignment Between Scattered and Reference Beams

A heterodyne signal output is only obtained from those regions on the PM cathode surface where there is overlap between the Scattered and Reference beams. The heterodyne signal loss caused by transverse misalignment between the Scattered and Reference Beams is worst for the case when the areas illuminated on the photocathode by each beam are equal, as seen in Figure 2.10-1(b). It is also noted that in the equal area case,

a Bessel function distribution, as would be obtained from a focused or apertured system, is less sensitive to misalignment than a rectangular distribution, if such were obtainable (1).

Clearly, the use of unequal areas, as in the right hand diagram of the figure, allows transverse misalignment with no effect on _signal_. However, while the _signal_ is not reduced, such an approach does increase the system _noise_, (Section 2.10.6 below), so that the Signal to Noise ratio is reduced.

Evidently, while the use of focused beams alleviates the angular misalignment problem, it _accentuates_ that of trans-verse alignment, as seen in example (1) of Section 2.10.1, where the total dimension of each focused spot is only .0014 cms. Again, this conclusion is supported by our experimental work.

In all cases it is assumed that the PM cathode is so much larger than the laser beams that no stringent requirements are placed on its transverse adjustment.

2.10.4 _Alignment in Depth (Focusing)_

If parallel beams are used, the requirement for con-straint in the direction of the optical axis is removed for the beams and the PM tube. The use of focused beam (s) requires positioning along the optical axis of the PM cathode and the beam focusing optics to within the depth of focus, given by (2, 3)

$$\Delta z \approx \pm\ 2\ F^2\ \lambda,$$

where F = lens F number, λ is the wavelength, and Δz is the extent of the focal region on either side of the focal plane.

With our example 1 in Section 2.10.1,

F = 11.7, λ = 4880 $\overset{\bullet}{\text{A}}$, total depth of focus

$$= (4)(11.7)^2\ \frac{(4880)}{(10^8)} = .027\ \text{mm}.$$

This is a relatively easy design requirement to meet. In aligning experimental Laser Doppler Velocity Instrument systems it is found that this "tuning" adjustment is indeed a "comfortable" one -- no high-precision adjusting device is needed, provided a lens system having an F number of 11 or more is used.

2.10.5   Alignment of Beam Polarizations

In deriving equation (2) in Section 2.5.3.1 for the magnitude of the total wave generated by the superposition of the Scattered and Reference beams, it was assumed that the beams were both polarized, and that their electric field vectors had the same direction of polarization. If, in fact, the polarization directions differed by angle α, the component of one vector in the direction of the other would have to be used in the coherent interaction term, i.e., the last term, of equation (4), which would thus be reduced by a factor $\cos \alpha$. This factor would thus appear as a direct multiplier to the signal power in the signal-to-noise equation,

$$\text{i.e., } \mu_{DP} = \cos \alpha.$$

The importance of maintaining coincident polarization of the two beams is clearly illustrated.

2.10.6   Selection of Beam Spot Sizes

If parallel Scattered and Reference Beams are used in the superposition at the PM cathode, the spot sizes can be selected arbitrarily. If focused beams are used, the spot size is fixed by the Airy Circle diameter, viz: (using the same symbols as earlier in Section 2.10):

$$\text{spot diameter} = \ell_D = 2.44 \, \lambda F.$$

Hence, the relative spot diameters are determined

completely by the F numbers of the respective focusing lenses. Thus if, in order to alleviate translational alignment problems, we wish to use twice as large a spot for the Reference than for the Scattered beam, a lens of twice the F number would be needed.

The advantages of using different spot sizes for the Scattered and Reference beams was pointed out in Section 2.10.2. We will now consider the price which has to be paid in terms of loss of Signal-to-Noise Power Ratio if the spot sizes are different.

Equation (3) of Section 2.6 for the Mean Square Signal-to-Noise Power Ratio can be written as:

$$\left(\frac{S}{N}\right)_{A,MS} = \mu_D \left(\frac{S_k}{ek}\right) \left(\frac{1}{\Delta f}\right) \frac{P_{LO} \, P_s}{P_{LO} + P_s} \tag{1}$$

where just the detector geometrical alignment efficiency is shown. Suppose a larger spot size is used for the Reference (Local Oscillator) beam, such that $\frac{\text{Scattered Beam Spot Area}}{\text{LO Beam Spot Area}} = \gamma \, (<1)$.

Now in the beam interaction which produces the heterodyne signal output, obviously only that portion of the LO beam spot which coincides with the Scattered beam spot contributes to the signal output; whereas the whole LO beam spot contributes to the total anode "D.C." output current component, and therefore contributes noise. Assuming a uniform intensity across the LO beam, then the power per unit spot area is constant; hence LO beam power contributing to noise = P_{LO}, whereas LO beam power contributing to signal is reduced to $P'_{LO} = \gamma \, P_{LO}$. Hence equation (5) of Section 2.5.3.1 for the photomultiplier anode current output becomes:

$$I_{TA} = S_A \left(P_s + P_{LO} + 2\sqrt{P_s P'_{LO}} \, \cos \Delta \, \omega t\right)$$

$$= S_A (P_s + P_{LO} + 2 \sqrt{\gamma \, P_s P_{LO}} \, \cos \Delta \omega t)$$

and the equation for Signal-to-Noise Power Ratio, equation (7) from Section 2.5.4, becomes:

$$\left(\frac{S}{N}\right)_{A, MS} = \gamma \left(\frac{S_k}{ek}\right) \left(\frac{1}{\Delta f}\right) \frac{P_{LO} P_s}{P_{LO} + P_s}$$

i.e.,

$$\left(\frac{S}{N}\right)_{A, MS} = \mu_{DA} \left(\frac{S_k}{ek}\right) \left(\frac{1}{\Delta f}\right) (P_s) \frac{1}{+ \left(1 + \frac{P_s}{P_{LO}}\right)} \tag{2}$$

where geometrical alignment efficiency loss caused by the use of beam spots differing in area is

$$\mu_{DA} = \frac{\text{Scattered beam spot area}}{\text{LO beam spot area}} \equiv \gamma \tag{3}$$

Hence we note that, although increasing the area of the LO beam relative to the scattered beam alleviates criticality in transverse alignment, Signal-to-Noise Power Ratio is reduced. For example, if a LO beam spot diameter twice that of Scattered beam spot diameter were used, $\gamma = 4$, and a loss in $\left(\frac{S}{N}\right)$ power ratio of 6 db would result. Note that the factor $\left(1 + \frac{P_s}{P_{LO}}\right)$ is not appreciably affected in the low scattered power operating mode, when $\frac{P_s}{P_{LO}} \ll 1$. It might appear that we could "have our cake and eat it," if we used the larger LO beam spot size; then used a small aperture centered around the scattered beam axis, to cut off the "surplus" area of the LO beam spot, so preventing the "surplus" part of the LO beam from reaching the cathode and thus increasing the output noise. However, the catch is that this small aperture itself still has to be located with the same high precision as that required for the beams in the original equal-area case! There might be a slight practical advantage

to this case because it is probably easier to make a final adjustment of such a separate aperture, than to adjust the transverse location of either of the beams.

The above analysis for unequal areas holds whether either or both beams are focused or parallel. It has always been assumed in the analysis that relatively unlimited LO beam power is available, up to the maximum power handling capability of the PM mixer tube.

2.10.7 Note in Summary of Alignment Problems

In summary it is seen that to alleviate angular alignment problems we must use small beam spots at the photocathode, whereas to alleviate transverse alignment problems we must use large spots. Hence the final choice must be based on design judgment supplemented by operating experience. A useful additional tool in aiding judgment would be the calculation of parametric variational curves of signal-to-noise ratio misalignments in each degree of freedom.

REFERENCES FOR SECTION 2.10

1. Lee, Cullen Q., "An Investigation of Photoelectrically Heterodyning Light" NASA George C. Marshall Space Flight Center, Astrionics Research and Development Report #2 (1966).

2. Born and Wolfe, Principles of Optics, The MacMillan Company, New York (1964).

3. Kingslake, R. (ed.) et al, Applied Optics and Optical Engineering, Academic Press, New York and London (1965).

2.11 Spectral Broadening of Scattered Light

The frequency (and wavelength) spectrum of laser light scattered from the particles in the turbulent medium will be broadened, i.e., departing from pure monochromatic, for reasons stemming from several different physical phenomena. Since the Laser Doppler Velocity Instrument is based on the analysis of the scattered light frequencies to obtain velocity and turbulence information, it is of prime importance to examine and understand the several causes of spectral broadening. An estimate must be made of their importance in relation to the interpretation of velocity and turbulence data. It must be determined which effects are significant and which are negligible in the system. Those which cannot be so eliminated must be corrected for either in the signal processing system or during the data analysis.

The processes contributing to spectral broadening may be usefully and somewhat arbitrarily classified in relation to Laser Doppler Velocity instrumentation as follows (1, 2). For the purposes of the discussion, it is assumed that the ideal (or standard) instrument is probing a volume (the scattering volume) which is (a) small compared with macroscopic fluid parameters, (b) of the order of several wavelengths in physical dimension and therefore (c) large compared with molecular dimensions and separations at the gas pressures which will be encountered in probable applications.

1. Macroscopic Processes

    a. Turbulence

    b. Flow fluctuations and instabilities

Characteristic deviations above and below the mean velocity (and therefore mean doppler-shift frequency f_c) may be up to the order of 50% of the mean velocity (and f_c) i.e., up to, say, 50 MHz in present instrument concepts; occurring at a relatively "slow" rate of up to approximately 200 kHz. Character-

istic lengths are much larger than the scattering volume.

 2. Microscopic Processes

   a. Temperature Broadening, i.e., doppler broadening
      due to relative motion of the particles and the
      observer
   b. Pressure (Lorentz & Holtsmark) Broadening -- not
      applicable to scattering processes
   c. Field (Stark and Zeeman) - not applicable to scat-
      tering processes
   d. Natural Broadening - not applicable to scattering
      processes.

It should be noted that 2, 3, 4 above do not apply to
scattering processes, since the frequency of the radiation is de-
termined by the wave incident on the scatterer from the light
source; it is not generated by energy level transitions within the
scatterer. Thus only doppler effects can cause a frequency dif-
ference between the incoming and scattered light beams. The
magnitude of the Temperature Broadening effect for massive parti-
cles (e.g., graphite particles) is calculated in Section 2.11.2,
and is seen to be negligible for the laser doppler velocity in-
strument using light scattering from such particles.

 3. Instrumental Broadening

   a. Finite aperture
   b. Finite scattering volume

Instrumental broadening is the major contributor to
frequency spreading, other than that caused by turbulence. It
is analyzed below in detail.

To aid in separating the turbulence spectrum from
spectral broadening arising from other causes, one must exploit
the fact that characteristic parameters differ. The principal
parameters are:

2.11-2

1. Total frequency deviation above and below the mean,
2. Frequency or rate at which the frequency deviation occurs,
3. Characteristic dimensions of the effect which is causing the broadening, as compared with the dimensions of the scattering volume.

These three parameters have a special interrelation in the case of the turbulence doppler shift signal, as discussed in Section 2.12. This special interrelation is also exploited to separate out the velocity and turbulence information from frequency spreading stemming from the other causes. The variation in velocity across the scattering volume in a direction x is given by the product of the component of the velocity gradient in that direction multiplied by the dimension of the scattering volume in that direction, i.e.,

$$dU = \frac{\partial U}{\partial x} dx \tag{1}$$

As a result of this spread in velocity dU across the scattering volume, the scattered light frequency at any instant of time will have a frequency spread df. Because the scattering volume is very small compared with the characteristic size of the turbulence phenomenon, df is very much smaller that frequency deviation caused by turbulence fluctuations in velocity. Further, this spread df is a "continuum" spread, i.e., all values of frequency over the interval df are present simultaneously. The turbulence velocity doppler shift, on the other hand, represents only one localized mean velocity, $\bar{U} + U'$, (the mean velocity of gas inside the scattering volume) at an instant of time, which localized mean velocity, and therefore, localized doppler frequency shift $f_c + f_{DEV}$, fluctuates about the mean stream velocity $\bar{U}$ whose corresponding mean doppler shift is f_c. The frequency at which it fluctuates is random, and may be as high as 200 kHz as an approximate upper limit. This fluctuation frequency we shall

call the "signal frequency" f_s, for reasons which will become
evident in Section 2.12. Thus, if we could "sit on" this velo-
city $(\bar{U} + U')$ and track it up and down at the signal frequency,
we could observe at any instant, an instantaneous mean frequency
$(f_c + f_{DEV})$, with a frequency spread df about $(f_c + f_{DEV})$, pre-
sent at all values of $(f_c + f_{DEV})$. With small scattering volume,
df $<<f_{DEV}$ max, the maximum value of f_{DEV}. Figure 2.11-1 illus-
trates the frequencies involved in a graph of Intensity of Scat-
tered Light at frequency f, versus f. Note that this is not a
Fourier Analysis Spectrum as would be given by a spectrum analy-
zer. The latter would appear much more complex.

The finite aperture of the scattered light collecting
optics will have an exactly similar effect on the observed dop-
pler frequency. Because of its finite aperture size, it accepts
light scattered over a range of scattering angles and thus Dop-
pler-shifted over a range of frequencies. Because light from all
angles within the solid angle of the aperture arrives simultane-
ously, this will also result in a "continuum" frequency spread
about the instantaneous mean doppler shift f. This continuum
spread will add directly to the continuum spread caused by the
velocity gradient across the finite scattering volume. The total
continuum frequency spread is what we term "Instrument Broadening",
since it is entirely determined by the design parameters of the
Laser Doppler Velocity Instrument.

Broadening caused by microscopic processes will also be
a continuum spread, if it is observable. Some magnitudes are
calculated in a following section. An important parameter
bearing on this effect is particle size. Clearly, the question
arises in large particles as to whether or not they are at the
same temperature as the gas. This point is not studied in the
present report, LTE being assumed throughout. In the calculation
of temperature broadening below, it is certainly quite reason-
able to assume that, in the case of very small particles, say

f_C IS CALLED THE CARRIER FREQUENCY
f_{DEV} IS CALLED THE DEVIATION FREQUENCY

THIS FREQUENCY BAND
MOVES UP AND DOWN BETWEEN
$(f+f_{DEV})$ and $(f-f_{DEV})$ WITH A
FREQUENCY f_S CALLED THE
SIGNAL FREQUENCY

SCATTERED LIGHT
INTENSITY AT
FREQUENCY f

$f_{DEV_{MAX}}$

$f_{DEV_{MAX}}$

CONTINUUM OF
FREQUENCIES
CAUSED BY
INSTRUMENT
BROADENING

$(f_C - f_{DEV_{MAX}})$

f_C

f (INSTANTANEOUS)

$(f_C + f_{DEV_{MAX}})$

FREQUENCY f ⟶
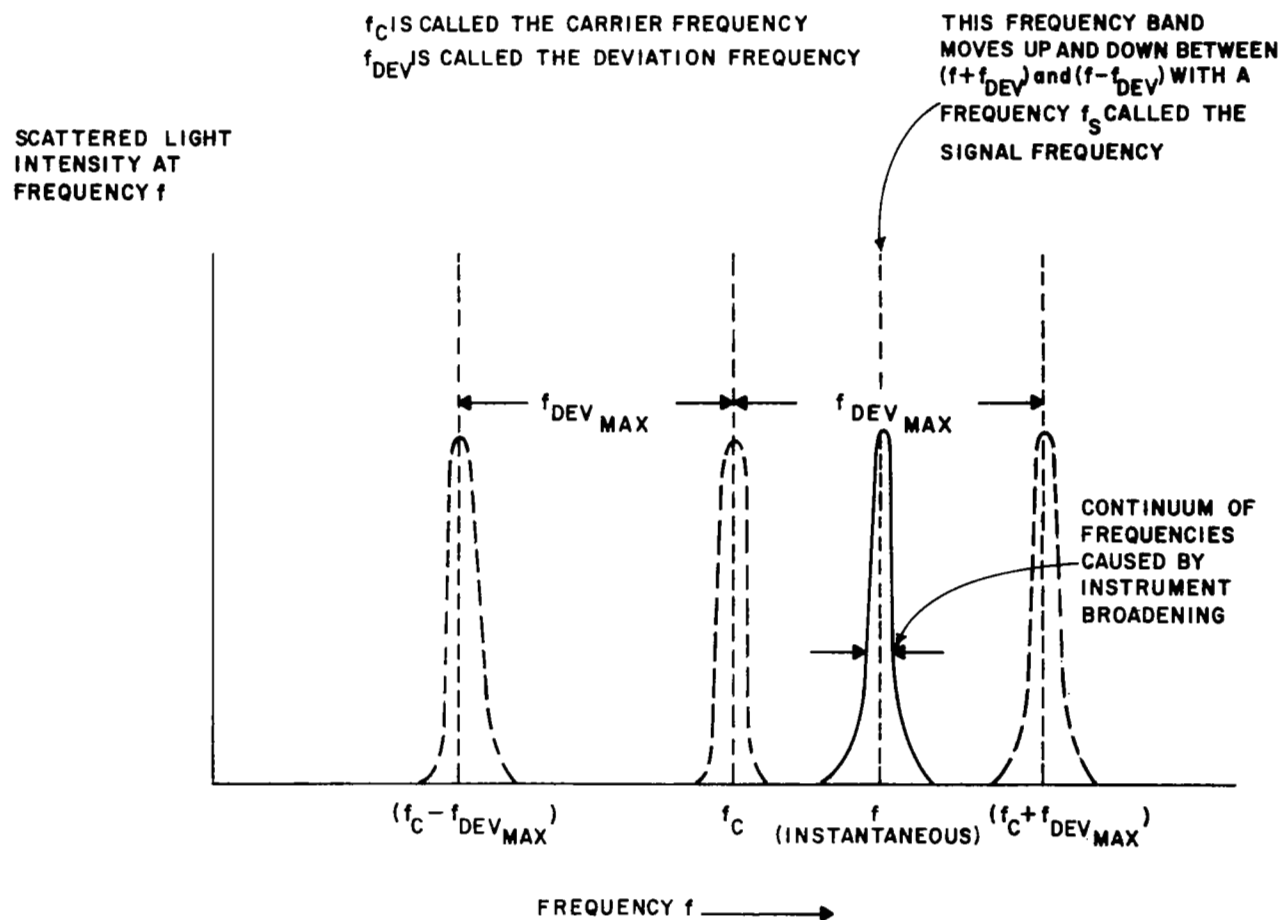
Figure 2.11-1   Spectral Broadening of Scattered Light

carbon macromolecules, the particle temperature is very close to the local gas temperature.

2.11.1 Instrumental Broadening

Some estimates of the magnitude of the two instrumental broadening effects - aperture size and scattering volume size - are calculated below:

2.11.1.1 Effect of Aperture Size on Instrumental Broadening

Since the input aperture of the detector often has finite size, the optics will accept light scattered over a range of angles. Because the Doppler shift depends upon scattering angle, the detector will eceive a range of frequencies. To compute the resulting broadening of the detected spectrum, let $\alpha = 90^{\circ}$ and $\theta = 10^{\circ}$ (Figure 2.11-2). Then the Doppler frequency shift, from Section 2.2, is given by

$$f_D = f_o \frac{U}{c} \sin \theta \qquad (2)$$

It should be noted that this analysis is one dimensional and that the consequent approximations may break down when a larger aperture and/or a smaller scattering angle is used.

Hence:
$$\frac{df_D}{d\theta} = f_o \frac{U}{c} \cos \theta$$

$$\approx 550 \ M \cos \theta \quad MHz | radian,$$

where M is the Mach number at $20^{\circ}C$. at He-Ne laser wavelength, 6328A.

Now if $\Delta\Omega$ steradians is the solid angle subtended at the scattering volume by the collecting lens aperture, then (Figure 2.11-2)
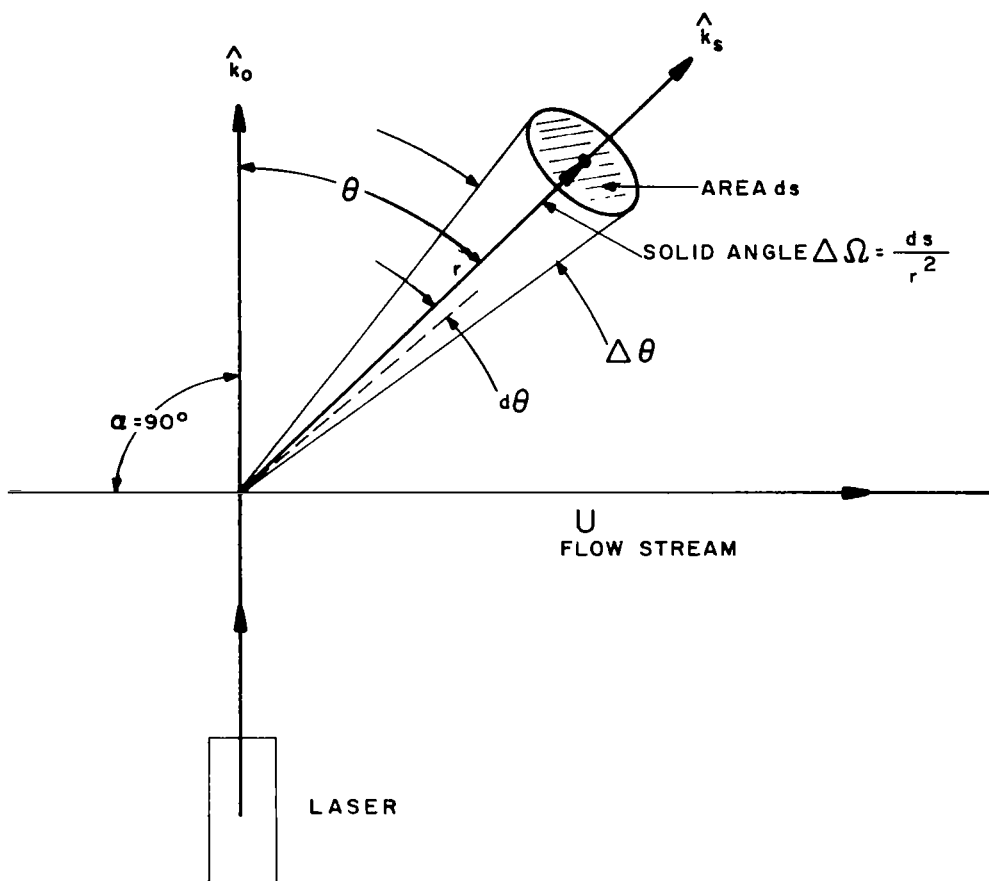
Fig. 2.11-2.   Geometry of Instrumental Aperture Broadening.

$$\Delta\Omega \equiv \frac{ds}{r^2} \approx \pi \left(r\frac{\Delta\theta}{2}\right)^2 \frac{1}{r^2} = \frac{\pi (d\theta)^2}{4}$$

$$\therefore \Delta\theta = \sqrt{\frac{4}{\pi}\Delta\Omega} \text{ radians} \tag{3}$$

The total spread of frequency (instrument breadth) is then

$$\Delta f_A = \frac{d f_\theta}{d\theta} \Delta\theta = f_o \frac{U}{c} \cos\theta \sqrt{\frac{4}{\pi}\Delta\Omega} \tag{4}$$

It is immediately obvious that the larger the scattering angle, θ, the smaller is the instrumental aperture broadening f_A. Unfortunately, we are forced to use a small θ for large velocities (Section 2.4), because of limitations in the bandwidth of the photomultiplier and electronics system.

When θ is small, so that $\cos\theta \approx 1$,

$$\Delta f_A \approx \frac{f_o U}{c} \sqrt{\frac{4}{\pi}\Delta\Omega}$$

$$\Delta f_A \approx 550M \sqrt{\frac{4}{\pi}\Delta\Omega} \tag{5}$$

Where a larger scattering angle can be used,

$$\Delta f_A = 550M \cos\theta \sqrt{\frac{4}{\pi}\Delta\Omega} \tag{5A}$$

To hold this breadth down to a reasonable level, $\Delta\Omega$ must be made very small. For example to limit Δf_A to 20% of f_D requires $\Delta\Omega \simeq .003$ steradians ($\Delta\theta \simeq 2°$).

The problem of instrument broadening must be carefully considered in processing the scattered signal, to apply the proper corrections when the velocity spectrum is to be measured. Clearly, the use of a larger scattering angle would alleviate the problem, but to use an increased scattering angle one must either forego the use of convenient photomultipliers, or work at a lower flow velocity.

A more detailed analysis now follows, in which the limits placed on collecting aperture of the optical system are calculated, based on an examination of loss of sensitivity to velocity fluctuations caused by instrument aperture broadening.

2.11.1.2   Sensitivity to Velocity Fluctuations in Relation to Instrumental Aperture Broadening

In order that useful measurements of turbulence intensity and scale may be made, the Doppler Flowmeter must be sensitive to velocity fluctuations both parallel to and perpendicular to the direction of the gas stream. A brief analysis of ability to meet this requirement follows. The quantity examined is the ratio of Doppler shift resulting from velocity components perpendicular and parallel to the stream as compared with the frequency spread caused by Instrumental Aperture Broadening.

Figure 2.11-3 shows a velocity vector diagram where O is the coordinate origin, U is the stream velocity and ΔU is the velocity vector of velocity fluctuations. U is assumed steady, while ΔU fluctuates with time. Then at any instant, the resultant velocity U is the vector joining O with a point on the surface of the sphere whose center lies at the tip of U_o, and whose radius is ΔU. The laser beam is taken perpendicular to the flow velocity.

Now consider the situation shown in Figure 2.11-3 where an incremental velocity ΔU is added to the stream velocity

$\underset{\sim}{U}_o$ = FLOW VELOCITY VECTOR.

$\hat{k}_o$ = UNIT PROPAGATION VECTOR IN DIRECTION OF LASER BEAM.

$\hat{k}_s$ = UNIT PROPAGATION VECTOR IN DIRECTION OF SCATTERED LIGHT DETECTOR.

θ = SCATTERING ANGLE
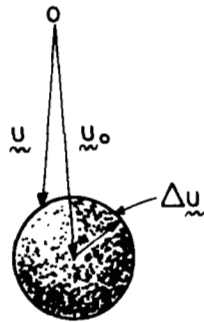
(a) VELOCITY VECTOR DIAGRAM
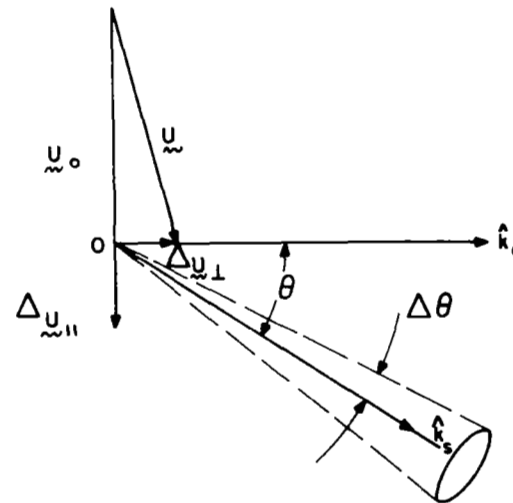
(b) PARALLEL AND PERPENDICULAR VELOCITY COMPONENTS

Figure 2.11-3   Scattering Geometry Showing Velocity Fluctuations

$\underset{\sim}{U}$o. The Doppler shift is given by (3)

$$\Delta f_D = \frac{f_o(\underset{\sim}{U}_o + \Delta \underset{\sim}{U}_1) \cdot (\hat{k}_o + \hat{k}_s)}{c}$$

$$= \frac{f_o \underset{\sim}{U}_o \cdot (\hat{k}_o + \hat{k}_s)}{c} + \frac{f_o \Delta \underset{\sim}{U} 1 \cdot (\hat{k}_o + \hat{k}_s)}{c} \quad (6)$$

The rate of change of Δf_D with $\Delta \underset{\sim}{U}_1$ is

$$\frac{d(\Delta f_D)}{d(\Delta U_1)} = \frac{f_o(1 + \cos\theta)}{c} \underset{\sim}{\approx} \frac{2f_o}{c} = 4 \times 10^{-2} \text{ MHz/cm/sec} \quad (7)$$

Secondly, consider an increment of velocity parallel to the stream velocit $\Delta \underset{\sim}{U}_{11}$ as shown in the Figure. The effect of this fluctuation ca be found immediately from the equation for Doppler shift used by the stream velocity. It is -

$$\frac{d(\Delta f_D)}{d(\Delta U_{11})} = \frac{1}{2} f_o \frac{\theta}{C} = 1.7 \times 10^{-3} \text{ MHz/cm sec},$$

a factor of about 20 less than the rate of change of Δf_D with U_1.

Now with a solid angle subtended by the detector of approximately 10^{-3} steradians, as determined in Section 2.11.1.1 to limit instrument broadening to $\Delta f_I \approx 20\%$ of Δf_D, we find that the instrument broadening is

$$\Delta f_1 = 10M \text{ MHz} \quad (8)$$

where   is the Mach number of the flow at 20°C.

Let $\Delta(\Delta U_1) = \beta U_o$ so that the change in Δf_D due to $\Delta(\Delta U_1)$ is

$$\Delta(\Delta f_D)_1 = 1200 \text{ M } \beta \text{ MHz.} \tag{9}$$

Hence, the magnitude of the frequency fluctuation due to ΔU_1 is equal to the instrumental breadth if $\beta \simeq 10^{-2}$, i.e., if the transverse velocity fluctuation is 1% of the flow velocity.

On the other hand, if $\Delta(\Delta U_{11}) = \beta U$, then the change in Δf_D due to ΔU_{11} is

$$\Delta(f_D) = 51 \text{ M}\beta \text{ MHz,} \tag{10}$$

so $\Delta(\Delta f_D)_{11} \simeq \Delta f_1$ if ΔU_{11} is about 20% of the flow velocity.

The conclusion is that small variations in the flow velocity with components perpendicular to the main stream flow can be detected very easily. Fluctuations in velocity in the direction of the stream velocity are significantly obscured by Instrumental Broadening unless those fluctuations are relatively large. If detailed knowledge of $\Delta \underset{\sim}{U}$ is required, a change in laser beam direction can be considered.

This situation is, of course, a consequence of 1) choosing $\hat{k}_o$, i.e., the direction of the laser beam, to be at right angles to the stream flow, and 2) choosing a small scattering angle, so that Instrumental Broadening is an appreciable fraction of velocity Doppler shift.

Calculations have been made of the Acceptance Angle (and Solid Angle) of the optical detector system which will result in Instrumental Aperture broadening of 20% of the Doppler shift for

a range of scattering angles and of angles of incidence of the laser beam on the flow stream. The results are plotted in fig. 2.11-4.
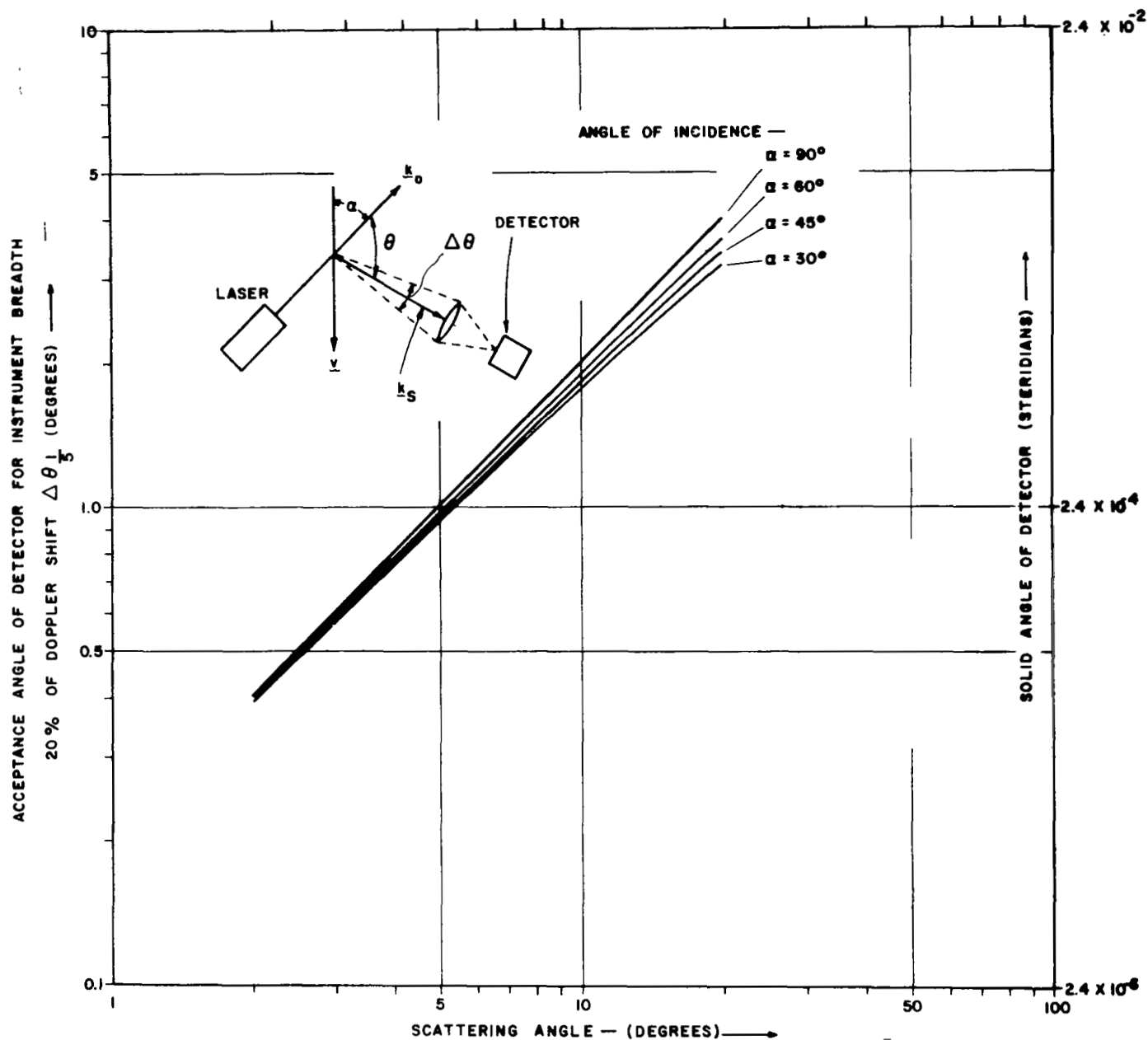
Figure 2.11-4 Acceptance Angle of Detector for which Instrument
Broadening Equals 20% of Doppler Shift

2.11.1.3 Effect of Scattering Volume Magnitude on Instrumental Broadening

In the presence of a velocity gradient, the Doppler shift of the scattered light will span a range of velocities, which will appear as a broadened frequency spectrum in the scattered light. As already explained, this is a continuum broadening, since all frequencies in the range are present simultaneously. The total span of frequencies will be

$$\Delta f = \frac{\partial f}{\partial u_i} \, \Delta u_i = \frac{\partial f}{\partial u_i} \frac{\partial u_i}{\partial x_i} \, \Delta x_i \tag{11}$$

where x_i is the dimension of the scattering volume in the direction x_i considered; and u_i is the component of gas velocity in direction x_i.

Using scattering volume parameters from section 2.13, and apparatus arrangement such that the laser beam is at right angles to the flow velocity, with scattering angle θ (see fig. 2.11.2), equation (11) gives

$$f_D = f_o \frac{u_i}{c} \sin \theta$$

$$\frac{\partial f}{\partial u_i} = \frac{f_o}{c} \sin \theta \tag{12}$$

so that

$$\Delta f = \left(\frac{f_o}{c} \sin \theta \right) \left(\frac{\partial u_i}{\partial x_i} \right) \Delta x_i \tag{13}$$

Assuming the principal gradients are transverse to the direction of flow, Δx will be approximately the depth of focus of the detector system collecting lens, i.e. $4 F^2 \lambda$, (section 2.13), where F = lens F number, $= \dfrac{\text{focal length}}{\text{aperture}}$,

and equation (13) becomes

$$\Delta f \simeq \left(\frac{f_o}{c} \sin \theta\right) \left(4F^2 \lambda\right) \frac{\partial u_1}{\partial x_i} \sec^{-1} \tag{14}$$

(all units cms and secs)

To illustrate the order of magnitude of the broadening effect, which is clearly greatest in the flow shear layer where

$\dfrac{\partial u_i}{\partial x_i}$ is greatest, take

$f_o = 6.14 \times 10^{14} \sec^{-1}$ (Argon laser)

$c = 3 \times 10^{10}$ cm sec

$\theta = 7^\circ$, $\sin \theta = .122$

$F = \dfrac{810mm}{25mm} = 32.4$

$\lambda = (4880)(10^{-8})$ cm (Argon laser)

Then $\Delta f = 512 \dfrac{\partial u_1}{\partial x_i}$ \hfill (15)

where the units of $\dfrac{\partial u_i}{\partial x_i}$ are cm/sec/cm. If we take, say,

$\dfrac{\partial u_i}{\partial x_i} \approx$ 60,000 cm/sec/cm, for a stream velocity on the order of

Mach 1, then

$$\Delta f = 30.72 \text{ MHz} \qquad (16)$$

clearly not negligible.

To reduce this spread, one should use the instrument in regions of less steep velocity gradient, and/or use an optical collecting lens of smaller F number, (i.e. smaller focal length and larger aperture). For example,

if $\dfrac{\partial u_i}{\partial x_i}$ is, say, $\sim$ 600 cm/sec/cm, a more reasonable value outside

the shear layer, and F $=$ 16, then

$$\Delta f \sim 80 \text{ kHz is the maximum frequency spread.}$$

It will be noted that the spread is rather a strong function of detector aperture, so that for conditions where large velocity shears exist, a small F number system should be used. This is not unexpected, since it is somewhat akin to saying that when one wishes to make measurements in a region of strong rates of change, one should use a device with optics more like those of a microscope!

It is important to note that the Δf calculated above is the frequency spread, not the "line width", which would be substantially less. In order to calculate the line width of the mean Doppler shift, one must know the distribution function of

$$\left(\frac{\partial u_i}{\partial x_i}\right)$$ with respect to x.

2.11.2 Temperature Broadening

The only microscopic process which will cause broadening of the frequency spectrum of the scattered laser light is Temperature broadening. It will cause a continuum broadening, all frequencies in the broadened spectrum being present at all times, just as for Instrumental Broadening. It results from the fact that the thermal statistical spread of velocities of particles because of their finite temperature causes a spread of Doppler shifts in frequencies exactly like that we use to measure flow velocity and turbulence. The only differences between the two are that:

a) The whole spread of thermal Doppler shift frequencies is present at all times, whereas the macroscopic velocity and turbulence shifts vary with time.

b) The different frequencies in the temperature broadening process occur in molecular particles separated by molecular distances, whereas the turbulent doppler shift frequency differences come from particles separated by distances of the order of the turbulence scale.

c) Since we are utilizing Mie (Rayleigh-Gans) scattering from massive particles in the Laser Doppler Velocity instrument, the temperature broadening of the spectrum

will be very small compared with the span of frequencies arising from instrumental broadening and from turbulence Doppler shifting, as shown below.

When nearly monochromatic laser light is scattered by free gas particles such as free electrons, molecules, or massive particles as in aerosols, the line profile is broadened by the Doppler effect. The Doppler broadening of the line depends upon the temperature of the scattering particles and on the angle between the incident and scattered waves. The angular dependence arises because the frequency shift of radiation scattered by a single particle depends upon the components of the particle's velocity along the directions of both the incident and scattered beams. The relation between the magnitudes of these two velocity components depends upon the scattering angle. In the following paragraphs the temperature and angular dependence of the spectral profile is derived.

A coordinate system is chosen in which the wave vector of the incident radiation is along the y axis and the wave vector of the scattered radiation is in the x-y plane, as shown in Figure 2.11-5. Consider a scattering event in which the scatterer has velocity v in an arbitrary direction. Then the wavelength of the incident radiation as seen by an observer moving with the scatterer is

$$\lambda_p = \lambda_o (1 + \frac{v_y}{c}) \tag{1}$$

where λ_o is the wavelength seen by a fixed observer and c is the speed of light. The wavelength of the scattered radiation as seen by a fixed observer is Doppler shifted with respect to λ_p
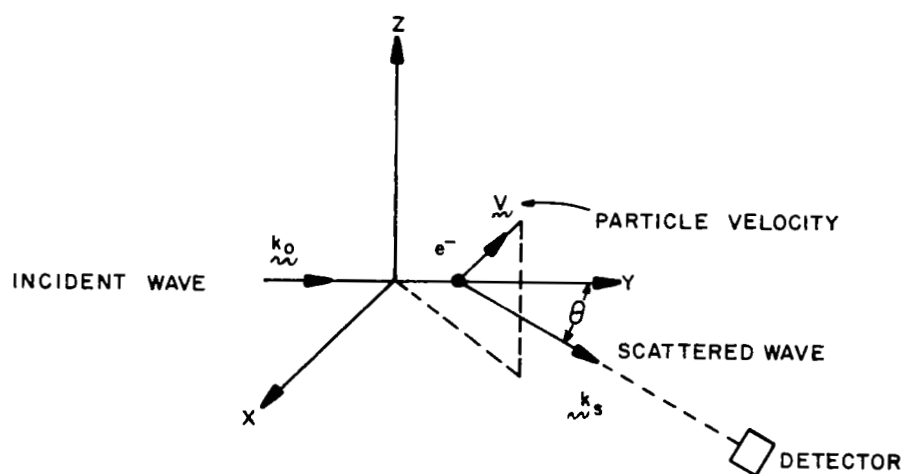
Fig. 2.11-5.   Optical Scattering Geometry for Temperature
              Broadening Analysis.

so that the fixed detector receives radiation of wavelength.

$$\lambda = \lambda_p \left(1 - \frac{\underset{\sim}{v} \cdot \underset{\sim}{k}_s}{c}\right) \tag{2}$$

where $\underset{\sim}{k}_s$ is a unit vector in the direction of the scattered radiation incident upon the detector. Combining these expressions, neglecting $\frac{v}{c} \ll 1$, and writing $\underset{\sim}{v} \cdot \underset{\sim}{k}_s = v_x \sin \theta + v_y \cos \theta$ yields the result

$$c \left(\frac{\lambda - \lambda_o}{\lambda_o}\right) = v_x \sin \theta - v_y (\cos \theta - 1) \tag{3}$$

The velocity components v_x and v_y are both random variables which are assumed to be distributed according to the Maxwell-Boltzman distribution function. Since the right hand side of equation (3) is normally distributed about zero, the left hand side must also be so distributed.

Therefore, the distribution function for $x = \lambda - \lambda_o$ is taken to be the normalized function

$$F(x) = \lambda_o \beta \pi e^{\frac{-c^2 x^2}{\lambda_o^2 \beta^2}}$$

where β is a parameter to be determined. The determination of β is performed by equating moments of the left and right hand sides of Equation 3. The first moment vanishes because both sides have zero average. The second moment equation yields β^2 as follows:

$$\left\langle \frac{c^2 x^2}{\lambda_o^2} \right\rangle = \left\langle \left[-v_x \sin \theta - v_y (\cos \theta - 1)\right]^2 \right\rangle \tag{4}$$

$$= \sin^2 \theta \langle v_x^2 \rangle + (\cos \theta - 1)^2 \langle v_y^2 \rangle + 2 \sin \theta (\cos \theta - 1) \langle v_x v_y \rangle$$

Since v_x and v_y are independent variables $\langle v_x v_y \rangle = \langle v_x \rangle \langle v_y \rangle = 0$ and equation (4) becomes

$$\frac{c^3}{\lambda_o^3 \beta \ \pi} \int_{-\infty}^{\infty} x^2 e^{\frac{-c^2 x^2}{\lambda_o^2 \beta^2}} dx = \left[\sin^2\theta + (\cos \ \theta - 1)^2\right] \sqrt{\frac{m}{2\pi k t}} \int_{-\infty}^{\infty} v_x^2 e^{\frac{-mv_x^2}{2kT}} dv_x \quad (5)$$

$$\frac{\beta^2}{\sqrt{\pi}} \int_{-\infty}^{\infty} u^2 e^{-u^2} du = 2(1 - \cos \ \theta)\frac{2kT}{m\sqrt{\pi}} \int_{-\infty}^{\infty} u^2 e^{-u^2} du \quad (6)$$

$$\beta^2 = \frac{4kT}{m} (1 - \cos \ \theta) \quad (7)$$

Thus $F (\lambda - \lambda_o)$, which is called the normalized shape function, is given as a function of the scattering angle θ by

$$F(\lambda - \lambda_o) = \frac{c}{2\lambda_o} \sqrt{\frac{m}{\pi kT}} \frac{1}{1 - \cos \ \theta} e^{\frac{-mc^2}{4kT} \frac{(\lambda - \lambda_o)^2}{\lambda_o^2}\frac{1}{(1 - \cos \ \theta)}} \quad (8)$$

The width of the profile increases with increasing angle. Figure 2.11-6 shows the half width at half maximum, $\Delta\lambda_{1/2}$, as a function of scattering angle for electrons and for 100 Å diameter carbon macromolecules. The "half width at half maximum" is defined as the value $(\lambda - \lambda_o)$ such that $F(\lambda - \lambda_o) = 1/2F(o)$ as is shown on the figure. The curve is drawn for k T = 1 e.v. To obtain $\Delta\lambda_{1/2}$ for other values of kT, multiply the ordinate of the graph by kT. The profile width goes to zero at zero scattering angle only because the breadth of the laser light has been neglected. This simplification is also responsible for the

(1 - cos θ) in the denominator of F ($\lambda - \lambda_o$). For scattering angles appreciably less than 1° the laser breadth is appreciable compared to the Doppler breadth and the analysis given above breaks down. However, for practical reasons scattering angles used in the Laser Doppler Velocity Instrument are not likely to be less than 5°.

The half width at half maximum is obtained readily from Equation (8). It is

$$\Delta f_T(1/2) = \frac{v_{th}}{c} \sqrt{\frac{4}{3}(\ln 2)(1 - \text{cox } \theta)} \tag{9}$$

where v_{th} is the thermal speed

$$v_{th} = \sqrt{\frac{3kT}{m}} \tag{9a}$$

Profile widths for particles of different masses can readily be calculated from the curve of fig. 2.11-6, using the inverse square dependence on mass as given in equation (9).

In performing calculations for the carbon macromolecules, a diameter of 100 Å and carbon density of 2.25 gm/cc were assumed. This results in a carbon particle mass of 7 x 10" atomic mass units, i.e. nearly 10^{12} times as heavy as a hydrogen atom. Clearly the temperature broadening for particles even as small as this is expected to be very small.

As an example of use of the curve consider, say, carbon 100 Å diameter macromolecules, scattering angle $\theta = 8^o$. Read off curve, fig. 2.11-6, $\Delta\lambda_{1/2} = 1.5$ Å. Multiply by $(2.78)(10^{-8})$, giving half width of $(4.17)(10^{-8})$ Å or full width $\Delta\lambda$ of approximately 10^{-7}Å. Using
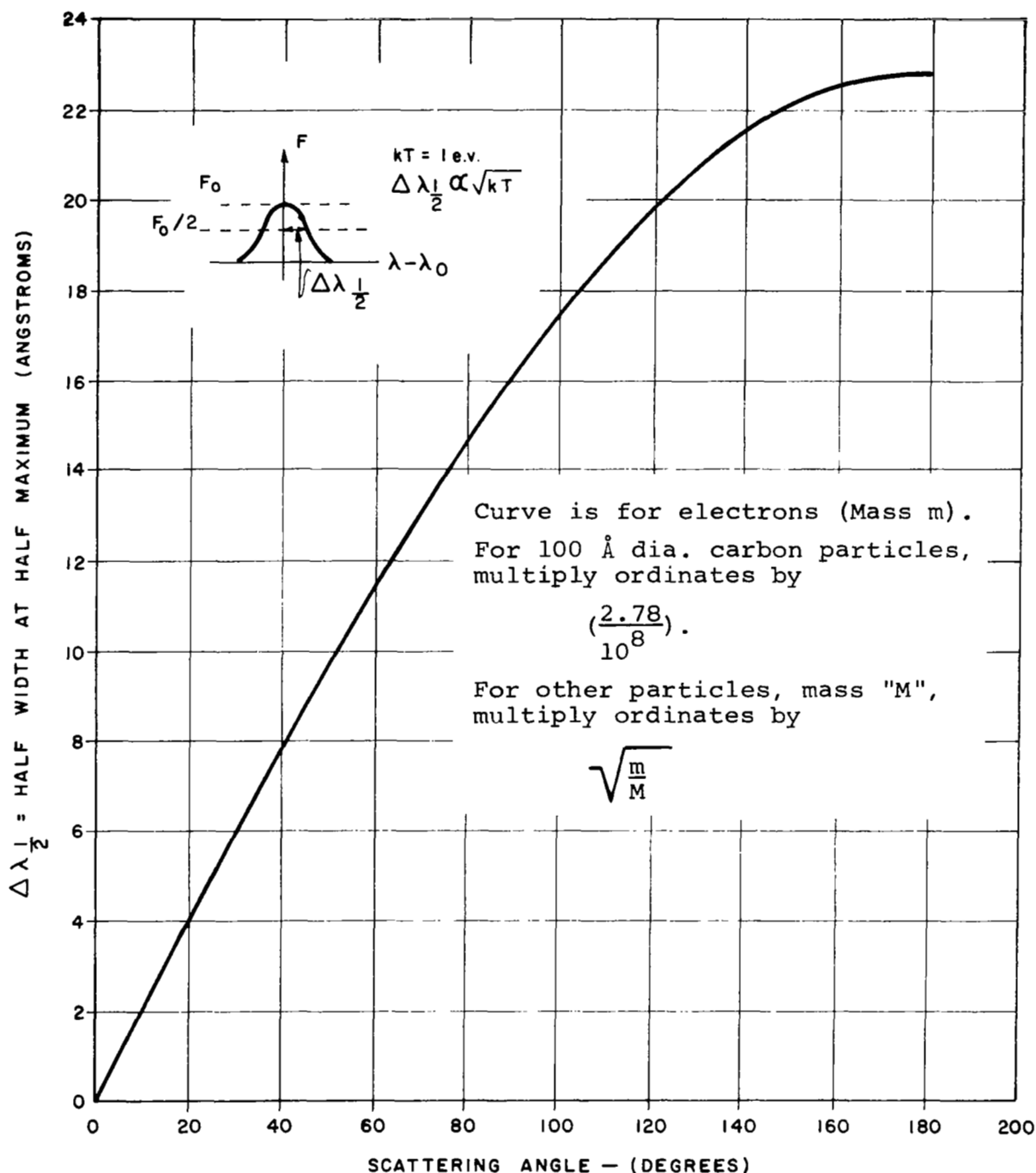
Fig. 2.11-6.   Spectral Width of Scattered Laser Light vs.
Scattering Angle.

2.11-24

$$\left| \Delta v \right| = \frac{v}{\lambda} \Delta\lambda = -\frac{c}{\lambda^2} d\lambda = (12.597)(10^{18}) \Delta\lambda,$$

where c is the velocity of light, λ the laser wavelength in cms,
then the width of frequency spectrum broadening $\approx$ 12.6 kHz,
which is negligible compared with instrumental broadening.

This it will be concluded from the discussion in this
section that only Instrumental Broadening, because of finite
aperture and because of finite scattering volume, is significant
to the operation of the Laser Doppler Velocity Instrument. The
only other broadening process which applies is Temperature
broadening, and this is negligible because of the massive size
of the particles from which scattering Doppler shift measurements
are made.

It is important to note that by taking advantage of the
different characteristic features noted above, the Signal
Processing technique developed in Section 2.12 in principle (i.e.
within practical limitations of electronic circuits) removes the
effects of all types of continuum frequency broadening from the
frequency shifts caused by flow velocity and turbulence, the
quantities we wish to measure.

REFERENCES FOR SECTION 2.11

1. Mavrodineau and Boiteux, _Flame Spectroscopy_, 520, John Wiley and Sons, Inc. (1965).

2. Mitchell and Zemansky, _Resonance Radiation and Excited Atoms_, Cambridge University Press (1961).

3. Landau and Lifshitz, _Classical Theory of Fields_ Addison-Wesley Publishing Company

2.12 Signal Processing

Before an investigation of signal processing techniques
can be fairly started, one must obviously know in what form the
processed information is to appear. Since the information is
to be presented in a form most useful for the measurement of
turbulence and velocity, unavoidably one must start with a brief
review of turbulence and its measurable parameters.

2.12.1 The Parametric Description of Turbulence

It is an unfortunate fact that literature bearing
on turbulence is very long on mathematical formulations and
very short on comprehensive experimental data. In fact, most
of the latter are confined to subsonic flow measurements. The
reason is that, until the advent of the Laser Doppler Velocity
Instrument, only the hot wire anemometer, in its various forms,
has been available for making such measurements. Among its dis-
advantages are (1) it disturbs the natural flow; (2) its time
constant is relatively long, certainly with respect to character-
istic times of high speed flow; (3) because of disturbances it
creates in the flow, spatial correlation measurements, especial-
ly in the mean flow direction, are severely restricted; (4) being
sensitive also to temperature, the separation of temperature ef-
fects from velocity signals is difficult, especially in super-
sonic flows;(5) with supersonic flows, where short time constants
are needed, the hot wire sensor must be made very small, a para-
doxical requirement since it should be robust to withstand the
high forces under these conditions.

We do not wish to belittle the fine work done by many
workers with hot wire anemometers, and it should be emphasized
that almost all turbulence data so far have been measured with
this type of instrument. Of particular note in this respect is
the work of Davies and his coworkers (1) who routinely make

2.12-1

probe wires whose dimensions are measured in microns and whose response times can be measured in microseconds. However, all hot wire anemometer probes basically have these disadvantages. The Laser Doppler Velocity Instrument has none of them. What other disadvantages it may have is one of the points for investigation in the present work.

Because of the random nature of the turbulent motions in a fluid (gas or liquid), analysis and solution of the turbulent flow field must be in statistical terms. This approach was first inaugurated by Osborne Reynolds in 1894, and later developed to an elegant mathematical formulation by G. I. Taylor (c. 1938) from which springs all modern turbulence theories. Reynolds assumed that the flow could be divided into temporal-mean and turbulent parts. Thus the velocity component in the mean-flow, x, direction is written:

$$U = \overline{U} + U'$$ (1a)

where $\overline{U}$ = mean velocity part, averaged over a relatively long time period

U' = turbulent velocity fluctuation part.

Similar expressions are written for the y direction (transverse to the mean flow) and z direction (normal to the xy plane), viz:

$$V = \overline{V} + V'$$ (1b)

$$W = \overline{W} + W'$$ (1c)

The fluctuations U', V', W' are treated and characterized by statistical techniques. For detailed development of the theory beyond these basic postulates, the reader is referred

to references (2) through (10), provided by Prof. Barbin (3).
Our discussion will now be confined to a much simplified picture,
bearing on development of the signal processing system for the
Laser Doppler Velocity Instrument.

The correspondence between Doppler frequency shift of the
scattered light and the local instantaneous fluid velocity
(Section 2.2) enables us immediately to write equation (1) in
terms of corresponding Doppler frequency components.

$$\Delta f_s \quad = \quad f = f_c + f_{DEV} \tag{2}$$

The frequency output is just a mean frequency modulated by
frequency fluctuations caused by turbulence. In the terminology
of communications engineers, it is the equivalent of a frequency-
modulated carrier frequency in a "frequency modulation" (fm)
system. That is,

$$f_c \equiv \text{carrier frequency-corresponds to } \bar{U} \text{ and}$$

$$f_{DEV} \equiv \text{frequency deviation-corresponds to } U$$

The correspondence is shown diagrammatically in Figure 2.12-1(a).
Similar equations can clearly be written for equations (1b) and
(1c), but the remaining discussion will be in terms of one com-
ponent for simplicity. Multi-component treatment is discussed
briefly in Section 2.20, but detailed analysis will be left to
later reports. The three basic turbulence parameters will now
be defined and related to the Laser Doppler Velocity Instrument:

Turbulence Intensity

Because of the statistical nature of turbulence, the
Relative (i.e., to the mean flow) Turbulence Intensity is de-
fined and measured by

2.12-3
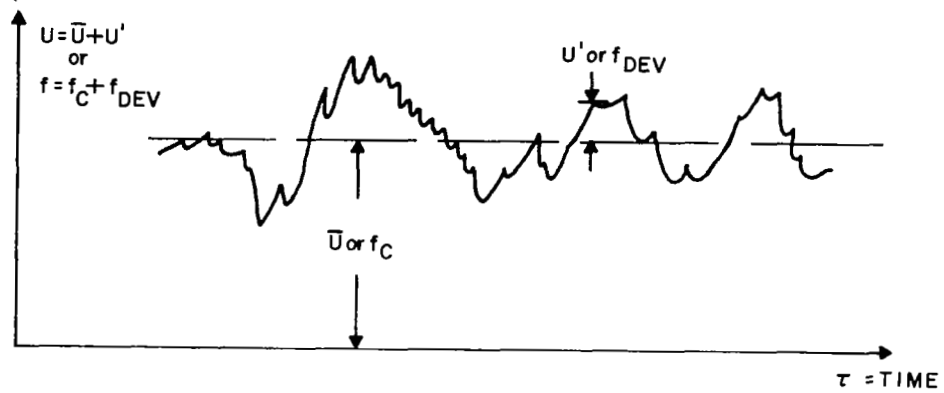
(a) CORRESPONDENCE BETWEEN U and f
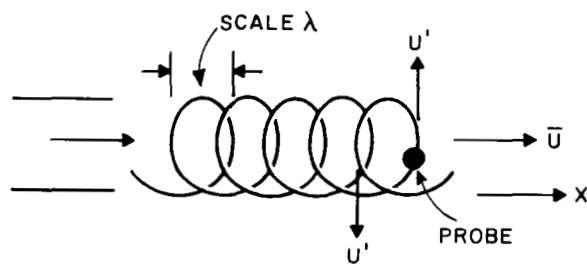
(b) IDEALIZED TURBULENT EDDIES
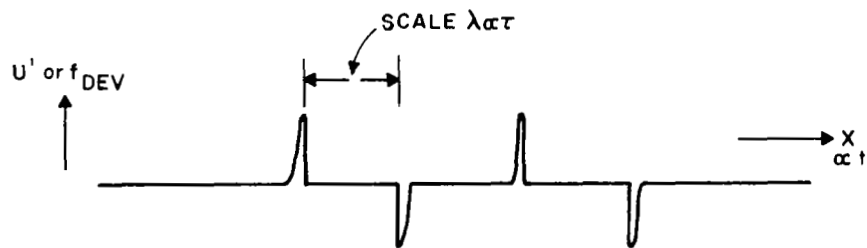
(c) IDEALIZED U′or f′MEASURED BY PROBE SMALL COMPARED WITH SCALE

Figure 2.12-1 – Turbulence Diagrams

$$\frac{U'(RMS)}{\overline{U}} = \frac{\sqrt{\overline{U'^2}}}{\overline{U}} \quad , \text{ which,} \tag{3}$$

in terms of the laser measurement is immediately expressible as:

$$\text{Relative Turbulent Intensity} = \frac{\sqrt{\overline{f_{DEV}^2}}}{f_c} \tag{4}$$

Turbulence Scale

A simplified concept of turbulence might depict a stream of clearly defined "turbulence eddies" (Figure 2.12-1(b)). A small turbulence velocity probe would then show a velocity (or frequency) deviation U' ($\sim f_{DEV}$) from the mean $\overline{U}$ ($\sim f_c$) as in Figure 2.12-1(c). The Scale of Turbulence would then be the span of a "turbulent eddy" in space. Using a single turbulence probe, if the turbulence pattern is consistent, the abscissa of Figure 2.12-1(c) can be immediately scaled in time. If λ = scale size, then τ, the periodic time of velocity fluctuations as seen by the stationary probe, is clearly related to λ by

$$\tau = \frac{\lambda}{\overline{U}} \tag{5}$$

This is immediately expressible as a frequency

$$f_s = \frac{1}{\tau} = \frac{\overline{U}}{\lambda} \, , \tag{6}$$

where f_s is the frequency of the observed velocity deviations, as measured by any type of turbulence velocity measuring instrument. In the Laser Doppler Velocity Instrument, this frequency is the frequency of fluctuation of f_{DEV}. In fm system terminology, this is called the "Signal Frequency". Thus we

2.12-5

immediately have

$$\text{Scale, } \lambda = \frac{\overline{U}}{f_s} \tag{7}$$

We must bear in mind, of course, that this is a simplified picture, with a single value of f_s (and λ).

In practice, the $U^\backprime(f_{DEV})$ "spikes" are actually smeared out. In this situation we can only determine the scale either by suitable Cross-Correlation measurements, using two probes and varying the distance between them; or by Auto-Correlation measurements using one probe.* Most conveniently these are Eulerian correlations, i.e., measured by stationary probes, as opposed to equivalent Lagrangian Correlations as would be measured by a probe moving with the fluid particles. We shall always assume an Eulerian reference frame unless otherwise specified.

For the relationship in fluid dynamics between Eulerian and Lagrangian Coordinate Systems, the reader is referred to (2).

Hence in a real fluid, the frequency f_s, whether measured by a hot wire or laser probe, is continuously and randomly varying, as is the scale, but "buried" in the random fluctuations is a "pattern" of the turbulence scale structure. As a means of extracting turbulence scale from these statistical data, one is lead to define the third important turbulence parameter:

Turbulence Energy Spectrum

The manner in which the energy of the fluctuations is distributed among the various sized eddies, i.e., how it varies with scale, requires the consideration of the turbulence energy spectrum. Since one is usually observing the assemblage of eddies to be transported past the point of measurement (Eulerian system), the spectrum is most commonly evaluated in terms of the frequency f_s of equation (6). Considering the frequency as characteristic of a wave motion, the spectra may also be presented

_____
* If the random turbulent motions are "stationary" (12).

as functions of the wavelength $= \dfrac{\overline{U}}{f_s}$ which is identical with the turbulence scale or eddy size, or the wave number

$$k = \frac{2\pi}{\lambda} = \frac{2\pi f_s}{\overline{U}} \tag{8}$$

The spectral function E_{f_s} (or E_λ or E_k similarly) is defined as the fraction of the turbulent energy (divided by $\rho/2$) lying between f_s and $(f_s + \delta f_s)$ and is related to the intensity squared by

$$\overline{U'^2} = \int_0^\infty E_{f_s} \, d \, f_s \tag{9}$$

In summary, the turbulence of a fluid is described in terms of three fundamental parameters: Turbulence Intensity, Turbulence Scale, and Turbulence Energy Spectrum. It is the function of the Laser Doppler Flowmeter to extract, and continuously record signals in a form suitable for data processing to obtain these three parameters.

We will terminate the discussion, until later reports on the Laser Doppler Velocity Instrument, by noting that (G. I. Taylor) the turbulence spectrum is the Fourier transform of the correlation functions mentioned earlier. Either the spectrum or the correlation functions tells us all that the other can about the nature of the turbulence. In practice one tries to measure both, as a check on validity of measurement. Finally, if this brief introductory resumé of turbulence in relation to the Laser Doppler Velocity Instrument is read by a Communications Theorist, he must be struck by the definitions of turbulence parameters, which need only redefinition of symbols to become familiar functions in Statistical Communication Theory. Thus it is reasonable to suppose that all the

corresponding advanced electronics techniques for extracting information in a background of noise should be readily applicable to optimizing the signal processing system of the Laser Doppler Velocity instrument.

2.12.2   The Velocity and Turbulence Signals from the Laser Doppler Velocity Instrument

Having determined the nature of the information which must be extracted from the photomultiplier mixer signal output, i.e. intermediate frequency stage output (see Section 2.5) we will now review the nature of the signals themselves and how they must in principal be processed.

The photomultiplier-mixer output signal voltage is a wave of variable amplitude and frequency (at (1) in Figure 2.12-2). All the velocity information in which we are interested is contained in the frequency variations of the wave. The amplitude variations represent information on gas density, not needed in the Laser Doppler Velocity Instrument. The amplitude variations may be removed by a suitable electronic Amplitude Limiter, leaving a signal voltage of constant amplitude, variable frequency ((2) in Figure 2.12-2). This constant amplitude signal can be processed through a frequency detecting circuit, generally referred to as a Frequency Discriminator. Such a device gives an instantaneous output proportional to the instantaneous _frequency_ of the voltage applied to its terminals, assuming this voltage is of constant amplitude. The output waveform is depicted at (3) in Figure 2.12-2. Its amplitude is expressible as two components: a mean amplitude directly proportional to the mean frequency f_c, and therefore to the mean velocity $\overline{U}$; and a fluctuating amplitude component f_{DEV}, proportional to U'. Furthermore, the wave which is the fluctuating component f_{DEV} has itself a frequency of variation which is the frequency f_s, shown in Section 2.12.1 to be inversely proportional to turbulence scale.

2.12-8

THESE SIGNALS CANNOT BE RECORDED

(1) PHOTOMULTIPLIER
OUTPUT
SIGNAL

TIME

AMPLITUDE
LIMITER

AMPLITUDE
DETECTOR

(2)

FREQUENCY
DISCRIMINATOR

f_c

0

THESE SIGNALS CAN BE RECORDED

(3) DOPPLER
FREQUENCY
SHIFT f
(VELOCITY)

LOCAL
OSCILLATOR
FREQUENCY

$f_{DEV} (\sim \dot{u})$

$f_c (\sim \bar{u})$
$\sim$ 200 MHZ at M3

TIME

SCATTERED
AMPLITUDE
(DENSITY)

(5)

TIME

SPECTRUM
ANALYZER

FOURIER
ANALYSIS

SPECTRUM
ANALYZER

THESE SIGNALS CAN BE PHOTOGRAPHED OR RECORDED

(4) NO. OF PARTICLES
AT FREQUENCY f
(VELOCITY $\dot{u}$)

0

f (VELOCITY $\dot{u}$)
$\sim$ 200 KHZ at M3

NO. OF REGIONS
OF PARTICAL
DENSITY ρ

MAIN
STREAM
DENSITY ρ_0

(6)

DENSITY ρ

Figure 2.12-2 Key Waveforms in Signal Processing

2.12-9

Hence _in one waveform, the alternating component of f_
plotted against time, we have all the information to give the
three fundamental turbulence parameters as follows:

Turbulence Intensity

-by processing the a.c. portion through an electronic
circuit designed to measure true RMS value of a wave,
we get $\sqrt{\overline{u'^2}}$, the Turbulence Intensity parameter.

Turbulence Scale

-exactly as with a hot wire anemometer, the frequency
of the wave gives inverse Turbulence Scale.

Turbulence Energy Spectrum

-again, as with a hot wire anemometer, processing
the a.c. portion of the wave through a spectrum
analyzer immediately produces the Turbulence
Energy Spectrum ((4) in Figure 2.12-2).

It remains to point out a further important feature of the
data processing system, namely the facility of continuously re-
cording, simultaneously, all three turbulence parameters. Clear-
ly the photomultiplier mixer output signal, occurring at frequen-
cies up to two hundred MHz or more, cannot be recorded. However,
the a.c. component of the f wave, having frequencies of 200 kHz
at the most, is well within the recording frequency range of a
number of commercially available recorders (Ampex, Sony, Hewlett-
Packard), and contains all the information we need for data pro-
cessing to produce the three turbulence parameters.

Electronic Spectrum analysis can be carried out at any
point in the development of waveforms (1), (2), (3) (Figure
2.12-2). It is a useful probe in checking the operation of the
electronic system. However, it is only meaningful with refer-
ence to turbulence parameters when carried out at stage (3).
Spectrum analysis at stage (1), besides simultaneously including

the spectrum of unwanted amplitude variations, gives a very com-
plex spectrum which may be virtually impossible to "unscramble"
to produce the turbulence parameters (see discussion in a later
section).

We may also process the information in the photomultiplier
mixer output voltage amplitude envelope. This can be done
through a simple Amplitude Detector, and will give an instantan-
eous record of density fluctuations in the gas((5) in Figure 2.12-2.)
Again, an energy spectrum of these can be obtained by spectrum
analysis ((6) in Figure 2.12-2). No plans are being made to
follow this line in the present work.

Since it also affects the PM output signal and signal pro-
cessing, an instrumental defect should be recalled, namely,
Instrumental Broadening. It was pointed out in Section 2.11
that whereas the turbulence signal has instantaneously a single
frequency (f) which varies randomly with time, superimposed on
this will be a continuum band of frequencies, caused by Instru-
mental Broadening. The band is a continuum in that all frequen-
cies in the band are simultaneously present. Their presence
will cause a "blurring" of the frequencies discussed above. In
experiments to date, they do not appear to have been a serious
problem. Their precise effect on the performance of the elec-
tronic apparatus will be determined in signal processing studies
shortly to be undertaken.

In the section which follows, a more detailed study of im-
portant possible signal processing systems is presented, bearing
particularly on the problems of the necessary electronic engin-
eering, in order to arrive at the optimum system.

2.12.3 Analysis of the Electronics Problems of Signal Processing Systems

Five methods of measuring the Doppler frequency shift of a Laser Doppler Flowmeter are discussed in the following section:

1.   Spectrum Analyzer applied directly to the PM output signal.

2.   Wide band frequency discriminator

3.   Filter Bank

4.   Doppler Frequency Tracker

5.   Phase-Locked Receiver

The instantaneous local fluid velocity can be defined as:

$$U(t) \equiv \overline{U}(t) + U'(t) \tag{1}$$

Since the resulting Doppler frequency shift is proportional to the velocity, it can be expressed as:

$$f(t) \equiv f_c(t) + f_{DEV}(t) \tag{2}$$

Note that the relationships between equations (1) and (2) are simple for the one-dimensional flow case, but not so straight-forward for the vector 3-dimensional case. This is because the angular relation between $\overline{U}$ and U' varies continuously with time in accordance with turbulence velocity variations. Equation (2) can be rewritten in the form

$$f(t) = f_c(t) + \Delta f\, S(t) \tag{3}$$

Equation (3) represents the instantaneous frequency of a FM

signal, where f_c is the carrier frequency, Δf the maximum frequency deviation ($\Delta f = f_{DEV}(t)_{max}$) and S(t) the modulating signal, which may vary between -1 and +1 in a random manner ($|S(t)| \leq 1$). Equation (5) gives the relation between Δf and the degree of turbulence, which is defined in Equation (4).

$$\% \text{ turbulence} \equiv \frac{U'(t)_{RMS}}{U(t)} \equiv \frac{f_{DEV}(t)_{RMS}}{f_c(t)} \quad \text{(one vector component)} \tag{4}$$

$$f_{DEV}(t)_{rms} = \frac{f_{DEV}(t)_{max}}{\sqrt{2}} = \frac{\Delta f}{\sqrt{2}} \tag{5}$$

For convenience in the present study, the following assumptions are made:

1. $f_{DEV}(t)$ is assumed in this report to be in the range from 50 to 150 MHz; variations of $f_{DEV}(t)$ with time are very slow.

2. Maximum turbulence 25%, i.e. $\Delta f = 35\%$

3. Bandwidth of S(t): $f_S = 0$ to 100 kHz.

The important system characteristics considered in the following discussion are:

1. Ability of the system to measure f_c, Δf and S(t)

2. S/N ratio, which is inversely proportional to the signal processing bandwidth and determines resolution and accuracy.

3. Loop response time.

4. Feasibility

Analysis of the five measurement methods follows.

2.12.3.1 Spectrum Analyzer

The power spectrum of f(t), measured on a spectrum analyzer, can only be interpreted in terms of the modulation signal S(t) if this is a sine function. Then it is

possible to determine Δf and f_s, the signal frequency. However, for a signal containing several frequency components, it may be impossible to get meaningful data from a spectrum analyzer. f_c and an average value for Δf can be obtained, but the actual modulation signal cannot be determined.

This may be seen from the following brief explanation (11). Consider a simple frequency modulated (fm) signal of carrier frequency f_c, which is being deviated by frequency $\pm f_{DEV}$ above and below f_c, at a frequency f_s, the signal frequency. Figure 2.12-3 shows the fourier spectra of the fm signal, f_c and f_{DEV} being held constant, with f_s varied from a low to a high frequency. An important parameter is the

$$\text{Modulation Index } \beta \equiv \frac{f_{DEV}}{f_s}$$

With low $\beta = 0.5$, i.e. a relatively high signal frequency f_s, the simple spectrum at the top is obtained. However, as f_s is reduced, i.e. β increased, the spectra become more cluttered, and change in shape and width. Even in this very simple case, it is clear that the derivation of f_{DEV} and f_s from the spectrum would be relatively difficult. With the Laser Doppler Velocity Instrument, both f_{DEV}, and f_s are fluctuating in random fashion, resulting in a variation of β from low values to several hundred. Instrumental Broadening further complicates the spectrum. Thus, to interpret f_{DEV} and f_s accurately from a spectral display would be exceedingly difficult, if not impossible. In fact, it is not clear that unique values of f_{DEV} and f_s would be obtainable from such complex spectra.

2.12.3.2 Wide Band Frequency Discriminator

An ideal frequency discriminator is a device whose output voltage magnitude has an instantaneous value proportional to the instantaneous frequency of the input signal; i.e., a signal of varying frequency is transformed into one of varying amplitude. Since most discriminators are sensitive to
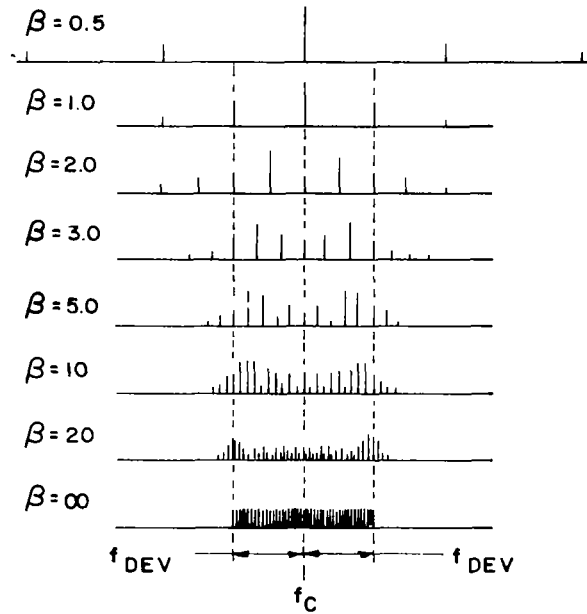
Figure 2.12-3 - FM Spectrum of Single-Tone Modulation
Bandwidth vs. Modulation Index $\beta = \dfrac{f_{DEV}}{f_s}$

2.12-15

amplitude variations of the FM signal, a limiter is normally
used ahead of the FM detector. The frequency modulation is con-
verted into an amplitude modulation by means of a network whose
amplitude and phase characteristics are linear functions of fre-
quency, and then detected by an envelope detector (AM demodu-
lator). A tuned circuit (Figure 2.12-4) is an approximation to
such a frequency discriminator, although the linear range is
small and the output voltage variations are superimposed on the
large signal present with an unmodulated carrier.

The envelope detector may consist of a diode and a RC filter
circuit. The operation of a frequency discriminator is illus-
trated in Figure 2.12-5. Better performance is obtained if two
such networks are combined in a balanced differential manner as
shown in Figure 2.12-6. The linearity is improved considerably,
and the discriminator output is zero for an unmodulated carrier
($f'(t) \equiv 0$).

Since the maximum frequency deviation in our assumed $f(t)$
is $0.35 \, f_{c_{max}}$ = 52.5 MHz, the linear range of the discriminator
has to be 105 MHz. This may require a high discriminator center
frequency f_{IFO}, e.g. 500 MHz, in order to achieve a sufficient-
ly wide linear region. The Doppler frequency $f(t)$ has therefore
to be translated to this IF by heterodyning $f(t)$ with a local
oscillator frequency, f_{VCO}. The LO frequency may be controlled
manually or, in case of varying $\bar{f}$, by means of an automatic
tracking loop, Figure 2.12-7, whose function is now described.

If the difference between f_{VCO} and f_c is not equal to the
discriminator center frequency f_{IFO} the average discriminator
output voltage (measured after the low pass filter) will not be
zero, therefore producing a voltage change at the output of the
integrator. This in turn causes the LO frequency f_{VCO} to change
until the equilibrium, $f_{VCO} - f_c = f_{IFO}$ is reached and the
average discriminator output is zero. Under these conditions,
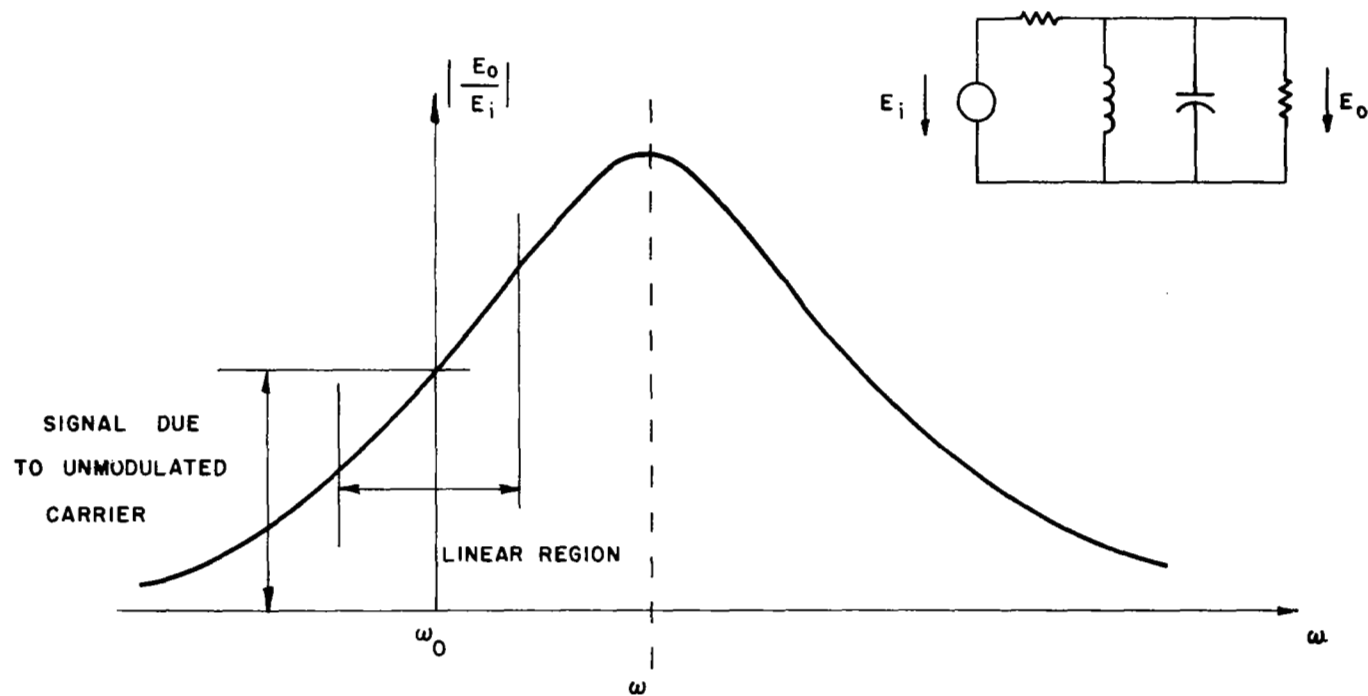
Figure 2.12-4   Tuned Circuit as FM to AM Converter

FM INPUT → LIMITER → FM—AM CONVERSION → ENVELOPE DETECTOR → SIGNAL OUTPUT

FM, VARYING AMPLITUDE   FM, CONSTANT AMPLITUDE   AM   0   DEMODULATED SIGNAL
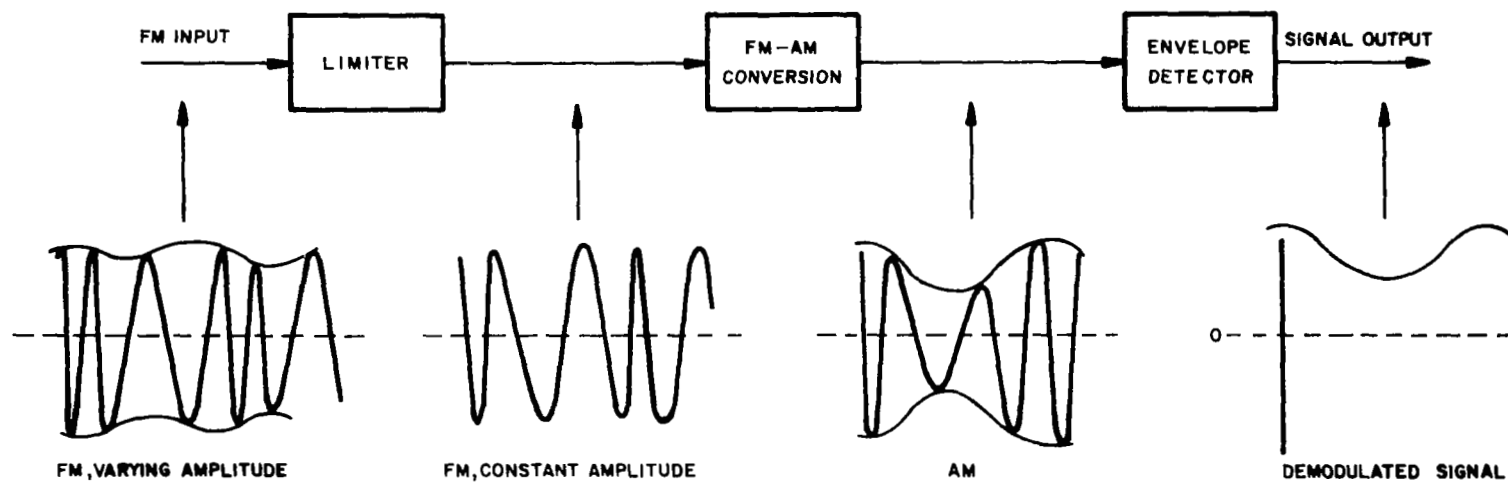
Figure 2.12-5 - Basic Frequency Discriminator
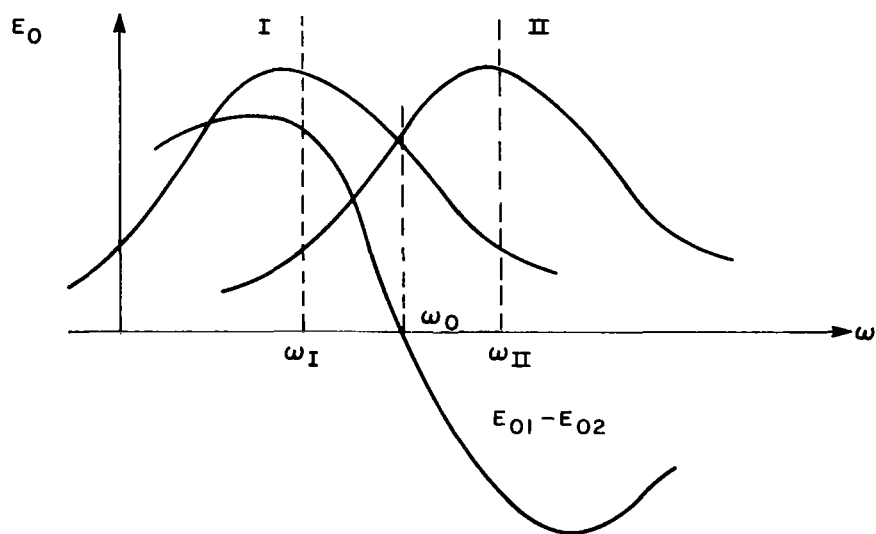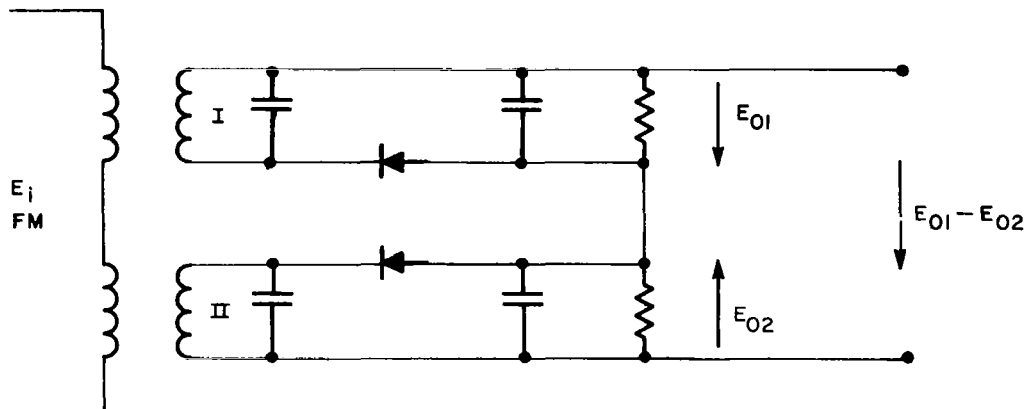
Figure 2.12-6 - Balanced Discriminator
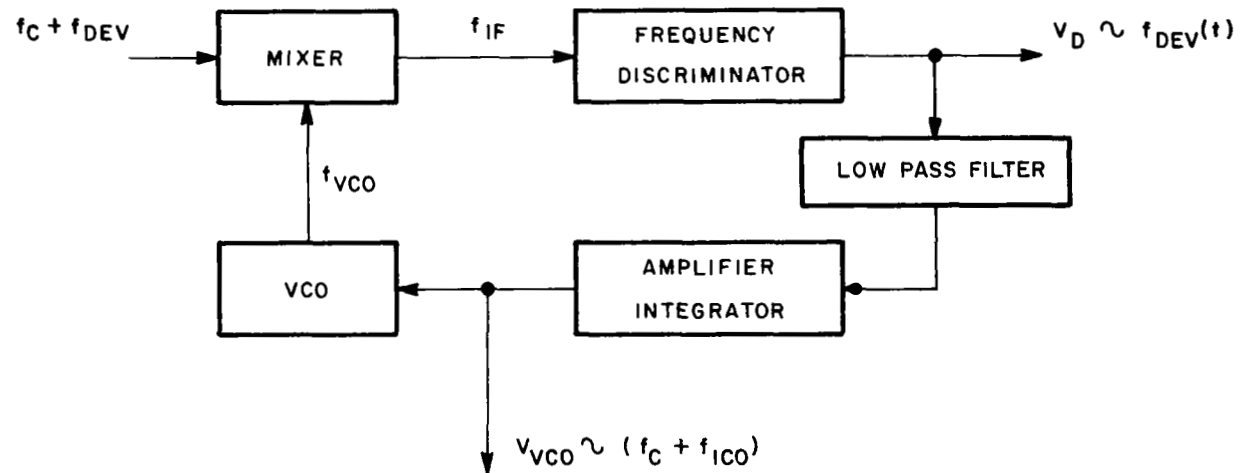
Figure 2.12-7 Wide Band Frequency Discriminator

V_{VCO} the driving voltage of the voltage controlled oscillator, is a measure for f_c (and therefore $\bar{U}$), and V_D the discriminator output voltage, is proportional to f_{DEV} (and therefore U'). The tracking loop response may be very slow, corresponding to the slow changes of f_c.

The signal-to-noise ratio (S/N) is determined by the IF bandwidth, which is 105 MHz. The large bandwidth seems to make this system impractical for an application in the Laser Doppler Velocity Instrument, at least for high degrees of turbulence. The performance of a frequency discriminator in the presence of noise is presently being investigated, which will then allow an estimate to be made of the practical limitations of this system.

2.12.3.3 Filter Bank

The S/N ratio of the above described system can be improved by analyzing the IF signal with a filter bank instead of a frequency discriminator. The Doppler signal bandwidth, $2f_{DEV}$, would be covered by N filters each of an individual bandwidth of B_i, where $NB_i = 2\Delta f$. The output noise of each filter is 1/N of the total noise, while the signal, which activates only one filter at a time (corresponding to the instantaneous frequency) is not affected by the filters, as long as the rate of change of the instantaneous frequency, df/dt, is small enough compared with B_i, namely:

$$\frac{df}{dt} \leq B_i{}^2 \tag{6}$$

Under these conditions, the S/N is improved by a factor N; for larger df/dt, the improvement is less. The rate of change of the Doppler frequency, assuming a sinusoidal variation

$$f = f_c + f_{DEV} \sin \omega_m t$$

is:

$$\frac{df}{dt} = f_{DEV}\omega_m \cos \omega_m t$$

and:

$$\left(\frac{df}{dt}\right)_{max} = f_{DEV}\omega_m \tag{7}$$

Combining Equations (6) and (7):

$$f_{DEV}\omega_m \leq B_i^2$$

or

$$f_{DEV}f_m \leq \frac{B_i^2}{2\pi} \tag{8}$$

Equation (8) states the limitations of this system. Assuming a filter bandwidth B_i = 1 MHz and a maximum frequency deviation f_{DEV} = 52.5 MHz, the maximum allowable signal frequency f_s is 3 kHz, and for f_s = 100 kHz, the maximum allowable frequency deviation is 1.6 MHz.

A frequency tracking loop similar to that described in Section 2.12.3.2 is used to translate f_c to the center frequency of the filter bank, f_{IFO}. The VCO control voltage is obtained from the filter bank by generating weighted voltages from each filter output, resulting in a linear voltage vs frequency characteristic, with the output voltage for $f_{IF} = f_{IFO} = |f_c - f_{VCO}|$ being zero. Figure 2.12-8 shows a block diagram of this system.

Since the combination of filter bank and control voltage generator acts as a linear frequency discriminator, the output of the control voltage generator is proportional to $f_{DEV}(t)$ as in the case of the wide band frequency discriminator. The resolution of this system is given by the number N of filters.
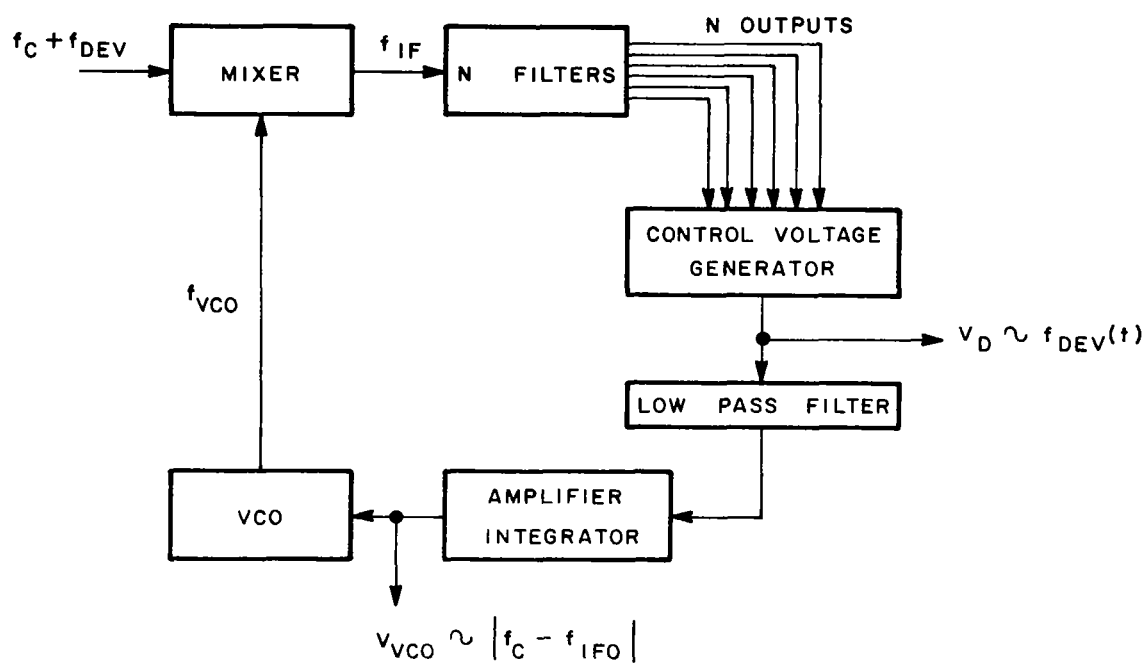
Figure 2.12-8 - Filter Bank

2.12.3.4 Doppler Frequency Tracker

The frequency tracking loop is similar to
that used with the wide band frequency discriminator, but the
loop bandwidth is made wide enough to be able to track the in-
stantaneous frequency, instead of the average frequency. A
block diagram of the Doppler Frequency Tracker is shown in
Figure 2.12-9. The necessary IF bandwidth is 200 kHz, which
also determines the S/N of this system and which means an im-
provement of 105/0.2 = 525, compared with the wide band discrimi-
nator system. This technique is also known as "Frequency Com-
pressive Feedback" or "Frequency Locked Loop" and has been used
in space communication systems for the detection of FM signals.

The driving voltage of the VCO is a function of the instan-
taneous frequency f(t) and therefore U(t). The DC component of
this voltage is a measure of f_c (and $\bar{U}$), and the AC component is
proportional to $f_{DEV}(t)$ and therefore U'(t).

This system seems to be feasible and meets the requirements
for minimum processing bandwidth and ability to measure f_c, f_{DEV}
and S(t) in the range assumed at the beginning of 2.12.3. The
possibilities of extending this range are now discussed. In an
ideal frequency locked loop there are no limitations to the mag-
nitude of f_{DEV}, which is equivalent to the amplitude of the
loop input signal. In practice, however, f_{DEV} will be limited
by the nonlinearities of the various loop components (e.g., in-
tegrator, VCO). The signal bandwidth, $f_{s\ max}$ = 100 kHz, can be
increased, but, since the required IF bandwidth is $2f_{s\ max}$,
only at the expense of S/N. The range of f_c (assumed to be 50
to 150 MHz) can be extended up to the bandwidth limitations of
the photomultiplier and down to a frequency which still allows
heterodyning to a reasonable IF.
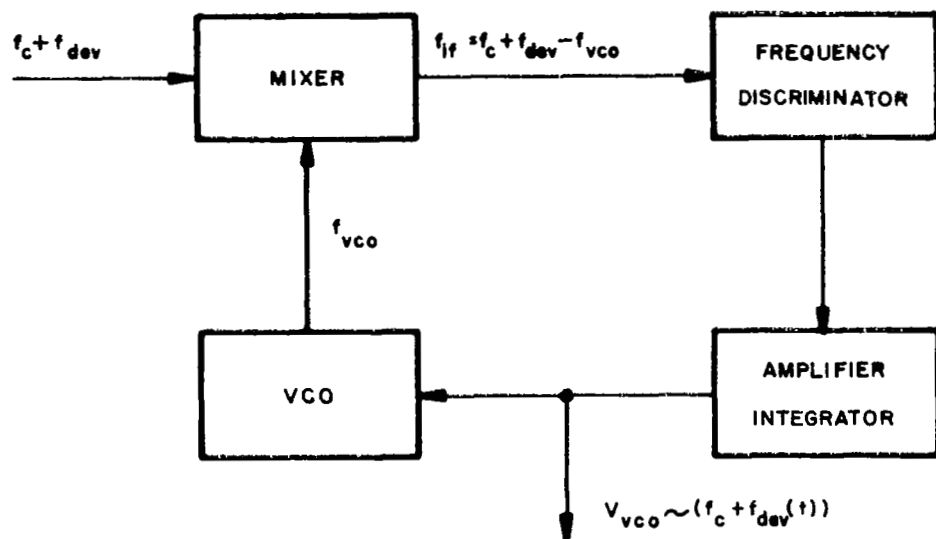
Figure 2.12-9 - Doppler Frequency Tracker

2.12.3.5 Phase Locked Receiver

The block diagram of a phase locked loop is
shown in Figure 2.12-10. The phase of the Doppler signal is com-
pared with the phase of a local oscillator (VCO). The output of
the phase detector, which is proportional to the phase differ-
ence, is fed to the loop filter and controls the VCO frequency
so that the phase difference between Doppler signal and VCO
never exceeds θ, which is less than 2π. The required loop band-
width depends on the rate of change of the input frequency and
the allowable phase lag (13):

$$B = 10 \sqrt{\frac{1}{\theta} \frac{df}{dt}} \ , \qquad\qquad (9)$$

where θ = allowable phase lag in degrees between VCO
          frequency and Doppler frequency.

$\dfrac{df}{dt}$ = rate of change of Doppler frequency.

With Equation (7), the maximum rate of change for f_{DEV} = 52.5 MHz
and f_s = 100 kHz is:

$$\frac{df}{dt} \text{max} = 52.5 \cdot 10^6 \cdot 2\pi \cdot 10^5 \approx 3.5 \cdot 10^{13} \text{ Hz/sec.}$$

For a maximum phase error of 10° the bandwidth is therefore:

$$B = 10 \sqrt{10^{-1} \cdot 3.5 \cdot 10^{13}} = 18.7 \text{ MHz.}$$

The driving voltage of the VCO is a function of the frequency
f(t), and can be interpreted in terms of f_c, f_{DEV} and S(t).

Realization of a loop bandwidth of 18.7 MHz does not seem
practical. Furthermore, it seems that this system does not have
the advantage of a much reduced noise bandwidth.
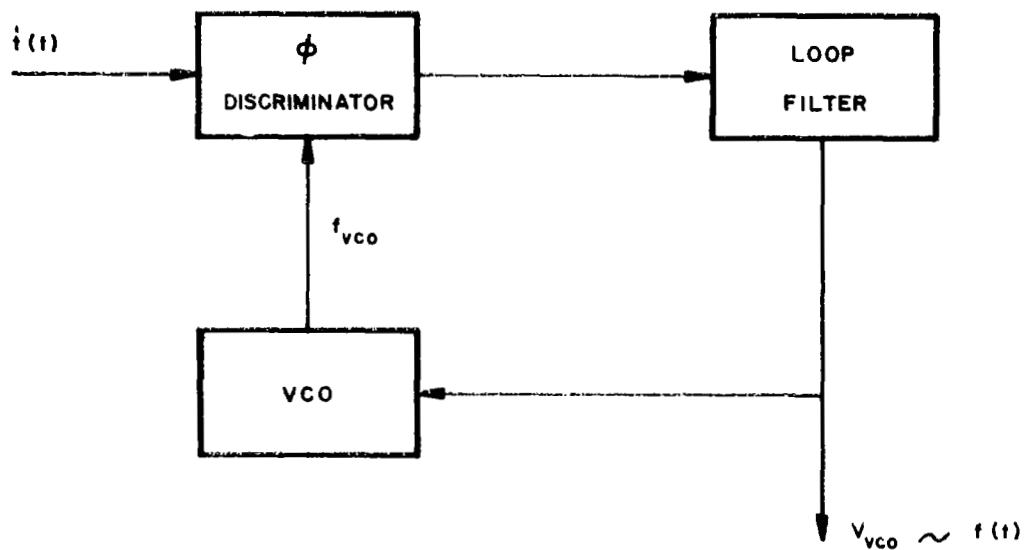
Figure 2.12-10 - Phase Locked Loop

Although the phase locked loop has found wide application in space communication systems for its ability to detect signals in the presence of high noise, it seems that it does not offer the same advantages for the processing of the Doppler signal of the Laser Doppler Flowmeter. This point is subject to further investigation.

2.12.3.6 Conclusions and Recommendations on Electronic Signal Processing

The results of the analyses in the preceding sections are summarized in Table 2.12-1.

Only the filter bank and the frequency tracker allow a considerable reduction of the noise bandwidth. Both systems also have the ability of measuring f_c, f_{DEV} and S(t), although the filter bank is not useful for the whole assumed range of f_s and f_{DEV}. The frequency tracker also accepts the widest range of Doppler signals.

The spectrum analyzer measures the average spectrum of f(t); i.e., f_c and an average value for the frequency deviation, $\bar{f}_{DEV}$. It is impossible to determine S(t) with the spectrum analyzer.

The wide band frequency discriminator and the phase locked loop have the disadvantage of a wide noise bandwidth. While the realization of the wide band frequency discriminator system should not present any problems, it might be impractical to build a phase-locked loop with the required loop bandwidth of 18 MHz.

It is therefore recommended that the frequency locked loop be used as a Doppler signal processor. Since the filter bank is expected to give useful results for a limited range of Doppler signals, a filter bank system should also be designed and built, and tested on a Laser Doppler Velocity Instrument. A preliminary design of these two systems follows.

TABLE 2.12-1 - SUMMARY OF SYSTEMS CHARACTERISTICS

System	Measurements	Equivalent Noise Bandwidth	Resolution	Loop Response Time	Electronic Feasibility
Spectrum Analyzer	$\bar{f}$, $\overline{\Delta f}$	Narrow	-	-	-
Wide Band Frequency Discriminator	$\bar{f}$, Δf, $S(t)$	105 MHz	Continuous	Slow	Good
Filter Bank	$\bar{f}$, Δf, $S(t)$	$B_i = \dfrac{105 \text{ MHz}}{N}$	Quantized (Depending on N)	Slow	More Complicated
Doppler Frequency Tracker	$\bar{f}$, Δf, $S(t)$	200 kHz	Continuous	Fast	Good
Phase-Locked Receiver	$\bar{f}$, Δf, $S(t)$	18.7 MHz	Continuous	Extremely Fast	Not Practical

2.12.4 Preliminary Design of Two Signal Processing Systems

2.12.4.1 Filter Bank

The design of a filter bank system is based on a filter bank which is available for feasibility tests. It consists of 50 filters, each 1 MHz wide, covering the range of 0.5 to 50.5 MHz. Important design considerations are:

1. Is the filter bandwidth, $B_i = 1$ MHz, narrow enough to give adequate S/N?

2. The original Doppler spectrum $f_e \pm f_{DEV}$ and the heterodyned spectrum $f_{IFO} \pm f_{DEV}$ must not overlap.

3. Equation (8), which relates f_s and f_{DEV} to B_i.

Preliminary design data for a filter bank system are given in Figure 2.12-8. A detailed block diagram of the filter bank-control voltage generator (frequency discriminator) is shown in Figures 2.12-11 and 2.12-12 which are now described.

Each narrow band filter is followed by an envelope detector which feeds a level detector. The level detector controls a switch, which when it is activated by a signal in that channel causes a voltage characteristic of that particular channel (i.e., proportional to the difference between filter frequency and filter bank center frequency, $f_c - f_{IFO}$) to appear at the output of the discriminator. The switches insure that only the output of one channel at a time goes to the low pass filter and integrator, thus preserving the S/N capability of the system which was obtained by dividing the frequency range into N sections.

```
   f(t)                    ┌──────────────────┐     f_IFO = 25 MHZ   ┌──────────────────┐
  ─────────────────────▶   │      MIXER       │    ─────────────────▶│  I F -AMPLIFIER  │
  f_C= 70 TO 150 MHz       │                  │                      │                  │
  f_DEV= 16.6% f_C         │ HEWLETT-PACKARD  │                      │  TO BE SPECIFIED │
  (12% TURBULENCE)         │     10514A       │                      │                  │
                           └──────────────────┘                      └──────────────────┘
                                    ▲                                          │
                                    │                                          ▼
                           ┌──────────────────┐                      ┌──────────────────┐
                           │       VCO        │                      │  FILTER BANK     │
                           │                  │                      │  FREQUENCY       │
                           │  45 TO 125 MHz   │                      │  DISCRIMINATOR   │
                           │ KAY ELECTRIC CO. │                      │                  │
                           │ MULTISWEEP 15gB  │                      │  DETAILS SEE     │
                           │                  │                      │  FIG. 2.12-12    │
                           └──────────────────┘                      └──────────────────┘
  V_VCO ~ |f_C - f_IFO| ◀──────────�│                                          │───────▶ V_D ~ f_DEV(t)
                                    ▲                                          ▼
                           ┌──────────────────┐                      ┌──────────────────┐
                           │    AMPLIFIER     │                      │ LOW PASS FILTER  │
                           │    INTEGRATOR    │                      │                  │
                           │                  │ ◀──────────────────  │  TO BE DESIGNED  │
                           │  TO BE DESIGNED  │                      │  AND BUILT BY    │
                           │  AND BUILT BY    │                      │  RAYTHEON        │
                           │  RAYTHEON        │                      │                  │
                           └──────────────────┘                      └──────────────────┘
```
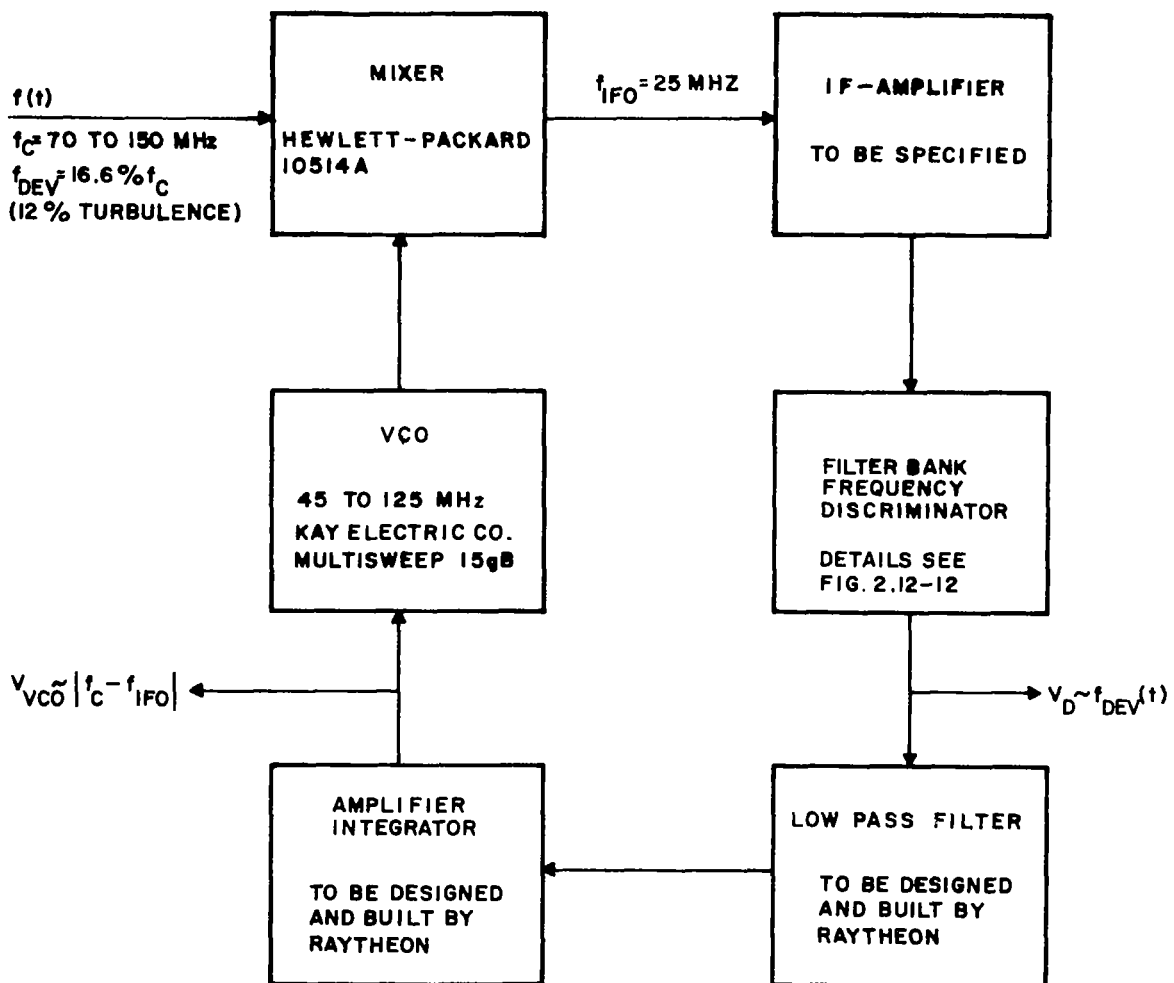
Figure 2.12-11 - Filter Bank System

FROM IF AMPLIFIER

TO 50 FILTERS

n^{TH} FILTER
CENTER FREQUENCY: f_{cn}
BAND WIDTH: I MHz

ENVELOPE
DETECTOR

$f_{cn} = n$ MHz

n: I TO 50

LEVEL
DETECTOR

REFERENCE VOLTAGE
SOURCE
$V_n \sim (f_{cn} - f_{ifo})$

SWITCH

FROM 50 CHANNELS

OUTPUT (TO LOWPASS FILTER)
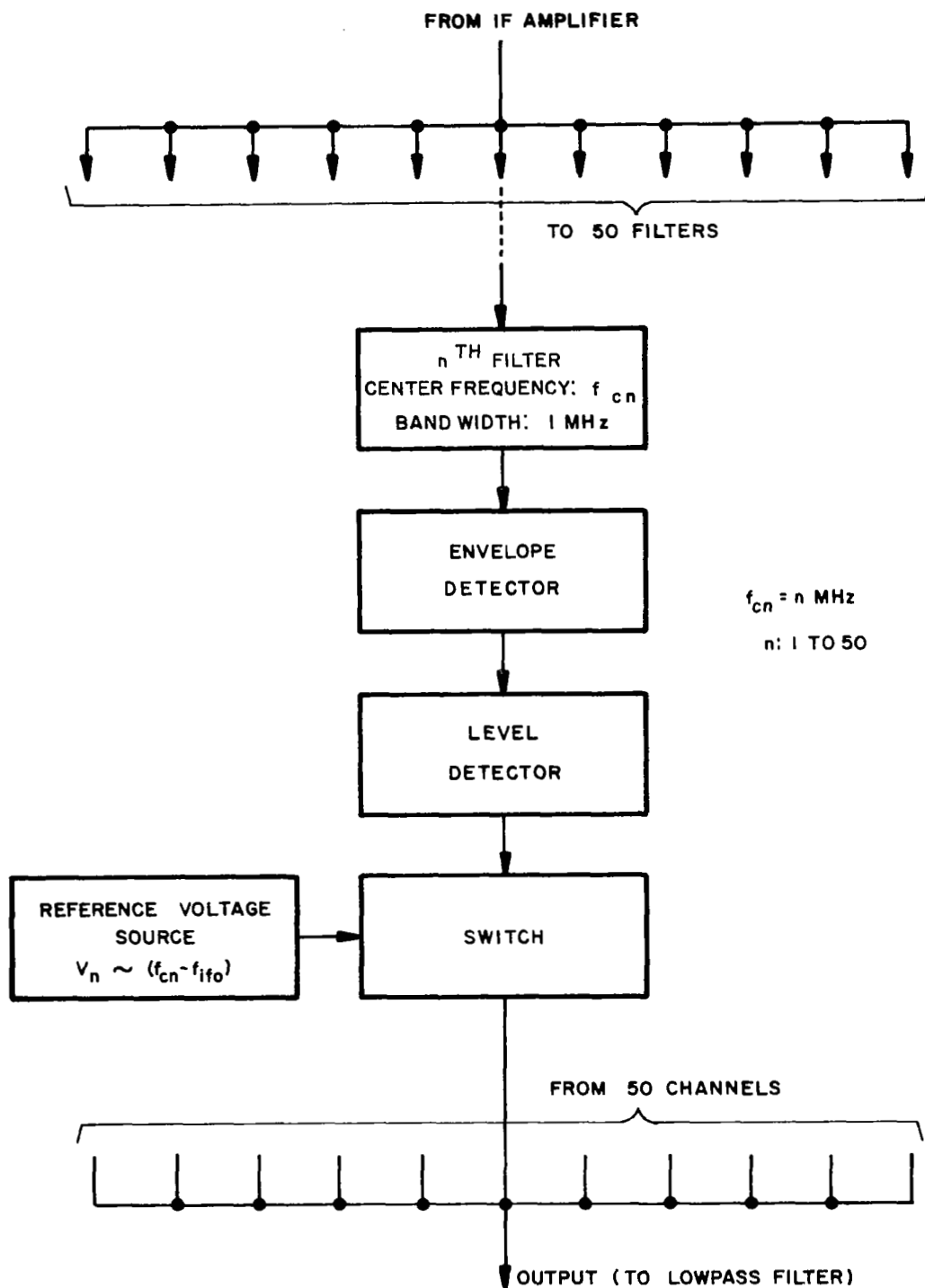
Figure 2.12-12 - Filter Bank Discriminator

2.12.4.2 Frequency Tracker

A more detailed block diagram is shown in Figure 2.12-13 including preliminary component specifications and design data. In addition to the frequency tracker, as discussed in Section 2.12.3.4, an automatic signal acquisition loop is included in the design. This is to enable the system to acquire the Doppler signal by sweeping the VCO frequency until the difference between VCO and Doppler frequency is equal to f_{IF} , and then activating the tracking loop. If the signal is lost; i.e., if there is no output from the IF narrow band filter, another "sweep" cycle is initiated.

2.12.5 Experimental Investigation of Frequency Discriminator Behavior with Varying Input Signal and Noise Levels

A frequency discriminator system was set up and used in joint experiments for the measurement of turbulent flow from a nozzle, with NASA and Hayes International personnel at the George C. Marshall Space Flight Center. In the course of the experiments, the discriminator output was found to be unpredictable and asymmetrical under some conditions. Preliminary investigation suggested that this was because the signal input level was too low, or the input signal-to-noise ratio was too low, or because of a combination of these conditions. The validity of this hypothesis required experimental verification.

The discriminator system used was therefore set up in the laboratory at Raytheon Sudbury, and subjected to varying input signals and noise levels under controlled conditions from separate signal and noise generators.

It was concluded that, as generally accepted, the discriminator was very insensitive to changes in input levels. However, when the input signal level was very low, below design level, or

MIXER

HEWLETT PACKARD
10514A

$f(t)$

$f_{if} = 10$ MHz

IF AMPLIFIER

TO BE
SPECIFIED

$f_c = 50$ TO 150 MHz
$f_{dev} = 35\%$ $\bar{f}$
(25 % TURBULENCE)

VCO

42.5 TO 212.5 MHz
KAY ELECTRIC CO
MULTISWEEP 15gB

NARROW BAND
FILTER

10 ± 0.1 MHz

TO BE DESIGNED AND
BUILT BY RAYTHEON

INTEGRATOR
AMPLIFIER

AMPLIFIER

TO BE
SPECIFIED

LIMITER

TO BE
SPECIFIED

SWEEP BIAS

VOLTAGE SOURCE

SWITCH

DETECTOR

TO BE
SPECIFIED

FREQUENCY
DISCRIMINATOR

LINEARITY,
SENSITIVITY
TO BE SPECIFIED

Figure 2.12-13   Frequency Tracker System

the noise level very high, the type of output irregularities ob-
served in the Laser Doppler Velocity Instrument experiments was
generated. Operating levels for good operation were determined.
A set of oscillograph photos was prepared, which could be used
to diagnose such input signal defficiencies.

A good feature, again generally accepted for frequency dis-
criminators, was that the onset of output irregularities occurred
quite suddenly, in a recognizable manner, as input signal levels
and S/N ratios were progressively lowered.

The experiments are reported below:

2.12.5.1 Measurements

The purpose of this experiment was to observe
the operation of a commercially available type of discriminator
under varying conditions of signal level and signal-to-noise
ratios. Three different situations were investigated:

A.   Constant signal amplitude, increasing noise level
B.   Constant noise amplitude, decreasing signal level
C.   Constant S/N, decreasing both signal and noise levels

Under the above conditions it was possible to observe at
the DC output, the following discriminator characteristics:

1.   Effect of varying S/N
2.   Effect of the amplitude limiting stages
3.   Sensitivity of the pre-amp and discriminator
      combination.

2.12.5.2 Test System

A block diagram of the actual test setup is
shown in Figure 2.12-14. The discriminator and associated
matching pre-amplifier used were made by RHG and supplied by
NASA. The discriminator center frequency was 30 MHz with a
bandwidth 9 MHz. Pre-amplifier center frequency was 30 MHz with
a 10 MHz bandwidth and a gain of 40 db. The unit Model No. was
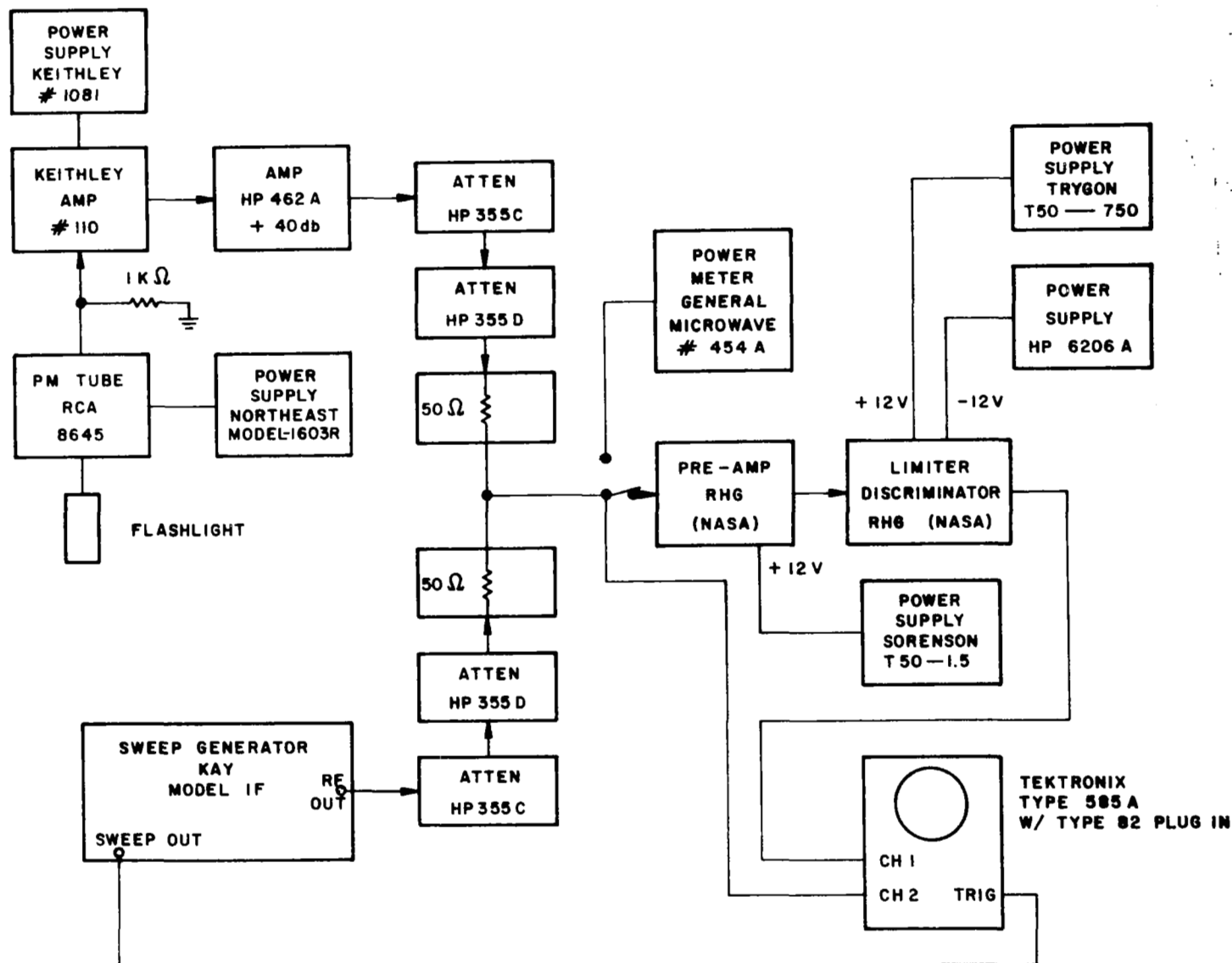
Figure 2.12-14   Schematic Diagram Discriminator Signal-to-Noise
Behavior Test Relay

DT 30E43   and Serial No.3-082-4   . A photomultiplier tube illuminated by a flashlight was used as a noise course.

Accordingly, the RF sweep generator was set at a center frequency of 30 MHz with a sweep width slightly greater than 10 MHz. The PM tube was activated by using a flashlight in a light-tight box as a source. Anode to cathode voltage was 800 volts DC with a 1000-ohm resistor to ground on the anode. Both the signal channel and the noise channel amplitudes were controlled by Hewlett-Packard decade attenuators. Each source contained a 50 ohm pad in series so that the combination of the two presented an impedance of 50 ohm to the pre-amp input.

For purposes of calibration, the average power of each source was measured at the pre-amp input by a thermoelectric power meter which had a frequency response of 10 MHz to 12 GHz.

A typical power calibration obtained by adjusting the internal power level of the RF oscillator and also adjusting the PM tube supply voltage was as shown in Figure 2.12-15.

2.12.5.3 Results

The photographic data obtained and reproduced in Figures 2.12-16 thru 2.12-20 show the discriminator output S-curve detected at the DC output connector as the upper trace on the oscilloscope. The lower trace is the combination of the signal and noise at the input of the pre-amp.

2.12.5.4 Recommendations

Parts A, B and C of Section 2.15.5.1 should be repeated with the addition of a 30 MHz ±5 MHz bandpass filter at the input of the pre-amp. In addition, Part C should be extended to cover S/N ratios of 3 db, 0 db, and less: It might also be useful to obtain photographs of a typical input waveform with varying S/N ratios. It would also be interesting to repeat this series of measurements using a discriminator supplied by a different manufacturer such as LEL, or using another model by RHG.

2.12-37

KAY RF GENERATOR

HP ATTENUATOR

Imw OR
O dbm

(O db SETTING)

PM RCA8645

KEITHLEY AMP

HP-462A AMP +40 db

HP ATTENUATOR

IOmw OR
-20 dbm

(O db SETTING)
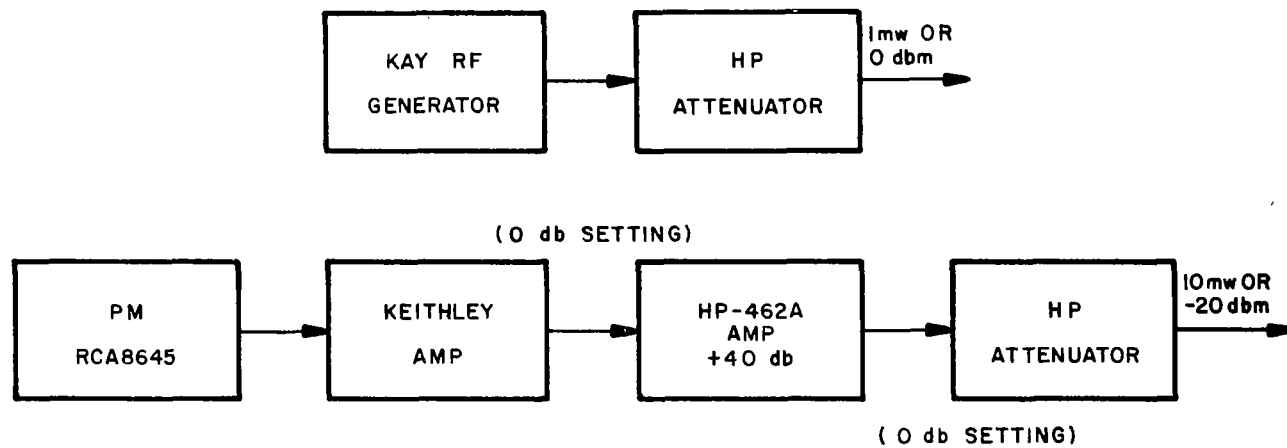
Figure 2.12-15   Schematic Diagram of Source Power Calibration
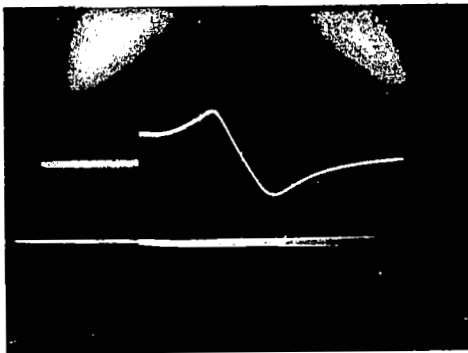
$$S/N = \frac{-50 \text{ dbm}}{-66 \text{ dbm}} = 16 \text{ db}$$
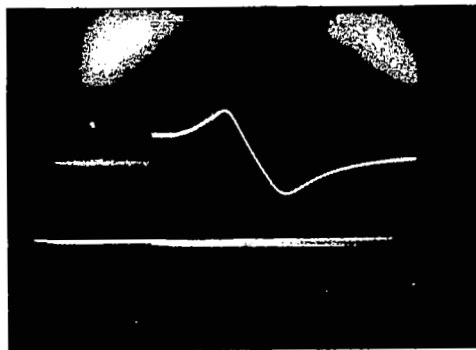
$$S/N = \frac{-50 \text{ dbm}}{-56 \text{ dbm}} = 6 \text{ db}$$
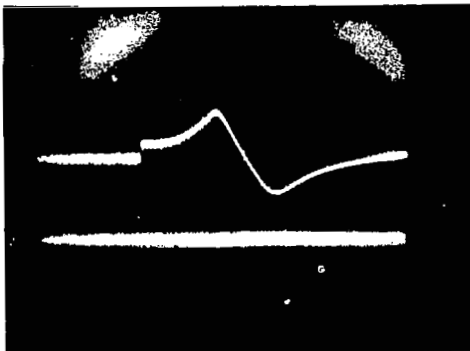
$$S/N = \frac{-50 \text{ dbm}}{-46 \text{ dbm}} = -4 \text{ db}$$
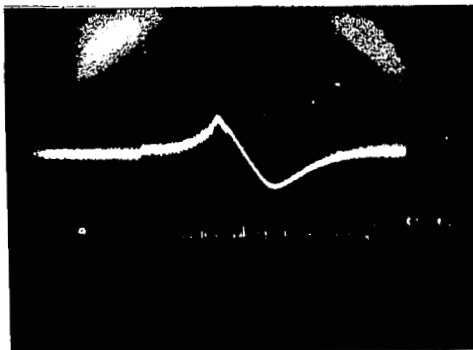
$$S/N = \frac{-50 \text{ dbm}}{-36 \text{ dbm}} = -14 \text{ db}$$
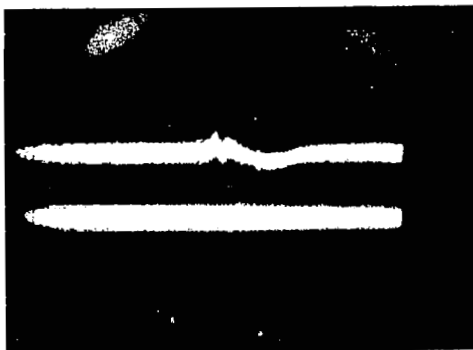
$$S/N = \frac{-50 \text{ dbm}}{-26 \text{ dbm}} = -24 \text{ db}$$

$$S/N = \frac{-50 \text{ dbm}}{-16 \text{ dbm}} = -34 \text{ db}$$

Upper Trace – Output Amplitude; Lower Trace – Input Amplitude;
Centre Frequency – 30 MHz; Frequency Sweep – 25 to 35 MHz

Figure 2.12-16   Frequency Discriminator Output Signal, with Swept-
Frequency Input Signal Added to White Noise, Input
Signal Amplitude Constant, Input Noise Amplitude
Progressively Increased
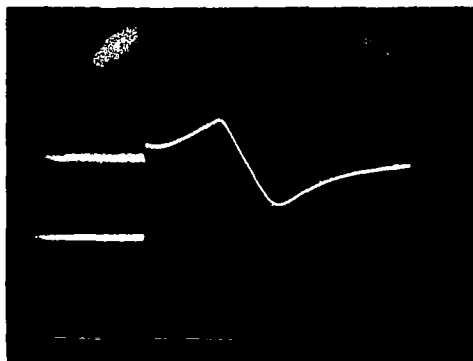
$$S/N = \frac{0 \text{ dbm}}{-16 \text{ dbm}} = 16 \text{ db}$$
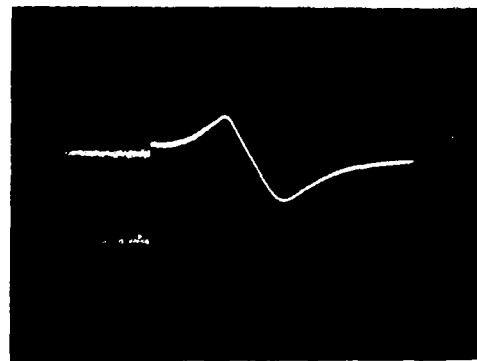
$$S/N = \frac{-10 \text{ dbm}}{-16 \text{ dbm}} = 6 \text{ db}$$
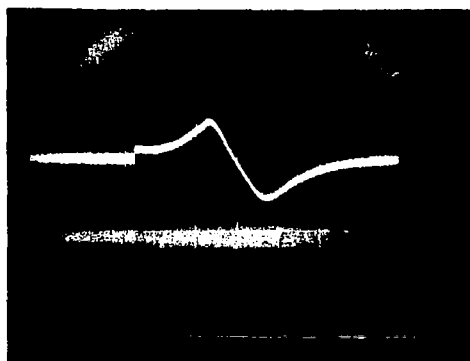
$$S/N = \frac{-20 \text{ dbm}}{-16 \text{ dbm}} = -4 \text{ db}$$
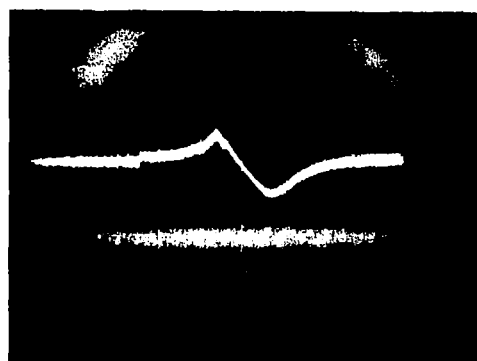
$$S/N = \frac{-30 \text{ dbm}}{-16 \text{ dbm}} = -14 \text{ db}$$
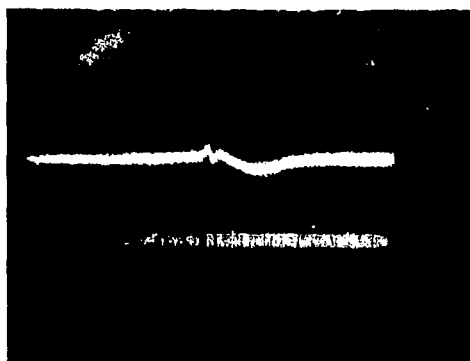
$$S/N = \frac{-40 \text{ dbm}}{-16 \text{ dbm}} = -24 \text{ db}$$
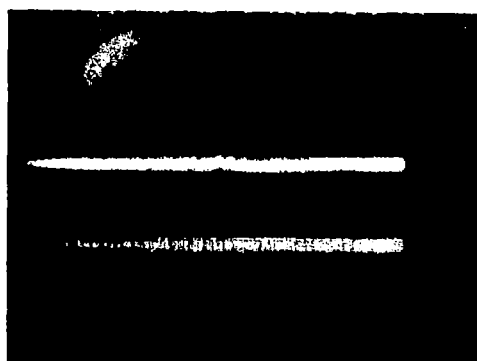
$$S/N = \frac{-50 \text{ dbm}}{-16 \text{ dbm}} = -34 \text{ db}$$

Upper Trace - Output Amplitude; Lower Trace - Input Amplitude;
Centre Frequency - 30 MHz; Frequency Sweep - 25 to 35 MHz

Figure 2.12-17   Frequency Discriminator Output Signal, with Swept-
Frequency Input Signal Added to White Noise; Input
Signal Amplitude Progressively Decreased, Noise
Level Maintained Constant
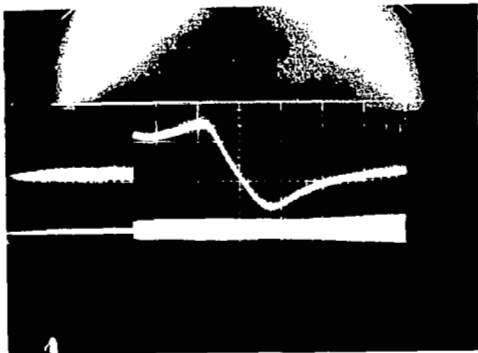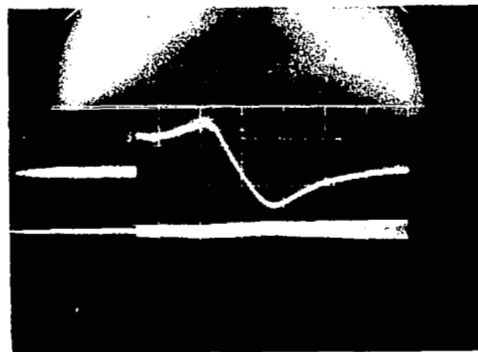
$$S/N = \frac{-20 \text{ dbm}}{-60 \text{ dbm}} = 40 \text{ db} \qquad S/N = \frac{-50 \text{ dbm}}{-90 \text{ dbm}} = 40 \text{ db}$$
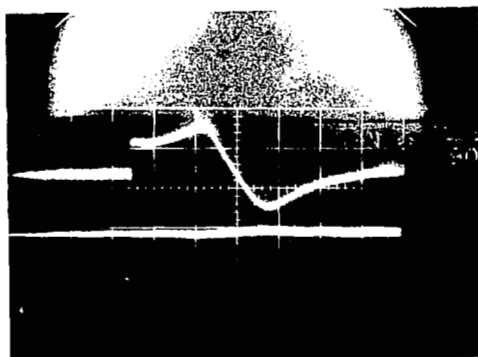
$$S/N = \frac{-60 \text{ dbm}}{-100 \text{ dbm}} = 40 \text{ db} \qquad S/N = \frac{-70 \text{ dbm}}{-110 \text{ dbm}} = 40 \text{ db}$$
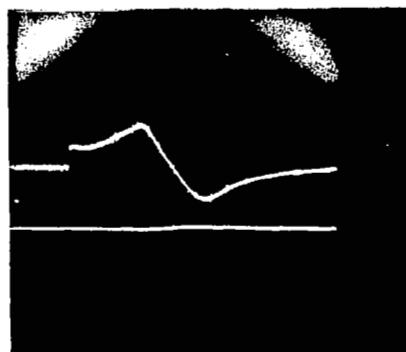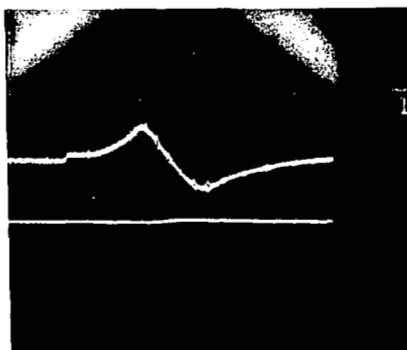
$$S/N = \frac{-80 \text{ dbm}}{-120 \text{ dbm}} = 40 \text{ db} \qquad S/N = \frac{-90 \text{ dbm}}{-130 \text{ dbm}} = 40 \text{ db}$$
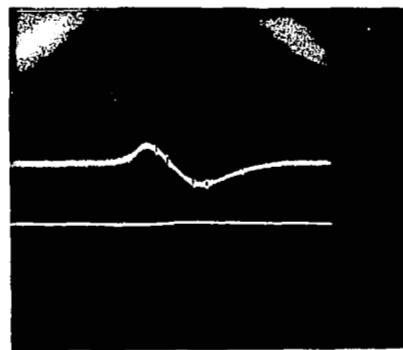
Upper Trace - Output Amplitude; Lower Trace - Input Amplitude;
Centre Frequency - 30 MHz; Frequency Sweep - 25 to 35 MHz

Figure 2.12-18   Frequency Discriminator Output Signal, with Swept-
Frequency Input Signal Added to White Noise; Signal
and Noise Progressively Decreased, Signal-to-Noise
Power Ratio Maintained Constant at 40 Decibels
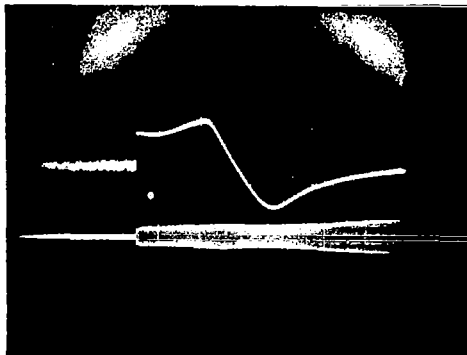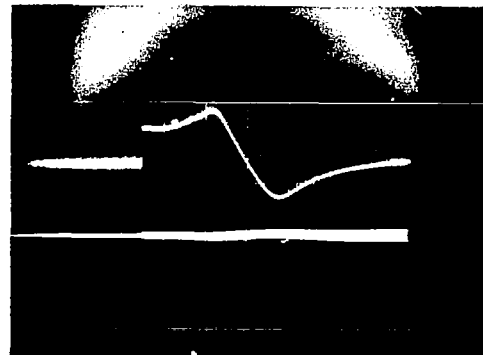
$$S/N = \frac{-20 \text{ dbm}}{-36 \text{ dbm}} = 16 \text{ db} \qquad S/N = \frac{-50 \text{ dbm}}{-66 \text{ dbm}} = 16 \text{ db}$$
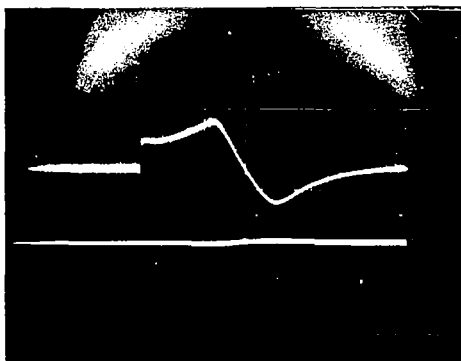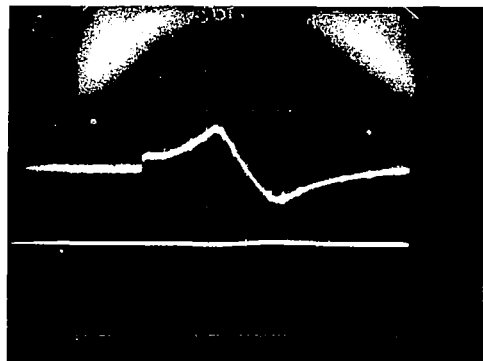
$$S/N = \frac{-60 \text{ dbm}}{-16 \text{ dbm}} = 16 \text{ db} \qquad S/N = \frac{-70 \text{ dbm}}{-86 \text{ dbm}} = 16 \text{ db}$$
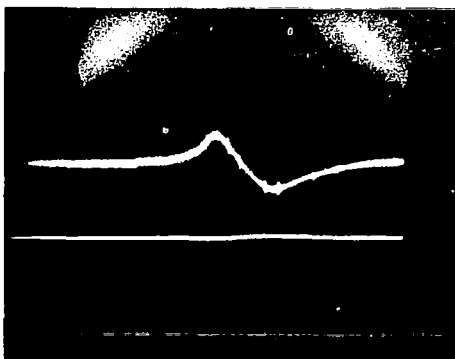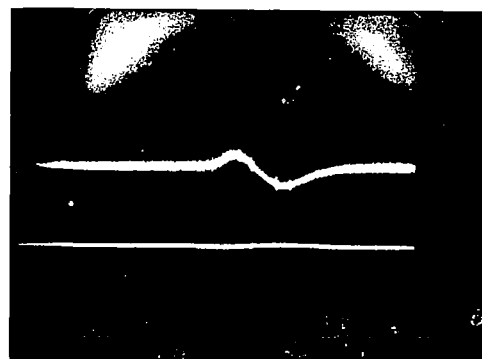
$$S/N = \frac{-80 \text{ dbm}}{-96 \text{ dbm}} = 16 \text{ db} \qquad S/N = \frac{-90 \text{ dbm}}{-106 \text{ dbm}} = 16 \text{ db}$$

Upper Trace – Output Amplitude; Lower Trace – Input Amplitude;
Centre Frequency – 30 MHz; Frequency Sweep – 25 to 35 MHz

Figure 2.12-19   Frequency Discriminator Output Signal, with Swept-
Frequency Input Signal Added to White Noise; Signal
and Noise Progressively Decreased, Signal-to-Noise
Power Ratio Maintained Constant at 16 Decibels
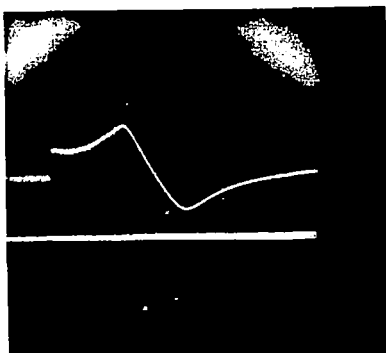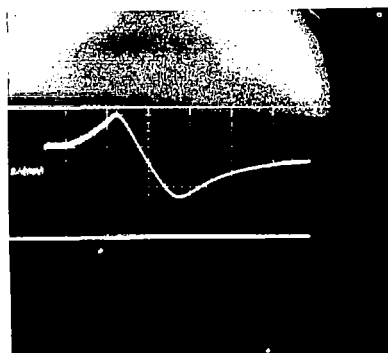
$$S/N = \frac{-24 \text{ dbm}}{-30 \text{ dbm}} = 6 \text{ db} \qquad S/N = \frac{-54 \text{ dbm}}{-60 \text{ dbm}} = 6 \text{ db}$$
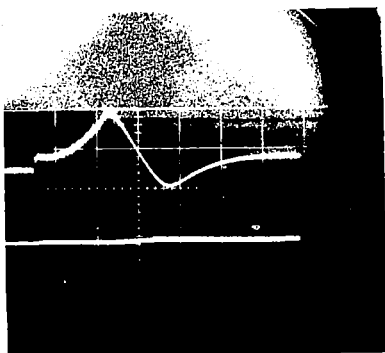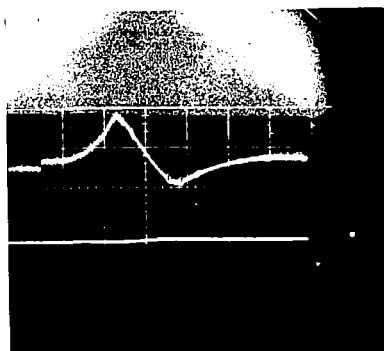
$$S/N = \frac{-64 \text{ dbm}}{-70 \text{ dbm}} = 6 \text{ db} \qquad S/N = \frac{-74 \text{ dbm}}{-80 \text{ dbm}} = 6 \text{ db}$$
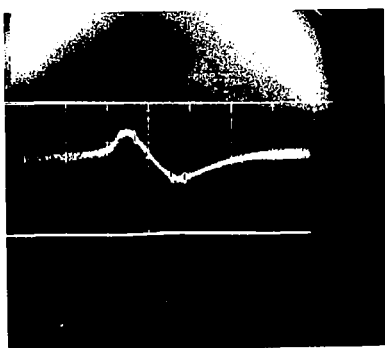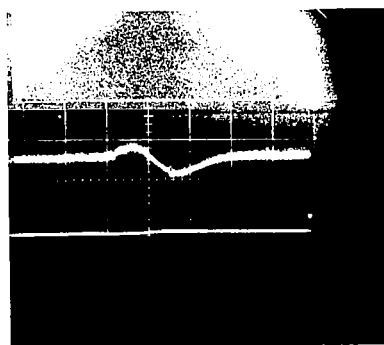
$$S/N = \frac{-84 \text{ dbm}}{-90 \text{ dbm}} = 6 \text{ db} \qquad S/N = \frac{-94 \text{ dbm}}{-100 \text{ dbm}} = 6 \text{ db}$$

Upper Trace - Output Amplitude; Lower Trace - Input Amplitude;
Centre Frequency - 30 MHz; Frequency Sweep - 25 to 35 MHz

Figure 2.12-20   Frequency Discriminator Output Signal, with Swept-
Frequency Input Signal Added to White Noise; Signal
and Noise Progressively Decreased, Signal-to-Noise
Power Ratio Maintained Constant at 6 Decibels

REFERENCES FOR SECTION 2.12

1. Davies, POAL, University of Southampton, Southampton, England.

2. "A Turbulence Primer", University of Illinois (author unknown).

3. Barbin, Notes on Turbulence, (unpublished), Auburn University, Alabama.

4. Rouse, Hunter, Advanced Mechanics of Fluids, Chapter VI, John Wiley and Sons.

5. Pai, Shih I., Viscous Flow: Vol.II Turbulent Flow, D. Van Nostrand & Co.

6. Townsend, A. A., Turbulent Shear Flow, Cambridge University Monograph.

7. Schlichting, M., Boundary Layer Theory, McGraw Hill.

8. Hinze, J. O., Turbulence, McGraw-Hill.

9. Landon and Lifshitz, Fluid Mechanics, Pergamon Press-Addison Wesley, (1959).

10. Cooper and Tulin, Agardograph #12 (NATO publication), ed. W. C. Nelson, University of Michigan (Aug. 1955) - excellent summary of hot-wire techniques.

11. Panter, P. F., Modulation, Noise, and Spectral Analysis, McGraw-Hill (1965).

12. Harman, W.W., Principles of the Statistical Theory of Communication, McGraw-Hill Book Company, New York (1963).

13. Optical Doppler Recording System, Final Report, prepared by Data Corp., April 1967, for NASA, MSFC.

2.13 Spatial Resolution

By spatial resolution we mean the size of the volume of gas whose velocity (mean velocity and spatial and temporal components) the Laser Dopper Velocity Instrument will measure. We are limited, ultimately, by the sharpness with which a diffraction pattern can be defined. As is well known (1, 2, 3), the boundary of a diffraction pattern is a rather indefinite location, in terms of modern metrologic capabilities, since the diffraction pattern is always some form of oscillating function. Thus we must arbitrarily decide where to "cut off" the region in which we are interested. A customary cutoff limit is that at which the light intensity falls off by 20%. This results in approximately 70% of the total light energy falling within the region so defined (3).

However, even with this somewhat "blurred" definition on which to base an estimate of resolution, a target volume calculation is still useful, and the uncertainty, depending on the lens aperture and wavelength, is relatively small from a practical point of view.

Proceeding as above, the three-dimensional focal volume of a perfect lens is conveniently and customarily defined by the following two dimensions:

1. in the focal plane, by the diameter of the
    first zero in the Airy disk diffraction pattern (2)

$$D_A = 2.44 \, \lambda F \qquad\qquad (1)$$

2. perpendicular to the focal plane, (i.e., along
    the light beam axis), the distance at which the
    light falls in intensity by about 20% is
    given by (3)

$$\Delta z = \pm \, 2 \, F^2 \, \lambda \quad ,$$

where Δz is measured on either side of the focal plane, so that total length of focal region is

$$\ell = 2\Delta z = 4F^2 \lambda \qquad\qquad (2)$$

where λ = wavelength of light

$\quad\quad$ F = "f number" of lens

$\quad\quad\quad$ $\equiv$ $\dfrac{\text{lens focal length}}{\text{lens diameter}}$

3. hence volume of focal region, i.e. Scattering Volume is

$$V_s \approx \frac{\pi D_A^2}{4}\ \ell = \frac{\pi(2.44\lambda F)^2}{4}\ (4F^2\lambda) = 18.7F^4\lambda^3 \qquad (3)$$

Using equations (1), (2) and (3) the target volume dimensions have been calculated for typical lasers and lens F numbers, the results being given in Table 2.13-1.

It should be noted that the actual shape of the target volume is somewhat irregular, as can be seen from Figures 8.41, 8.43 and 8.44 of Reference (3). Further, the calculations above are based on the assumption of a simple, perfect lens, with no account taken of aberrations. The effects of aberrations on resolution of the Laser Doppler Velocity Instrument will be studied in more detail. However, it is not expected that they will be a problem of the magnitude of that in photographic applications, firstly because we tend to use large f number lens configurations, secondly because we are dealing with monochromatic laser light and thirdly because our light beams are axial.

TABLE 2.13-1

LASER DOPPLER VELOCITY INSTRUMENT APPROXIMATE
SCATTERING VOLUME DIMENSIONS

Wavelength λ	Lens F Number											
	1.9			11.0			22.0			44.0		
	D_A mm	ℓ mm	V_s mm^3	D_A mm	ℓ mm	V_s mm^3	D_A mm	ℓ mm	V_s mm^3	D_A mm	ℓ mm	V_s mm^3
4,880Å	.0023	.007	$.0236 \times 10^{-6}$	.013	.236	31.32×10^{-6}	.026	.945	5.02×10^{-4}	.052	3.78	80.28×10^{-4}
6,328Å	.0029	.009	$.055 \times 10^{-6}$	.017	.306	69.45×10^{-6}	.034	1.23	11.17×10^{-4}	.068	4.90	17.795×10^{-3}
1.6 microns	.007	.023	$.88 \times 10^{-6}$	.043	.774	11.24×10^{-4}	.086	3.097	17.99×10^{-3}	.172	12.390	.2879
10.5 microns	.049	.152	2.87×10^{-4}	.282	5.082	.317	.564	20.328	5.079	1.13	81.312	81.55

Notes: 1)   Assumes Scattering Volume completely determined by diffraction pattern of Scattered Light Collecting Lens.

2)   Assumes Scattering Volume is a cylinder, from which approximately 70% of the collected Scattered Light emanates.

LIST OF REFERENCES FOR SECTION 2.13

1.   Sommerfeld, A., <u>OPTICS, Lectures on Theoratical Physics</u>,
      Volume IV, Academic Press (N.Y. and London) (1964)

2.   Walther, Kingslake (Ed.) <u>Applied Optics and Optical
      Engineering</u>, Volume I, 271 (1965)

3.   Born, M., Wolf, E., <u>Principles of Optics</u>, 441 (1964 edition).

2.14 Scattering From Dilute Injectant Concentrations

As a preliminary investigation of the characteristics and de-
sirable parameters of various flow stream particle injectants,
Doppler shift measurements of light scattered from three different
kinds of injectant were made:

1) Smoke bombs, as made by E. Vernon Hill of Lake Geneva,
    Wisconsin.

2) Water droplets, as produced under varying feed-pressures
    and flow settings of the air-liquid spray nozzle supplied
    with water from the pressurized container, i.e., the
    system described in Section 2.15.

3) Teflon/Freon suspension made by the Miller-Stephenson,
    Company, Danbury, Connecticut, and injected using the pres-
    surized, stirred container and air-liquid nozzle of Section
    2.15.

4) As a reference, Doppler measurements of light scattered
    from a Scotchlite tape-faced wheel were made.

Without exception, each system had major shortcomings, as de-
scribed below, prompting a continuing search for better injectants,
and, of course, for an improved Laser Doppler Velocity instrument
having the capability of using light scattered from natural con-
taminants (dust, condensed water droplets, etc.) in the flow
stream.

A summary of the rather meager information gathered so far
on injectants appears in Table 2.14-1, with comparative data on a
knife edge and Scotchlite tape.

A promising further possibility, yet to be explored, is the
wide variety of controlled-size carbon particle dispersions (DAG-
dispersions) made by Acheson Colloids of Port Huron, Michigan.

TABLE 2.14-1

ABSOLUTE POWER OF LIGHT SCATTERED AT
12 DEGREES BY VARIOUS TARGETS AND MEDIA

Target or Medium	Laser Focused	Unfocused	Scattered Light Power at Photomultiplier Cathode Microwatts	Notes on Coherence, Judged on Width of Doppler Shift Peak on Spectrum Analyzer	Other Features
Knife Edge	X		2.35	--	Good line-up target
Light scattered in passing through 1/16 in. thick rotating fiberglass wheel	X		8.56	Fair to good	Good calibration and check-out target
Water jet from air-atomizing nozzle*	X X	X	1.17, minimum water 8.56, maximum water 1.94, maximum water	Very poor	--
50 psi air only, through air atom-izing nozzle	X		1.2×10^{-5}	Not discernible	--
Smoke in 6" x ½" wind tunnel, 150 fps. air	X		.417 maximum	Good	Very corrosive, and causes severe dis-comfort when inhaled
Teflon-freon suspension				No good data yet available	Good lubricity non-toxic, but settles out and clogs nozzle.

* Air atomizing nozzle made by Spraying Systems Company, Bellwood, Illinois
Catalog No. ¼ JN, Set-up #1

The problem should also be reviewed with research workers in aerosols technology.

A somewhat startling discovery was made in the case of water droplet and teflon particle injection. It was found that the scatterers were so dispersed that scattered light was received in a succession of discrete pulses, a most undesirable condition. These measurements and their implications in terms of signal processing are summarized below.

2.14.1 Considerations in the Selection of Scattering Injectants

One might consider that three essential factors govern the performance of a scattering injectant in relation to the operation of the Laser Doppler Velocity Instrument.

1) The scattering cross section, σ , of particles within the Scattering Volume, at the laser light wavelength and given polarization.

2) The particle concentration, N particles per unit volume, within the Scattering Volume should be large to avoid the "particle pulse counting" behavior as discovered in 2.14.3 below. An acceptable concentration can readily be calculated using the scattering volume dimensions given in the Table of Section 2.13, e.g., $(100)^3$ in 5×10^{-4} mm^3, i.e., 10^{10} particles $-$mm^{-3} for F22 lens, using an Argon laser (4880Å).

3) The coherence loss caused by random phase scattering should be minimal (the relationship with particle parameters has yet to be established, if it exists - Section 2.8).

2.14-3

4) The volume and mass (therefore the geometrical
    size) of the particles must be small, so that the
    particles partake in the gas motion without modi-
    fying the flow field.

5) The injectants should be non-corrosive and mech-
    anically harmless to machinery, such as pumps
    and compressors.

6) The injectant material (and vehicle if used)
    should be non-toxic.

7) The injectant should be easy to handle and inject.

8) The material should be cheap to prepare.

The product of the first two, that is $N\sigma$ multiplied
by the incident laser light intensity, determines the total
scattered light power, P_{sc}, in the Signal to Noise equation of
Section 2.6. The third determines the Coherence Loss Factor μ in
this equation. Background material on these parameters in general
has been given in earlier sections. From this point of view, the
problem of injectant choice would seem straightforward. The
stumbling block in the way of quick solution arises partly from
the dearth of the analytical and experimental data necessary,
and partly from the difficulty of identifying sources of inform-
ation, because the data are buried in widely scattered scientific
disciplines. For example, research into colloid chemistry, aero-
sols, atmospheric pollution, milling processes (e.g., flour,
cement), organic chemistry, electron microscopy, X-ray diffraction,
food technology and so forth undoubtedly can contribute much of
the needed information if one had time to collect it.

Given a promising injectant, analysis in the light of (1)
through (8) above is readily conducted, on the lines of calcul-

ations in Sections 2.1 and 2.5, supplemented by the wealth of analytical data compiled by Van der Hulst (1). The experimental measurements used in this report, based on Doppler Signal to Noise ratio as the criterion, provide a formal and explicit technique for comparison of injectant performance. Such data have been compiled for a calibration wheel (Section 2.18). It now remains to repeat the experiments for suitably chosen injectants.

2.14.2 Smoke Injection

The smoke from bombs made by E. Vernon Hill of Lake Geneva, Wisconsin, proved to be excellent for scattering measurements. All the data obtained with the Laser Doppler Velocity Instrument at the NASA Marshall Space Flight Center were obtained with its use.

This smoke injectant fails on counts (5) and (6) above. It is very corrosive, depositing an oily substance on surfaces over which it passes. Thus damage to apparatus and fogging up of windows occurs. As a result of its use on the NASA MSFC Seven Inch Wind Tunnel facility, the latter had to be shut down for several weeks to repair consequent damage. In use at Raytheon, if inhaled, it was found to cause severe soreness of the throat, which persisted for 48 hours after exposure. Care should therefore be exercised in using it to ensure adequate exhaust facilities. For this reason, an exhauster was added to the Raytheon tunnel so that the whole system operated at a pressure slightly below atmospheric.

2.14.3 Water Droplets

The air atomizing nozzle, supplied from a pressurized container, as described in Section 2.15, was used first to generate a spray of water droplets only. After proper adjustment of

air and water pressures, an apparently excellent water "fog" was obtained, and probed with the Laser Doppler Velocity Instrument. It was tried first in the low velocity nozzle facility at MSFC. The presence of the water injectant could be clearly seen by the formation of a very bright "pencil" where the laser beam passed through the air stream, although the water droplets themselves were not visible. S/N ratio as viewed on the spectrum analyzer was about 2/1. Smoke injectant under similar conditions gave a S/N ratio of about 5/1.

In an effort to determine the reason for the inferior performance with water, the atomizing nozzle was set up at Raytheon. Laser light scattering was studied both directly through the spray, and then with the nozzle spraying into the tunnel. It was thought that the reason for the loss in Coherent Signal to Noise ratio compared with smoke might have been because of differences in randomness of particle distribution, because of differences in uniformity of drop size (perhaps aglomeration), or because of actual differences in fluid turbulence caused by the different effects on the gas of particles of different sizes, densities, shapes and surface characteristics.

However, our laboratory measurements suggested a totally different reason. Figure 2.14-1 shows a succession of "single shot" exposures of photomultiplier output signals, photographed on the Tektronix 647 oscilloscope. Clearly, only a few, perhaps one or two water droplets were in the scattering volume seen by the photomultiplier at any instant. The volume was approximately defined by the diameter of the first Airy circle, and depth of the focal region (Section 2.13). These two dimensions were 0.003 centimeters and 0.1 centimeter for the F25 light collecting lens and 6300 Angstrom wavelength used in the
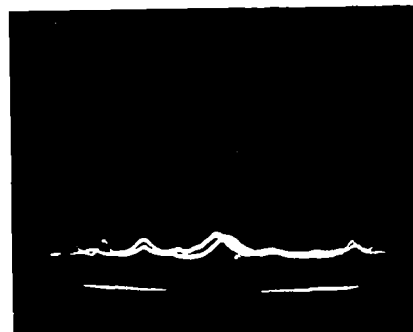
① Time Between Drop

② "Size" of Drop

10mV/cm

0.5 μsec/cm

10mV/cm

0.5 μsec/cm

10mV/cm

1mV/cm

1 μsec/cm

1st drop triggers sweep   2nd drop is displayed

Nozzle Pressure: ≈ 0.13 inches water
Photomultiplier Volts: 750 V
Anode Load: 72 ohms
Peak Light Power: ≈ 5 microwatts

Test Section Pressure: 1.5 inches water
Photomultiplier Volts: 750 V
Anode Load: 72 ohms

(a) Laser Beam in Direct Water
     Spray from Air-Atomizing Nozzle

(b) Laser Beam in Direct Water
     Spray from Air-Atomizing Nozzle

(c) Laser Beam Passing Through
     Raytheon Wind Tunnel Test Section,
     Water Sprayed in Before Smoothing
     Section, From Air-Atomizing
     Nozzle

Figure 2.14-1 Single-Shot Oscillograms of Scattered
              Light Pulses Produced by Water Drop-
              lets Passing Through 50MW He-Ne
              Laser Beam

experiment.

Thus we had a "sampling" system, with the photomultiplier
responding to a random train of pulsed wave trains of scattered
light. The effect of the sampling was to broaden the Doppler
frequency band as displayed on the spectrum analyzer. Inspection
of the oscillogram pulses in Figure 2.14-1 showed that, with a
pitot tube - measured spray velocity of 150 ft/sec., the water
droplets were about 5-10 microns in diameter, and about 25 to
400 microns, i.e., 5 to 40 diameters, apart (using the oscillo-
gram time scale).

In spectrum-analyzing the series of scattered-light
pulses, a spectrum of width $\frac{1}{\tau}$ is produced, where τ seconds is the
time duration of the pulse envelope containing the scattered light
heterodyne frequency. Furthermore, this spectrum is only sampled
at time intervals of T seconds, where T is the time for a particle
to traverse the separation distance between particles. This means
that the spectrum of width $1/\tau$ is split into a series of spikes
separated by $\frac{1}{T}$, the envelope of the spikes forming the $\frac{1}{\tau}$ spectrum
width. The total effect is to give a broad spectrum, which since
its energy is widely spread, is essentially obscured by the white
noise background.

With these relative particle sizes, particle separations
and wavelengths, the signal processing problem is analogous to
that encountered in a pulsed Doppler radar system. Presumably
sophisticated electronic techniques developed in this field could
be used in our problem, if no better injectant could be found.

Relevant to the calculation of particle scattering cross
section (1), it is of interest to note that here we have ka $\approx$ 60,

where k = Wave Number $=\frac{2\pi}{\lambda}$, a = particle radius, λ = laser wavelength.

Some suggestion of a doppler frequency spectrum was observed with air only. However, this was believed actually to be caused by random phase and amplitude (not Doppler shift) changes through a highly turbulent, inhomogeneous gas.

2.14.4 Teflon-Freon Suspension

Using the injection system described in Section 2.15, a teflon-freon suspension was given preliminary trials as an injectant. Based on detailed aerosol particle size distribution measurements by the Illinois Institute of Technology·Research Institute (2) this mixture, prepared by Mr. Stephenson of the Miller-Stephenson Company, Danbury, Connecticut, showed good promise. The particle size was mostly below 2 microns in size (detailed distribution in reference 2), teflon has good lubricity, it is chemically very inert, and the freon used evaporated rapidly and was non-toxic.

Extensive tests have not yet been made with this material. Preliminary runs indicate the following application problems:

1) The teflon settles out rapidly (in a minute or two after thorough mixing). This problem may be eliminated by continuous agitation and pump-around.

2) Hence it rather rapidly clogs the atomizing nozzle, in the absence of a pump-around system. Again, higher pressures on the atomizing air may help resolve the difficulty.

3) Some tendency to cling to the walls of the chamber is evidenced, perhaps because of static charge

2.14-9

build-up. Here, the solution may be to use con-
ducting coatings on the viewing windows (Dupont
Corporation, Wilmington, Delaware).

4) The cost is rather, though not prohibitively, high
-$60 per gallon.

In view of the otherwise excellent attributes of this
slurry, further investigation, is recommended, directed towards
overcoming the problems listed.

2.14.5 Scotchlite Tape Wheel Measurements

As a reference figure, the heterodyne signal to noise
ratio of light scattered from a rotating wheeel, faced with writing
paper on top of Scotchlite tape was measured. This diffuse scat-
tering introduced a coherence loss, μ, of about 35 decibels. This
agreed reasonably well with calculated diffuse target loss (3).
Coherence losses caused by lenses appeared to be virtually neg-
ligible.

REFERENCES FOR SECTION 2.14

1. Van der Hulst, H. C., <u>Light Scattering by Small Particles</u>, John Wiley and Sons, Inc. (1957).

2. Prosser, D. W., Fisher, M. J., "Optical Measurement with High Temporal and Spatial Resolution", IITRI Report #M6114-28 (Oct. 10, 1966).

3. Born and Wolf, <u>Principles of Optics</u>, the MacMillan Company, N. Y., 2nd Edition (1964).

2.15 Design, Construction and Calibration of the Subsonic Wind Tunnel

For parametric investigation of the Laser Doppler Velocity Instrument system and for measurements on a standard test section at subsonic speeds, a wind tunnel was designed and constructed and is described in detail in the following section. Calibration measurements will follow in a subsequent report, at the same time as tunnel flow measurements are presented.

2.15.1 Tunnel Design and Construction

Since the primary purpose of the tunnel was the investigation of the flow instrument and not the fluid dynamic research, the apparatus was designed and constructed as quickly and economically as possible. Design and construction, including necessary drawings, took about one and a half weeks, and construction about three weeks. Readily available standard materials were used throughout. Supporting structure was build of Dexion, air conditioning duct components were used wherever possible, and respectively.

Figure 2.15-1 is a photograph of the test section, manometers, and flow straightening section. Figure 2.15-2 shows the compressor, smoke bomb and slurry injection systems, the controls for the flow of recirculating and exhaust air. An exhauster was also used to aid in control of tunnel static pressure, but is not shown in the photographs. The compressor was purchased especially for the tunnel, and the exhauster was obtained from an old industrial vacuum cleaner.

In designing the tunnel, a brief literature search was conducted, the important references being listed in References (1) through (20). To preserve simplicity in flow, it was decided, after consultation with the NASA Contract Monitor,
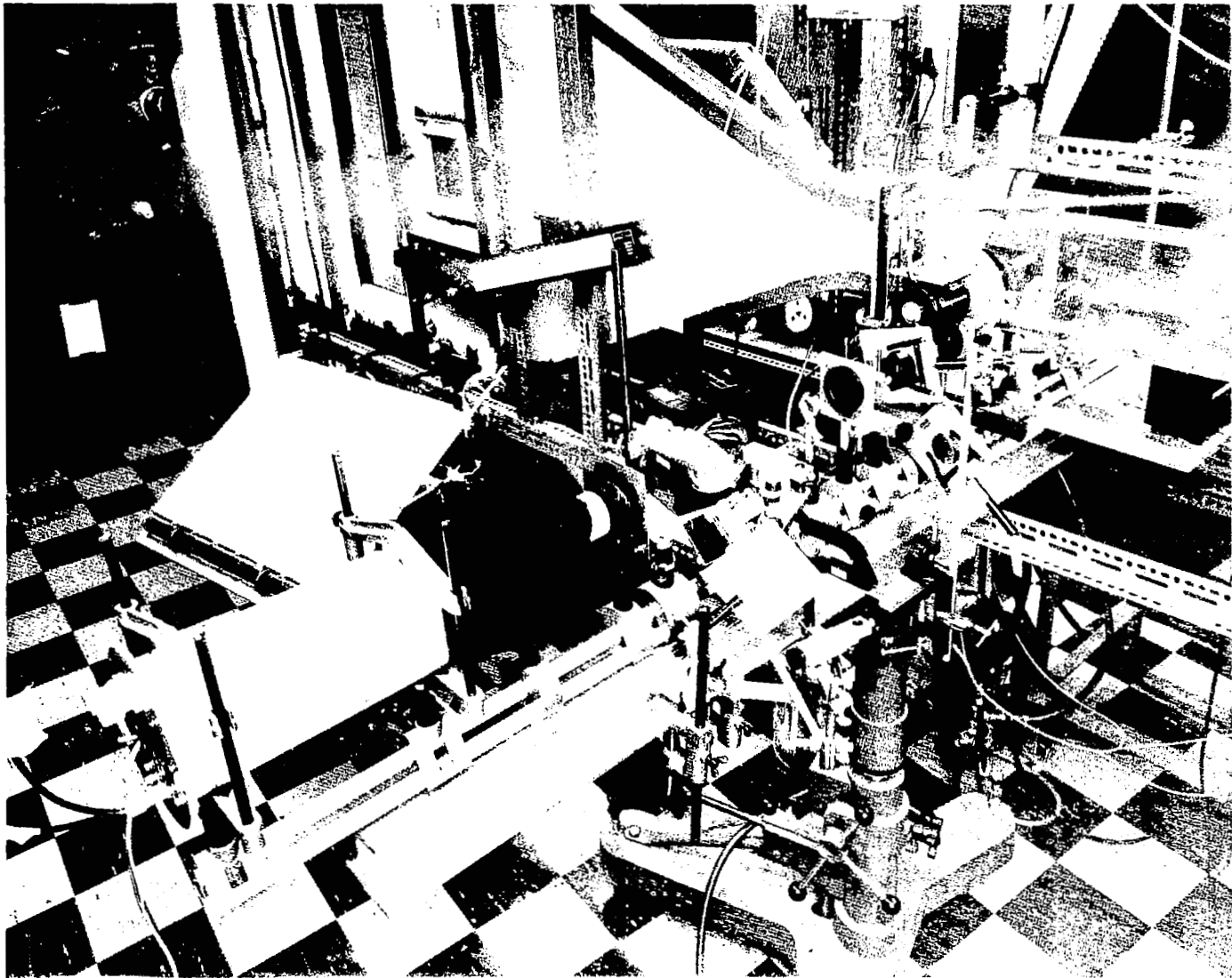
2.15-1

Figure 2.15-1   Photograph of Subsonic Wind Tunnel showing Test Section,
                Manometers, and Flow Straightening Section
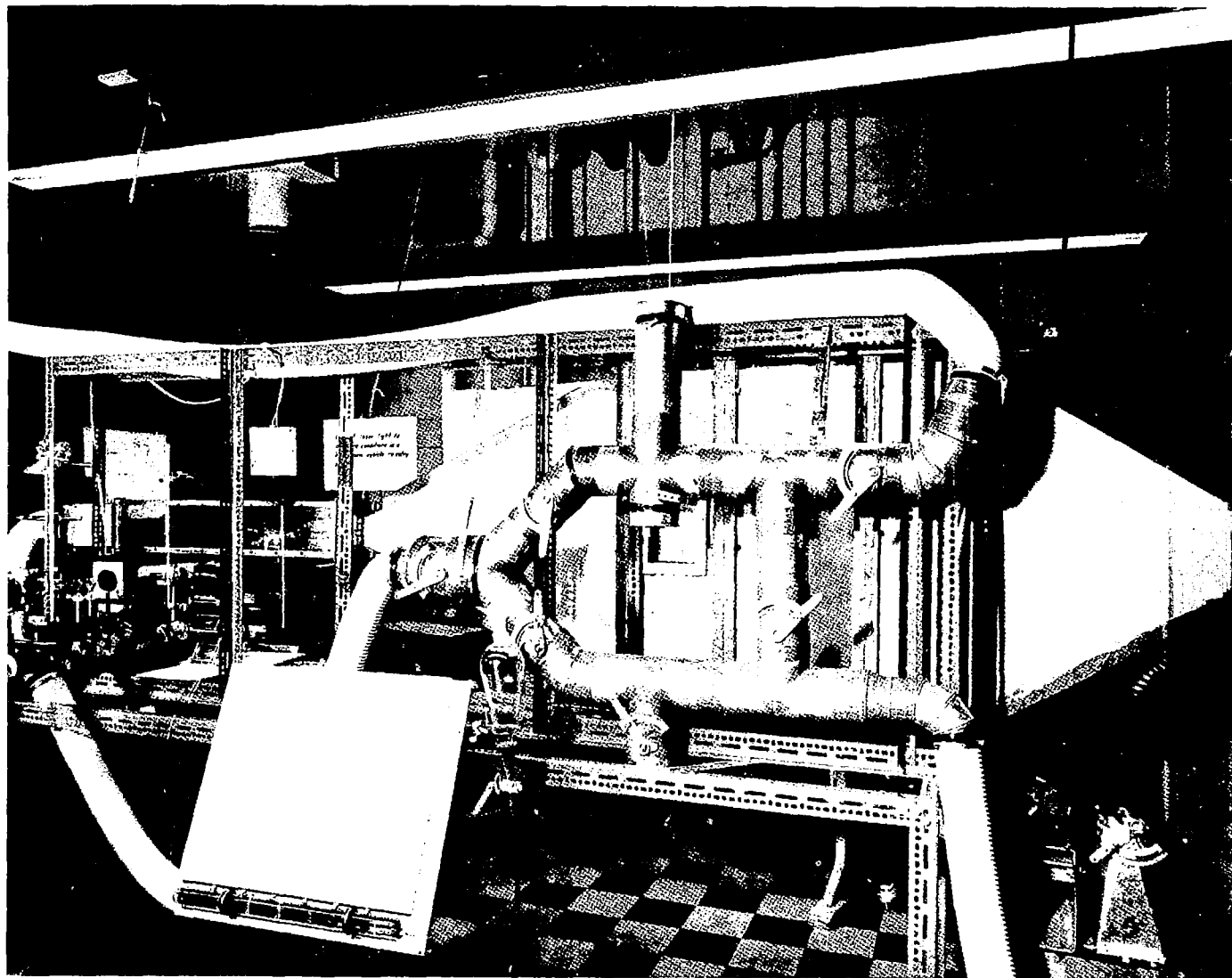
Figure 2.15-2 Photograph of Subsonic Wind Tunnel showing Compressor,
Smoke Bomb and Slurry Injection Systems, Flow and
Mixing Controls

Mr. Milton Huffaker of the George C. Marshall Space Flight Center, to use a test section designed to produce substantially two-dimensional flow. The test section design and operating conditions followed the work of Laufer (1,2,3). Notes on the design of the various sections are given below. Figure 2.15-3 is a schematic diagram of the tunnel showing the principal operating parameters.

2.15.1.1 Test Section

In accordance with Laufer (1), the aspect ratio of the test section was chosen to be 12:1. The overall length was selected to allow 50 channel widths from the entrance to the test section, a test section several channel widths long, followed by a smooth section 24 channel widths long. A drawing of the test section appears in Figure 2.15.4. Again in line with Laufer's operating conditions, a Reynold's number of about 12,300 was chosen for the test section.

These specifications determined the test section relative proportions. Actual dimensions were chosen by trying several different test section widths, calculating velocity and mass flow using the 12,300 Reynold's number and estimating the total pressure drop throughout the remainder of the system. From these data the required compressor performance could be calculated. The test section dimensions were then settled by choosing a readily available and economically priced compressor.

The two equations used for the calculation were as follows:

$$R_e = \frac{DU\rho}{\mu} \, , \tag{1}$$

$$\dot{m} = \rho AU \, , \tag{2}$$
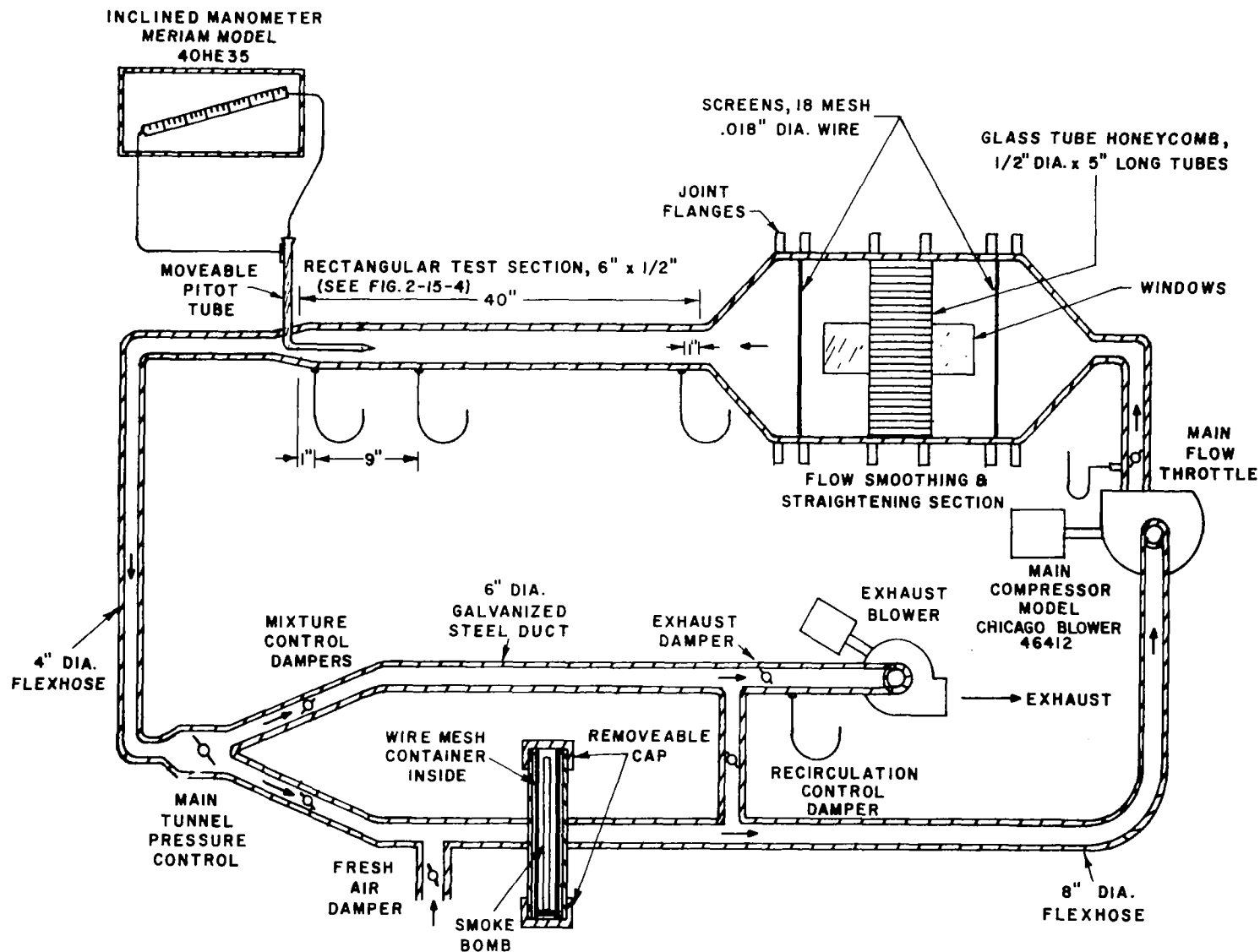
Figure 2.15-3   Raytheon Subsonic Wind Tunnel Pictorial Diagram and Principal
Parameters

Figure 2.15-4 Detailed Drawing of Subsonic
Tunnel Rectangular Test Section

where   U = mean velocity
            ρ = density
            μ = viscosity   } in consistent units
            D = test section width
            R_e = Reynold's number (dimensionless)
            $\dot{m}$ = mass flow rate
            A = test section cross sectional area

It will readily be seen that for a given Reynold's number, a relationship can be established between mass flow rate and test section width by suitable elimination between the two equations, on the assumption that pressure in the test section is atmospheric, and that the 12:1 aspect ratio in the test section is used.

A test section width of ½ inch was finally selected. This and other operating parameters are compared with those of Laufer in Table 2.15-1.

It will be noted that with a velocity of 90 ft/sec in the test section, the Reynold's number for flow through the section is about 12,300, corresponding to Laufer's measurements (1).

2.15.1.2   Flow Straightening and Smoothing Section

An essential requirement of the tunnel, both from the point of view of consistent measurements and of correspondence with Laufer's results, was that flow in the test section would be initially smooth and laminar, changing in a consistent and stable manner to fully developed turbulence as the air passed along through the section. Since any flow irregularities or disturbances will travel upstream against the gas flow at the speed of sound, this requirement was in some respects more difficult to meet in a subsonic wind tunnel than in a supersonic system. A very substantial body of literature exists on methods of achieving correct flow conditions in subsonic wind tunnel test sections (4, 5, 6, 7, 9, 15). The design basis for

2.15-7

TABLE 2.15-1

COMPARISON OF TUNNEL DESIGN PARAMETERS WITH THOSE OF LAUFER (REF. 1)

Parameter	Raytheon Subsonic Test Section Design Parameters	Laufer's Subsonic Test Section Parameters
Length	40 ins.	192 ins.
Width ($\equiv$ 2d)	½ in.	5 ins.
Height	6 ins.	60 ins.
Aspect Ratio	12	12
Distance (x) Test Point to Exit (Range)	1 in. – 10 ins.	2 ins. – 62.5 ins.
Ratio $\frac{x}{d}$	2 – 20	1 – 25
Distance (x') Entrance to Test Point (Range)	30 ins. – 39 ins.	129.5 ins. – 190 ins.
Ratio $\frac{x'}{d}$	60 – 78	51.8 – 76
Scale of Turbulence	To be measured	0.49 ins.
Max. Mean Velocity (in-sec^{-1})	300 1,080 1,200 1,800	183 295 590
Reynold's Number	3,400 12,300 13,600 20,400	12,300 30,800 61,600
Absolute Pressure at Test Section	Approx. 1 atmos.	Approx. 1 atmos.
Absolute Temperature at Test Section	300° K approx.	300° K approx.

the smoothing section used in this tunnel was developed after extensive study of these and other references.

Although, as already mentioned, the importance of careful design downstream of the test section must be stressed in a subsonic tunnel, for reasons of economy, and based on judgment developed from the literature background, the elimination of disturbances traveling upstream from the compressor was achieved rather simply. It was done by using a fairly long corrugated and flexible large-diameter hose between the rectangular-to-circular adaptor at the end of the test section and the compressor. It was expected that any flow pulsations or noise would be damped out by this arrangement. So far as can be ascertained from our measurements, this appears to have been the case.

As will be seen in Figure 2.15-3, the flow straightening and smoothing section consisted of a diffuser (or expansion section) which reduced the gas velocity to a low magnitude, leading to a smoothing section of large cross-section in which was placed a fine mesh screen, followed by a honeycomb, followed by a further fine mesh screen. The same aspect ratio was used for the diffusing section as for the test section. Literature search showed that the provision of additional screens, used by some experimenters, gave doubtful further advantages in our case. As seen in Figures 2.15-1 and 2.15-2 the smoothing section was built in sections which could be dismantled for cleaning or inspection. One side of the smoothing section was removable to expose the honeycomb for cleaning. Ample windows in either side of the smoothing section permitted inspection of the flow when made visible by a suitable injectant.

2.15.1.3 Screens

The purpose of screens in the smoothing section is to shed small scale turbulence which decays rapidly.

The intensity of incoming turbulence to a single screen is reduced by a factor of

$$f = \frac{1}{\sqrt{1 + k}} \quad , \tag{3}$$

For n screens together,

$$f = \frac{1}{(1 + k)^{n/2}} \tag{4}$$

where k is the pressure drop coefficient for the screen, i.e., the ratio of the pressure drop across the screen to the mean kinetic energy density in the flow; so that

$$k = \frac{\Delta p \text{ (screen)}}{\frac{1}{2} \rho U^2} \quad . \tag{5}$$

The parameter k is given by

$$k = \frac{1 - b}{b^2} \tag{6}$$

where   b = solidarity ratio

         = area of the holes per unit area of screen

         = $(1 - md)^2$

for square mesh screen, with wire of diameter d and mesh designation m.

Each screen introduces a small scale turbulence, unless the Reynold's number is low (less than 30 to 60). This turbulence decays very rapidly because of the viscosity of the gas. The low velocity in the flow stilling section allows sufficient residence time for this decay process to occur.

The formulae show that it is advisable to use two or more screens of coarser mesh rather than one of fine mesh, to reduce the turbulence in the tunnel without creating a large pressure drop (4). As shown in Figure 2.15-3, two screens were chosen of mesh m = 18, wire diameter .011 inches and k therefore equal to

.897. A Δp across each screen of approximately 2.16 inches of water was estimated.

2.15.1.4 Honeycomb

Flow straightening was achieved by the inclusion of a honeycomb between the two screens. The honeycomb consisted of 13 millimeter diameter glass tubing, each piece of tubing being 5 inches long, stacked into the stilling section. At flow rates of 100 ft/second, it was estimated that the pressure drop across the honeycomb would be negligible. The glass tubes were assembled into a honeycomb by making one side of the tunnel removable. The U-shaped remaining portion of the tunnel was then used as an assembly form, after lining the walls with a thin sheet of plastic to avoid having the honeycomb stick to the wall. A dab of glue on each tube before laying into the form resulted in a solid honeycomb structure.

2.15.1.5 Diffuser (Expansion Section)

The diffuser or expansion section contained flow straightening vanes as recommended by Dryden and Abbott (4), to minimize separation of the boundary layer from the walls. The diffuser opened into the large cross-section of the stilling section. The effect of diffusers has been studied by Pash and Bailey (5) and by Tucker (6).

2.15.1.6 Contraction

A smooth contraction connected the smoothing section to the test section. If one assumes that this section added no turbulence to the flow, then the ratio of turbulent velocity to mean velocity would decrease as the flow accelerated through the contraction. The design of the contraction section was somewhat arbitrary, and was subsequently criticized by Professor P.O.A.L. Davis of Southampton (England) University. He pointed out that because of the rather high second differential of transverse dimension with respect to distance travelled through

the section, it would be expected that either asymmetric or unstable flow might occur in the test section. After construction, careful Pitot tube profiles of velocity at the end of the test section showed his predictions unfortunately to be true. The flow was not unstable, but was asymmetric, as will be seen in curves to appear in a later report on tunnel measurements. A redesign of this contraction section is being considered, although the change will be deferred until flow measurements have been made with the Laser Doppler Velocity Instrument.

2.15.2 Wind Tunnel Instrumentation

Instrumentation used to map the test section flow pattern and to monitor operation was relatively simple. A multi-point static pressure manometer was connected to 3 points down the test section, and to other key points in the system. The multi-point manometer was constructed of glass and other simple materials in the laboratory. Its angle of tilt and reference reservoir level could be varied to suit different flow conditions. Water with coloring agent and wetting additives (purchased from Meriam Instrument Corp.) were used in the manometer. For the Pitot tube differential pressure, a Meriam Model 40HE35WM inclined tube manometer was used. These instruments can be seen in Figure 2.15-1.

A Dwyer Manufacturing Company .047-inch I.D. Pitot tube was used for making velocity profile measurements in the test section. The vertical and horizontal traverses were made near the exit only, for reasons of convenience in construction. The Pitot tube was mounted in a gland in the exit adaptor duct, and its tip projected 0.75 inches up into the test section. Vertical traverse was made by sliding the tube in and out of the gland nut, and horizontal traverses by rotating the tube around the vertical center line of the gland nut. Since the Pitot tube tip was three inches long and the tunnel only ½ inch wide, the effects of change of angle presented by the air flow to the Pitot tube as it

traversed horizontally was neglected. Measurements reasonably
close to the walls could be made, since the Pitot tube was only
0.120 inches overall outside diameter.

2.15.3 Flow Control and Injectant System

The schematic diagram 2.15-3 shows the tunnel flow
and injectant control arrangements. The injectant is inserted
through the removable cap. Suitable manipulation of valves en-
able one to mix in varying proportions of injectant, and to
operate the tunnel system in any combination of conditions from
full recirculating to full flow-through.

Two injectant materials have been investigated so far. The
first, a smoke bomb, has been used in all Tunnel and Jet Doppler
flow measurements to date. The second, a teflon-freon dust sus-
pension, is under development. The smoke bombs are made by the
E. Vernon Hill Company, P. O. Box 189, Lake Geneva, Wisconsin.
They are obtainable in ½, 1, 2, 3, 5, and 8 minute sizes and are
ignited by a fuse at one or both ends. The smoke generated has
good laser light scattering characteristics at 6328 and 4880 $\overset{\circ}{\text{A}}$,
i.e., a large cross-section, high concentration, and good coher-
ence properties. The serious drawbacks to the smoke, however, are
that it leaves a very corrosive tar-like deposit in the system,
and it causes very unpleasant and lasting (48 hours) soreness
of the throat if breathed in for more than a few seconds. For
this reason, an alternative is essential.

A teflon dust suspension is now being investigaged. Teflon
has the strong advantages that it is chemically very inactive,
and furthermore, has a high lubricity. Thus, provided it is used
in particles of size much less than mechanical clearances in com-
pressors and exhausters, its effect on vacuum pumps and other
machinery used in Wind Tunnel installations should be minimal.

Following detailed studies of the parameters of teflon-freon
aerosols by IITRI (22), it was planned to use them as tunnel in-
jectants.

IITRI performed rather complete measurements of particle size distributions and slurry parameters. Their measurements gave particle size distributions for several different teflon-freon Aerosols. Number MS138D aerosol, manufactured by the Miller-Stephenson Company of Danbury, Conn. was selected for our experiments. IITRI data shows that 75% of the particles are less than two microns in size.

In use, the freon rapidly evaporates, leaving a fine suspension of teflon dust. Characteristics of teflon suspensions are reviewed analytically in 2.14, and preliminary experimental data are presented.

After trying several different injection nozzle systems, a nozzle with air pressure atomization was selected from a comprehensive range of nozzles made by the Spraying Systems Company, 3201 Randolph Street, Bellwood, Illinois. The nozzle used was type 1/4 JN with set up #11 inserts. Two inlet connections were provided, one for pressurized teflon-freon slurry, and one for air as shown in Figure 2.15-5. Operating pressure ranges for each inlet were about 0-100 psig. The teflon-freon slurry was maintained in suspension and pressurized by placing it in a Paasche Air Brush Corp. ASME pressure paint tank of 3 gallons capacity. It was equipped with an air-motor-driven propeller stirrer, and pressure regulator. Figure 2.15-6 is a photograph of the system major components.

The system worked well at high flow rates. At low flow rates, the nozzle tended to clog because the teflon settled out of the slurry. Separate tests on the slurry showed that it would substantially settle out in two to three minutes if not continuously stirred. For future operation of this system it is therefore planned to modify it, as in Figure 2.15-5, by providing a continuous slurry pump-around circuit right up to the nozzle. By locating the pump close to the nozzle, system injection can be made at much higher pressures than required in the pressurized container
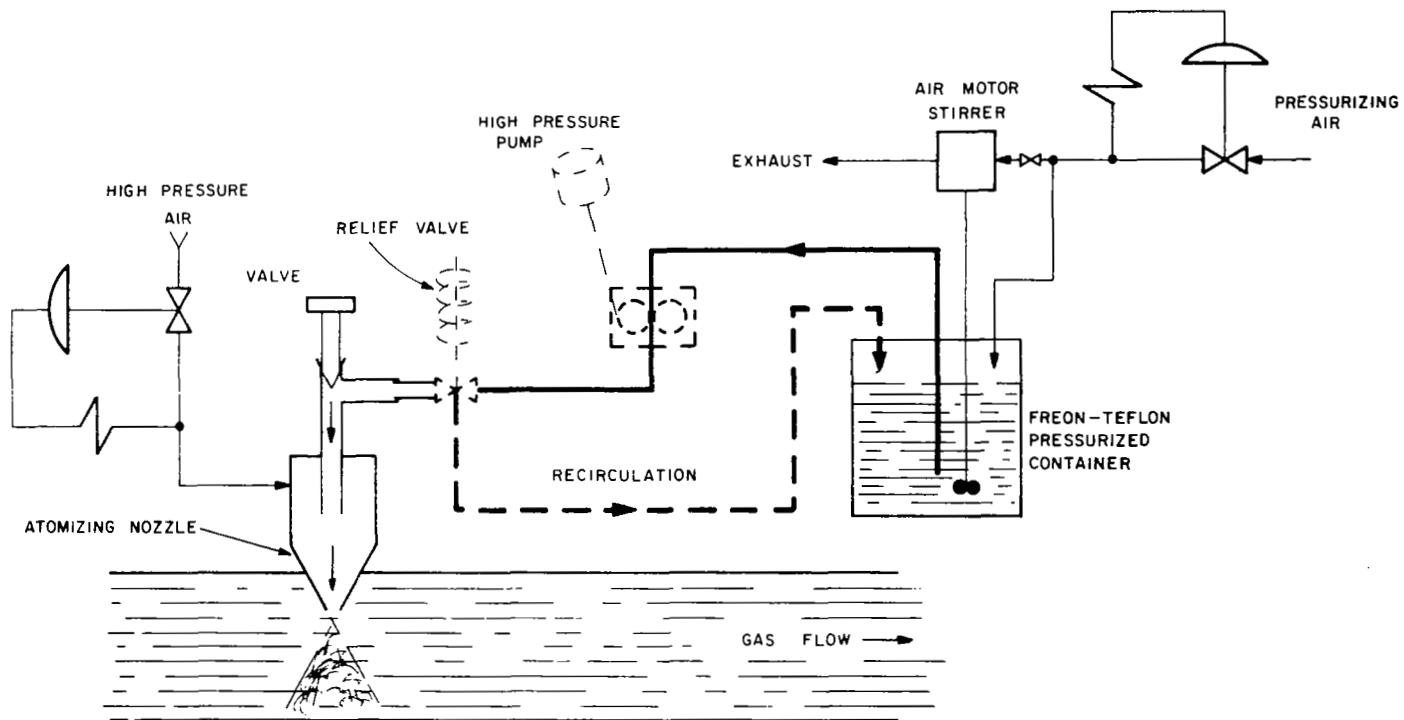
Figure 2.15-5   Diagram of Slurry Pressurization, Flow Control, and
Atomizing Injection System
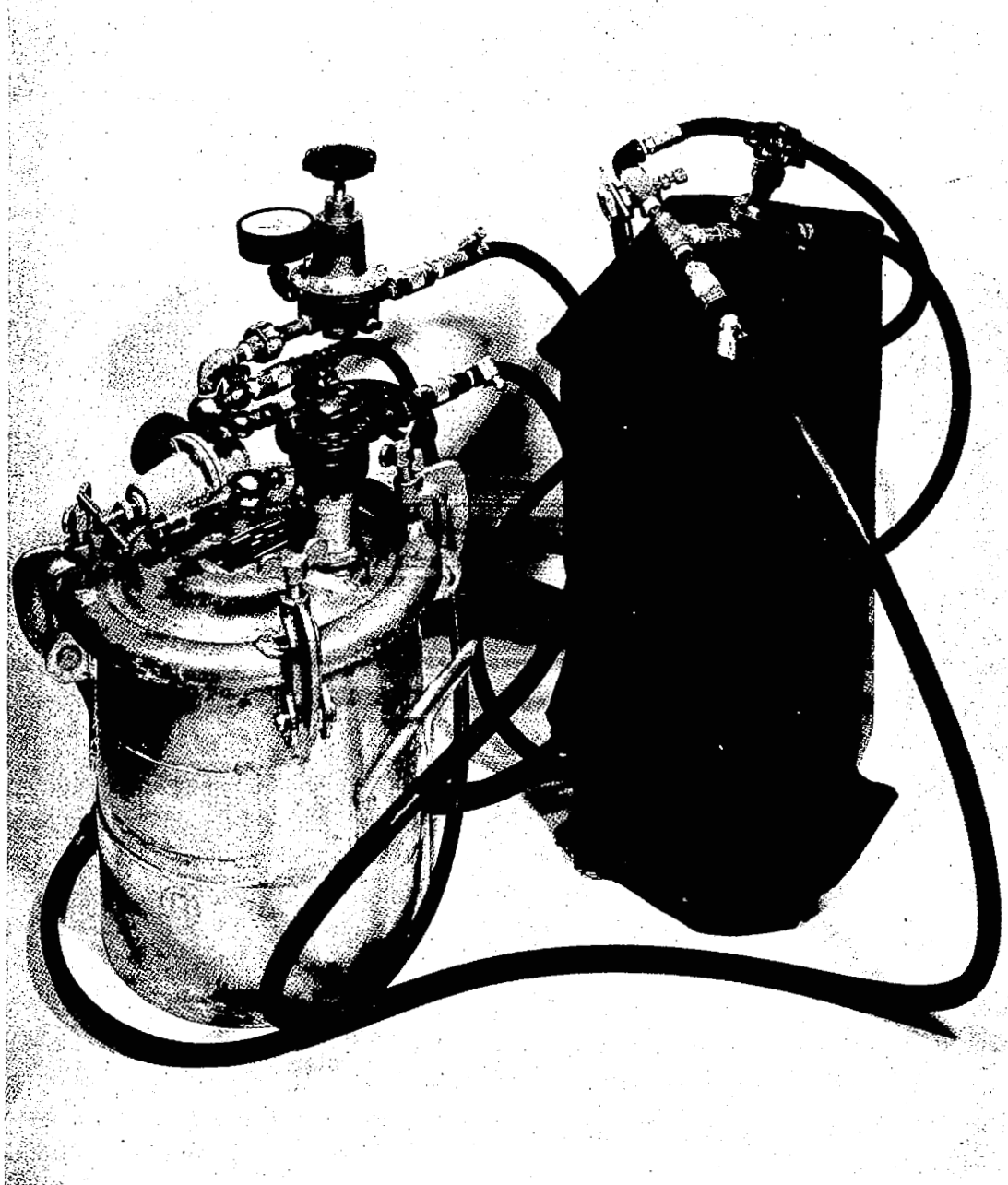
Figure 2.15-6   Photograph of Injectant Slurry Pressurized
Container and Atomizing Nozzle

and feed and return piping system. This arrangement will be advantageous and perhaps necessary for injectant addition to large high-pressure wind tunnel and jet systems.

REFERENCES FOR SECTION 2.15

1. Laufer, J., "Investigation of Turbulent Flow in a Two-
    Dimensional Channel", NACA Technical Note 2123 (1950).

2. Laufer, J., "Investigation of Turbulent Flow in a Two-
    Dimensional Channel", NACA Report 1053, Formerly TN 2123
    (1951).

3. Laufer, J., "Structure of Turbulence in Fully Developed
    Pipe Flow", NACA Report 1174, Formerly TN 2954 (1954).

4. Dryden, H.L., and Abbott, I.H., "The Design of Low Turbu-
    lence Wind Tunnels", NACA Report 940 (1949).

5. Parsh, J., and B.M. Bailey, B.M., "Effect of Surfacr Rough-
    ness over the Downstream Region of a 23° Conical Diffuser",
    NACA Technical Note 3066 (1954).

6. Tucker, M., "Combined Effort of Damping Screens and Stream
    Convergence on Turbulence", NACA Technical Note 2878 (1953).

7. Parsh, J., "The Effect of Surface Roughness on the Per-
    formance of a 23° Conical Diffuser at Subsonic Mach Numbers",
    NACA RM L51K09 (January 1952).

8. Wood, "Preliminary Investigation of the Effects of Rectang-
    ular Vortex Generators on the Performance of a Short 1.9:1
    Straight-Wall Annular Diffuser", NACA RM L51G09 (Oct. 1951).

9. Dryden and Abbott, "The Design of Low Turbulence Wind
    Tunnels", NACA TR 940 (1949).

10. Deissler and Taylor, "Analysis of Turbulent Flow and Heat
    Transfer in Non-Circular Passages", NACA TN 4384 (Sept. 1958).

11. Mills et al., "Turbulence and Temperature Fluctuations Behind
    a Heated Grid", NACA TN 4288 (August 1958).

12. Wood and Higginbotham, "Performance Characteristics of a 24°
    Straight-Outer-Wall Annular-Diffuser-Tailpipe Combination
    Utilizing Rectangular Vortex Generators for Flow Control",
    NACA RM L53H17a (October 1953).

REFERENCES FOR SECTION 2.15 (Cont'd)

13. Wood and Higginbotham, "Influence of Vortex Generators on the Performance of a Short 1.9:1 Straight-Wall Annular Diffuser with a Whirling Inlet Flow", NACA RM L52L01a (February 1953).

14. Wood and Higginbotham, "Effects of Diffuser and Center Body Length on Performance of Annular Diffusers with Constant-Diameter Outer Walls and with Vortex-Generator Flow Controls", NACA RM L54G21 (September 1954).

15. Browand, F.K., "An Experimental Investigation of the Instability of an Incompressible Separated Shear Layer", Ph.D. Thesis, MIT Department of Aeronautics and Astronautics (January 1965).

16. Valentine and Carroll, "Effects of Several Arrangements of Rectangular Vortex Generators on the Static-Pressure Rise through a Short 2:1 Diffuser", NACA RM L50L04 (Feb. 20, 1951).

17. Kofskey and Allen, "Smoke Study of Nozzle Secondary Flows in a Low Speed Turbine", NACA TN 3260 (November 1954).

18. Deissler, "Analytical and Experimental Investigation of Adiabatic Turbulent Flow in Smooth Tubes", NACA TN 2130 (July 1950).

19. Ukurad, "Laws of Flow in Rough Pipes", NACA TM 1292 (November 1950).

20. Nakofski, "Charts for Analysis of Flow in Whirling Duct", NACA TN 3950 (May 1957).

21. Prof. P.O.A.L. Davies, "Private Communication", University of Southampton, England.

22. Prosser, D.W., Fisher, M.J., "Optical Measurements with High Temporal and Spatial Resolution", IITRI Report No. M6114-28 (October 10, 1966).

23. Prandtl "Report on Investigation of Developed Turbulence", NACA TM 1231 (September 1949).

2.16 Design, Construction and Alignment of the Experimental Laser Doppler Flowmeter System

Figure 2.16-1 is a diagram of experimental Laser Doppler Flowmeter and Wind Tunnel system set-up in the Raytheon laboratories at Sudbury, Massachusetts. As seen in Figure 2.16-2, the detector and preamplifier assembly and the bulk of the optical components were mounted on a single triangular optical bench rail, which in turn was bolted to an aluminum I-beam whose top and bottom surfaces were ground flat. The I-beam, in turn, was supported on a Keuffel and Esser Optical Tooling Stand, whose top could be rotated, or translated a few inches with a fine-thread screw. The stand could be raised or lowered by a capstan-rack-and-pinion mechanism, and locked in any position. Its base was supported and levelled by three jacking screws, and it could be moved about by lowering three castor wheels. This arrangement permitted ready adjustment of the laser scattering volume location, and of the scattering angle.

The laser, a Spectra-Physics Model 125, was mounted on a firm bench parallel with the wind tunnel. Two directional mirrors, fastened to CENCO scissor-jack stands, permitted ready focussing of the laser beam on to the scattering target or gas volume. With the exception of the laser and the first mirror, all other optical components were mounted on the optical bench, clamped to the I-beam, or clamped on to a flat plate fastened between the I-beam and optical bench at the laser end of the system. Thus, except for the laser and first mirror, the whole optical set-up was movable as a unit on the K. and E. stand.

Referring to Figure 2.16-1, light from the laser via the directing mirrors passed through a beam splitter to provide the
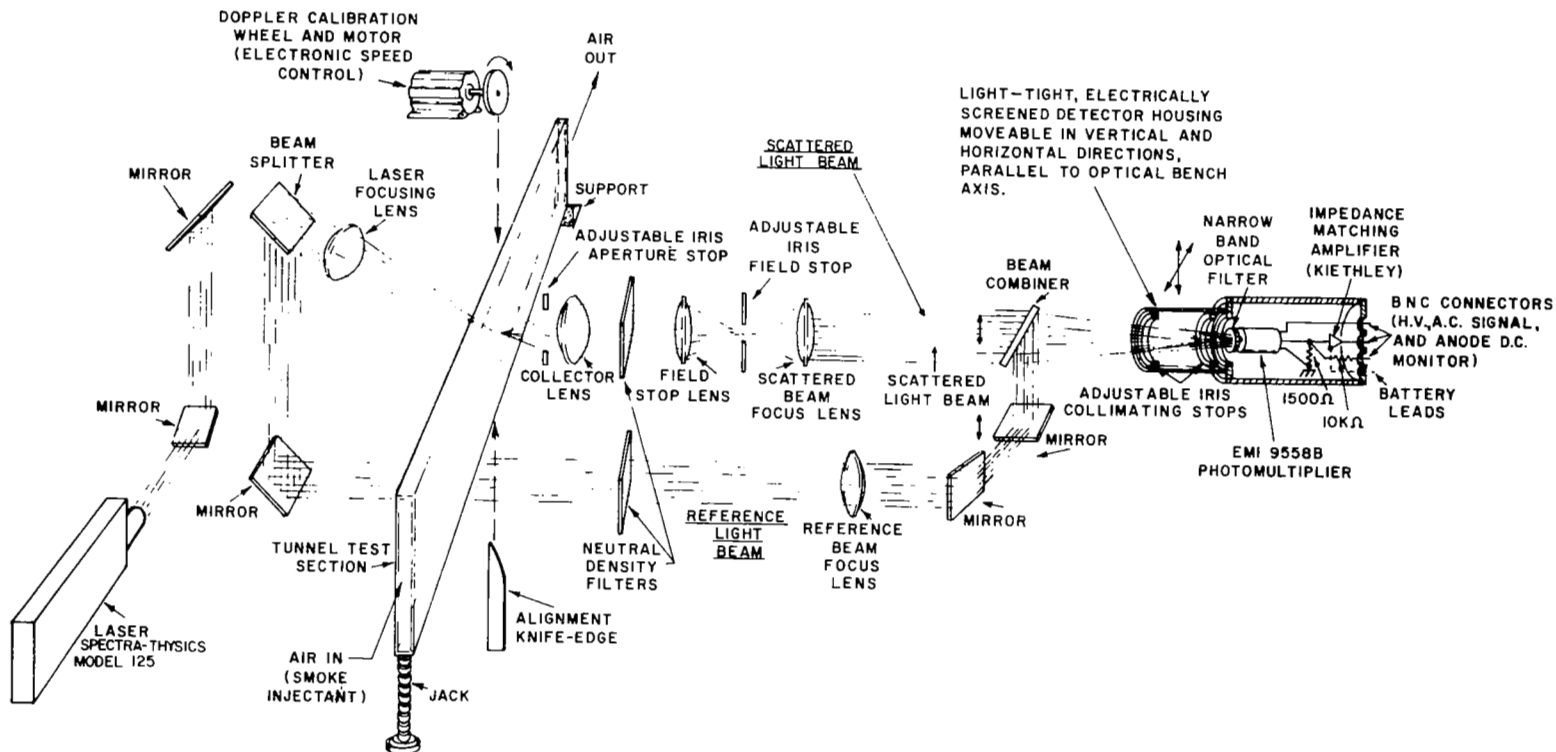
Figure 2.16-1 - Pictorial Diagram of Experimental Laser Doppler Flowmeter System
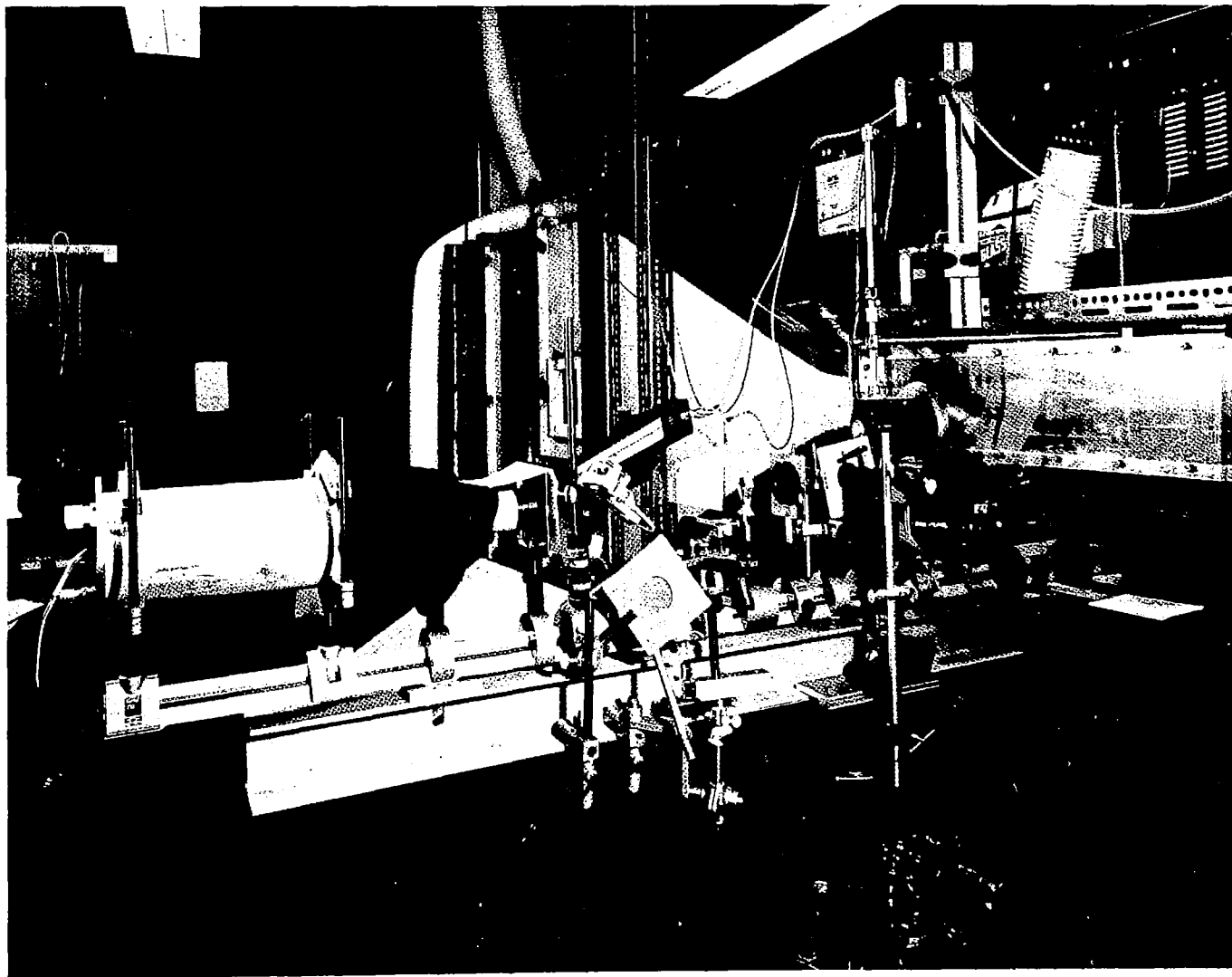
Figure 2.16-2   Photograph of the Laboratory Laser Doppler Flowmeter Experimental
Setup, showing Photomultiplier Housing, Optical Bench and Compo-
nents, Wind Tunnel, and Air Velocity and Pressure Instruments

Reference beam, then focussed on to the scattering volume or target. It was decided to bypass the Reference beam around the tunnel in this system to avoid its variable extinction by the tunnel gas or target, during precise signal to noise measurements and exploration of heterodyning parameters.

Scattered light, at the chosen angle set by the direction of the optical bench axis, passed through an adjustable iris aperture stop into a collecting lens, whose distance from the scattering volume was chosen to be its focal length. Parallel light emerging from the collecting lens passed through a second lens, coming to a focus in the plane of an adjustable iris field stop. With this arrangement, the collector lens and its focal point could be moved along the optical bench axis for a transverse tunnel scan without disturbing the lineup of the remainder of the optical system. While this scanning facility was not essential for the laboratory system, it was used for convenience in the 3-D system design, so that an operational check in the laboratory was desirable.

The use of a field stop has some important advantages. Besides rejecting unwanted and extraneous light, it selects the location and cross-sectional area of the total light passing through the focal plane of the collector lens (also the location of the scattering target or volume) which will reach the plane of the detector. Analysis and experiments (1) have also demonstrated that the field stop is selective in depth, so that light scattered at points along the optical axis on either side of the collector focal plane is rejected entirely, or strongly attenuated, compared with light scattered from a target exactly in the collector lens focal plane. The apertures represented by the

various lenses along the system also operate to reject light not emerging from the focal point in the collector lens focal plane. Figure 2.16-3 illustrates this selection process. Reference (2) contains a very useful chapter on the geometrical analysis of the various types of optical stops and apertures, and their functional differences.

Light emerging from the field stop was focussed through a beam combiner on to the active cathode surface of an EMI 9558B photomultiplier. The reference beam was also focussed, via a mirror and the beam combiner, on to the same spot as the scattered light beam, along the same optical axis. The advantages and disadvantages of focussed versus parallel reference and scattered beams are discussed elsewhere in this report.

The photomultiplier tube, anode load resistor, and output preamplifier were all mounted in a light-tight electrically screening aluminum housing, seen to the left of Figure 2.16-2. Extraneous light was kept to a minimum by mounting in front of the photomultiplier a narrow-band optical filter designed to pass a narrow band of light wavelengths centered around that of the laser; and by mounting two additional iris stops at either end of a black-painted cardboard tube secured to the front of the detector housing.

These two stops performed the following multiple and important functions: (1) they rejected all extraneous light not passing along the common reference and scattered beam axis; (2) they provided a further stage of selectivity of the scattering volume, as described earlier; (3) they were used during line-up to collimate the reference and scattered beams, i.e., to bring the axes of the two beams to coincidence with each other,

LIGHT FROM SCATTERING VOLUME —CONTRIBUTES WANTED HETERODYNE SIGNAL

] LIGHT FROM EXTRANEOUS LIGHT CONE— CONTRIBUTES UNWANTED WIDENING OF
THE SPECTRUM AND ADDITIONAL NOISE.
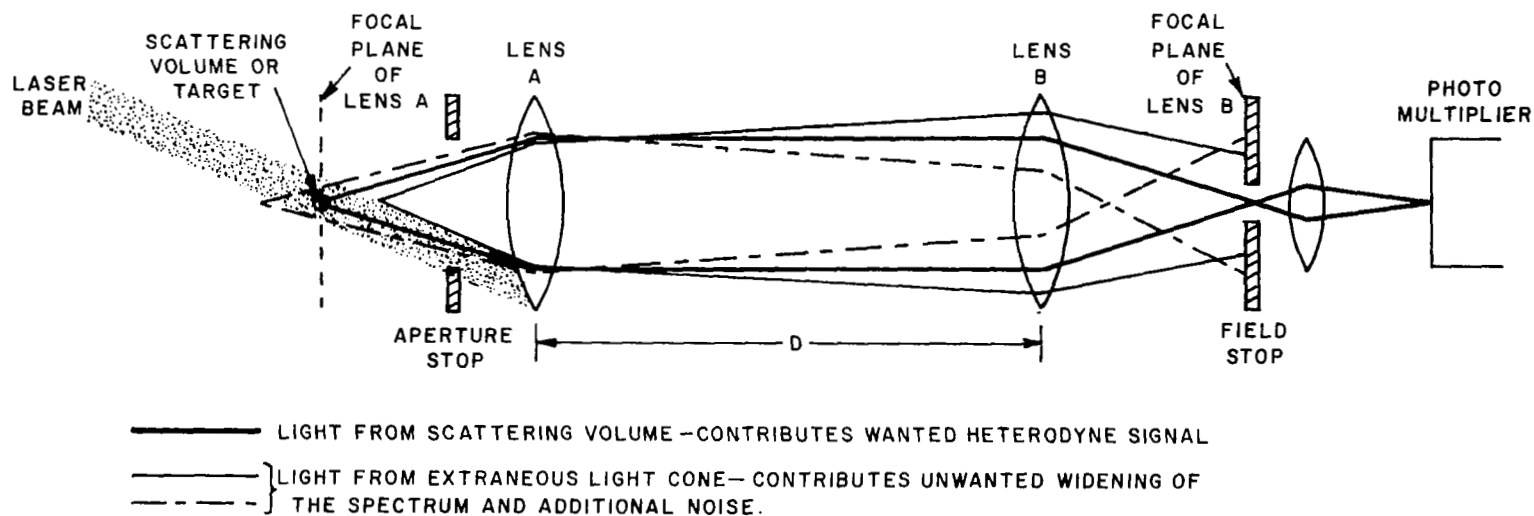
INCREASING DISTANCE "D" REDUCES FRACTION OF EXTRANEOUS LIGHT REACHING
PHOTOMULTIPLIER CATHODE.

Figure 2.16-3   Diagram Illustrating Target Selective Effects of Field
Stops and Lens Apertures

parallel with the mechanical axis of the optical bench, and perpendicular to the cathode surface of the photomultiplier. During the collimation process, the detector housing was slid away from the collimating tube, and an optical mount holding a 45° mirror interposed between the two. This redirected the two beams at right angles to the bench so that tests for axis parallelism could be made with a long, sensitive "optical lever arm".

The importance of eliminating all extraneous light must be strongly emphasized. Here "extraneous light" is defined as all light reaching the photosensitive cathode which does not satisfy both the following conditions simultaneously (1) the light is part of either the scattered or reference beams (2) the light falls on the coincidence region on the photomultiplier cathode of the scattered and reference beams. Extraneous light must be eliminated because:

1) the noise output power from the photomultiplier is proportional to the total light flux falling on the photocathode (Section 2.6). Thus extraneous light contributes noise but makes no contribution to the heterodyne signal, causing a reduction in the system signal to noise ratio.

2) There is a maximum output specified for the photomultiplier, above which saturation and fatigue effects occur (3). The photomultiplier must therefore be operated at conditions such that the anode current remains below this limit. Hence the higher the extraneous light level, the lower must be the allowable useful signal output to keep within this limit.

To eliminate errors caused by drift during recovery from fatigue, a black cloth was kept over the photomultiplier iris aperture at all times when not in use. Careful tests for light leaks were made by "painting" the enclosure with an ac-powered lamp. The presence of a leak was indicated on an oscilloscope display of the photomultiplier output by a rise in white noise level, and by the presence of a 60 Hz ripple (from the sine wave modulation of lamp intensity).

The following external connections were mounted on the photomultiplier housing:

1) High voltage BNC connector for photomultiplier supply
2) BNC a.c. signal output from the preamplifier in the housing
3) Battery leads supplying the preamplifier
4) BNC connector carrying resistance – decoupled d.c. output for monitoring photomultiplier anode current.

The a.c. voltage appearing across the anode load resistor was connected directly to a Kiethley Model 110 Wideband Amplifier, contained in the housing. This amplifier was necessary 1) to decouple the anode circuit from output lead capacitances 2) match the impedance of the anode load resistor to 50 ohms, to allow the use of high bandwidth 50 ohm impedance coaxial signal lead to the external electronic apparatus, without placing impedance matching restrictions on the anode load resistor. The Kiethley impedance matcher was designed for any input circuit impedance up to 10 megohms, and to match to an output circuit impedance of 50 ohms.

The anode circuit prior to the preamplifier was of critical importance since it determined the bandwidth of the detector

system, and the output signal level. The anode load resistor had to be a compromise between two conflicting requirements. A high resistance was desirable for maximum anode signal output, but a low resistance was needed for wide frequency bandwidth.

A study of circuit parameters showed that the most critical parameter was bandwidth. The bandwidth limitation was also the reason for mounting the preamplifier input circuits as close to the photomultiplier anode as possible, to minimize stray capacitance. For example, with the 450 ohm anode load resistor used in our experiments, and with an estimated 20 picofarads circuit capacitance (with the Kiethley impedance matcher mounted inside the photomultiplier housing using shortest possible leads to the anode and resistor), the 3 db point bandwidth was 111 MHz. This was quite adequate for our subsonic laboratory experiments.

However, for high Mach number velocity measurements, this bandwidth must be increased, which can only be done by reducing the anode load resistor (excluding the use of resonant circuit elements and/or feedback techniques), with consequent loss in signal voltage output. Fortunately this presents no problem, since there is virtually no practical restrictions on the gain of the amplifiers which may be used to amplify the a.c. voltage developed across the anode resistor. This is because of the somewhat special situation which exists in the laser doppler flowmeter system, wherein the shot-noise generated in the photomultiplier tube is far greater than that generated by subsequent signal amplifiers, as discussed in Sections 2.5 and 2.12.

For alignment and absolute velocity calibration purposes, a knife edge and a rotating wheel could be placed in the target volume in place of the tunnel. To facilitate set up, the tunnel

could be jacked up and down at one end, so that once alignment
and calibration were completed, gas velocity measurements could
be made at any point over the tunnel height without disturbing
the optical alignment.

It will be seen (Figures 2.16-2 and 2.16-4) that standard
optical bench components (Spindler and Hoyer, and Ealing Corp-
oration) were used to mount optical components on the optical
bench. The alignment of the optical components for optimum
heterodyne signal was very critical. In fact, jumping on the
concrete floor of the laboratory would cause an amplitude ripple
to appear in the oscilloscope trace of the photomultiplier output
a fact which was frequently used to test for good alignment!
Provided no permanent change in alignment was caused by vibration,
such output signals would not affect the laser doppler flowmeter
data since there is a limiter-frequency discriminator system in
the electronic system which eliminates signal amplitude changes,
making the system sensitive only to frequency. Furthermore,
high-pass or band-pass filters in the circuit remove any signals
having frequencies in the normal range of mechanical vibrations.
The cause of the vibration-sensitivity is an important question.
In our system it was probably because a focussed heterodyning
technique was used (Section 2.10), which rendered the amplitude
of the PM tube output signal sensitive to lateral beam misalign-
ments of only a few thousandths of an inch. A change in geometry
would reduce or eliminate this effect (Section 2.10) in a strong
vibration environment. Despite sensitivity to vibration our
laboratory system, with its standard, relatively low-cost optical
bench components, would maintain alignment for days on end, with
a minimal, if any, retuning necessary before each test run.
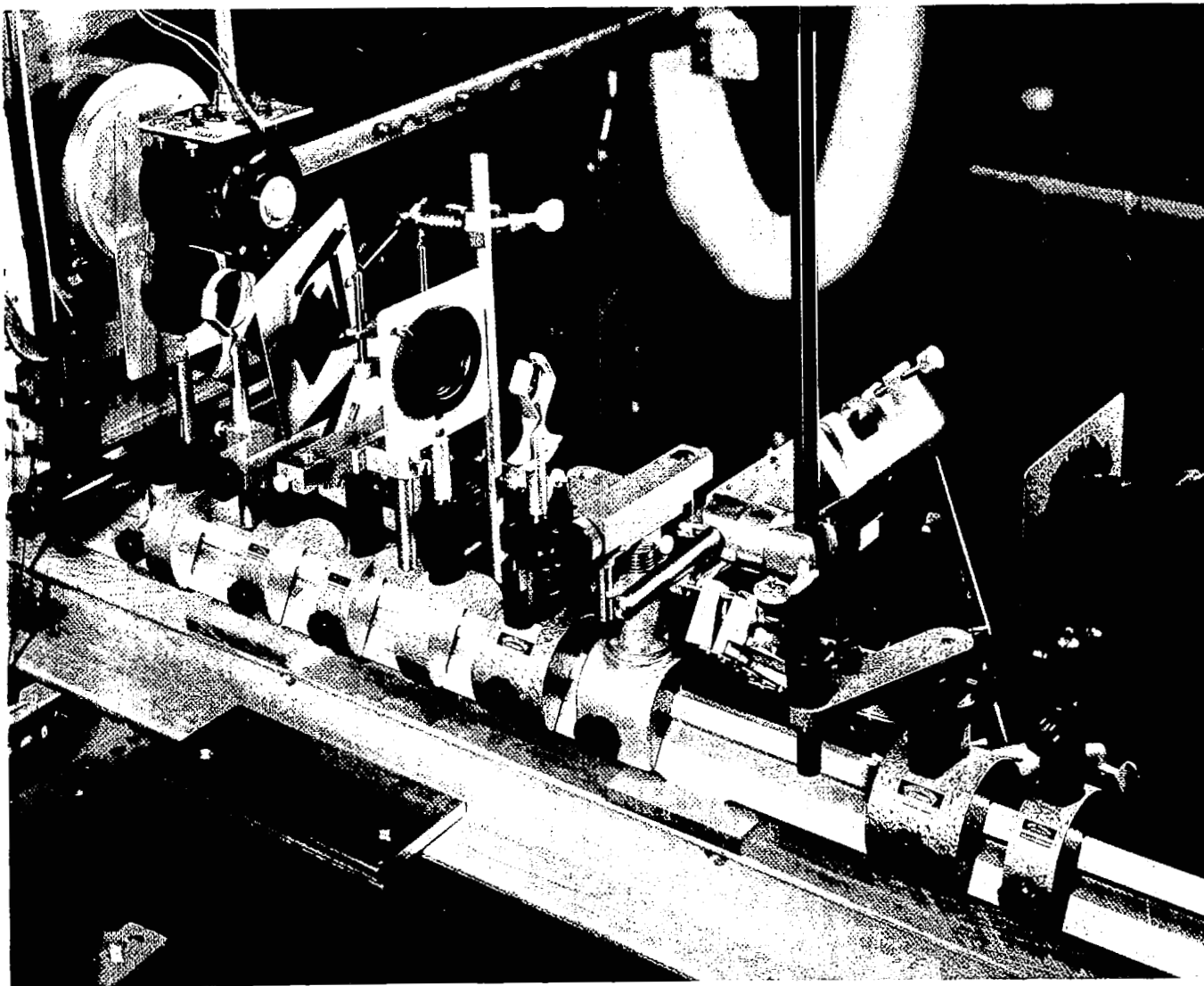
Figure 2.16-4   Close-up Photograph of Optical Bench Components showing Rotating Calibration Wheel, and Typical Fine Adjustment Optical Components

Figure 2.16-4 shows that screw thread-adjustable lens, iris, and mirror supports were necessary at most locations to permit smooth alignment "tuning" or "peaking". At least one mirror in the reference path, together with the beam splitter and beam recombiner required very fine screw thread adjustments (120 TPI), using the specially made holders seen in the photographs.

Some notes follow which illustrate the important points to be observed in lining up the optical and electronic systems.

2.16.1 Optical Alignment Procedure for the Laboratory System

If one keeps in mind the prime objectives of the alignment procedure, the actual step-by-step details become relatively straightforward. Indeed, a wide variation in approach is possible without violation of the alignment objectives. Thus the procedure described here is to be used as a guide rather than a detailed instruction.

An object of well defined optical geometry, such as a knife edge, was set up as the scattering target during static line up, and a rotating wheel used as a dynamic check both for final "peaking" or "tuning" of the lineup, and correct operation of the electronic system. Section 2.16.1.2 describes target selection and use in more detail.

Two approaches to alignment of optical systems may in general be used. The first, which we will term the Mechanical Alignment approach, is to calculate and build to exact dimensions, observing the required tolerances. The second is to align by "tuning" or "peaking", using a succession of well defined optical criteria. This we will call the Optical Alignment approach.

The first technique is used, with a minimum of "peaking" adjust-
ments in the building of a well defined optical instrument, and
was adopted in the design of our 3-D instrument (Section 2.20).
The second approach, common in the laboratory use of optical
benches, was used in our laboratory experiments. In this ap-
proach, the principal consequence of good accuracy requirements
is to require the addition of fine, screw-controlled adjustments
to the optical bench riders. These may be seen in use at criti-
cal locations in Figure 2.16-4.

2.16.1.1 Alignment Objectives

The alignment objectives are fundamentally con-
cerned with the target or scattering volume at one end of the
system, and the sensitive photocathode at the other. They are
summarized below:

Scattering Volume

1) The laser light is to be directed to the
    target or scattering volume, which is
    chosen to be over the center of the optical
    bench. If a focussed beam is used, the
    focal point must be over the optical bench
    center, and accurately focussed on the tar-
    get (knife edge or rotating wheel in lining
    up).

2) If a knife edge is used for lining up,
    the laser beam axis should preferably be
    in a plane perpendicular to the knife edge
    and parallel to the optical bench axis, to
    take advantage of the shape of the knife
    edge scattering polar diagram.

3) The collecting lens, with its axis aligned at the chosen scattering angle, must be located so that its focal point is accurately located on the scattering target. That is, the focal regions of the laser focussing lens (with a focussed laser system) and the collecting lens must be accurately coincident (see discussion of accuracy order in 2.16.2).

Photocathode

1) The Reference and Scattered beams must have maximum area overlap.
2) The Reference and Scattered beam axes must be closely in angular alignment.
3) Both beam axes must be perpendicular to the plane of the photocathode.
4) If focussed beams are used, the two focal planes should be closely coincident with each other and with the plane of the photocathode.

The optics of detector alignment are reviewed in Section 2.10.

2.16.2 Alignment Targets: Design and Use

The use of a static scattering target in aligning the heterodyning optical system is virtually essential. In addition, some form of dynamic target is most useful both for final "peaking" or "tuning" of the optical setup and for checking the complete system, including the electronics.

For convenience a vertical knife edge was selected, as a simple static target whose diffraction pattern is well-known.

Sommerfeld (4) in Chapter 5 and Section 37C gives a lucid and detailed account of optical scattering by a straight edge, to which a knife edge is a reasonable approximation. In use, the knife plane is set perpendicular to the incident light beam.

In setting up the knife edge, first a precise, adjustable height conical point (Ealing Corporation) is placed on the optical bench, and the laser light directed symmetrically on to its tip. The tip of the cone exactly defines the scattering target location, which is thus precisely over the optical bench center at the selected height of the cone tip. This cone, on its stand, is then used as a reference for height and axis throughout the remainder of the alignment procedure. If a focussed laser beam is used, the lens is set so that it is spaced away from the cone by its focal length.

The knife edge, on a movable cross-slide optical stand, is then put in place of the cone and adjusted in position until (a) its edge is vertical (b) its edge is located exactly where the cone tip was (c) its edge bisects the laser beam (checked by a viewing screen or scrap of paper placed behind it).

Finally, the knife edge position is "tuned", by close adjustment in a horizontal direction perpendicular to the laser beam axis, to optimize the scattering "wings" as seen on a screen behind the knife edge, and finally as seen by a screen placed behind the closed-down aperture stop (Figure 2.16-1). One must be quite sure that the scattered light is a good diffraction pattern, for best final heterodyning alignment, rather merely diffused laser light. As an indication of this, the scattered light should show the typical striated diffraction pattern, falling off in intensity from one side to the other.

The care and precision with which this initial set up
of scattering target is performed has a most critical effect on
the final alignment, and hence the signal to noise ratio of the
whole system. The reason is that this target alignment is actu-
ally the means of locating the scattering target in the focal
region of both the laser beam (if a focussed laser beam is used)
and the scattered light collecting lens. This focal region is
defined by the depth of focus and the Airy circle diameter.
Using equations from Section 2.13, typical focal region dimensions
for the largest F numbers used in our laboratory systems are cal-
culated below, by way of illustration:

Light wavelength λ = 6328Å = .00006328 cms

Lens F number $\quad F_1$ = $\dfrac{4 \text{ ins}}{1/8 \text{ inch}}$ = 32

Hence <u>Diameter of focal region</u> in focal plane (first zero
in Airy disc (5))

$$D_A = 2.44 \lambda F$$

$$= (2.44) \ (.00006328) \ (32)$$

$$= .00494 \text{ cms} = .0019 \text{ ins}$$

<u>Depth of focal region</u> along axis (20% fall-off in in-
tensity (6))

$$2 \Delta z \sim F^2 \lambda$$

$$= 4(32)^2 (.00006328)$$

$$= .2592 \text{ cms} = .102 \text{ ins}$$

It is clear from this illustration that the precision required of target location alignment is by no means trivial. It is of the order expected of average machine tools used in tool and die work, such as that of the Bridgeport milling machine.

In the final overall system check, a rotating wheel is used to "peak up" the heterodyne signal. Techniques tried in our laboratory have been to use diffuse reflection from "Scotchlite" tape on the face of a rotating wheel, and to use light scattered by passing through a thin rotating fiberglass disc (photograph in Figure 2.16-4). The latter system was finally selected, since it can be interposed in the optical system in place of the knife edge without change in the optics. It was found necessary to use the thinnest possible fiberglass sheet for the disc to minimize loss of coherence caused by random phase scattering (Section 2.8), which in turn necessitated metal support discs bolted on either side of the disc to stop whirling vibration. Because of precision requirements, just discussed, in location of the scattering target, the wheel was necessarily designed and constructed to "tool and die" accuracy, and care was needed to stop vibration in use, by selecting a well balanced motor and stiff motor supports. A Bodine electronically controlled motor and system was used, giving good stable speeds over 0 to 3,500 rpm range, with a well balanced motor.

In the concurrent experiments at the George C. Marshall Space Flight Center, a calibration wheel consisting of a thin glass disc with one side roughened was constructed by K. Smith and gave good signal to noise performance; no doubt because the very thin scattering surface resulted in minimum random phase coherence loss. For this reason, the principal of using light

scattered through one roughened surface of a transparent disc is
perhaps the best. The difficulty in execution lies in creating
a rough surface without a superimposed periodic irregularity.
For example, we tried a thin transparent plastic disc, with one
surface roughened in a Blanchard grinder. The characteristic
machining marks created a strong sawtooth pattern on the spec-
trum analyzer display of the heterodyne signal. It was finally
concluded that a roughening process inherently random in nature
must be used; for example, chemical etching, sand or shot blast-
ing, random lapping, or some process such as is used for the
manufacture of "ground glass" screens. Since the thin fiber-
glass disc was good enough for our purpose at this stage in the
program, further work on the production of a roughened trans-
parent disc was suspended.

2.16.3 Scattered Beam and Detector Alignment

In aligning the scattered beam, the procedure is
primarily concerned with achieving the objective above in terms
of correct alignment of beams arriving at the photocathode sur-
face. These requirements are rigidly fixed by the physics of
the heterodyning process. Alignment of optical components bet-
ween the collecting lens and the components effecting the align-
ment at the cathode surface is subject to less restraints. For
example, between the intermediate lenses, the optical beam axis
can change angle with respect to the optical bench axis without
detriment to the final alignment, provided the photocathode
alignment is performed correctly. However, for convenience,
generally it was decided to maintain the intermediate beams
parallel with the bench axis and vertically above it at a
height corresponding to the scattering target.

The progress of the beam was checked for angle and position transverse to the system by continual use of the conical point already mentioned. Transverse alignment was checked by allowing the beam to shine on the cone tip, or by inspection of the cone shadow on a paper screen behind. Angular alignment was checked by moving the cone back and forth on its slider along the optical bench and adjusting until no movement of the beam image relative to the cone point could be observed. The adjustable iris stops were set at focal points by using target screens, and positioned so that the beams passed exactly through stop centers.

As already mentioned, at points where the beam was focussed, adjustment in five degrees of freedom was necessary; where the beam was parallel, four degrees of freedom had to be aligned. Recognizing this fact, it was always found that by far the easiest way to achieve the alignment was to separate out the angular from the translational degrees of freedom. This meant the selection of appropriate screw-adjusted optical bench components. These may be seen in Figure 2.16.4.

For example, by proper arrangement of the mirrors in the Reference Beam, separate angular and translational adjustments could be provided. The angular adjustments were made by using special mirror holders. Translational adjustments were made by arranging the mirrors so that each mirror stand height adjustment performed by a height adjusting screw translated the beam either horizontally or vertically, but not both. Since the angular adjustments were basically less pure, that is each also entailed a slight measure of transverse adjustment, the angular adjustments were always performed first.

Angular alignment between the Reference and Scattered Beams was checked by moving a paper target back and forth along the rail and observing to see that the displacement between the two images remained constant. When this condition had been achieved, it was then a simple matter to translate first vertically then horizontally one or other beams until the two were coincident. Final alignment was checked by placing a 45° mirror on the optical bench and inspecting the superposition of the two images at a distance of about 5 to 7 meters away from the bench. In this way, very precise angular alignments could be achieved in a relatively straightforward manner.

One encouraging finding was that, provided care was taken in this geometrical alignment procedure and that no compromise was made in the alignment, heterodyne signals were always achieved immediately, and relatively little subsequent tuning was required. This finding is particularly important since, because of the many elements effecting heterodyning in the whole system, the absence of heterodyne signals could be caused by many different factors. Elimination of the optical factor by correct alignment meant that the problem was confined either to the electronics or to the nature of the scattering target.

In setting up the Reference Beam, it is most desirable to use front surface mirrors throughout, except for the beam splitter and beam recombiner. This is because if the beam is allowed to pass through a thickness of glass, reflections occur both at the front and the rear surface, resulting in a multiplicity of images at the end of the system, the number being 2^{n} where n is the number of mirrors. Using just front surface

mirrors, except for the beam splitter and recombiner, just four Reference Beam images are then obtained. Careful tracing of the beam through the reflection paths identified which image was the prime one (that is, the image which was always obtained by re-flection at the front surface). The other beams were then eli-minated by placing small pieces of adhesive black optical tape to obscure them, on the reflecting surfaces of the splitter and combiner. This elimination of secondary images is especially necessary when a focussed reference beam system is used; since, except at the focal point, all the unwanted image beams overlap, creating an almost impossible image for alignment purposes.

2.16.4 Set-up and Adjustments of the Electronics System

Figure 2.18-1 is a schematic diagram of the electro-nics system used in the measurement of heterodyne signals and signal-to-noise ratios. With the exception of the components immediately connected to the photomultiplier anode, standard electronic apparatus was used throughout. The following points summarize the important design features and steps which must be observed for successful operation:

1. All input and output impedances throughout the circuit must be carefully and correctly matched. Measurements or observations made without ex-plicit impedance matching are quite meaningless.

2. All signal levels at all points in the circuit must be carefully and correctly set within the voltage or current range specified by the manu-facturer of each component. Only high impedance input devices such as oscilloscopes can be moved to various parts of the circuit relatively freely.

Even when these are used, if they are the only
component in the circuit, a termination impedance
must be placed at their terminals so as to match
correctly the rest of the circuit component im-
pedances. In our case we used 50 ohms circuit
impedance levels throughout, with the exception
of the circuit immediately at the photomultiplier
anode. BNC connectors and cables were also used
consistently for all connections. Level settings
are very much simplified if a plentiful supply of
correctly matched designed and matched attenu-
ators such as the Hewlett-Packard 1000 are placed
in key points of the circuit.

3. A first objective in setting up the electronics
   should be to display the photomultiplier output white
   noise at all parts of the circuit. This insures
   that firstly, the gain is sufficient and secondly,
   that no saturation is occurring at any place in
   the circuit; and thirdly, that pickup problems
   have been eliminated.

4. After aligning the heterodyne system, a very de-
   finite sensitivity to vibration of various parts
   of the apparatus should be demonstrated by tapping
   the optical bench gently and observing the photo-
   multiplier output on the oscilloscope.

5. Having displayed noise with a steady level of
   light flux, next a spectrum analyzer display of
   the frequency shift caused by the rotating wheel
   is necessary. Circuit filters should be used
   wherever possible to eliminate all unused regions

of the spectrum. These are necessary for two
reasons: a) the photomultiplier noise output
is white noise and therefore proportional to the
total system bandwidth and b) low frequency pick-
up, which is hard to eliminate, is removed by
proper filtering.

6. Finally, care should be taken to eliminate all
spurious oscilloscope and spectrum signal displays.

This latter is important because the spectrum analyzer
displays signals which may be derived either from AM or FM modu-
lation. For the doppler measurements we are interested only in
FM signals, so that AM signals are spurious. AM signals may be
detected by observing the photomultiplier output on a sensitive
oscilloscope. Typical sources of AM modulation are (a) vibrating
components, (b) irregularities in the wheel, (c) wheel running
out of true, (d) oscillations of the laser source. Spurious AM
modulations may be tracked down by observing the frequencies
and then deducing their source from known natural frequencies of
vibration. The laser amplitude modulations may be checked by
making slight adjustments to the laser mirrors and observing to
see if the AM modulation changes.

The electronic system shown in Figure 2.18-1 is re-
latively straightforward to set up and operate correctly, pro-
vided these precautions are observed. The only critical part of
the circuit is that at the photomultiplier anode, which places
the upper limit on bandwidth and signal-to-noise ratio of the
whole system.

LIST OF REFERENCES FOR SECTION 2.16

1. Rolfe, Holway, Janos, McDonald, Shapiro and Silk, "First and Second Quarterly Technical Note, Energy Processes in Shock-Waves - The Plasma Parameters of an Irradiated Shock Wave and Their Measurement by Optical Techniques", RADC-TDR-62-503, Rome Air Development Center Contract AF30(602)-2716, Raytheon Company Equipment Division (Oct. 1962).

2. Jacobs, D. H., _Fundamentals of Optical Engineering_, McGraw-Hill, (1943 edition).

3. Engstrom, R. W., "Multiplier Photo-Tube Characteristics: Application to Low Light Levels", J. Optical Soc. of America, 37, 420 (June, 1947).

4. Sommerfeld, A., _OPTICS, Lectures on Theoretical Physics_, _Vol. IV_, Academic Press (N.Y. and London)(1964).

5. Walther, Kingslake (ed), _Applied Optics and Optical Engineering_, Vol. I, 271 (1965).

6. Born, M., Wolf, E., _Principles of Optics_, 441 (1964 edition).

2.17 Calibration of the Photomultiplier Tube

The EMI 9558B photomultiplier used in the laboratory measurements described in this report was calibrated absolutely. This section describes the method in detail and gives the final calibration curves.

2.17.1 Method

The calibration source constructed for use on the Laser Doppler Velocity Instrument investigation consists of the following components:

a) A tungsten ribbon lamp used as a standard source for intensity calibration.

b) A six-volt lamp and solar cell detector used to provide a trigger signal.

c) A control box to supply power for the lamps, with control and meter for setting the calibration lamp brightness.

The following paragraphs describe the use of this equipment.

The calibration source is a G.E. 18A/T10/3P tungsten ribbon lamp (18 ampere ribbon) and is described in Reference (1). Figure 3b of Reference (1) gives the color temperature of the lamp as a function of current and the calibration procedure is based on data from this curve. The brightness temperature of the lamps can be determined from Table 2.17-1 which shows data from the American Institute of Physics Handbook. The emission (watts/ cm^2/μ/ster) has been computed as a function of wavelength in the course of previous work in the Raytheon Company (2) for brightness temperatures $2195^{O}K$, $2182^{O}K$ and $2175^{O}K$. The results of these calculations have been reproduced and are given as Tables 2.17-2, 2.17-3, 2.17-4 and Figure 2.17-1. The computations include the effect of the Pyrex glass envelope of the bulb.

TABLE 2.17-1

TUNGSTEN TEMPERATURES

T^{O} K	Brightness Temp. 0.65 μ	Color Temp.
1000	966	1007
1100	1059	1108
1200	1151	1210
1300	1242	1312
1400	1332	1414
1500	1422	1516
1600	1511	1619
1700	1599	1722
1800	1687	1825
1900	1774	1928
2000	1861	2032
2100	1946	2136
2200	2031	2241
2300	2115	2345
2400	2198	2451
2500	2280	2556
2600	2362	2662
2700	2443	2769
2800	2523	2876
2900	2602	2984
3000	2681	3092
3100	2759	3200
3200	2837	3310
3300	2913	3420
3400	2989	3530
3500	3063	3642
3600	3137	3754

TABLE 2.17-2

INTENSITY OF SPECTRAL RADIATION FROM TUNGSTEN RIBBON LAMP AT 2195°C BRIGHTNESS TEMPERATURE

Wavelength λ(cm)	Intensity (watts/cm³/ster)	Wavelength λ(cm)	Intensity (watts/cm³/ster)	Wavelength λ(cm)	Intensity (watts/cm³/ster)	Wavelength λ(cm)	Intensity (watts/cm³/ λ(cm))
2.00×10^{-5}		8.50×10^{-5}	2.11×10^5	15.00×10^{-5}	1.39×10^5	21.50×10^{-5}	5.69×10^6
2.25		8.75	2.14×10^5	15.25	1.35×10^5	21.75	5.51×10^6
2.50	4.02×10^1	9.00	2.17×10^5	15.50	1.30×10^5	22.00	5.31×10^6
2.75	1.78×10^2	9.25	2.19×10^5	15.75	1.26×10^5	22.25	5.15×10^6
3.00	5.78×10^2	9.50	2.20×10^5	16.00	1.22×10^5	22.50	5.00×10^6
3.25	1.48×10^3	9.75	2.20×10^5	16.25	1.18×10^5	22.75	4.85×10^6
3.50	3.24×10^3	10.00	2.20×10^5	16.50	1.14×10^5	23.00	4.70×10^6
3.75	6.29×10^3	10.25	2.19×10^5	16.75	1.10×10^5	23.25	4.53×10^6
4.00	1.07×10^4	10.50	2.16×10^5	17.00	1.06×10^5	23.50	4.37×10^6
4.25	1.69×10^4	10.75	2.13×10^5	17.25	1.03×10^5	23.75	4.23×10^6
4.50	2.49×10^4	11.00	2.10×10^5	17.50	9.92×10^6	24.00	4.09×10^6
4.75	3.47×10^4	11.25	2.07×10^5	17.75	9.61×10^6	24.25	3.96×10^6
5.00	4.63×10^4	11.50	2.04×10^5	18.00	9.28×10^6	24.50	3.84×10^6
5.25	5.94×10^4	11.75	1.99×10^5	18.25	8.97×10^6	24.75	3.72×10^6
5.50	7.35×10^4	12.00	1.95×10^5	18.50	8.66×10^6	25.00	3.59×10^6
5.75	8.79×10^4	12.25	1.91×10^5	18.75	8.37×10^6	25.25	3.48×10^6
6.00	1.03×10^5	12.50	1.87×10^5	19.00	8.07×10^6	25.50	3.38×10^6
6.25	1.18×10^5	12.75	1.82×10^5	19.25	7.80×10^6	25.75	3.28×10^6
6.50	1.32×10^5	13.00	1.78×10^5	19.50	7.53×10^6	26.00	3.18×10^6
6.75	1.46×10^5	13.25	1.73×10^5	19.75	7.28×10^6	26.25	3.08×10^6
7.00	1.59×10^5	13.50	1.67×10^5	20.00	7.03×10^6	26.50	2.99×10^6
7.25	1.71×10^5	13.75	1.63×10^5	20.25	6.79×10^6	26.75	2.90×10^6
7.50	1.81×10^5	14.00	1.58×10^5	20.50	6.58×10^6	27.00	2.82×10^6
7.75	1.90×10^5	14.25	1.53×10^5	20.75	6.34×10^6	27.25	2.74×10^6
8.00	1.98×10^5	14.50	1.48×10^5	21.00	6.13×10^6	27.50	2.65×10^6
8.25	2.05×10^5	14.75	1.44×10^5	21.25	5.90×10^6		

TABLE 2.17-3

INTENSITY OF SPECTRAL RADIATION FROM
TUNGSTEN RIBBON LAMP AT 2175°C BRIGHTNESS TEMPERATURE

Wavelength λ (cm)	Intensity (watts/cm^3/ster) 2175°C	Wavelength λ (cm)	Intensity (watts/cm^3/ster) 2175°C
2.00×10^{-5}		15.00×10^{-5}	1.35×10^5
2.50	3.32×10^1	15.50	1.26×10^5
3.00	4.93×10^2	16.00	1.18×10^5
3.50	2.83×10^3	16.50	1.10×10^5
4.00	9.48×10^3	17.00	1.03×10^5
4.50	2.24×10^4	17.50	9.64×10^4
5.00	4.21×10^4	18.00	9.02×10^4
5.50	6.74×10^4	18.50	8.43×10^4
6.00	9.50×10^4	19.00	7.86×10^4
6.50	1.23×10^5	19.50	7.34×10^4
7.00	1.49×10^5	20.00	6.85×10^4
7.50	1.70×10^5	20.50	6.41×10^4
8.00	1.87×10^5	21.00	5.98×10^4
8.50	1.99×10^5	21.50	5.56×10^4
9.00	2.06×10^5	22.00	5.19×10^4
9.50	2.09×10^5	22.50	4.88×10^4
10.00	2.10×10^5	23.00	4.59×10^4
10.50	2.06×10^5	23.50	4.27×10^4
11.00	2.01×10^5	24.00	3.99×10^4
11.50	1.95×10^5	24.50	3.75×10^4
12.00	1.88×10^5	25.00	3.51×10^4
12.50	1.80×10^5	25.50	3.30×10^4
13.00	1.71×10^5	26.00	3.11×10^4
13.50	1.61×10^5	26.50	2.93×10^4
14.00	1.53×10^5	27.00	2.76×10^4
14.50	1.43×10^5	27.50	2.60×10^4

TABLE 2.17-4

INTENSITY OF SPECTRAL RADIATION FROM

TUNGSTEN RIBBON LAMP AT 2182°C BRIGHTNESS TEMPERATURE

Wavelength λ (cm)	Intensity (watts/cm^3/ster) 2182°C	Wavelength λ (cm)	(watts/cm^3/ster) 2182°C
2.00×10^{-5}		15.00×10^{-5}	1.36×10^5
2.50	3.56×10^1	15.50	1.28×10^5
3.00	5.21×10^2	16.00	1.19×10^5
3.50	2.97×10^3	16.50	1.12×10^5
4.00	9.89×10^3	17.00	1.04×10^5
4.50	2.32×10^4	17.50	9.73×10^4
5.00	4.36×10^4	18.00	9.11×10^4
5.50	6.95×10^4	18.50	8.51×10^4
6.00	9.77×10^4	19.00	7.94×10^4
6.50	1.26×10^5	19.50	7.40×10^4
7.00	1.52×10^5	20.00	6.91×10^4
7.50	1.73×10^5	20.50	6.47×10^4
8.00	1.91×10^5	21.00	6.03×10^4
8.50	2.03×10^5	21.50	5.60×10^4
9.00	2.10×10^5	22.00	5.23×10^4
9.50	2.13×10^5	22.50	4.92×10^4
10.00	2.14×10^5	23.00	4.63×10^4
10.50	2.10×10^5	23.50	4.30×10^4
11.00	2.04×10^5	24.00	4.03×10^4
11.50	1.98×10^5	24.50	3.78×10^4
12.00	1.90×10^5	25.00	3.54×10^4
12.50	1.82×10^5	25.50	3.33×10^4
13.00	1.73×10^5	26.00	3.13×10^4
13.50	1.63×10^5	26.50	2.95×10^4
14.00	1.55×10^5	27.00	2.78×10^4
14.50	1.45×10^5	27.50	2.62×10^4

INTENSITY WATTS/cm^2/MICRON/STER

Figure 2.17-1   Intensity of Spectral Radiation From Tungsten
Ribbon Lamp at 2195° C Brightness Temperature

Hence to set up the tungsten light source at a desired emission $(watts/cm^2/\mu/ster)$, and a desired and a desired wavelength, one obtains the corresponding brightness temperature from Tables 2.17-2, 2.17-3 or 2.17-4, determines the corresponding color temperature from Table 2.17-1, and then the necessary lamp operating current from the curve in reference (1).

2.17.2 Experimental Measurements and Sample Calculations

The apparatus arrangement for the calibration is shown in Figure 2.17-2. The photomultiplier was left on the optical bench in the normal position used for laser Doppler experiments, a long with the immediately adjacent set of three iris diaphragms. A mirror was set on the optical bench to direct the light from the tungsten ribbon source, through the iris diaphragms and a filter, and onto the photocathode of the photomultiplier.

The filter used between the last iris diaphragm and the photocathode was an Optics Technology, Inc. interference filter #633, having the maximum transmission of 36% at 6330 Å with a band width of 175 Å as measured at the points of one-half maximum transmission. This filter was used so that the calibration of the wavelength-sensitive detector was at the He-Ne laser wave length, 6328 Å.

The total power of light falling on the photocathode is:

> I = Emitted power (watts/cm^3 steradian) x Bandwidth
> transmitted (cm) x Area of tungsten filament (cm^2)
> x Solid angle intercepted (steradians) x Transmission
> of interference filter (%).

From Reference (1) and Tables 2.17-1, 2.17-2, we find the emitted power from the lamp at 2195°C (corresponding to a filament current of 13.7 amps) to be 1.224 x 10^5 watts/cm^3 steradian, and the area of the filament to be .16 cm^2.

LIMITING APERTURE

PHOTOCATHODE

PHOTOMULTIPLIER

MIRROR

OPTICS TECHNOLOGY
INTERFERENCE FILTER

APERTURE TO REDUCE SCATTERED LIGHT

NEUTRAL DENSITY FILTERS

CHOPPER

STANDARD LAMP
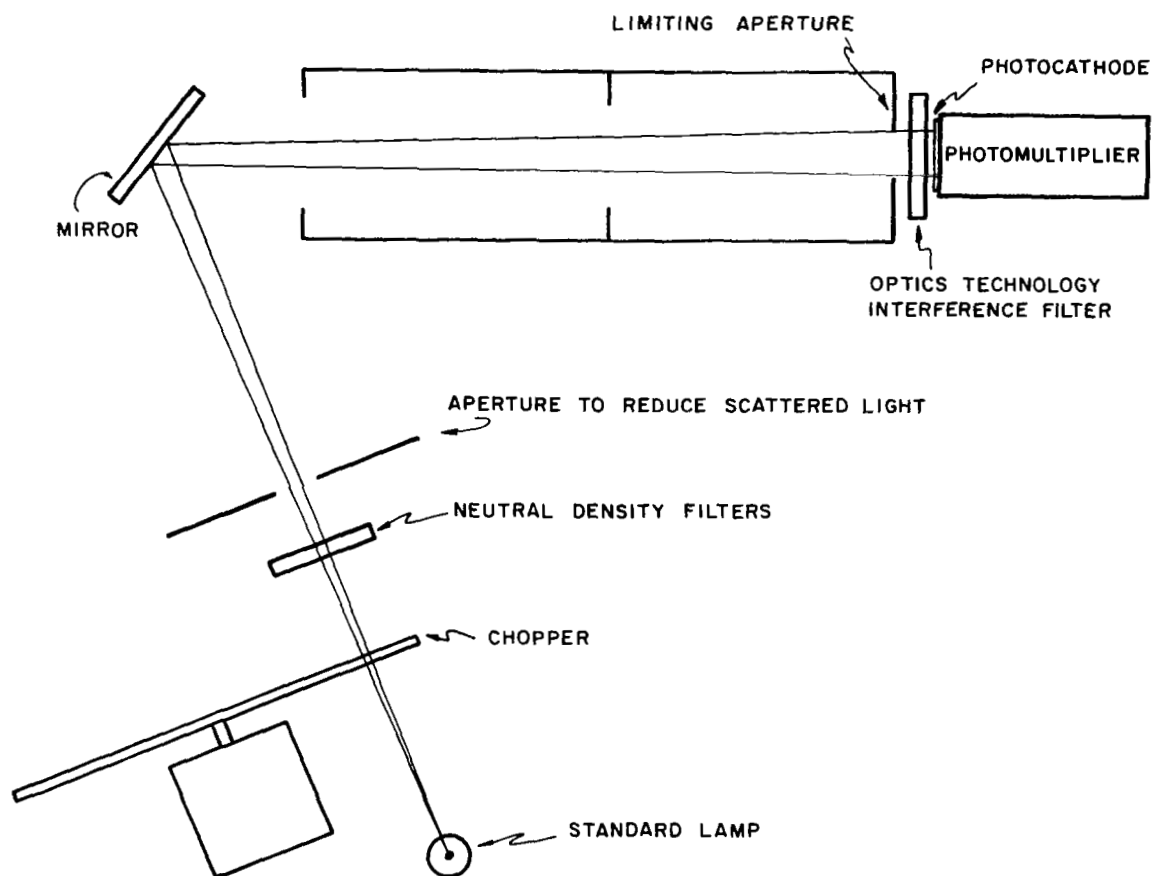
Figure 2.17-2 - Apparatus Set-up for Photomultiplier
Calibration

The solid angle intercepted is defined by: Ω = Lighted area at photocathode/the square of the distance between photocathode and tungsten ribbon lamp.

The last iris immediately adjacent to the interference filter and photocathode was set with a 3/4" diameter aperture, and the measured distance between photocathode and tungsten ribbon lamp was 39". Thus:

$$\Omega = \frac{\text{Area}}{(\text{Distance})^2} = \frac{\pi(3/8")^2}{(39")^2} = \frac{.442}{1521} = 2.9 \times 10^{-4} \text{ steradians}$$

Hence, the total power falling on photocathode when lamp is operating at 13.7 amps (2195°C) is:

$$I = (1.224 \times 10^5 \text{ watts/cm}^3 \text{ steradian}) \times (175 \times 10^{-8} \text{ cm})$$
$$\times (.16 \text{ cm}^2) \times (2.9 \times 10^{-4} \text{ steradians}) \times (36\%)$$
$$= 3.57 \times 10^{-6} \text{ watts.}$$

The anode current was measured as a function of voltage applied to the tube, at 50 volt intervals, from 500 volts to 2,000 volts. Of necessity, the magnitude of the light had to be reduced at higher voltages to avoid saturation of the photomultiplier. The light was so reduced by intercepting the beam with neutral density filters, having optical densities of 1.0, 2.0, and 3.0, thus reducing the light intensity striking the photocathode to 3.57×10^{-7}, 3.57×10^{-8}, and 3.57×10^{-9} watts, respectively. The data are shown in Figure 2.17-3.

The beam of light going to the photocathode was chopped at approximately one kHz, and the output voltage through a 1500 ohm photomultiplier load resistor was read on an oscilloscope. The photomultiplier anode currents were obtained by dividing the voltages by 1500 ohms. From the data we can determine the sensitivity of this photomultiplier at 6330 Å at all applicable anode-cathode voltages, as the units of sensitivity are amps/watt, or microamps/microwave.
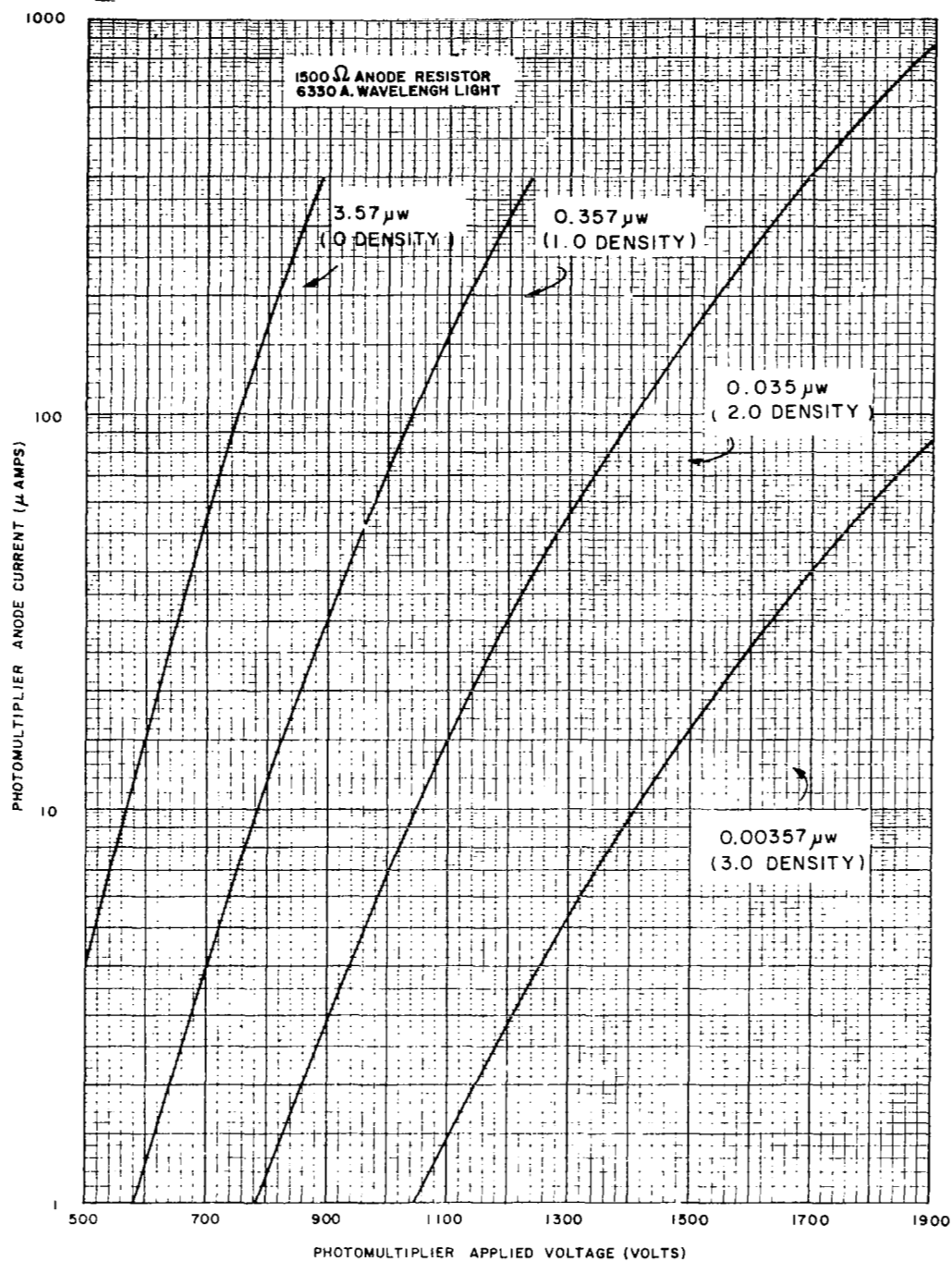
Figure 2.17-3   EMI 9558B Photomultiplier Anode Current vs Applied
Voltage for Various Incident Light Intensities

2.17.3 Calibration Results

However, it is more convenient for us to calculate
and plot the reciprocal sensitivity in units of watts/amp, or
microwatts/microamp, as a function of photomultiplier anode-
cathode voltage. The plotted data (Figure 2.17-4) of reciprocal
sensitivity versus photomultiplier voltage presents the result
of the calibration.

At any given photomultiplier anode-cathode voltage, it is now
only necessary to multiply the given reciprocal sensitivity by the
anode current, in microamps, to know the laser power incident on
the photocathode, in microwatts.

2.17.4 Check Calibration Using Different Reference Source

The above calibration was checked with a different
reference light source, a G. E. 6.6A/T40/1CL-200W Quartz Iodine
Tungsten lamp, having a calibrated light output traceable to the
National Bureau of Standards. The same apparatus arrangement
was used for these measurements, except the distance between
photocathode and lamp was 38½".

In this case, the lamp was calibrated in units of micro-
watts/cm^2-nanometer at a distance of 43 cm. Thus, the total
power falling on photocathode is:

I = Emitted power (microwatts/cm^2-nanometer) x (correction
   factor for new distance) x Aperture Area (cm^2) x
   Bandwidth transmitted (nanometer) x Transmission of
   interference filter (%).

At 6330 Å wavelength, and at specified calibration current
of 6.5 amps, this lamp produces a radiance of 4.80 microwatt/cm^2-
nanometer at a distance of 43 cm.

The correction factor for the distance used, is:
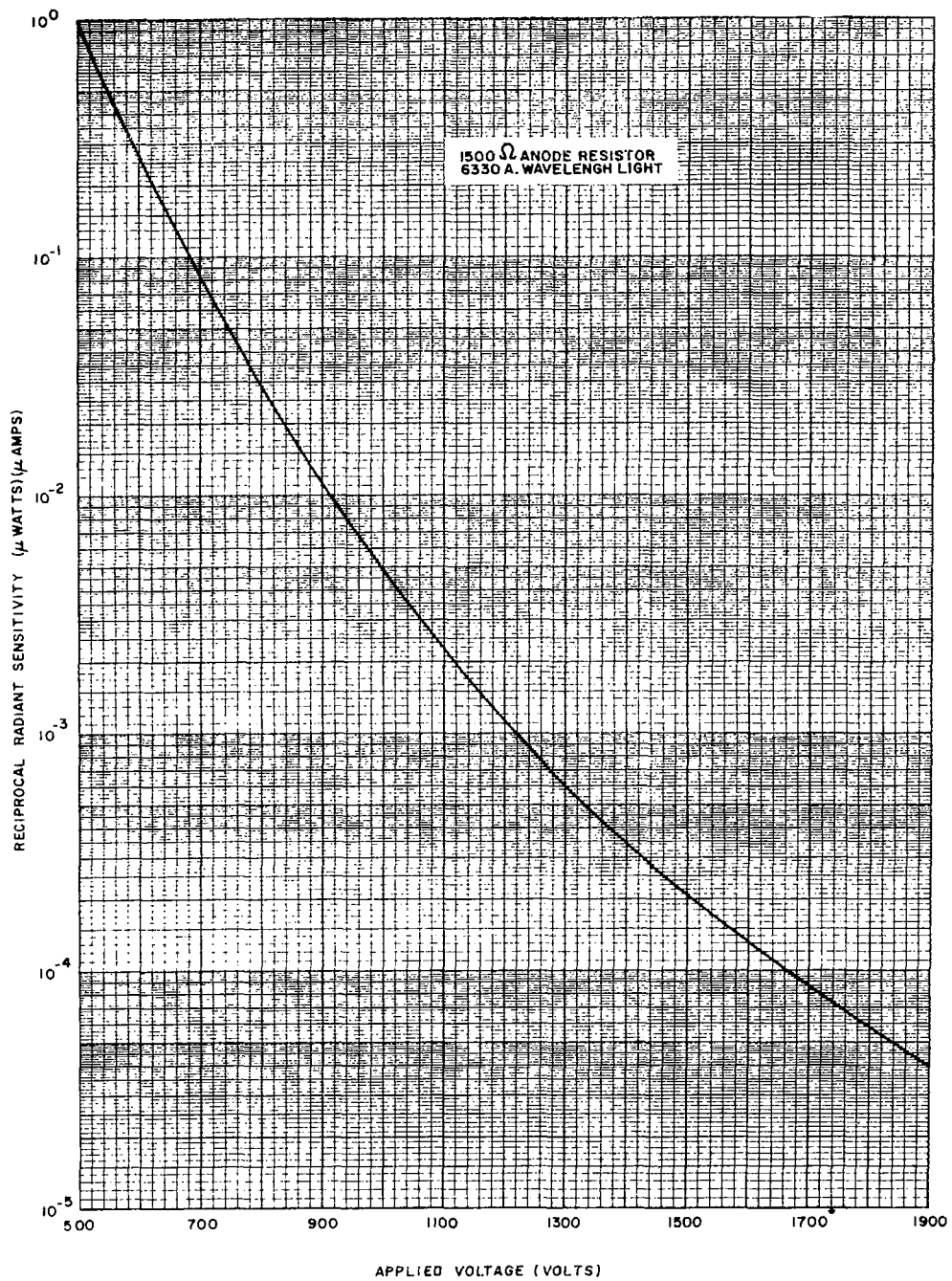
Figure 2.17-4   Reciprocal Radiant Sensitivity (Microwatts of
                Light per Microampere of Anode Current) vs
                Applied Voltage for EMI 9558B

2.17-12

$$\frac{(43\text{cm})^2}{(38\tfrac{1}{2}\text{ inches})^2} = \frac{(43\text{cm})^2}{(98\text{cm})^2}$$

$$= \frac{1850}{9600} = .193$$

The aperture area is:

$$\text{Area} = \pi(3/8")^2 = .442 \text{ in}^2 = 2.85 \text{ cm}^2$$

The bandwidth of Optics Technology interference filter #633, is 175 Å = 17.5 nanometer, and the transmission of the filter is 36%.

Thus, the intensity of light falling on photocathode is:

$$I = (4.80 \text{ microwatt/cm}^2 \text{ nanometer}) \times (.193) \times 2.85 \text{ cm}^2) \times$$
$$(17.5 \text{ nanometer}) \times (36\%)$$
$$= 16.65 \times 10^{-6} \text{ watts}$$

The data taken with this lamp were consistent with the tungsten lamp, within a factor of 1.5, when the reciprocal sensitivities were compared at a few selected voltages. The absolute accuracy of the primary standard can be improved if desired by introducing an ammeter of higher precision to read the value of 13.7 amps tungsten ribbon lamp current.

LIST OF REFERENCES FOR SECTION 2.17

(1) Leighton, L. C., "Characteristics of Ribbon Filament Lamps", paper presented at the National Technical Conference of the Illuminating Engineering Society, Sept. 24-29, St. Louis, Mo. (copies available from G. E.).

(2) Rolfe, Silk, Ferrar, Janos, Shapiro, Haynes, "Final Technical Report, Energy Processes in Shock Waves, Diagnostic Techniques", RADC-TDR-64-269, Raytheon Company Research Division (July, 1963).

2.18   Experimental Verification of Laser Doppler Velocity Instrument Basic Parameters

In earlier sections of this report, the analysis of the key parameters of the Laser Doppler Velocity Instrument have been presented. This section describes the methods and results of experiments by which the most important were verified. In addition, other useful results are given of general interest to those concerned with design or application of the Instrument.

2.18.1   Dependence of Signal-to-Noise Ratio on Local Oscillator Beam Power

It was shown in Sections 2.5 and 2.6 that the fundamental ratio of mean square Signal Power to mean square Noise Power measured at the photomultiplier tube anode is calculated to be:

$$\left(\frac{S}{N}\right)_{A,MS} = \mu_T \left(\frac{P_s}{\Delta f}\right)\left(\frac{S_k}{ek}\right)\left[\frac{1}{\left(1 + \frac{P_s}{P_{LO}}\right)}\right] \tag{1}$$

written in a form most convenient for use at low scattered signal

power, i.e., with $\frac{P_s}{P_{LO}} \ll 1$ (Section 2.5). The parameters are

defined in 2.5 and 2.6. It is noted that the signal-to-noise ratio is independent of wavelength, and of anode load resistor, except insofar as the latter affects the system bandwidth. As a convenient standard, a rotating thin transluscent disc (described in Section 2.16.2) was used as a moving medium, with the laser beam passing through it at an angle of 90°, and with the scattered beam optics set at a scattering angle of approximately 8°. Wheel speed was measured with a General Radio Strobotac. The apparatus and its alignment are described in detail in 2.16.

An EMI 9558B photomultiplier tube was used, its output carefully calibrated against absolute incident light power. The calibration method and curves appear in Section 2.17. Calibration was performed with a tungsten ribbon lamp as standard, masked by a narrow band filter passing light of the same wavelength as that used for the experiments, namely, the light output from a helium-neon laser.

The principal objectives of the measurements were to verify the relationship between $\frac{S}{N}$, $\frac{P_s}{P_{LO}}$, P_s, and Δf. As an incidental result, the heterodyning loss factor μ_T, defined in 2.6, was measured. Since considerable care was taken before each measurement to peak up the signal, since the atmospheric path length was short, and since the difference between Scattered Light and Reference Beam path lengths was small compared with the laser coherence length, it was assumed that the measured μ_T was for all practical purposes, equal to the Scattering Target Coherence Loss Factor, μ_s.

Since this latter is the most important parameter to be measured relative to the particle injectant in the fluid stream, clearly the signal-to-noise measurement technique used here is also most appropriate for experimental investigation of the efficacy of different injectants. In the case of the wheel used, it will be seen that μ_s was very low, for reasons which are analyzed in general in Section 2.8.

For convenience in plotting results, equation (1) was re-written as

$$\left(\frac{S}{N}\right)_{A,MS} = \mu_T \left(\frac{P_s}{\Delta f}\right)\left(\frac{S_k}{ek}\right) \frac{\dfrac{P_{LO}}{P_s}}{\left(\dfrac{P_{LO}}{P_s} + 1\right)} \tag{2}$$

$\frac{S}{N}$ was then measured for varying ratios $\frac{P_{LO}}{P_s}$, all other para-
meters, including P_s, being maintained constant; i.e. P_{LO} only
was varied in the first series of measurements by inserting
progressively more dense neutral density filters. A plot of
$\frac{S}{N}$ versus $\frac{P_{LO}}{Ps}$ should then be assymptotic to an upper bound of the
ordinate $\frac{S}{N}$, as $\frac{P_{LO}}{P_s}$ becomes much greater than unity.

The measurement of $\frac{S}{N}$ power ratio was not quite so straight-
forward as might appear at first glance. Actually, a single
value of $\frac{S}{N}$ required the measurement of seven separate parameters:

1) True Mean Square Signal power - a sine wave at
   heterodyne frequency;

2) True Mean Square Noise generated by P_{LO} - a random
   frequency;

3) True Mean Square Noise generated by P_{sc} a random
   frequency white noise;

4) Dark and Electronic system noise combined - a random
   frequency white noise;

5) P_{LO} average power - giving rise to a d.c. anode current;

6) P_{sc} average power - giving rise to a d.c. andoe current;

7) Average dark current - a d.c. anode current.

Suitable a.c. and filtered d.c. electronic circuits and
instruments were necessary, as shown diagramatically in Figure
2.18-1. The a.c. power measurements were made by passing the volt-
age developed across the 1500 ohm PM anode load resistor through
a very short connection to an a.c.-coupled impedance matcher
(see bandwidth discussion in 2.12) connecting to 50 ohm ex-
ternal circuits, through a 400 kHz band pass filter centered at

50 MW He - Ne LASER

ROTATING DISC

VARIABLE NEUTRAL DENSITY FILTER

50 Ω CIRCUITS

BALLANTINE TRUE RMS VOLTMETER

PHOTO-MULTIPLIER

KIETHLEY MATCHER

10M Ω

50 Ω

400KHz BANDPASS FILTER

2 MHz CENTER

H-P AMPLIFIER

ATTENUATOR

1500 Ω ANODE LOAD

25K

FILTER

5.1K

22 µf

TEKTRONIX 647 SCOPE HIGH-GAIN DIFFERENTIAL PLUG-IN

1 M Ω

PANORAMIC SPECTRUM ANALYZER MODEL SPA-3/25a

KINTEL ELECTRONIC D C AVERAGE MILLIVOLTMETER
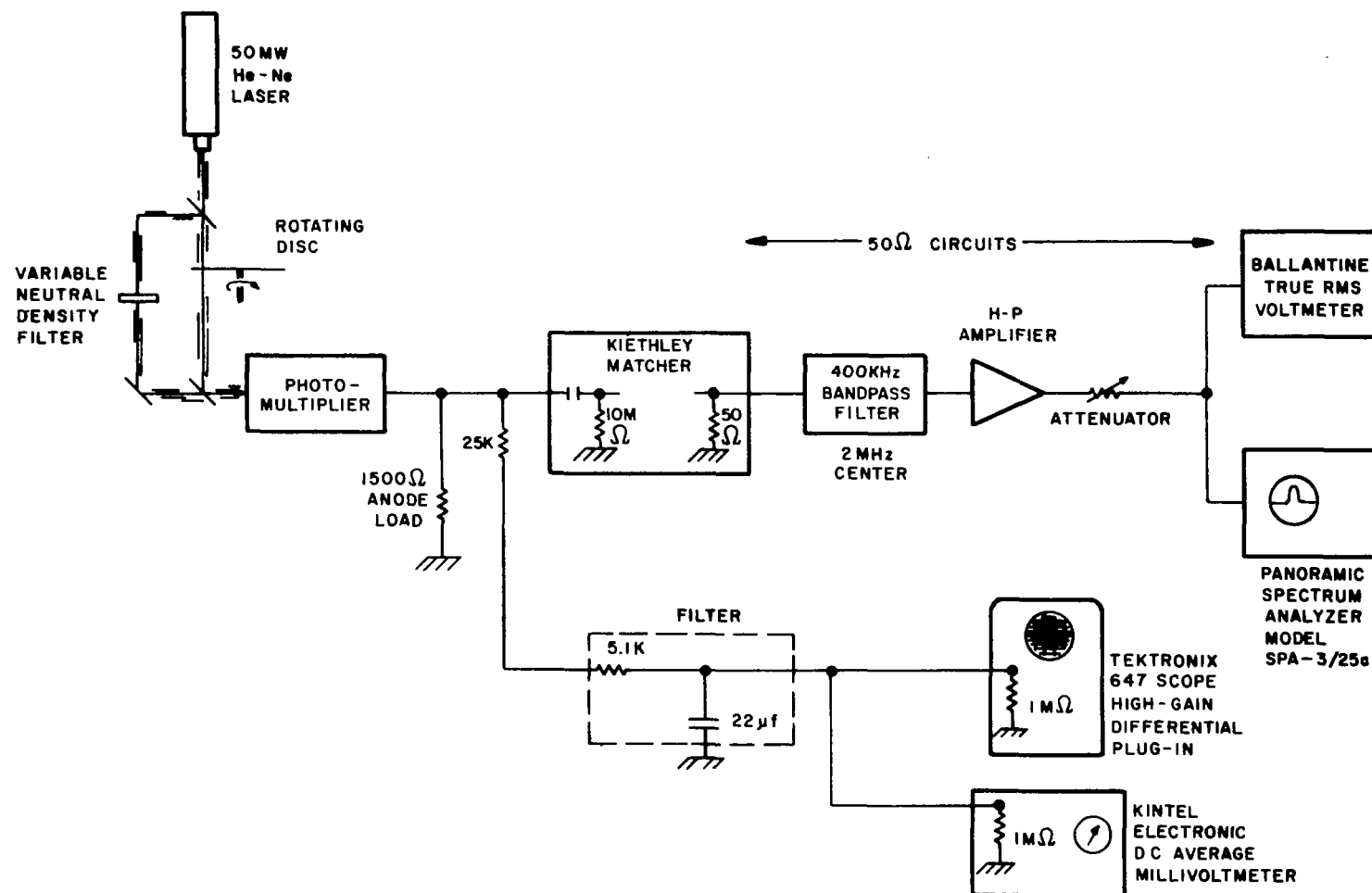
1 M Ω

Figure 2.18-1   Block Diagram of System for Heterodyne
Signal-to-Noise Power Ratio Measurement

2 MHz, the wheel Doppler frequency shift, through a Hewlett-Packard wide band amplifier (1 kHz – 200 MHz), a wide band HP attenuator (d.c. to 1 GHz), to a Ballantyne true RMS voltmeter and a Panoramic Model SPA-3/25a Spectrum Analyzer. The latter was used just as a monitor: to guide adjustment of the wheel speed so that its Doppler frequency shift was centered in the pass band of the filter; and for peaking up of the heterodyne a.c. signal. For a single S/N point, the following a.c. measurements were recorded, with alignment "peaked up":

   1)   Total True RMS power with both LO and Scattered
        beams incident on the PM cathode;

   2)   True RMS noise power with LO Beam blocked off;

   3)   True RMS noise power with Scattered beam blocked off.

   4)   True RMS noise power with all beams blocked off.

This procedure was necessary, since the signal cannot be generated independently of simultaneous noise generated by P_{sc} and P_{LO}. Signal-to-Noise power ratio was then calculated from these measurements as follows: where each symbol represents RMS meter readings, so that each reading must be squared to give mean power (only mean powers can be added and subtracted with random frequency signals): item numbers correspond to those just above:

   1)   Total power = T^2

   2)   Scattered Beam Total Noise Power = $N_{sc}^2 + N_e^2 \equiv N'_{sc}{}^2$
        where N_e^2 = electronic circuit noise (plus dark current
        noise (which is negligible)) and $N'_{sc}{}^2$ is the actual
        meter reading squared, since the two components N_{sc}^2 and
        N_e^2 cannot be separated out.

   3)   LO Beam Total Noise Power = $N_{LO}^2 + N_e^2 \equiv N'_{LO}{}^2$

4) Electronic circuit (Johnson) noise (plus dark noise – negligible) $= N_e^2$

Hence, Signal power is proportional to

$$S^2 = T^2 - N_{sc}^2 - N_{LO}^2 - N_e^2$$

$$= T^2 - N_{sc}'^2 - N_{LO}'^2 + N_e^2 \qquad (1)$$

and Noise Power is proportional to

$$N^2 = N_{sc}^2 + N_{LO}^2 + N_e^2$$

$$= N_{sc}'^2 + N_{LO}'^2 - N_e^2 \qquad (2)$$

Hence, $S^2 = T^2 - N^2$

Thus, $\left(\dfrac{Signal}{Noise} \right)$ Mean square (power) ratio

$$= \frac{T^2 - N^2}{N^2} \quad = \left(\frac{T}{N} \right)^2 - 1$$

i.e., $\left(\dfrac{Signal}{Noise} \right)$ power ratio $= \dfrac{T^2}{N_{sc}'^2 + N_{LO}'^2 - N_e^2} - 1 \quad (3)$

where all quantities in this equation are actual meter readings corresponding to steps (1) through (4) above.

The average beam power measurements were obtained by passing
the voltage developed across the 1500 ohm PM anode load through
a d.c. coupled circuit consisting of a low pass filter (upper
cut-off frequency approx. 10 Hz) to a high impedance electronic
d.c. millivoltmeter. A 25 kΩ decoupling resistor, having a neg-
lible effect on the millivoltmeter reading, was placed in series
with the circuit and located very close to the anode resistor.
This was necessary to remove the serious loading effect of the
d.c. circuit capacitances on the a.c. component of the PM anode
signal voltage. A Tektronix type 647 scope with a high gain dif-
ferential plug-in was also used to monitor both a.c. and d.c.
readings from time to time. With the excellent, accurate slide-
back feature of this plug-in unit, both a.c. and d.c. components
could be displayed directly, although estimation of accurate RMS
a.c. voltages was obviously impossible, as seen by the oscillo-
grams below. The following d.c. readings were taken simultane-
ously with the above listed a.c. readings:

5) d.c. millivoltmeter reading with Scattered beam blocked
off $\equiv I_{ALO}$, so that $P_{LO} = (I_{ALO})$ (PM tube calibration
constant) where I_{ALO} has been corrected for dark current
- (7) below.

6) d.c. millivoltmeter reading with LO beam blocked off $\equiv$
$I_{A_{SC}}$, so that $P_{SC} = (I_{A_{SC}})$ (PM tube calibration constant),
where $I_{A_{SC}}$ has been corrected for dark current

7) d.c. millivoltmeter reading with both beams blocked off,
giving the tube dark current.

Further notes on experimental procedures were given in Section 2.16. Typical measurements appear in the sample calculation below.

Later measurements were made with the following much simplified procedure, substantially reducing the number of readings necessary.

1) Total a.c. power with wheel Doppler frequency shift centered in a.c. band pass filter curve, as monitored on the spectrum analyzer $\equiv$ T in equation (3);

8) Same as (1), but with rotating wheel stationary or rotating slowly $\boxminus$ N in equation (3), i.e. without blocking off either beam.

Reading (8) gave N directly. This is because the noise, being white noise, gave the same meter reading irrespective of wheel speed and heterodyne signal, i.e. just the noise passing through the pass band of the filter. On the other hand, with the wheel frequency such that the heterodyne signal was well outside the filter passband, no heterodyne signal could pass through the filter. Thus, with the a.c. band pass filter, turning off or markedly changing the wheel speed was equivalent to "switching off" the heterodyne signal S, while leaving the total noise due to both beams unchanged.

Checks showed that the two methods were in complete agreement, so that the second, quicker, method was adopted as standard.

Because of the low signal-to-noise ratios (in the range of .001 to 1) at the low laser power ($\sim$ 50 mw) used, some random scattering of the data was to be expected. Hence initially three, and for the majority of reported results, five complete samples for each data point were taken. A full statistical calculation was performed for each point, to determine the best curve fit, and to show the data spread. The measured data, with 90%

probability brackets, are plotted in Figure 2.18-2. The method
used for the sample probability analysis is given below.

2.18.1.1 Error Analysis

Each point shown in the graph of signal-to-
noise vs. P_{ref}/P_{sc} is the arithmetical average of three measure-
ments. No data were discarded. The error brackets were computed
for 90% confidence level by standard techniques as follows:

Let three data points, for example three measurements of the
signal-to-noise ratio, for a given set of experimental condi-
tions be denoted by x_1, x_2, x_3. The mean value (plotted in the
figure) is

$$\bar{x} = \frac{1}{3} (x_1 + x_2 + x_s) \quad . \tag{4}$$

Then an estimate of the standard deviation of the results of
repeating the measurement under the sane condition many times,
denoted by S, is found from the formula

$$S \quad \cdot \quad \sum_{i=1}^{n} \frac{(x_i - \bar{x})^2}{n - 1} \quad ; \tag{5}$$

where for this case (three data points) n = 3. The probability
that μ, the mean of the results of many repetitions of the mea-
surement (under the same conditions) is in the range defined by

$$\bar{x} - \frac{sk}{\sqrt{n}} \leq \mu \leq \bar{x} + \frac{sk}{\sqrt{n}} \quad , \tag{6}$$

is given by Student's distribution (1). Again n denotes the
number of data points taken in the average, and k is a constant.
For the present case k was taken (from Student's tables) to give
an error bracket such that the probability is 90% that the mean
of many repetitions of the measurement will fall inside the error
bracket.

The plot shows POWER RATED S/N (vertical axis, from 0.001 to 10) versus $\frac{P_{REF}}{P_{SCAT}}$ (horizontal axis, from 0.001 to 100).

THEORETICAL CURVE REDUCED BY 52 D.B.

Photomultiplier: EMI 9558B
Wavelength Characteristics: S 20, filtered by
    narrow-band filter centered at 6328 Å
Photomultiplier Volts = 635
Lensitivity is 0.18 μW/μAmp
DC anode volts across 1500 Ω, Scattered Beam
only, is approximately constant at an average
value of .01438 volts (after subtracting average
dark current volts = .00015 V)

$\therefore$ Anode current = $\frac{.01438}{1500}$ x 10^6 μA = 9.586 μA

$\therefore$ Scattered beam power = (9.586) (0.18) = 1.7255 μWatts
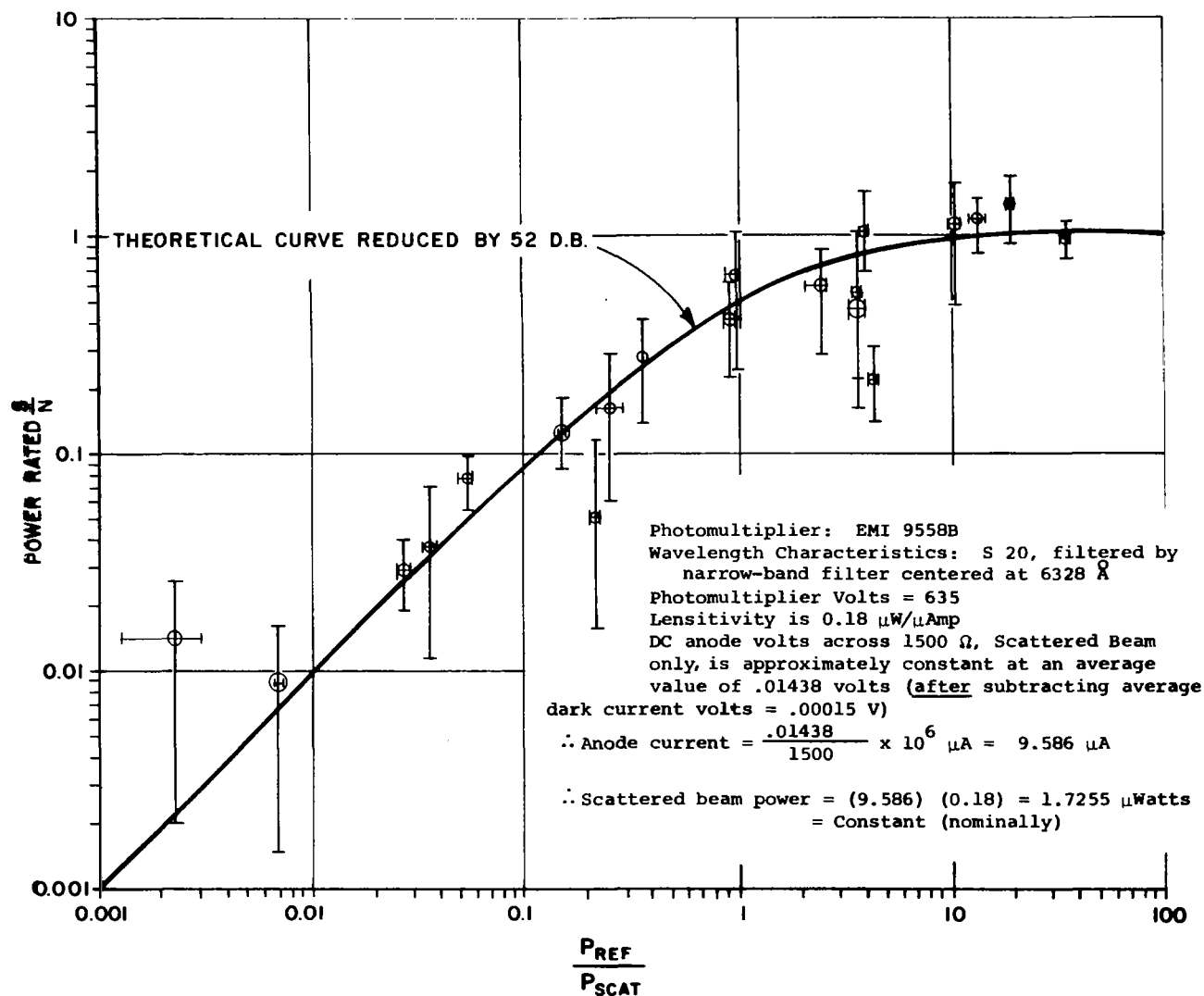   = Constant (nominally)

Figure 2.18-2 - Experimental Data Compared with Calculated S/N Plot
              S/N versus Pref/Pscat

2.18.1.2 Theoretical Curve

The final step in verification of the Signal-to-Noise power ratio formula was to calculate the theoretical S/N curve using equation (2) above, substituting in the photomultiplier and circuit constants used in the experiments. The formula involves the radiant sensitivity of the photocathode at the laser wavelength. This quantity was computed from the typical quantum efficiency for S-20 response quoted in the data sheet for the EMI 9558B photomultiplier tube used.

The scattered and local oscillator powers were measured in the experiment. The noise bandwidth was taken to be the bandwidth of the electronic filter at its 20 db points $(.457 \times 10^6$ Hz). The factor k representing the loss of signal-to-noise in the dynode chain of the multiplier was computed from the radiant sensitivity of the photocathode (as above) and the measured overall sensitivity of the particular tube used, as reported in Section 2.17.

During the period of time over the experimental data were recorded, the signal power drifted somewhat. This was not taken into account because the error brackets on the experimental points are large enough to cover this effect. The average of the signal power (maintained constant within experimental limits) over the whole experiment was used as signal power (P_s=1.72 microwatts).

The signal-to-noise equation, evaluated under these conditions (see Sample Calculation in 2.18.1.3), and assuming $\mu_T = 1$, is:

$$\left(\frac{S}{N}\right) = 1.62 \times 10^5 \left[\frac{P_{LO}/P_{scat}}{1 + P_{LO}/P_{scat}}\right] \tag{7}$$

This equation gives a signal-to-noise ratio in the flat, assymptotic region of Figure 2.18-2 of 1.62×10^5, about 52 db higher than the experiment. It was expected that the experiment would yield substantially lower S/N than theory because the heterodyne loss factor μ_T if, of course, less than unity. Hence $\mu_T = -52db$, and is assumed to be entirely due to loss from random scattering in the thickness of the rotating wheel.

While this is a fairly large difference, it is to be noted that the shape of the theoretical curve matches the experimental points fairly well and hence that nineteen data points have been fitted with a single adjustable parameter. Hence it is concluded that excellent experimental agreement with the theoretical S/N equation has been demonstrated. Sample calculations of theoretical and experimental data follow.

2.18.1.3 Sample Calculation of Ideal Signal-to-Noise Ratio

The expression for the mean square signal-to-noise power ratio at the photomultiplier anode is shown in Section 2.5 to be, assuming the heterodyning loss factor (or efficiency), defined in Section 2.6 to be unity:

$$\left(\frac{S}{N}\right)_{MSA} = \left(\frac{S_k}{ek\Delta f}\right) P_s \left(\frac{P_{LO}/P_s}{1 + P_{LO}/P_s}\right) = \left(\frac{P_s}{\Delta f}\right)\left(\frac{S_k}{ek}\right)\frac{1}{(1 + \frac{P_s}{P_{LO}})} \quad (1)$$

where the symbols have the following meanings

S_k is the radiant sensitivity (amps/watt) <u>of the cathode</u> for the wavelength at which measurements are made

e is the electron charge (1.6×10^{19} coulombs)

k is the noise figure for the dynode chain in the photo-multiplier = $\frac{\sigma}{\sigma-1}$,

σ = the current multiplication per stage in the dynode chain,

Δf is the bandwidth of the system (see Section 2.5)

P_s and P_{LO} are the powers of the scattered light and local oscillator reference beams, respectively.

The quantity S_k is computed as follows. The tube used in the laboratory Signal-to-Noise ratio measurements was an EMI 9558B photomultiplier, which has an S-20 spectral response. The laser source used was a Helium-Neon gas laser, generating a light beam of wavelength 6328Å. The radiant sensitivity is defined, in amps per watt, as:

$$S_k = \frac{\text{(quantum efficiency at incident light wavelength)}}{\text{(energy of photon at wavelength, joules)}} \quad \cdots\cdots$$

$$\text{x (electron charge coulombs)}$$

The EMI data sheet for the 9558B shows a quantum efficiency of about 6% at 6328Å. The energy in joules of a photon of wavelength λ Å is $(1.98 \times 10^{-15}/\lambda)$. Thus

$$S_k = \frac{(.06)(11.6 \times 10^{-19})(6328)}{(1.98 \times 10^{-15})} = .0307 \text{ amps/watt}$$

The quantity k is given by $k = \sigma/(\sigma-1)$ where σ is the current multiplication per state in the dynode chain. Hence

$$\sigma = \left[\frac{\text{(overall sensitivity)}}{\text{(cathode sensitivity)}}\right]^{1/n}$$

where n is the number of stages. The measurements were made with the photomultiplier supply voltage at 635 v. At this voltage and at 6328Å, the measured sensitivity of the particular tube used was 5.55 amps/watt (from calibration reported, and curves presented in Section 2.17). There are 11 stages in the tube, so that

$$\sigma = \left(\frac{5.55}{S_k}\right)^{1/11} = \left(\frac{5.55}{.0307}\right)^{1/11} = (18.1)^{1/11} \approx 1.3$$

and hence

$$k = \frac{\sigma}{\sigma-1} = \frac{1.3}{.3} = 4.34$$

The bandwidth Δf is taken to be the bandwidth of the electronic filter at 20 db points (from measured filter curve, (Figure 2.18-6)

$$\Delta f = .457 \times 10^6 \text{ Hz}$$

The scattered power P_s was held approximately constant during the measurements. Its measured value was

$$P_s = 1.72 \times 10^{-6} \text{ watts}$$

Substituting these numbers into the expression for S/N yields

$$\left(\frac{S}{N}\right)_{MSA} = \left(\frac{.0307}{1.6 \times 10^{-19} \times 4.34 \times .457 \times 10^6}\right)(1.72 \times 10^{-6}\left(\frac{P_{LO}/P_s}{1 + P_{LO}/P_s}\right)$$

i.e. $\left(\frac{S}{N}\right)_{MSA} = 1.62 \times 10^5 \left(\frac{P_{LO}/P_s}{1 + P_{LO}/P_s}\right)$ \hfill (2)

2.18.1.4 Sample Calculation of Experimental Data

Date: 7-15-67; Location: Raytheon, Sudbury, Mass.

TABLE 2.18-1 - INSTRUMENT READINGS

Average powers, D.C. mv			A.C. signals, mv RMS			
Ref. beam I_{ref}	Scat. Beam I_{sc}	Both Beams Blocked I_{Dark}	Ref. Beam only N'_{ref}	Scat. Beam Only N'_{scat}	Combined Beams T	Both Beams Blocked N_e
575	17	0.25	1.20	0.256	1.75	0.15
575	17	0.28	1.27	0.256	1.75	0.15
575	16.5	0.29	1.20	0.260	1.70	0.15

TABLE 2.18-2 - AVERAGE AND MEAN SQUARE POWER CALCULATIONS

Average Powers		Signal-to-Noise			
$I_{scat} - I_{dark}$ P_{sc}	$\dfrac{I_{ref} - I_{dark}}{I_{sc} - I_{dark}}$ $= P_{ref}/P_{scat}$	Noise Power $\equiv N^2$ $= N'^2_{ref} + N'^2_{scat} - N^{2*}_{e}$	(Signal+Noise) Power $= T^2_{MV^2}$	Signal Power $= T^2$ $= T^2 - N^2$	Signal Power Noise Power $= (\frac{S}{N})^2$
16.75	34.31	1.483	3.0625	1.58	1.0654
16.72	34.37	1.655	3.0625	1.407	0.850
16.21	35.45	1.483	2.890	1.407	0.9487

*N^2_e is subtracted, since we want the signal-to-noise ratio at the anode, and photo-multiplier dark noise is assumed nelgigible. since the d.c. - dark current was extremely small, as seen from Table 2.18-1. See description of procedure in 2.18-1.

2.18.1.5 Statistical Error Analysis

Confidence level chosen   90%

$\text{Average} \left(\dfrac{\text{Signal power}}{\text{Noise power}} \right)$ =   0.955

Standard Deviation   =   .1706

Brackets: $(0.955) \pm \dfrac{(.1706)(2.92)}{\sqrt{3}} = 0.955 \pm 0.288$

$\text{Average} \left(\dfrac{P_{ref}}{P_{sc}} \right)$ = 34.71

Standard Deviation   =   .6415

Brackets: $(34.71) \pm \dfrac{(0.6415)(2.92)}{\sqrt{3}} = 34.71 \pm 1.081$

2.18.2 Dependence of Signal-to-Noise Ratio on Scattered Beam Power

The objective of this experimental series was to verify that, in the low scattered power operating mode (see Section 2.5), signal-to-noise power ratio is proportional to Scattered Beam Power.

In the low power mode, the requirement, verified experimentally in 2.18.1 above, is that $P_{LO}/P_{sc} \gg 1$. Under these conditions, equation (2) can be rewritten as:

$$\left(\frac{S}{N}\right)_{A,MS} = \mu_T \left(\frac{P_s}{\Delta f}\right)\left(\frac{S_r}{ek}\right)$$

$$= (\text{const}) \ P_s \ , \tag{4}$$

with fixed system bandwidth Δf, and photomultiplier noise figure k = noise figure for the dynode chain. Since $k = \frac{\sigma}{\sigma - 1}$, where σ is the current multiplication per stage in the dynode chain, the experiments must be run either at constant photomultiplier voltage, or by correcting for changing k if PM voltage is changed.

Scattering from a rotating wheel was used, and the experiments of 2.18.1 essentially repeated, the only difference being that

1) Scattered average power (P_{sc}) and Reference Beam average power (P_{LO}) were measured, with no filters, by successively blocking the two beams. It was verified that $P_{LO}/P_{sc} \gg 1$, so that the conditions required by equation (4) were satisfied. (If the condition had been violated, a neutral filter in the appropriate beam would have readily corrected the condition.).

2) With this condition of $P_{LO}/P_{sc} \gg 1$, Signal-to-Noise power ratio measurements were made with sucessively reduced levels of P_{sc}. The level changes were simply brought about by inserting progressively dense neutral density filters in the incoming laser beam. Clearly such a procedure reduced P_{sc}, while leaving the ratio P_{LO}/P_{sc} unchanged.

After distribution analysis as described above, results are plotted in Figure 2.18-3. The theoretical straight line relationship of S/N to P_{sc} is drawn on the same curve. Good agreement was obtained, so that equation (4) was substantiated by experiment. Data scatter is reasonably attributable to the random scatter expected with measurements made at very low S/N levels. Comments on these results are made in Section 2.18.7.

2.18.3 Extrapolation of Results to Higher Laser Power

With the establishment of the Signal-to-Noise equation (4), the S/N power ratio to be expected from Doppler frequency shift measurements made with a rotating wheel using a laser of higher power can be readily calculated.

S/N ratio at 50 mw laser power ∼ | from 2.18.2

S/N ratio at 1 watt (e.g. argon) laser power = $\frac{1000}{50}$=20=30db.

This Signal-to-Noise ratio is a good working level for straightforward electronic circuit design. When calculating S/N for Doppler measurements from other scatterers, e.g. particles in gases, the ratio must be corrected for the appropriate value of $\mu_T \sim \mu_s$, in accordance with the relationship of equation (4) above.
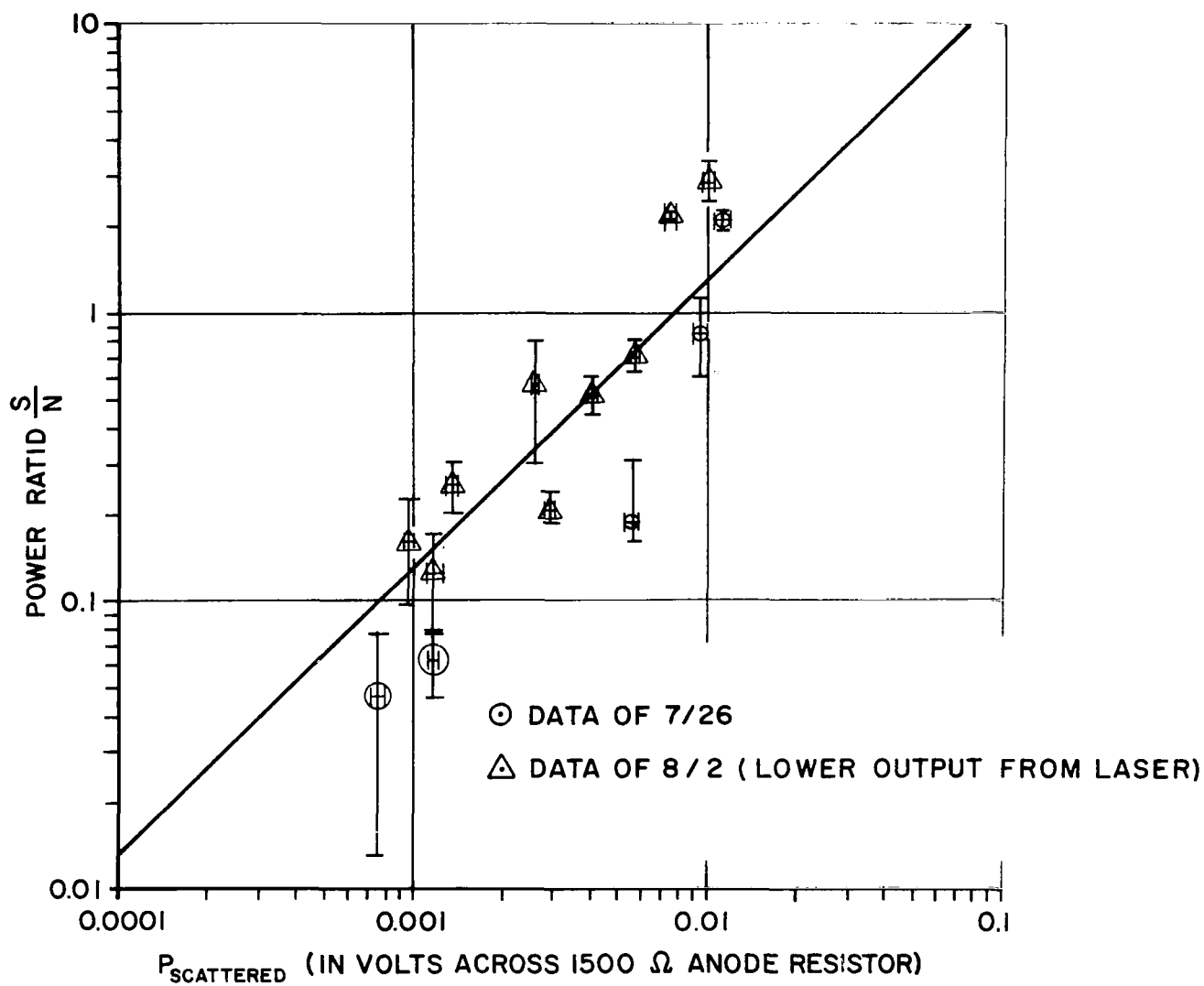
Fig. 2.18-3. Experimental Data Compared with Calculated S/N Plot:
S/N versus P_{sc}, $(P_{LO}/P_{sc} \gg 1)$

2.18.4 Instrumental Broadening

Section 2.11 analyzes the several causes of unwanted signal broadening, termed Instrumental Broadening, which are characteristic of the Laser Doppler Velocity Instrument.

To test the analysis specifically for the case of spectral broadening caused by the finite solid angle of the focused scattered light collecting lens (believed to be the major broadening mechanism), the Doppler frequency spectrum was observed of light scattered by passing through a rotating disc. According to Section 2-11, no other causes of spectrum broadening arise in this case, so that observed broadening should agree with equation (5) of 2.11.

Figure 2.18.4 shows relevant data and photographs of typical spectrum analyses displays of the Doppler frequency spectrum of light scattered by passing through the rotating plastic disc described in Section 2.16. Instrumental Broadening caused by the finite instrument aperture was calculated for the given conditions from equation (5) of Section 2.11 as follows:

$$\Delta f_A (6328\text{Å}) \quad = 545 M \, \frac{\cos \theta}{2F} \text{ MHz}$$

Wheel speed $\quad = 2,000$ r/m

Scatter diameter $= 5.625$ inches

$$U \quad = \frac{\pi \times 5.625 \times 2.54 \times 2000}{60}$$

$$= 1,496 \text{ cm/sec (49.1 ft/sec)}$$

$$M \quad = \frac{1,496}{34,500} = 0.0433$$

$$\cos \theta = 0.9782$$

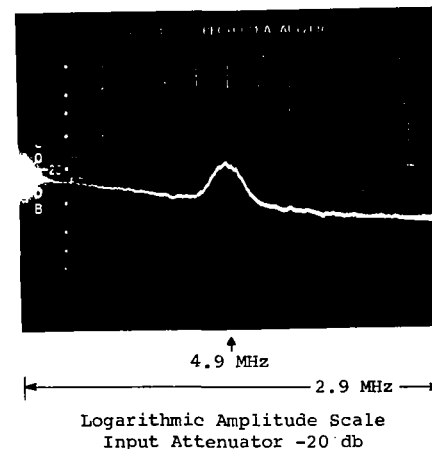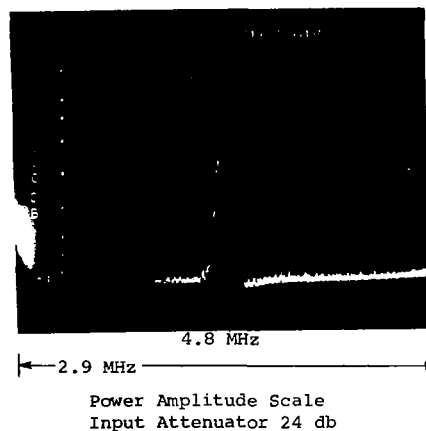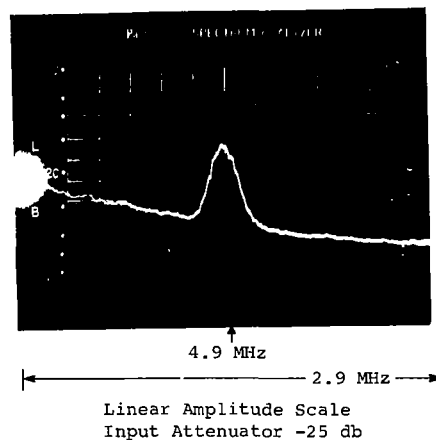$$F \quad = \frac{3 \ 1/2 \text{ inches}}{05/32 \text{ inch}} = 28$$

$$\Delta f_A (6328\text{Å}) \quad = \frac{(545)(0.0433)(0.9782)}{(2)(22.4)} = 0.515 \text{MHz}$$

$$= 515 \text{ kHz}$$

2.18-21

50 mV/cm

100 msec/cm

(a) Oscillogram of Doppler
     Frequency Waveform

4.9 MHz

|◄──────────── 2.9 MHz ───►|

Linear Amplitude Scale
Input Attenuator -25 db

4.9 MHz

|◄──────────── 2.9 MHz ───►|

Logarithmic Amplitude Scale
Input Attenuator -20 db

4.8 MHz

|◄─2.9 MHz ─────────────────►|

Power Amplitude Scale
Input Attenuator 24 db

DATA

Wheel Speed: 2,000 rpm
Distance from Edge: 3/16 inch
Spectrum Analyzer Settings:

   IF Bandwidth   – max
   IF Attenuator – 0 db
   Sweep Rate   – 2 sec
   Video Filter   – max

Test No. 05181; Date 5-18-67
Spectrum Analyzer – Panoramic
   (Singer) Model SPA-3/25a

(b) Photographs of Spectrum Analyzer Display

Figure 2.18-4 Oscillograms of Rotating Wheel Doppler Frequency
               Signal and Spectrum with Linear, Logarithmic,
               and Power Signal Amplitude Analyzer Modes

A comparison of calculated and experimental Doppler frequency can readily be made:

Doppler frequency shift $f = 545\ M \sin \theta$ MHz for 34,500 cm/sec sound velocity

$\lambda = 6328 \overset{\circ}{A}$

$\theta = 12^{\circ}$; $\sin \theta = 0.2079$

$M = 0.0433$ (from above)

$\therefore\ f = 545 \times 0.0433 \times .2079 = 4.906$ MHz

From figure 2.18-4, the mean Doppler frequency shift is seen to be 4.9 MHz. Again, agreement between calculation and experiment is excellent. Then the ratio

$$\frac{\text{Instrumental Broadening}}{\text{Mean Frequency Shift}} = \frac{0.522}{4.9} = 10.7\%$$

It is therefore concluded that, in agreement with the conclusions of Section 2.11, the Instrumental Broadening, stemming from the use of a focused lens scattered light collecting system, which therefore collects light over a range of scattering angles, is the cause of the spectral broadening observed in these experiments. As the F number $(\equiv \frac{\text{focal length}}{\text{aperture used}})$ of the collecting lens is decreased, this type of broadening becomes an appreciable fraction of the mean Doppler frequency shift.

It is also noted, from Figure 2.18-4, that with low signal-to-noise ratio, the power and linear spectrum analyzer amplitude scales give the largest display of signal compared with noise. Conversly, the logarithmic scale gives a "cleaner" display when higher signal-to-noise ratio is available.

From Figure 2.18-4, spectral broadening is seen to be:

$$\Delta f_A \text{(experimental)} = \left(\frac{1.8}{10}\right)(2.9)\text{MHz} = 522 \text{ kHz, in good agreement}$$

with calculation.

A comparison of calculated and experimental Doppler frequency can readily be made:

Doppler frequency shift $f = 545$ M $\sin\theta$ MHz for 34,500 cm/sec sound velocity

$$\lambda = 6328\text{Å}$$

$$\theta = 12°; \ \sin\theta = 0.2079$$

$$M = 0.0433 \text{ (from above)}$$

$$f = 545 \times 0.0433 \times .2079$$

$$= 4.906 \text{ MHz}$$

From Figure 2.18-4, the mean Doppler frequency shift is seen to be 4.9 MHz. Again, agreement between calculation and experiment is excellent. Then the ratio

$$\frac{\text{Instrumental Broadening}}{\text{Mean Frequency Shift}} = \frac{0.522}{4.9} = 10.7\%$$

It is therefore concluded that, in agreement with the conclusions of Section 2.11, the Instrumental Broadening, stemming from the use of a focused lens scattered light collecting system, which therefore collects light over a range of scattering angles, is the cause of the spectral broadening observed in these experiments. As the F $= \dfrac{\text{focal length}}{\text{aperture used}}$ of the collecting lens is decreased, this type of broadening becomes an appreciable fraction of the mean Doppler frequency shift.

It is also noted, from Fig. 2.18-4, that with low signal-to-noise ratio, the power and linear spectrum analyzer amplitude scales give the largest display of signal compared with noise. Conversely, the logarithmic scale gives a "cleaner" display when higher signal-to-noise ratio is available.

## 2.18.5 The Dependence of Noise Power on System Bandwidth

The theoretical Signal to Noise Power Ratio, developed as equation (7) in Section 2.5, shows an inverse dependence on system bandwidth. This is based on the assumption that the principal noise source is σwhiteσ noise (i.e., uniform over the whole frequency spectrum), generated in the photomultiplier tube ("noise in signal").

The first photograph of Figure 2.18-5 shows the Doppler frequency shift spectrum of light scattered by passing through the rotating plastic disc described in Section 2.16. The Doppler frequency shift is observed above on uniform noise background. The second photograph shows the Spectrum Analyzer display with the wheel removed from the laser beam, and an electronic filter inserted in the signal connection from the photomultiplier. The characteristic pass band of this filter, measured by conventional methods, is shown in Figure 2.18-6. It will be seen that the filter characteristic appears in the spectrum display, since it passes the white noise in its pass band, and removes it on either side of the band.

The last photograph again shows the wheel Doppler spectrum, but this time passed through the filter. The final result is the Doppler spectrum of the first photo "sitting on top of" the filtered noise spectrum of the second photo. The reduction in total noise power is proportional to the reduction in area under the curve as a result of inserting the filter.

This filter was used for all the Signal-to-Noise power ratio experiments described above. The gain in signal to noise, ratio through the use of the narrow band filter is evident. It is clear that such a filter must span the broadened Doppler spectrum, to avoid loss of signal. Since the broadening is instrumental broadening, and of a different shape from the filter characteristic, there is clearly a band pass filter shape which optimizes the Signal to Noise ratio, i.e., removes minimum signal, and maximum noise. This shape has to be determined by analysis.

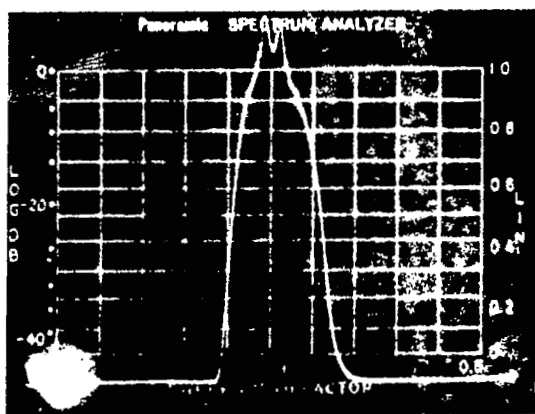2.18-25
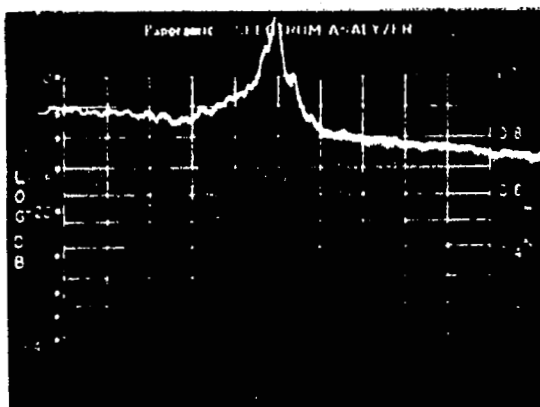
(a) Spectrum of Rotating Wheel
    Doppler Frequency, No
    Electronic Filter

    Sweepwidth: 500 kHz
    Centre Frequency: 2 MHz
    Wheel Speed: 1190 rpm
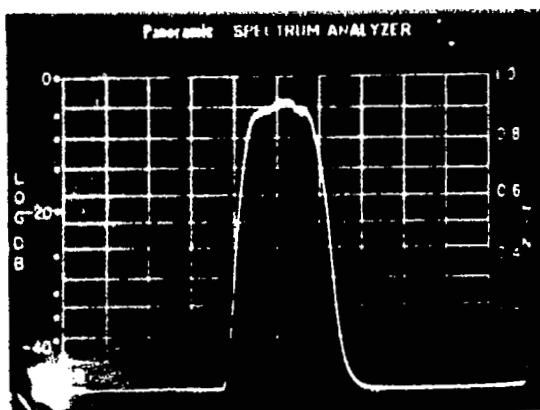
(b) Spectrum of Noise with
    Bandpass Electronic Filter
    Inserted

    Sweepwidth: 1 MHz
    Centre Frequency: 2 MHz
    Wheel Speed: Stationary

(c) Spectrum of Rotating Wheel
    Doppler Frequency, Elec-
    tronic Filter Inserted

    Sweepwidth: 1 MHz
    Centre Frequency: 2 MHz
    Wheel Speed: 1190 rpm

Figure 2.18-5   Photographs of Rotating Wheel Spectrum Analyzer
                Display showing Reduction of System Noise by
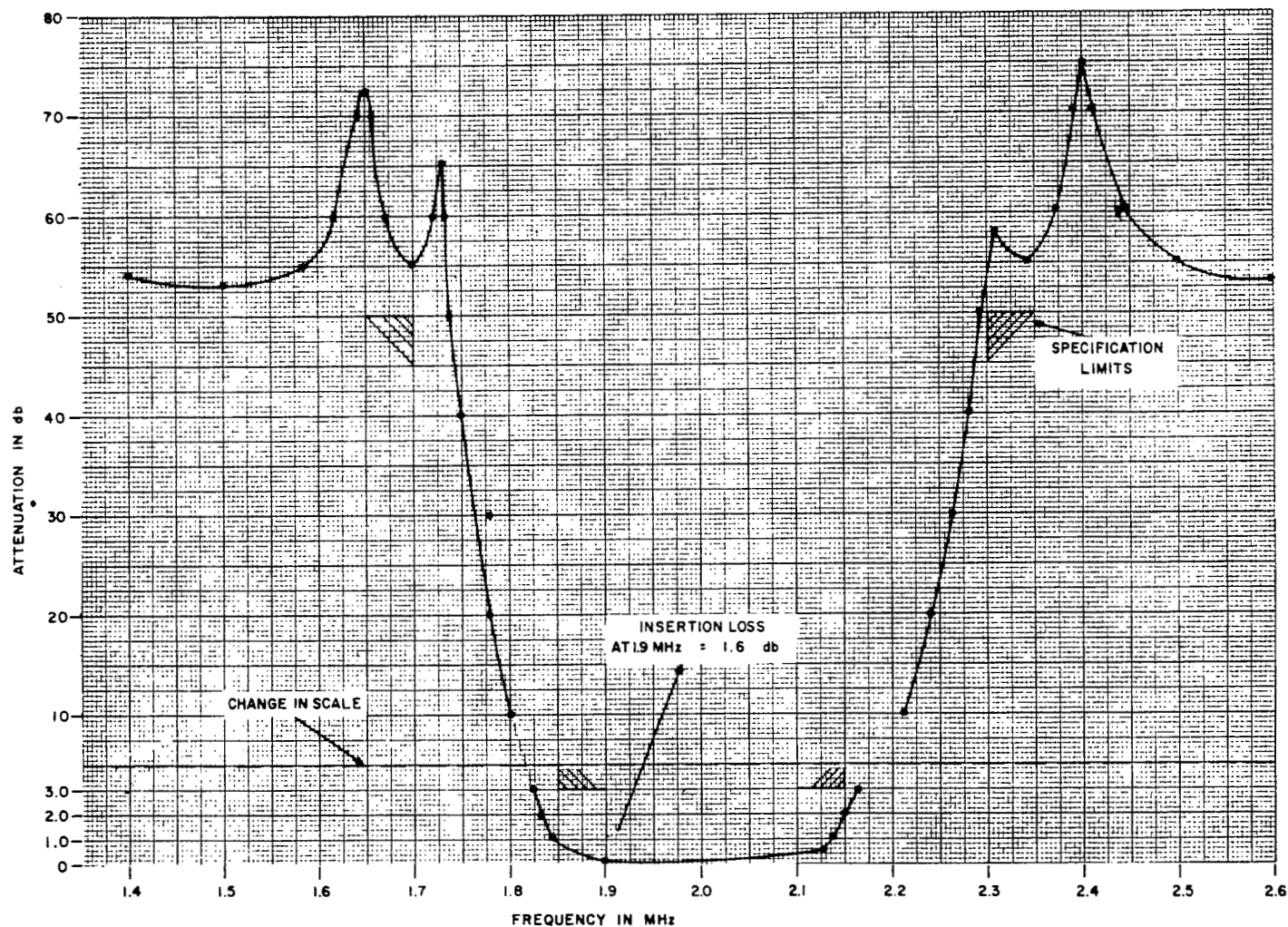   Narrow Bandpass Filter

Figure 2.18-6   Measured Pass Band of Electronic Filter used in Rotating
Wheel S/N Measurements

Finally, with the use of a filter of the same width as the signal, and only under this condition, the S/N ratio, as measured by the somewhat laborious but necessary techniques described above, can be read off directly from the Spectrum Analyzer Display. This was done in a few cases, and agreed with the direct measurement technique.

2.18.6   System Electronic Component Noise (Johnson Noise)

In analysis of the Signal-to-Noise Power Ratio to evolve equation (7) of Section 2.5, it was assumed that the prime noise source was the photomultiplier itself, and that Johnson noise from electronic components made a negligible contribution to the total system noise appearing in the denominator of the equation.

Our experimental data bear out this assumption. In the sample calculation of Section 2.18.1.4, measured data showed that electrical circuit noise voltage developed (obtained by completely masking off the photomultiplier) was only 0.15 mV RMS, compared with 1.20 mV RMS of Reference Beam Noise N_{ref} and 1.75mV RMS, of total Signal T. Since power is proportional to $(RMS)^2$,

$$\frac{\text{Electrical Noise Power}}{\text{Total PM Noise Power}} = \frac{0.15^2}{1.5} = 1.5\%,$$

indeed a negligible effect in our investigation. Note that the simple method of determining Johnson noise by merely masking off the PM tube cathode will give a noise power which also includes PM tube dark noise. Since to correct for this in the present investigation is a correction on a correction for Ne which is already second order, it was not considered worthwhile to separate out the two noise sources, so that they are both lumped together under Johnson noise.

2.18.7 Comments on Results of Measurements of Signal-to-Noise Ratio Dependence on Scattered Power (Section 2.18.2)

The following comments are made on results, pending further study where considered desirable:

1. There appears to be a systematic variation between results taken on two different days.

2. The spread of data generally tends to be lower as Signal-to-Noise Ratio increases.

3. The slope of the curve through the experimental points is approximately 45°, following theory. A line could be drawn at slightly greater slope, but no physical reason exists for doing so.

4. The spread of data is wider than desirable. Further experimental data should be taken to clarify the reason.

5. The scatter in experimental data could be caused by drift in optical alignment of the system. Measurements should be repeated with a more rigid optical system; for example, using the 3-D instrument (Section 2.20).

6. One could concede that the curve should be drawn concave upwards through the 9 sets of data, but again, no physical reason is known for doing so at this time; further experimental measurements should clear up this question.

2.19 Experimental Measurements of Turbulence and Velocity at NASA Marshall Space Flight Center

The experiments described in this section were performed at the NASA George C. Marshall Space Flight Center, in cooperation with R. M. Huffaker, E. Brewer, D. Takeuchi, A. Huelett of NASA and J. Reardon and K. Smith of the Hayes International Corp. Professors Earl Logan of Arizona State University and Alan R. Barbin of Auburn University consulted on fluid mechanics.

In summary, the experiments consisted of:

1. Comparison of turbulence measurements made by Laser Doppler Velocity Meter and Hot Wire Anemometer on an ASME experimental nozzle.

2. Measurement of air velocity up to Mach 2 on the 7 inch wind tunnel, using the Laser Doppler Flowmeter.

3. Measurement of system parameters and signal-to-noise ratios of the Laser Doppler Velocity Meter, using the experimental ASME nozzle.

In all cases, smoke bombs were used to provide the scattering injectant.

2.19.1 Comparative Turbulence Measurements, Laser Doppler Velocity Meter and Hot Wire Anemometer

Using a simple screened plenum chamber exhausting to atmosphere through a one-half inch diameter nozzle, turbulence measurements were made on the same flow stream, using a DISA Constant Temperature Hot Wire Anemometer Model 55A01, and an experimental (one dimensional) Laser Doppler Velocity Instrument (Figure 2.19-1). The region probed was on the nozzle axis, and two inches downstream from it (x/D = 4). A manometer provided nozzle upstream pressure conditions. The jet was directed into an exhaust duct leading
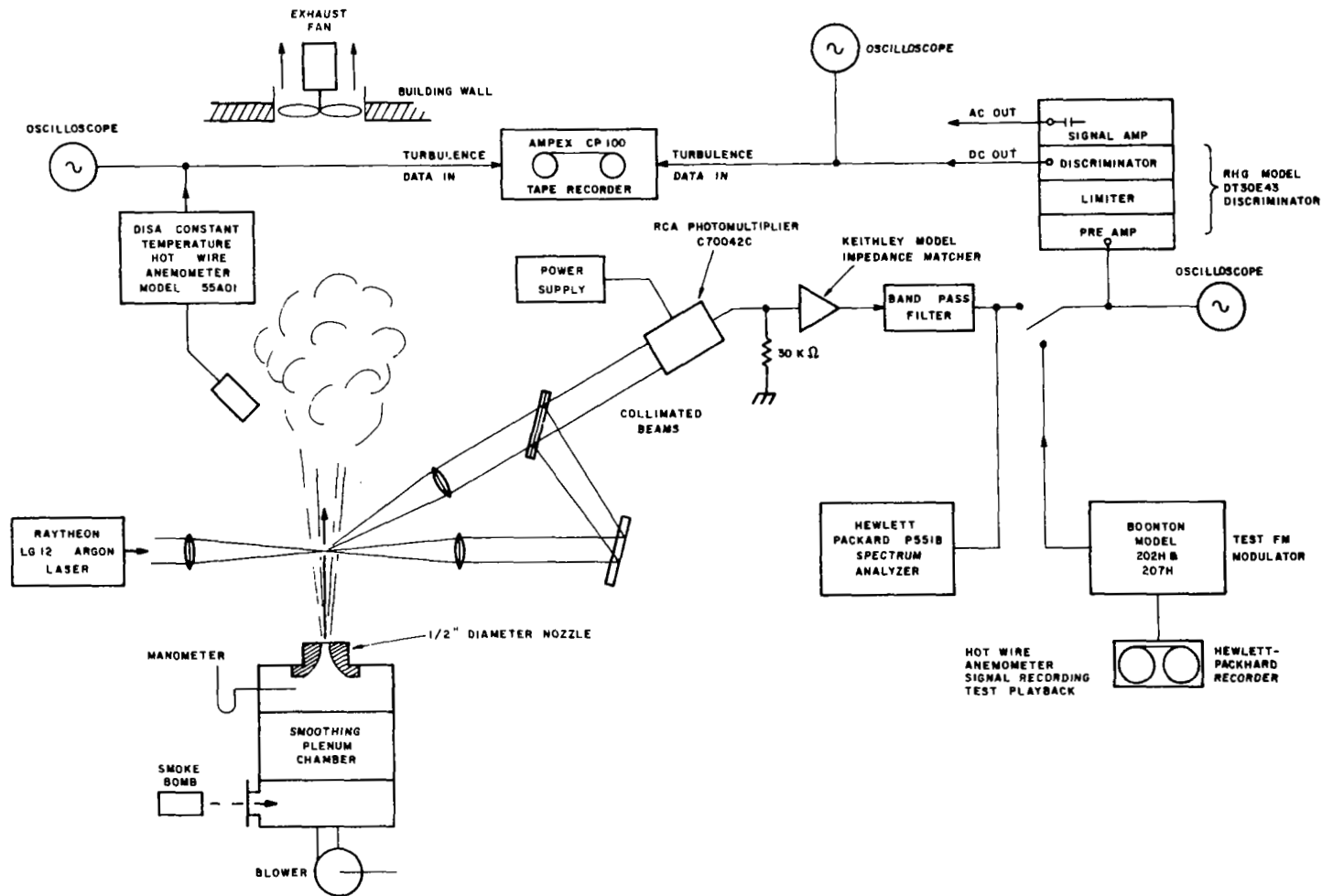
Figure 2.19-1   Diagram of Laser Doppler Velocity Meter – Hot Wire Anenometer
Comparative Turbulence Measurement Experiments

outside the building, to remove noxious smoke. Positioning of
the nozzle relative to the two instruments was arranged by
mounting the whole nozzle plenum chamber assembly on machine
tool slides.

The nozzle was similar to an ASME nozzle, except that it
was constructed, for simplicity, with a single 1 1/2 inch radius
of curvature, instead of two radii. The constant diameter
(1/2 inch) section was one inch long.

Checkout runs were made using the Hot Wire Anemometer, in
the course of which an approximate mapping of the nozzle turbu-
lence was obtained.

2.19.1.1 Checkout of Laser Doppler Flowmeter Signal Processing Electronics

Preliminary runs were also made with the
Laser Doppler Velocity Instrument. The electronic circuit
arrangement used for these measurements is shown schematically
in Figure 2.19-1. A 30,000 ohm anode load resistor was used.
The photomultiplier output signal was fed, through an impedance
matching amplifier to an RHG Model DT30E43 Discriminator, whose
specification is given in Table 2.19-1.

Particular attention is drawn to the filter and its use in
the circuit. As shown in the analysis of Section 2.5, the
signal-to-noise power ratio of the whole system is inversely
proportional to the bandwidth of the electronics. It is essential,
therefore, to reduce artifically the system bandwidth to the
minimum consistent with the passing of the Doppler frequency
signal. In this experiment, the filter was specially designed
and built so that its pass band just encompassed the measured

TABLE 2.19-1

SPECIFICATIONS OF FHG MODEL DT30E43
FREQUENCY DISCRIMINATOR

Model No. DT30E43	
Serial No. 3-082-4	
Center Frequency –	30 MHz
Peak-to-Peak Bandwidth –	9 MHz
Video Output Sensitivity –	.3V/MHz
DC-Output Sensitivity –	.15V/MHz
Risetime –	.2 μsec
Linearity –	> ±3% over ±3 MHz
Input –	−50 dbm ± 5 db
Dynamic Range –	40 db
Power Drain –	115 V at 0.2 amps.

operating frequency range of the RHG discriminator. Another
important function of the filter was to eliminate low frequency
(from power lines, machinery, etc.) noise pickup in the low level
circuits. Such low frequency noise distorts the frequency
spectrum, and can cause amplifier saturation. For the latter
reason, the filter was placed in the 50 ohm output circuit of
the impedance matcher.

The input and output circuits to the discriminator were
carefully set up to provide signal levels within the range of
its limiter. The operation of the discriminator was first
checked by plotting its "S"-curve, using a General Radio Sweep-
frequency Generator (type 1025-A). The discriminator charac-
teristics were excellent, better than specification. After
signal level adjustments for optimum operating conditions, a
final (and revealing) operational check was made of the whole
discriminator circuit chain by the following method.

A recording was first made on a Hewlett-Packard tape recorder
of the output signal from the hot wire anemometer, when measuring
turbulence in the experimental nozzle flow. The taped signal was
then played back into a Boonton Model 202H FM-AM signal generator
with a Boonton 207H Univerter, and the generated carrier frequency
was set to be the center frequency of the RHG discriminator,
namely 30 MHz. Thus the output of the FM Signal Generator repre-
sented a mean Doppler shift, modulated by turbulence fluctuations
- exactly the same signal as would be expected out of the photo-
multiplier. This FM modulated carrier was fed into the Laser
Doppler Velocity Instrument discriminator chain input circuit.

The tape recorder output and the discriminator output were then simultaneously displayed on a dual-channel oscilloscope. Single-shot Polaroid photographs were made of the dual display. Two samples of these photographs appear as Figure 2.19-2. The correspondence between the recorded hot wire anemometer signal and the processed discriminator output signal is seen to be virtually perfect.

2.19.1.2 Turbulence Measurements

With all apparatus in good working order, the runs were made. Since we were interested only in the turbulence measurements, no attempt was made to relate scales and velocities absolutely. The straightforward but lengthy scale calibrations were considered irrelevant with respect to experimental objectives, since scale runs had been made and verified independently on other occasions for both instruments.

During the turbulence runs, the signals from both instruments were recorded on the multichannel Ampex CP100 tape recorder. Figure 2.19-3 shows an oscillogram of a typical photomultiplier signal plus noise output signal, together with an oscillogram of the noise alone, obtained by blocking off the scattered light beam.

The recorded signals were sent to a data-processing computer group at the center, where the signals were plotted. Samples of the two signal plots appear in the lower half of Figure 2.19-4. These signals were recorded for a flow stream mean velocity of 200 ft/sec. The signals were also passed through an analog to digital converter, then processed through the RAVAN* computer

- - - - - - - -

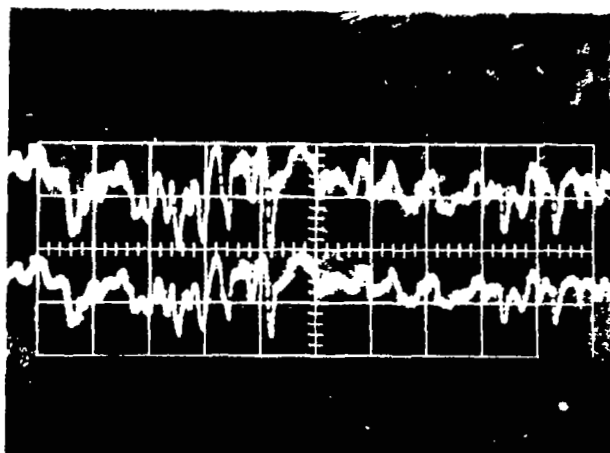*Random Vibration Analysis Program.
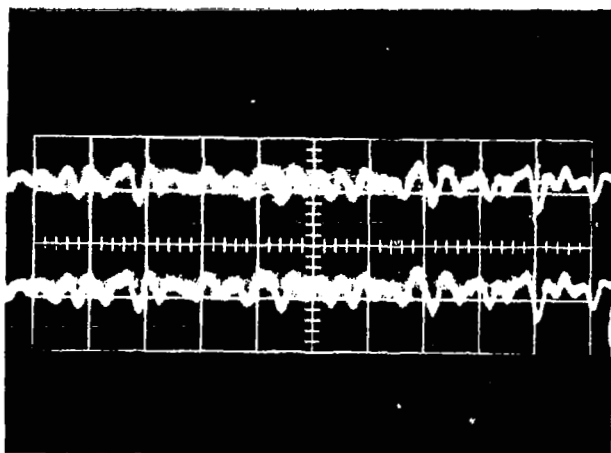
Discriminator
Output Signal

Input Signal to
Discriminator (Tape
Recorded Hot Wire
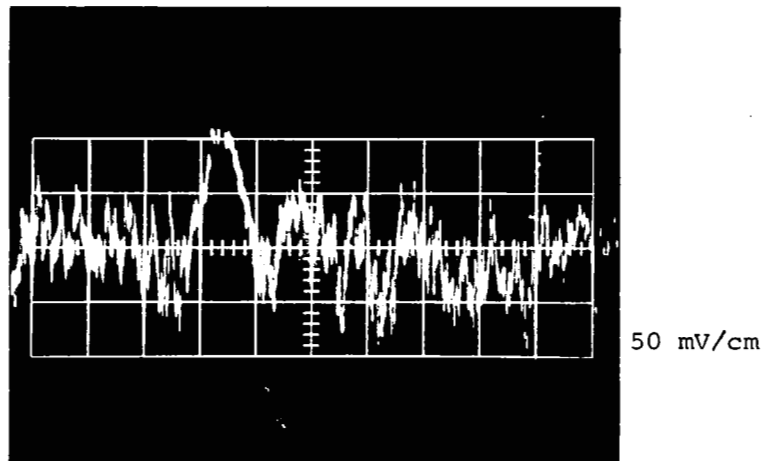Anemometer Output)

1 msec/div

Discriminator
Output Signal

Input Signal to
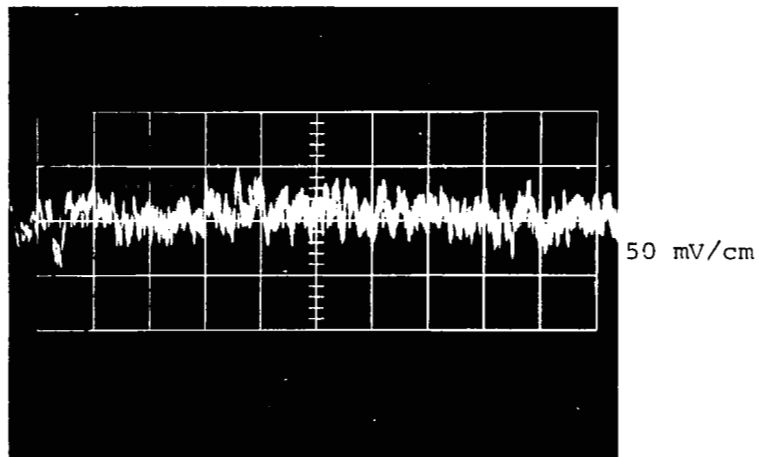Discriminator (Tape
Recorded Hot Wire
Anemometer Output)

1 msec/div

Figure 2.19-2   One-Shot Oscillograms of Typical Simultaneous
Discriminator Input and Output Signals

2.19-7

50 mV/cm

100 msec/cm

(a) Signal Plus Noise at
Photomultiplier Anode

50 mV/cm

100 msec/cm

(b) Noise Only - Scattered
Beam Blocked

Mean Frequency: 30 MHz
Measured 1-1/2 inches Downstream from 1/2 inch Nozzle Exit
Nozzle ΔP = 14 inches Water

Figure 2.19-3 Oscillograms of Heterodyne Signal with Noise, and
of Noise Alone, Measured at Photomultiplier Anode
(One-Shot)

2.19-8

LASER DOPPLER VELOCITY INSTRUMENTATION SPECTRAL DENSITY CURVES
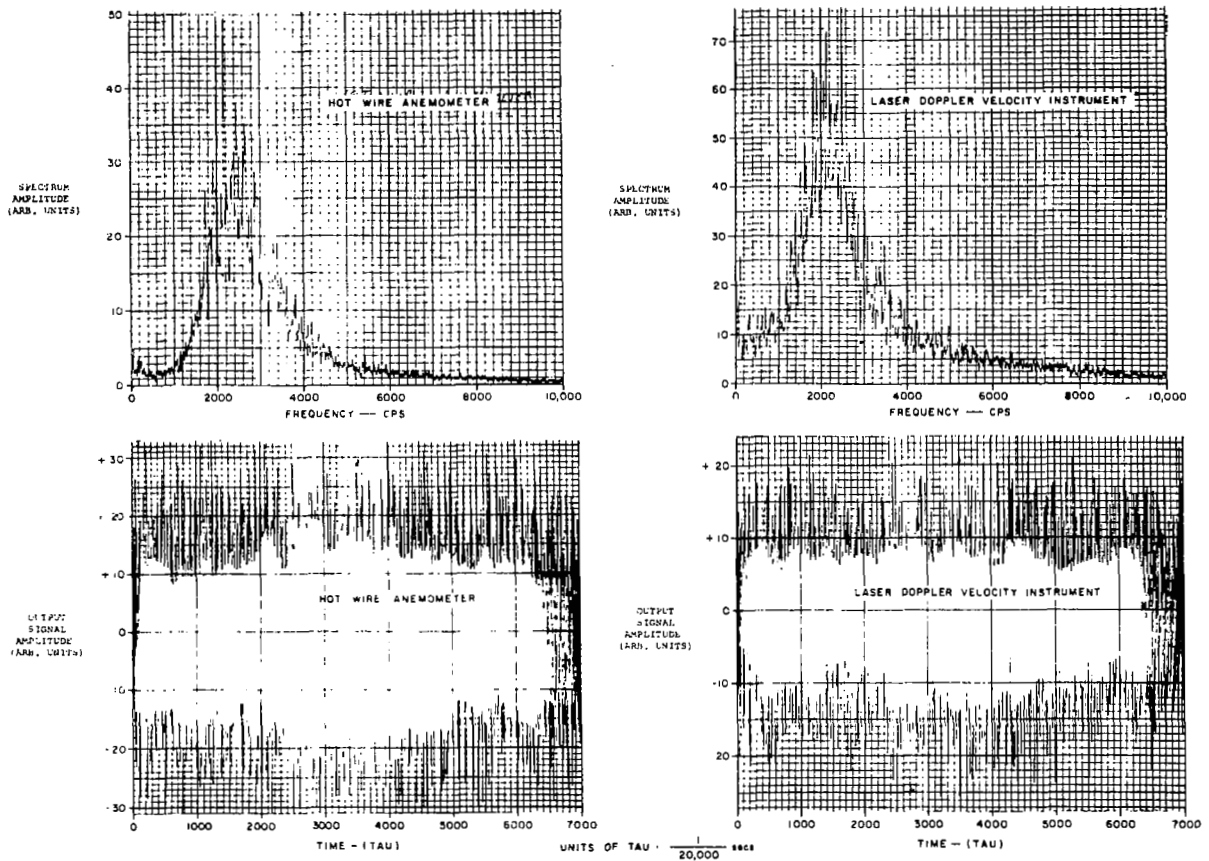MEASURED AT GEORGE C. MARSHALL SPACE FLIGHT CENTER

Figure 2.19-4   Output Signals and Power Spectral Density
Curves of Nozzle Flow Turbulence Measured
in the Same Flow with Laser Doppler Velocity
Instrument and Hot Wire Anemometer at NASA
George C. Marshall Space Flight Center

program already written by Murl H. Newberry of the MSFC Computation Laboratory. This program calculated the power spectrum (power spectral density) of each of the two signals (see Section 2.12 for power spectra as turbulence parameters), typical results appearing in the upper half of Figure 2.19-4. The two plots have been normalized to approximately the same maximum amplitudes. It will be seen that agreement between the two methods of measurement is very close. The slight difference in mean frequency seen in the upper plots exists because it was clearly impossible to probe exactly the same point with the two instruments, so that a slight difference in mean velocities was measured.

2.19.2   Supersonic Flow Measurements

An experimental Laser Doppler Velocity Meter was set up to measure gas velocities in the NASA seven inch wind tunnel, a blow-down facility. The laser scattered reference beam was passed through the tunnel windows. On several runs, excellent agreement was obtained up to about Mach 2, between velocities measured by the calibrated conventional instruments of the facility and the laser device. Since the measurement was quite straightforward and adds no information to that already appearing in this report, no further details will be given here.

More comprehensive supersonic tests will be run and analyzed when the 3-D instrument (section 2.20) is completed.

2.19.3   Measurements of Signal-to-Noise Ratio in Nozzle Turbulent Flow, Using Frequency Discriminator, Comb Filter Bank, and Spectrum Analyzer

Measurements relating to Signal-to-Noise parameters

were made on a system similar to that described in 2.19.1.
Principal differences were: that a discriminator with a center
frequency of 10 MHz was used; and some modifications were made
to improve the circuit bandwidth. Measurements were also made
using a Raytheon comb filter bank, having fifty filter elements
each one MHz wide, covering the frequency range zero to 50 MHz.
The same gas system as in Figure 2.19-1 was used.

The apparatus changes and measurements are summarized
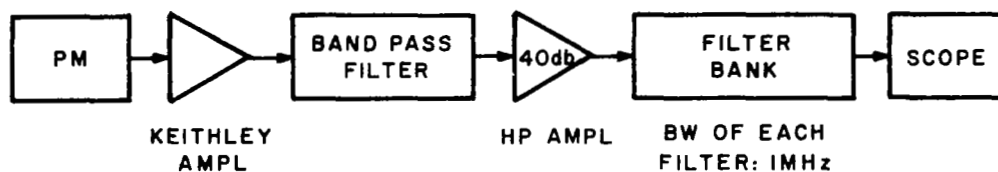below. Figure 2.19-5 is a schematic diagram of the electronic
system.

1. The anode load resistor was made equal to 470 ohms
in order to extend the bandwidth. Assuming a total anode load
capacitance of 20 pF (12 pF input capacitance of Keithley amplifier
+8 pF anode and stray capacitance) the bandwidth was 17 MHz.
(3 db points).

2. A decoupling resistor of 10K ohms, (to eliminate
the effect on the a.c. signal of external capacitance) was
connected to the spare BNC receptacle on the PM housing, to
measure PM DC current. Since the specified max. anode current
was 0.5 mA, the voltage across the 470 ohms resistor was not to
exceed 0.235V. With a PM supply voltage of 1500V, the reference
beam intensity had to be reduced with a neutral density filter by
a factor of approximately one tenth to get less than 0.5 mA
anode current.

It had been observed in some experiments that occasional
fading of heterodyne signal occurred. This fading was no longer
observed with the reduced reference beam power. The conclusion
was therefore that one cause of the fading had been photomultiplier
tube saturation.
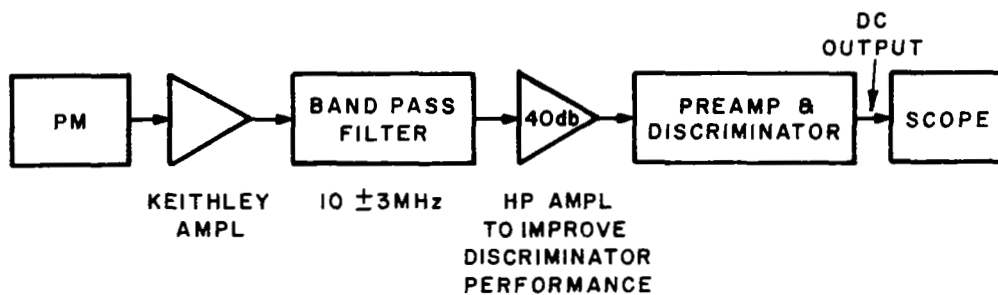
(a) DISCRIMINATOR MEASUREMENTS

(b) FILTER BANK MEASUREMENTS

Figure 2.19-5   Electronic Schematic Diagrams Discriminator
and Filter Bank Measurements

It was also noted throughout the experiments below, that the line width of the doppler signal with no turbulence (i.e. scattering at a point very close to the nozzle) was approximately 300 kHz. A calculation (as in section 2.11) showed that this was all accounted for by instrumental broadening.

2.19.3.1 Signal to Noise Discriminator Measurements

Using the light scattered from the flow system of Figure 2.19-1, relative reference and scattered beam powers were measured under various conditions. The powers were measured in terms of the d.c. voltage developed across the anode load resistor, with the aid of a high resistance electronic d.c. millivoltmeter connected through the 10K ohm decoupling resistor. Simultaneously, approximate signal-to-noise power ratio was read off from the spectrum analyzer display. Results are given below:

1. Neutral Density Filter ($\approx$10 db) in
   Reference Beam Only
   No turbulence (scattering region very close to nozzle exit).

Time min. after smoke bomb lighting	P_{ref} Voltage across 470 ohms anode resistor (mv)	P_{sc} Voltage across anode resistor (mv)	S/N in 300 kHz Bandwidth
0	250	0	
1	150	12	
2	40	11	20 db
3	45	11	
4	90	10	
5	150	7	

2. <u>Neutral Density Filter (≈10 db) at PM, i.e.,</u> both Scattered and Reference Power were attenuated. No turbulence, as before.

Time min. after smoke bomb lighting	P_{ref} Voltage across 470 ohms anode resistor (mv)	P_{sc} Voltage across anode resistor (mv)	S/N in 300 kHz Bandwidth
0	270	0	
1	150	1.2	
2	90	1.3	10 db
3	80	1.3	
4	180	0.8	
5	200	0.5	
6	230	0.4	

It will be noted that the power of the reference beam varied with time in each run, and further that the reference beam powers were different for the two runs. The first is explained by changing beam extinction as smoke density changed with the consumption of the smoke bomb. The difference in reference beam power between the runs was presumably because different smoke bombs do not develop the same smoke density.

The performance of the 10 MHz discriminator was checked by measuring the DC-output on the oscilloscope for various velocities. An additional gain of 40 db was needed to improve the linearity of the discriminator. The discriminator output was very noisy.

Discussion of Results of Nozzle Flow Signal to Noise Measurements

Based on these S/N measurements, the following S/N could be expected in operating either the discriminator or the filter bank in a signal processing system:

S/N measured in 300 kHz bandwidth	S/N Discriminator BW = 6 MHz S/N reduction: $10 \log \frac{6 \cdot 10^6}{3 \cdot 10^5} = 13db$	S/N Filter Bank BW = 1 MHz S/N reduction: $10 \log \frac{10^6}{3 \cdot 10^5} = 5db$
Reference power attenuated 20 db	7 db	15 db
Scattered and reference power 10 db attenuated	-3 db	5 db

The possibility of improving the S/N at the discriminator output by means of a low pass filter has to be investigated. If, e.g., the noise bandwidth of the discriminator output is in the order of 1 MHz, and the highest modulation frequency obtained with the present low velocity system is only a few kHz, a considerable improvement is to be expected.

An important conclusion is that these Signal-to-Noise results taken on the MSFC nozzle flow agreed with the results of Raytheon, Sudbury, measurements of Signal-to-Noise power ratio using a rotating plastic disc. This is readily seen if one observes that, in both cases,

$$\frac{P_{ref}}{P_{sc}} = \frac{P_{ref}\ (mv)}{P_{sc}\ (mv)} \gg 1.$$

By equation (7) of Section 2.5 and the corresponding experimental curves of Figs. 2.18-2/3, under these conditions:

a). S/N is independent of the ratio $\frac{P_{ref}}{P_{sc}}$. Hence the wide changes in P_{ref} of 1) and 2) above would not be expected to affect S/N; and this is just what was observed.

b). S/N is proportional to P_{sc}. Hence, since P_{sc} was attenuated 10 db in 2) above as compared with 1) above, a corresponding reduction in S/N would be expected, and this, too, is exactly what was observed.

An important overall conclusion, then, is that with the reference beam taken through the flowstream, any resulting relatively wide variations in P_{ref} will not affect S/N, provided $P_{ref}/P_{sc} \gg 1$ at all times; and clearly changes in contaminant concentration affect both beams simultaneously, so that the power ratio remains unchanged. Only if a _very_ dense contaminant were used would P_{ref} become excessively low. The affect on P_{sc} is more complicated in the dense injectant concentration case, since higher particle concentration increases the scattered power, but simultaneously increases the extinction of the scattered beam. However, no complications of this sort occurred in the experiments described, despite the fact that smoke density could be described as "very thick" by visual observation.

An important point to note, as demonstrated by this experiment, is that neutral density filters used to reduce the total power incident on the photomultiplier must be placed in the

reference beam only, not in the total laser beam.

2.19.3.2   Filter Bank Measurements

A block diagram of the basic setup used for
filter bank measurements is shown in Figure 2.19-5b. The measure-
ments and results are summarized below:

1.   Signal-to-Noise ratio at output of filter No.11
(Bandwidth 1 MHz) measured on oscilloscope, with no turbulence
near nozzle, neutral density filter in reference beam only:

Signal plus noise: 200 mv$_{pp}$

Noise alone: 50 mv$_{pp}$

$$S/N = \frac{(200)^2 - (50)^2}{(50)^2} = 15 \eqsim 12 \text{ db}$$

This value was in the same order as the one obtained from
spectrum analyzer measurements. The signal level was not high
enough to drive the indicator lights at the filter outputs.

Figures 2.19-6 through 2.19-9 show filter bank output
signals under various conditions.

Scale: Horizontal: 1 ms/div.

Vertical: 20 mv/div.

Mode: Single Sweep

At 3" downstream, the doppler spectrum was at least 6 MHz
wide, measured with the spectrum analyzer and the filter bank.

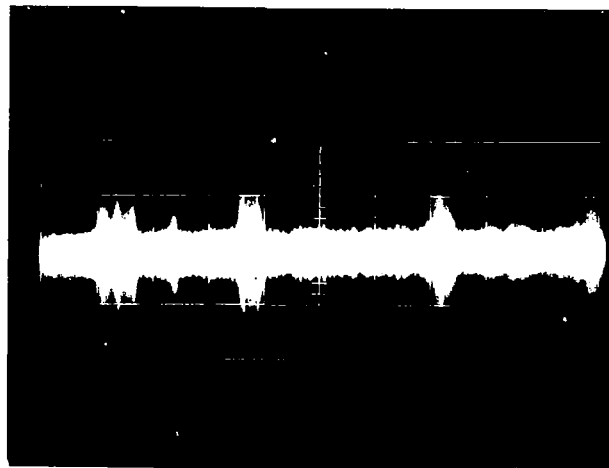Discussion of Results of Filter Bank Measurements

The S/N measurements made with the filter bank agreed with
those made with the Spectrum analyses in 2.19.3.1. The fluc-
tuating nature of turbulence can be seen in the second oscillogram

2.19- 17
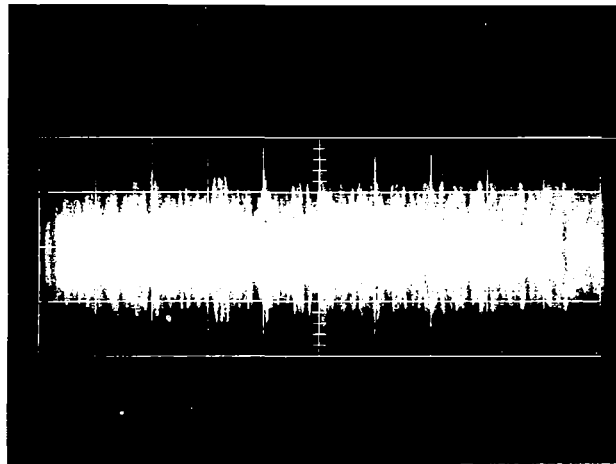
20 mV/div

1 msec/div
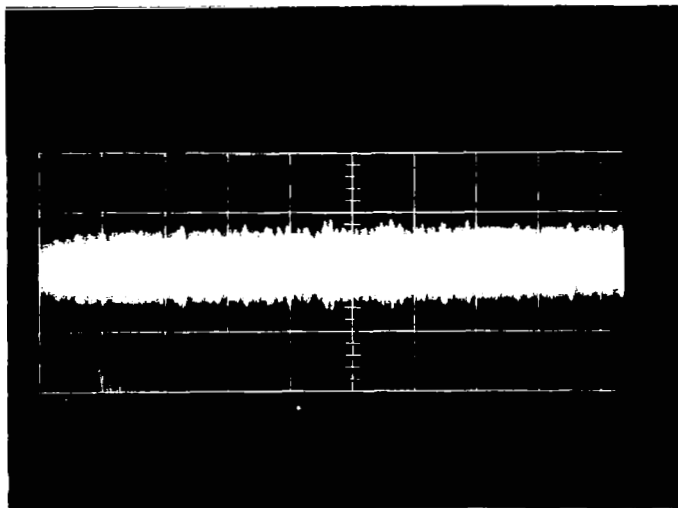
NO TURBULENCE
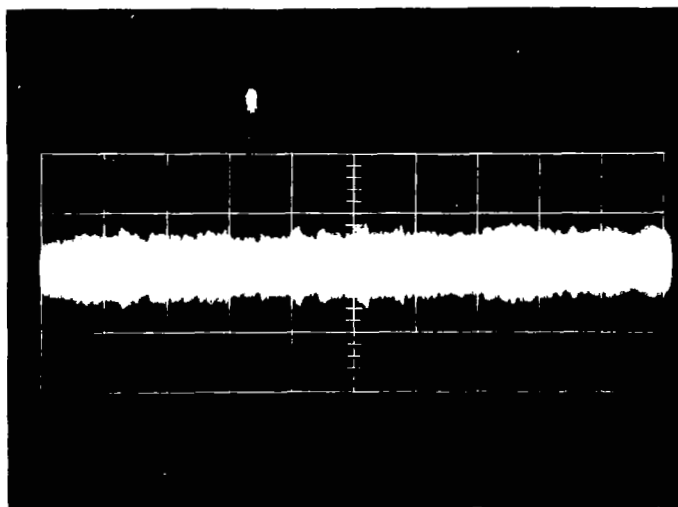(scattering region close to nozzle)

20 mV/div

1 msec/div

TURBULENCE

(scattering region approx. 1 inch downstream)

Doppler Frequency 11 MHz, Corresponding to a Velocity of
55 ft/sec;Neutral Density Filter in Reference Beam Only

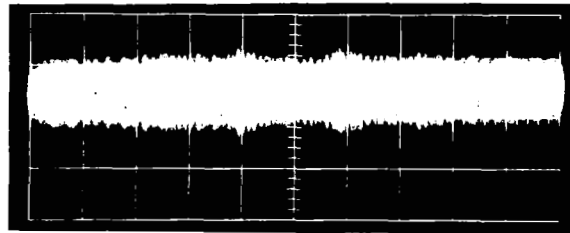Figure 2.19-6   Filter Bank Measurements: Output of Filter No.
(at 11 MHz)

NO TURBULENCE
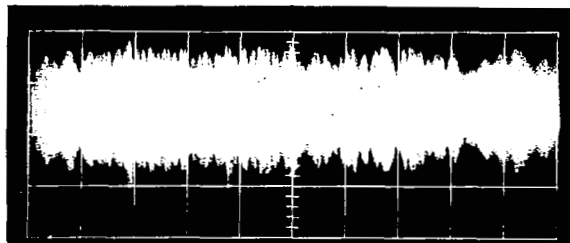(at nozzle)

TURBULENCE
(approx. 1 inch downstream)

Figure 2.19-7 Filter Bank Measurements: Same Conditions as in
Figure 2.19-6, but 10 db Neutral Density Filter
at Photomultiplier

Filter #8
7.5 to 8.5 MHz

20 mV/div

1 msec/div

Filter #9
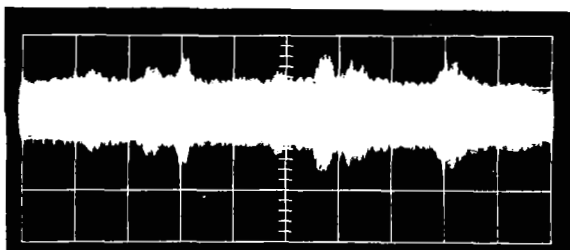8.5 to 9.5 MHz

20 mV/div

1 msec/div

Filter #10
9.5 to 10.5 MHz

20 mV/div

1 msec/div
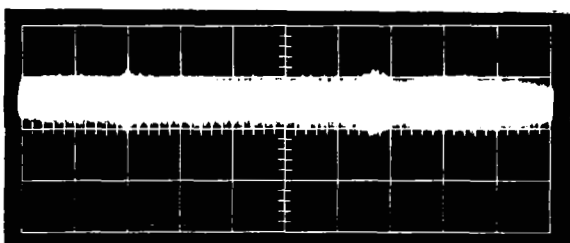
Filter #11
10.5 to 11.5 MHz

20 mV/div

1 msec/div

Neutral Density Filter in Reference Beam Only
Mean Velocity Approximately 50/ft/sec
PM Supply Voltage: 1500 Volts
Anode Current: 0.53 mA

Figure 2.19-8 Filter Bank Measurements: Turbulence Measured
              Approximately 1-1/2 inches Downstream
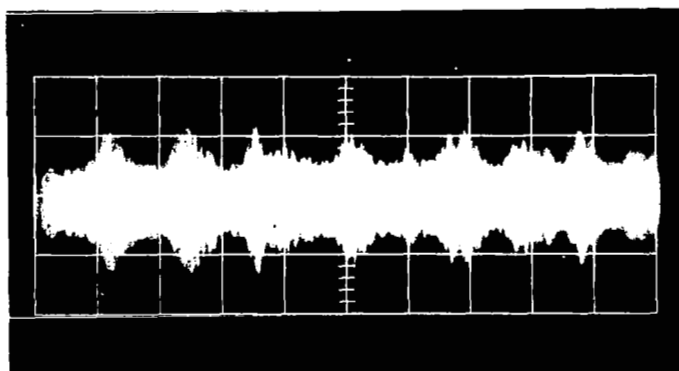
1/2 inch Downstream

20 mV/div
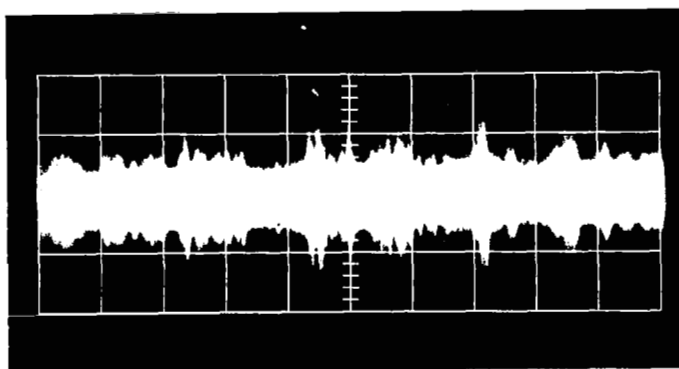
1 msec/div

2 inches Downstream

20 mV/div

1 msec/div

3 inches Downstream

20 mV/div

1 msec/div

Figure 2.19-9   Filter Bank Measurements: Output of Filter
#11 (10.5 to 11.5 MHz) for Different Degrees
of Turbulence

of Figure 2.19-9. This figure also shows that the most turbulent signal in this case was in the region of about 10 MHz.

Figure 2.19-9 shows how turbulence develops as the flow progresses downstream.

2.20 Design and Construction of the 3-D Instrument

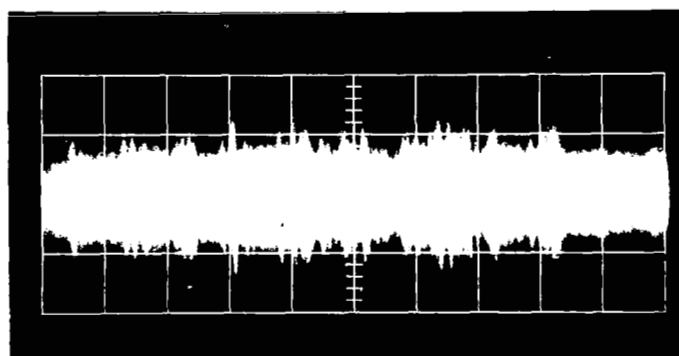The following section summarizes the basic design concept and briefly reviews the hardware design detail of an instrument for measurement of vector velocity. Since the vector measurement is performed by recording simultaneously three components of the velocity, it has been termed the 3-D instrument.

The general principles relevant to Doppler shift and its interpretation in terms of instantaneous velocity and turbulence are as described earlier in this report, and determination of the velocity vector from 3-D component measurements is reviewed in 2.20.3 below.

2.20.1 System Description

Figure 2.20-1 is a schematic diagram outlining the essential features of the system.

The light from the laser passes through a lens L-1 and a window in the wind tunnel or test facility to focus at a selected point in the flow stream. The unscattered beam is collected, after passing through a boresight alignment aperture, and rendered parallel by the lens L-2. The parallel beam passes through an optical attenuator for adjustment of beam intensity, in accordance with the operating criteria established in Section 2.5 of this report. The optical local oscillator (Section 2.5) beam is obtained for the three photomultiplier mixers by dividing the beam with a tetrahedral beam splitting prism, finally reflecting from a beam splitter mirror (marked "BS" in the diagram) inserted in each scattered beam. Lenses L-3, L-4, and L-5 focus the local oscillator signals on to the photomultiplier cathodes. By grinding off the top corner of the tetrahedral prism, a small portion of the beam passes straight through the prism, out of the base, and through a second boresight aperture marked "BA". By using the two boresight apertures, a reference base line is established for alignment of the whole instrument.
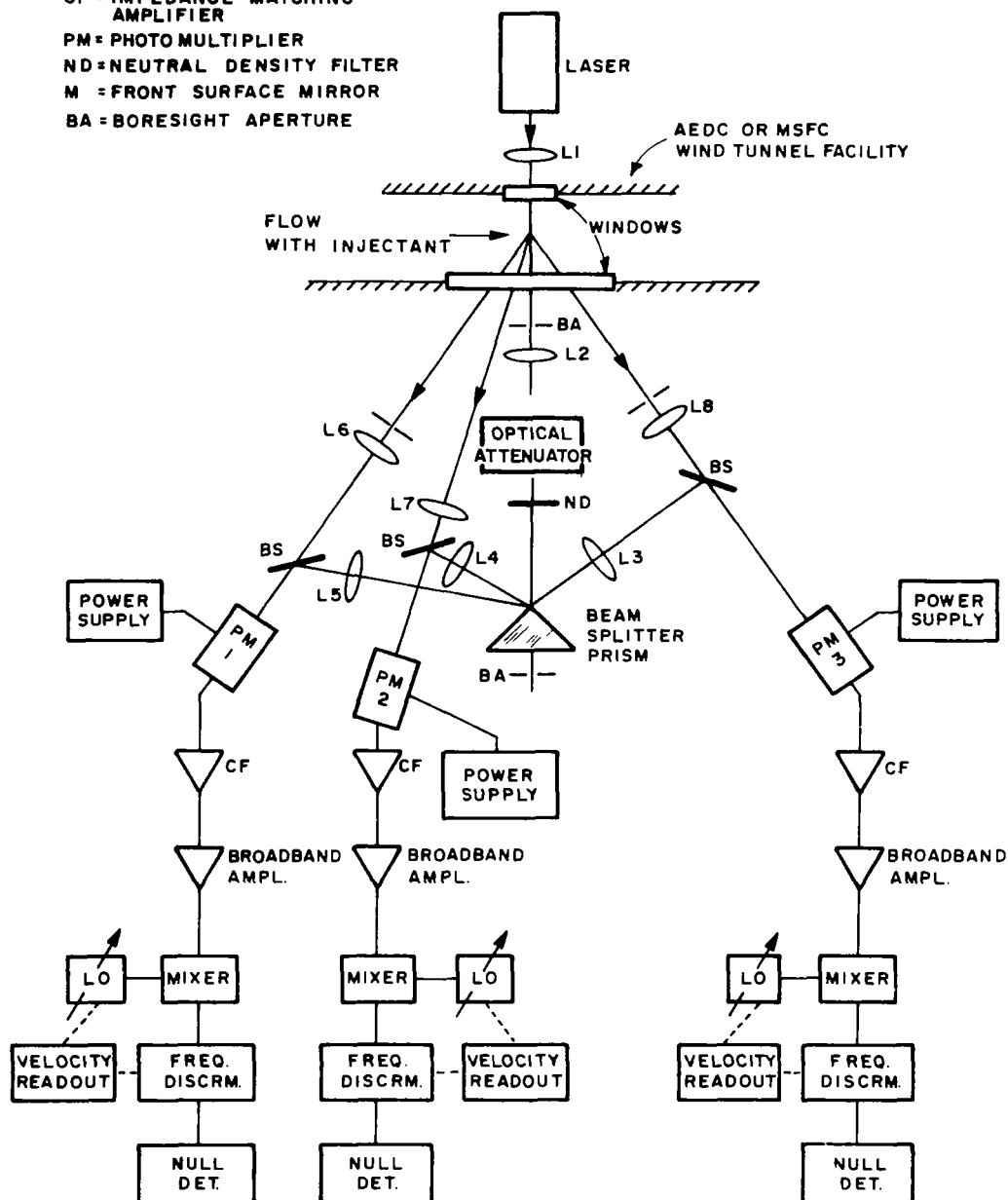
2.20-1

Figure 2.20-1   Three-Dimensional Laser-Doppler Flowmeter

Each scattered beam is picked up at an angle θ to the laser beam, the angles being symmetrically situated around the axis of the reference beam. Lenses L-6, L-7, and L-8, behind adjustable apertures, collect the scattered light at the chosen angle. After passing through suitable collimating and focussing optics, the scattered beams pass through the beam-splitter mirrors BS, and onto the photomultiplier cathode where the scattered signal is mixed with the local oscillator beam. The scattered beam lens system is somewhat more complicated than shown schematically, in order to provide independent control of the scattering volume and instrument broadening at one end (Sections 2.13 and 2.11), and of the mixing process at the opposite end of the optical systems (Section 2.10).

Refractor plates are situated at several places in the optical paths to permit of independent parallel alignment with respect to transverse locations of the beam at the photomultiplier cathodes. Angular beam adjustment at the photocathodes is provided by the beam-splitters. Complete details of the optics are left to a later report.

At each photomultiplier active surface, the scattered light heterodynes with the unscattered reference beam (local oscillator beam). The heterodyne outputs of the photomultipliers pass through the preamplifiers shown as "CF" in Figure 2.20-1. The signals are then amplified and processed in accordance with Section 2.12. Spectrum analyzers are used as monitors, while the turbulence and velocity information is obtained by processing through special discriminator circuits. The special requirements of the discriminators are discussed and described in Section 2.12. In brief, to optimize the signal-to-noise ratio, frequency tracking discriminators are used which continuously track the frequency of the fluctuating turbulence Doppler signals. For simplicity, Figure 2.20-1 shows a simple frequency discriminator system. The more complex form is described in the section mentioned above. A brief review of the determination of vector

velocity from the component measurement appears in Section 2.20.3 below.

2.20.2   Hardware Design and Construction of the 3-D Instrument

Detailed design of the hardware of the 3-D instrument will be given in later reports. A brief summary of the important features follows.

The instrument is basically divided into two main assemblies: the optical assembly and the mount assembly. The mount is designed for use at the AEDC Base Flow Test Facility and is also designed for use in the MFSC Cold Flow Test Facility or other wind tunnels, by virtue of its versatile construction. Further details of each are given below.

Front and rear view photographs of the optical assembly during construction alignment appear in Figures 2.20-2 and 2.20-3.

2.20.2.1   Optical Assembly (Raytheon Drawing E04934-367493)

The optical assembly drawing includes the laser and focussing lenses for convenience. Following the general system outline described above, the optical assembly consists of a single centrally located reference beam tube, with three scattered beam tubes mounted symmetrically around it. Their axes are set at the scattering angle relative to the axis of the reference beam tube. By changing sets of angle spacers, the scattering angles can be varied from approximately 8° to 30°, each channel independently.

Each tube contains an independent set of optics. To aid in alignment, each tube has a machined ring at each end of its exterior surface, and is terminated at the photomultiplier end with a flange face perpendicular to the axis. This face and the two machined rings provide the reference location and axis

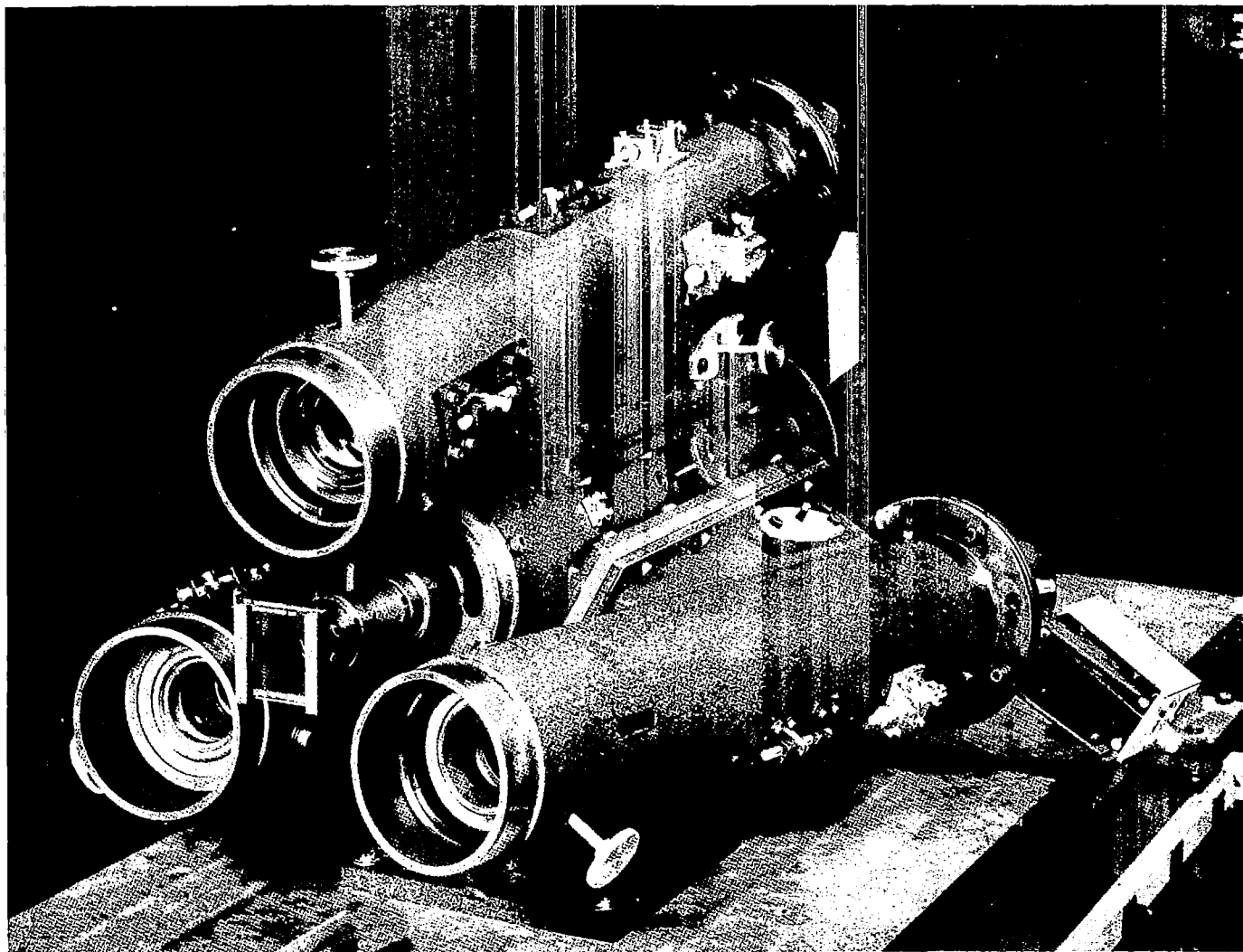Figure 2.20-2 Front View Photograph of the Three Dimensional Laser Doppler
Velocity Instrument Optical Assembly, showing the Three
Scattered Beam and the Reference Beam Assembly
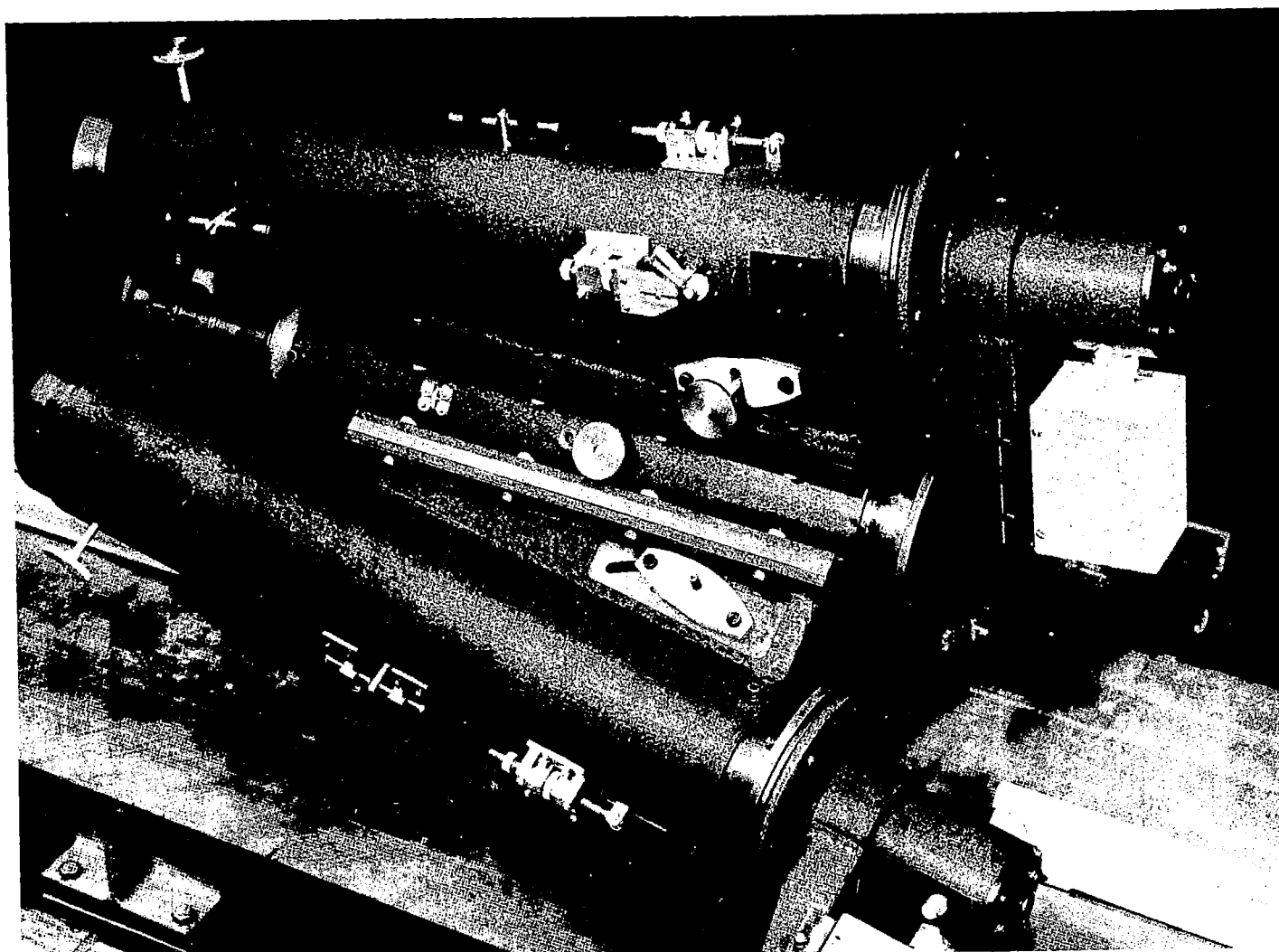
Figure 2.20-3   Side View Photograph of the Three-Dimensional Laser Doppler
                Velocity Instrument Optical Assembly, showing Photomultiplier
                Housings, Preamplifiers, and Instrument Operating Adjustments

respectively to which the instrument parts, and the instrument
as a whole are to be aligned.

Adjustments for location of the scattered volume
focal point are provided, as are all the other adjustments needed
for peaking up the heterodyne signal output. As pointed out in.
Section 2.10 above, the adjustments for angular and transverse
alignment of the reference with the scattered beam tube at each
photomultiplier mixer cathode are critical, so that fine adjust-
ments are provided at these points.

Each photomultiplier mixer is built as a separate
assembly, in a fully electrically and magnetically shielded
housing, as a single unit with its preamplifier. This has strong
advantages, among which are 1) the complete mixer-electronics
key components can be separately tested and adjusted independently
of the instrument; 2) changes in types of detectors which might
be required in later development programs can be readily made;
3) the electrical requirement that all anode connections have mini-
mum capacitance can be achieved by keeping leads short between the
photomultiplier anode and preamplifier. As pointed out in Section
2.12, this requirement is absolutely essential if the necessary
bandwidth to handle the relatively wide range of flow velocities
required is to be achieved. Alignment of the optical assembly
as a whole, after preliminary construction and production align-
ment of components, is made by sighting through the two boresight
apertures at the front and rear of the scattered beam assembly.

2.20.2.2 Mount Assembly (Raytheon Drawing 49956-367495)

This assembly is built, as is the optical assembly
above, of rather massive construction to minimize susceptibility
of the instrument to external vibration and noise in a rocket
engine environment. The Mount provides for mounting of the laser
on one side of the wind tunnel or engine base flow model, and for
the optical assembly on the other side.

2.20-7

The laser mounting mechanism and optical assembly mounting mechanism are each movable in three dimensions parallel to the flow, transverse to the flow and vertically. To minimize cost on this first experimental design, only transverse adjustment is synchronized between the two sides of the instrument. Since it is necessary always to coincide the focal points of the laser lens and scattered beam collecting optics, lead screws of machine tool accuracy are provided for the three adjustments. The whole base is mounted on two types of casters: one for moving between locations, and the second equipped with grooves for mounting on the rails of the NASA Marshall Space Flight Center Cold Flow Test Facility. In actual use, jacking screws are provided for leveling of the instrument and to ensure a stable platform during operation. Additional demountable jacking screw supports are provided to enable the whole Mount to be operated over a wider range of heights than available from one set of standard jacking screws. A steel box construction on either side of the main cross member provides storage for such loose parts associated with the mount.

2.20.3 Determination of Vector Velocity Components from Measurement of Doppler Shift at Three Scattering Angles

This section shows how the components of the vector velocity along three orthogonal axes can be determined from measurements of the Doppler Shift at three scattering angles. It is intended for illustration of the method only. Explicit analysis for the 3-D system will appear in a later report. The Doppler Shift for scattered light is given by

$$\Delta f_D = \left[\frac{\underset{\sim}{v} \cdot (\hat{k}_o - \hat{k}_s)}{c} \right] f_o \tag{1}$$

where $\underset{\sim}{v}$ is the vector velocity, $\hat{k}_o$ is a unit vector in the

direction of the incident laser beam, $\hat{k}_s$ is a unit vector in the direction of the scattered beam, c is the speed of light, and f is the frequency of the laser beam light.

For the geometry shown in Figure 2.20-4, $\underset{\sim}{v}$, $\hat{k}_o$, and $\hat{k}_{s1,2,3}$ are given by

$$\underset{\sim}{v} = v_x \hat{x} + v_y \hat{y} + v_z \hat{z} \tag{2a}$$

$$\hat{k}_o = -\hat{x} \tag{2b}$$

$$\hat{k}_{s1} = -\cos\theta \, \hat{x} - \sin\theta \, \hat{z} \tag{2c}$$

$$\hat{k}_{s2} = -\cos\theta \, \hat{x} + \sin\theta \, \hat{y} \tag{2d}$$

$$\hat{k}_{s3} = -\cos\theta \, \hat{x} + \sin\theta \, \hat{z} \tag{2e}$$

Substitution into the equation (1) for Δf_D yields

$$\frac{\Delta f_{D1}}{f_o} = \frac{v_x}{c} (\cos\theta - 1) + \frac{v_z}{c} \sin\theta \tag{3a}$$

$$\frac{\Delta f_{D2}}{f_o} = \frac{v_x}{c} (\cos\theta - 1) - \frac{v_y}{z} \sin\theta \tag{3b}$$

$$\frac{\Delta f_{D3}}{f_o} = \frac{v_x}{c}(\cos\theta - 1) - \frac{v_z}{c}\sin\theta, \qquad (3c)$$

where Δf_{D1}, Δf_{D2}, Δf_{D3} are the Doppler Shifts of light scattered in the directions of $\hat{k}_{s1}$, $\hat{k}_{s2}$ and $\hat{k}_{s3}$ respectively.

Solving these equations (1), (2), and (3) for the velocity components yields

$$\frac{v_x}{c} = \frac{\Delta f_{D1} + \Delta f_{D3}}{2(\cos\theta - 1)f_o} \qquad (4a)$$

$$\frac{v_y}{c} = \frac{\Delta f_{D1} - 2\Delta f_{D2} + \Delta f_{D3}}{2\sin\theta\, f_o} \qquad (4b)$$

$$\frac{v_z}{c} = \frac{\Delta f_{D1} - \Delta f_{D3}}{2\sin\theta\, f_o} \qquad (4c)$$

Thus all components of the mean velocity, $\underset{\sim}{v}$ are measured, so that $\underset{\sim}{v}$ is known in both magnitude and direction.
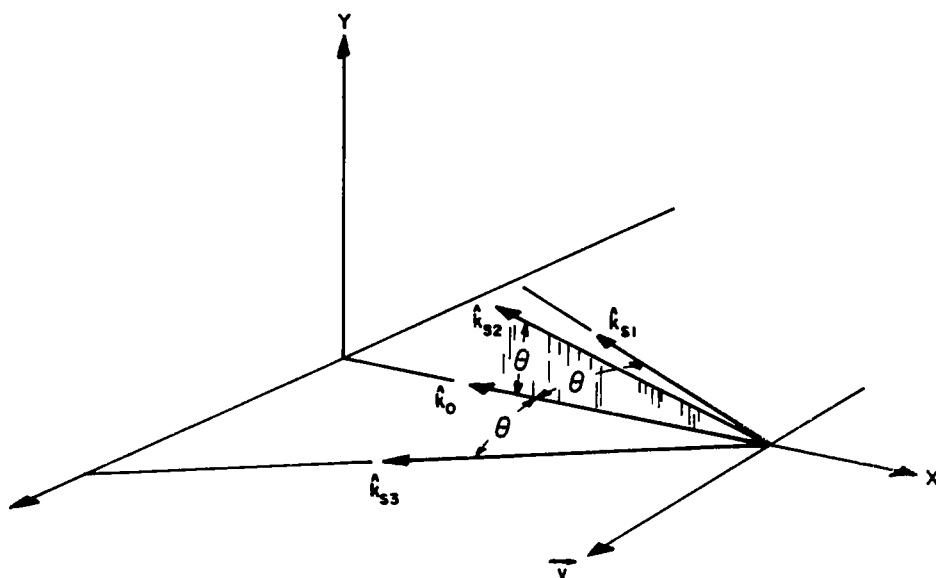
Figure 2.20-4 – Scattering Geometry and Coordinates

3.0   SUMMARY OF RESULTS, AND CONCLUSIONS

Since a considerable amount of detail appears in this
report, some conclusions are summarized below, grouped to aid
in their interpretation.

3.1   Measurement Capabilities of the Instrument

1.   Wind Tunnel Velocity measurements up to Mach 2 have
been demonstrated at the NASA George C. Marshall Space Flight
Center.

2.   Analysis shows that measurement of the highest cur-
rently attainable interplanetary reentry velocities with the
instrument should be feasible. This follows from the fundamental
reasons that the period of the light waves used to make the
measurement is very much smaller than the smallest conceivable
time needed to make any meaningful fluid dynamic measurements.

3.   Continuous measurement of all the parameters used to
define turbulence can be made, and turbulence data thus obtained
are just the same as those obtained using a hot wire anemometer,
within the accepted operating frequency range of the latter.

4.   Analysis shows that no fundamental obstacles stand in
the way of accurate turbulence measurements up to mean velocities
of the highest attainable Mach numbers.

5.   Output of the instrument is independent of gas temper-
ature at all velocities and under all conditions.

6.   The instrument does not perturb or modify the flow
field in any way.

7.   Very high resolution can be achieved, of the order of
10^{-6} mm^3 with suitable optical design.

3.2 Current Limitations of the Instrument

1. At the present time, a rather inconvenient injection of scattering particles is necessary in order to produce light scattering of sufficient intensity. The smoke particles currently used, although they do not appear to modify the flow, are corrosive in nature. However, experimental indications are that, with recommended improvements in the instrument, sufficient scattered intensity may eventually be obtained from natural air contaminants such as dust and water droplets.

2. Two sources of spurious continuum frequency broadening of the Doppler frequency signal have been identified: one results from the use of focussed scattered light collecting optics (aperture broadening); and the other from the velocity gradient which may exist across the resolution volume (resolution broadening).

3. By suitable design, broadening can be substantially reduced (a) by using a "balanced" scattered light focussed collection system (Figure 2.4-2) or a parallel beam (non-focussed) scattered light collection system, either of which eliminates aperture broadening, (b) if simple focussed collecting optics are necessary, by using an electronic signal frequency tracker which, in addition to other advantages, has an output independent of continuum frequency broadening (assuming it can track such a signal), (c) by using a large aperture system for measurements in regions of high velocity gradients, which results in a very small resolution volume, (d) by using a large scattering angle (limited by frequency bandwidth of the detector) so that instrumental broadening is small compared with total Doppler frequency shift.

It will be noted that some of these approaches to reduce or eliminate instrumental broadening are in conflict, for example, a larger aperture (low resolution broadening) results in greater aperture broadening. However, it also should be noted that in

practice, simultaneous conflict seems not to occur for natural reasons, e.g., high velocity gradients generally appear only in lower velocity regions, so that a convenient optimum combination of larger scattering angle with larger aperture can be found for minimum total continuum broadening.

4. An ambiguity in velocity direction exists, which is generally unimportant, but might become so in regions of intense recirculation, as for example, in rocket engine base flow.

3.3 Instrument Operation for Optimum Performance

1. Use of the photomultiplier tube as a mixer requires operating modes and criteria quite different from those applying when the tube is used as a low level light detector.

2. The photomultiplier tube mixer is the key component in the whole system; it determines both system signal-to-noise ratio and signal frequency bandwidth.

3. When the scattered light power is relatively low, optimum system signal-to-noise ratio is achieved simply by setting P_{LO} to a level such that $P_{ref}/P_{sc} \gg 1$, then setting the photomultiplier applied voltage to give maximum output anode current within the limitations of the tube. A convenient working guide is to set P_{ref}/P_{sc} = (5 to 40), by using neutral density filters in the reference beam. Operation with high scattered beam power requires a different operating condition (Section 2.5).

4. Under these conditions, system signal-to-noise power ratio, measured at the anode load resistor of the photomultiplier, is given by

$$\left(\frac{S}{N}\right)_{MS,A} = \mu_T \, A \, \frac{P_{sc}}{\Delta f}$$

3-3

where: P_{sc} = average scattered light power

Δf = system frequency bandwidth

A = constant of the instrument

μ_T = coherence loss factor

5. μ_T includes multiplicative constants which are a function of laser coherence length, characteristics of the scattering injectant material, and the geometry of alignment of the two beams at the photomultiplier cathode. Loss of coherence in the atmospheric beam paths is normally negligible because of the short distances involved. It might become appreciable if one or both beams had to pass through a highly turbulent flow field on either side of the scattering volume.

6. With conditions as in (3), the system signal-to-noise power ratio is independent of changes in reference beam power. This permits the mechanically convenient arrangement of passing the reference beam through the scattering region; beam extinction by the scattering particles will not affect the system output, assuming the electronic system meets the requirements of (12) below.

7. With conditions as in (3), (a) *Johnson noise* in the electronic circuit components is negligible, (b) photomultiplier dark noise and dark current are negligible, (c) the only noise source of significance is the photomultiplier "noise in signal", which is proportional to photomultiplier anode current.

8. The reasons for this noise source independence are that (a) the use of a relatively high level of P_{ref} makes other noise sources negligible, (b) the noise output of the photomultiplier tube is independent of total dynode gain, so that with the normal high operating gain, noise in subsequent electronic circuits becomes much smaller than PM anode signal.

9. Maximum system signal frequency bandwidth is limited (and generally determined) by the bandwidth of the photomultiplier tube anode circuit, which is given by (3 db points):

$$\text{sec}^{-1}$$

(anode load resis, ohms)(anode circuit stray capacitance, farads)

Considerable care must therefore be exercised in mechanical design of the anode circuit components and leads, to eliminate stray capacitances.

10. To reduce PM tube fatigue effects, maximum PM tube operating anode current should be set to about a half the maximum current allowed by the tube manufacturer.

11. The output signal from the Laser Doppler Velocity Instrument is a frequency modulated carrier frequency. The carrier frequency itself also varies over a wide range. Thus special signal processing circuits are needed.

12. All the needed velocity information is contained in the heterodyne signal _frequency_, not its amplitude. Since all frequency detectors (e.g., spectrum analyzer, frequency discriminator) are also sensitive, in some way or another, to changing signal amplitudes, all such amplitude fluctuations should be removed by a suitable circuit (such as a limiter) before processing the signal to obtain velocity.

13. The zero-crossing type of frequency discriminator is generally unsuitable for use in processing the instrument output signal. Besides being adversely affected by the random nature of the signal, since its output is artificially generated inside the instrument, information retrieval from the signal is likely to be less pure than in the case of a linear frequency discriminator.

14. PM average anode current should be frequently or continuously monitored to insure compliance with (3) and (10). Care should be taken not to introduce stray capacitance of the monitoring apparatus into the PM tube anode circuit.

15. The geometrical alignment of the reference and scattered beams at the photomultiplier cathode is of key importance. Each element, the two beams and photomultiplier tube, has six independent degrees of freedom. By suitable design, the total of 18 degrees of freedom can be reduced, and, in some directions, made relatively less sensitive to misalignment.

16. To allow for flexibility in designing the scattered and reference light collecting optics, and the photomultiplier beam mixing optics, the two subsystems should be made independent within the total optical system, e.g., by using collimated beams at some point in each beam system.

17. The most significant coherence loss occurs in the scattering medium.

18. With a one-watt argon laser, S/N power ratios of 20 to 30 db are to be expected with smoke particles as scattering injectant, or using a Doppler calibration wheel.

19. There is a close relationship between the formalisms of turbulence theory and of communications theory.

4.0 RECOMMENDATIONS

The following are considered to be of prime importance:

1) A special frequency tracking discriminator should be built as soon as possible for processing the instrument signal. Its use is expected (a) to reduce substantially the noise bandwidth and hence improve the signal-to-noise ratio, (b) to eliminate the effects of instrument broadening, (c) to produce, in a single, recordable, output signal, all information required on turbulence and mean velocity parameters.

2) Analysis of coherence loss in the scattering medium should be continued, and numerical calculations performed for checking with experiment.

3) A more desirable scattering injectant should be sought, less harmful to mechanical equipment and less toxic. Injectant coherence loss parameters should be measured using the signal-to-noise measurement technique developed in this investigation.

4) A means should be developed for removing the Doppler-measured velocity ambiguity.

5) Analytical and experimental work should continue to refine the signal processing system, improve signal-to-noise ratio, and extract maximum information from the output signal.

6) Cross-correlation and auto-correlation techniques should be developed, preferably using the 3-D instrument.

7) Performance of the 3-D instrument should be evaluated, and velocity vector measurements made on subsonic and supersonic flow systems.

APPENDIX A

Note on Optical Heterodyning With
Non-Critical Angular Alighment

R. G. McManus

SUMMARY

A serious question concerning the feasibility of a practical, coherent heterodyne detection system at optical frequencies has long prevailed; i.e., the problem of possible total signal cancellation at the detector. The stated argument is that the local oscillator and signal energy must be in spatial phase along the full length of the detector. But the ratio of the optical wavelength (approx. 10^{-4} cm) to the detector length (approx. 1 cm) is of the order of 10^{-4}. The obvious conclusion is that the beat frequency energy will be insignificant unless the misalignment of LO and signal is less than 10^{-4} rad.

This note will show that this is indeed so if, for example, two lasers are being aligned without the use of lenses. In this situation, the entire detector is illuminated. If, on the other hand, the detector is placed at the focus of a diffraction limited lens, the problem is significantly alleviated. The gist of the solution is that at the focus of a diffraction limited lens or mirror, the wavefronts in the Airy disk are plane and perpendicular to the direction of the incident light. In this situation, the rays of light are still parallel, but have now been focused to a much smaller spot, which now constitutes the essential size of the detector.

ANALYSIS

Consider the situation shown in Figure A-1, below, where LO energy (solid lines) is mixed with signal energy (dashed lines). Both inputs are assumed to start from arbitrary planes at the left, and proceed to the detector on the right. Here the LO energy is assumed coaxial, while the signal energy is misaligned. The size of the detector illuminated is designated as X, while the physical size of the detector is ℓ_D.
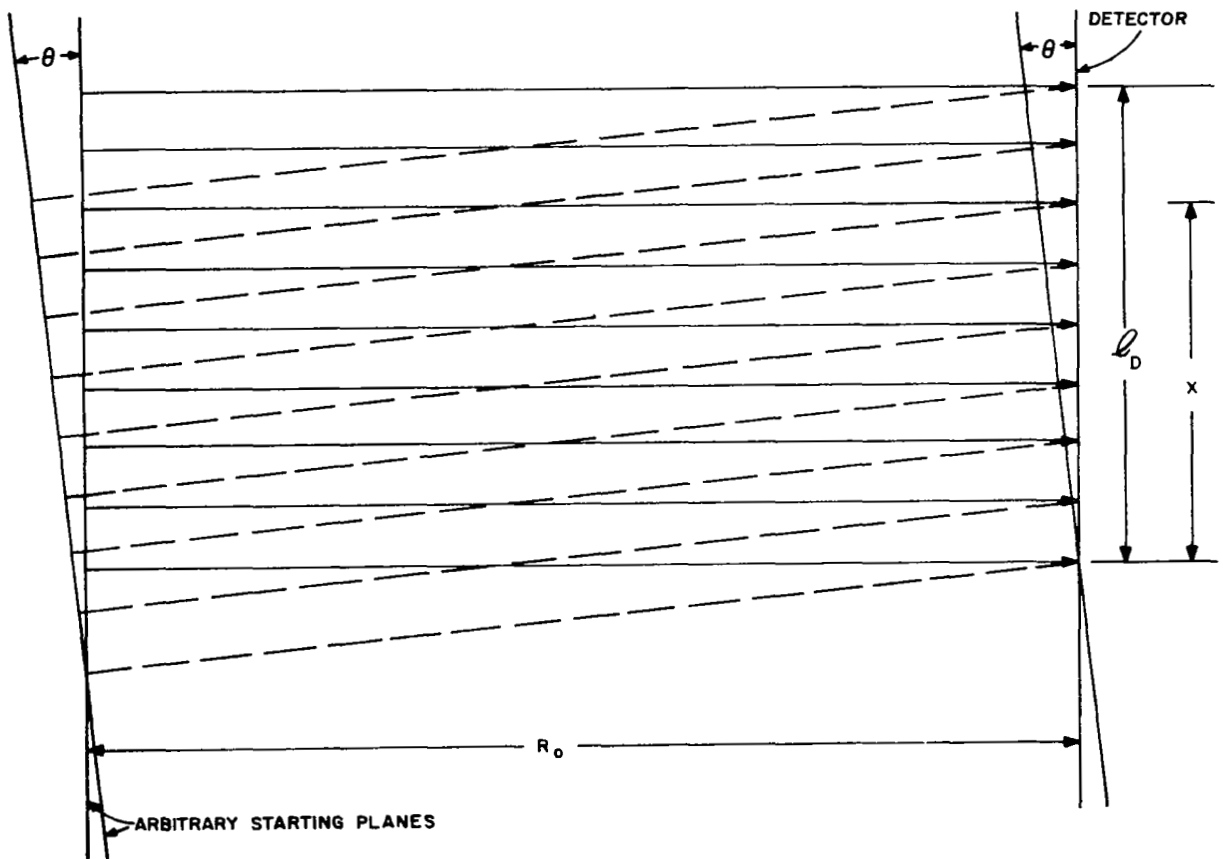

Figure A-1 Heterodyne Geometry

Starting from the arbitrary planes at time t, both LO and signal returns will be delayed in time such that:

$$e_{LO} = E_{LO} \sin \left[\omega_o (t - \tau_o) + \phi_{LO} \right] \tag{1}$$

$$e_S = E_S \sin \left[\omega_o (t - \tau_i) + \phi_S \right] \tag{2}$$

In Equation (1), the time delay (τ_o) is a constant, since the LO rays, by definition, are coaxial. This is not true for the signal. Assuming the misalignment is small, the signal must travel a distance $\chi \theta$ further than the LO to reach the detector. Therefore:

$$\tau_o = \frac{R_o}{c} \tag{3}$$

$$\tau_i = \frac{R_o + \Delta R}{c} = \frac{R_o + \chi \theta}{c} \tag{4}$$

Substituting Equations (3) and (4) into Equations (1) and (2), respectively:

$$e_{LO} = E_{LO} \sin \left[\omega_o t - \frac{\omega_o R_o}{c} + \phi_{LO} \right] = E_{LO} \sin \left[\omega_o t - \frac{2\pi R_o}{\lambda} + \phi_{LO} \right] \tag{5}$$

$$e_S = E_S \sin \left[\omega_o t - \frac{\omega_o R_o}{c} - \frac{\omega_o \chi \theta}{c} + \phi_S \right] = E_S \sin \left[\omega_o t - \frac{2\pi R_o}{\lambda} \right.$$

$$\left. - \frac{2\pi \chi \theta}{\lambda} + \phi_S \right] \tag{6}$$

where:

$$\omega_0 = 2\pi f_0$$

$$\lambda = c/f_0$$

Equations (5) and (6) are, of course, simplified versions of a somewhat more complicated model; i.e., the situation is simplified to a two-dimensional representation in t and χ, with no Doppler shift considered. These simplifications, however, will not affect the end result.

Heterodyning the signals of Equations (5) and (6) will yield the beat signal (neglecting the components at $2\omega_0$):

$$e_B(t, \chi) = \frac{E_{LO} E_S}{2} \cos\left[\frac{2\pi\chi\theta}{\lambda} + (\phi_{LO} - \phi_S)\right]\left(\frac{volts}{cm}\right) \qquad (7)$$

Assuming, for simplicity, that $\phi_{LO} = \phi_S$ (this is true when the same laser is used as transmitter and LO):

$$e_B(t, \chi) = \frac{E_{LO} E_S}{2} \cos\left(\frac{2\pi\chi\theta}{\lambda}\right) \qquad (8)$$

Equation (8) represents the beat voltage expected at any point (χ) on the detector. The total voltage anticipated of all points on the surface of the detector is obtained by integration of Equation (8) with respect to χ over the limits of $\chi = 0$ to $\chi = \ell_D$. This yields:

$$e_B(t) = \int_0^{\ell_D} \frac{E_{LO} E_S}{2} \cos\left(\frac{2\pi\chi\theta}{\lambda}\right) \, d\chi \quad (volts) \qquad (9)$$

A-4

$$= \frac{E_{LO} \, E_S}{2} \quad \frac{\lambda}{2\pi\theta} \quad \sin \frac{2\pi\chi\theta}{\lambda} \quad \Bigg|_{0}^{\ell_D} \tag{10}$$

$$= \left(\frac{E_{LO} \, E_S}{2} \right) \left[\frac{\sin \left(2\pi\ell_D \, \theta/\lambda \right)}{2\pi \, \theta/\lambda} \right] \tag{11}$$

Equation (11) is of the form $\sin K \, \epsilon/\epsilon$, and goes to zero whenever $2\pi\ell_D \, \theta/\lambda = \pi$. Therefore:

$$\frac{2\pi\theta\ell_D}{\lambda} = \pi \tag{12}$$

and;

$$\theta = \frac{\lambda}{2\ell_D} \tag{13}$$

If the wavelength (λ) is, for example, 1.065 μ and the detector length is 1 cm., then the critical angular value for θ, when the detector output is zero, is (by substitution into Equation (13)):

$$\theta = \frac{1.065 \times 10^{-4} \, cm}{2 \times 1 \, cm} = 0.5325 \times 10^{-4} \, (RAD.) = 10.984 \, \widehat{sec}. \tag{14}$$

This value represents a rather stringent requirement. However, one must bear in mind that the analysis presented above is an attempt to align two laser beams in a space either without lenses, or when the signal completely illuminates the physical detector.

However, in the case of a focused beam system, for example a 22-inch receiving lens system with the detector placed 78.23 cm away (f/1.4), the size of the Airy disk at the detector would be extremely small, 178.4 $\times 10^{-6}$ cm in diameter. Recognizing that

at the focus of a diffraction limited lens, the wavefronts in the
Airy disk are plane and perpendicular to the direction of the in-
cident light, the situation is identical analytically to that of
Figure A-1, except that the effective detector length is now
178.4×10^{-6} cm, instead of 1 cm. Again, substituting into Equa-
tion (13) will yield:

$$\theta = \frac{1.065 \times 10^{-4} \text{ cm}}{2 \times 178.4 \times 10^{-6} \text{ cm}} \times 57.3 = 17.1 \text{ (degrees)} \tag{15}$$

Equation (15) states that the signal will not go to zero until
the misalignment reaches 17.1 degrees. Alignment, in this case
is no longer a problem.

If, for practical reasons, one wished to restrict the angular
misalignment to one-quarter of a wavelength ($\pi/2$), substitution
into Equation (12) will yield:

$$\frac{2\pi\theta\ell_D}{\lambda} = \frac{\pi}{2} \tag{16}$$

and;

$$\theta = \frac{\lambda}{4\ell_D} \tag{17}$$

But the size of the Airy disk (ℓ_D) is given by the properties of
the lens:

$$\ell_D = \frac{1.22\lambda}{D} \quad F \tag{18}$$

where:

    F = focal length of lens

    D = diameter of lens

Substituting Equation (18) into Equation (17) yields:

$$\theta = \frac{\lambda}{4\left(\dfrac{1.22\lambda\ F}{D}\right)} = \frac{D}{4.88\ F} \tag{19}$$

where the angular misalignment (θ) is restricted to one-quarter wavelength. For the numbers assumed, θ equals approximately 8.5 degrees.